The Role of the Tumor Microenvironment in Cancer Stem Cell Regulation and the Development of Chemoresistance in Ovarian Cancer

by

Michael E. Bregenzer

A dissertation submitted in partial fulfillment
of the requirements for the degree of
Doctor of Philosophy
(Biomedical Engineering)
in the University of Michigan
2021

Doctoral Committee:

Associate Professor Geeta Mehta, Chair
Lecturer Stephen Guest
Assistant Professor Karen McLean
Professor Lonnie Shea
Professor Max Wicha

Michael Eric Bregenzer

mbregenz@umich.edu

ORCID iD: 0000-0002-6879-0534

Dedication

This work is dedicated to:

My family, from whom I have received undying support and motivation. Without you I would not be the person that I am today.

My wife, for being my best friend and closest confidant. You are the best part of each and every day.

Acknowledgements

Thank you to my advisor, my committee members, and University of Michigan's Research Core staff for all of the wisdom that you have imparted on me over the years.

To my co-workers, for all of your help, advice, and company.

To Maria Ward Rashidi and Shreya Raghavan, PhD for their work as the primary researchers behind Chapter 2.

To Pooja, for being my Tumoroid teammate, and friend.

Preface

The work presented in this manuscript was completed under the supervision and guidance of Prof. Geeta Mehta. The following details the work that has previously been published and what work is intended for future publications (text and figures).

Chapter 1 contains introductory material adapted from previous publications[1,2].

Chapter 2 contains materials previously published in *Neoplasia*[3], *Clinical Cancer Research*[4], and *JCI Insights*[5].

Chapter 3 includes materials intended for publication in the immediate future (draft complete and circulating with collaborators).

Chapter 4 contains materials intended for publication.

Chapter 5 contains information published previously[1,2].

Table of Contents

List of Tables

List of Figures

List of Appendices

Abstract

Tumors are a complex mixture of cancer cells, non-cancer cells, extracellular matrix, and other stimuli. To maximize clinical translation of *in vitro* models, it is critical to recapitulate the high degree of complexity found *in vivo.* This work presents three novel *in vitro* high grade serous ovarian cancer (HGSOC) models that recapitulate key features of the HGSOC tumor microenvironment (TME).

HGSOC is characterized by high rates of chemoresistance development and recurrence due to the presence of cancer stem cells (CSCs) which are inherently chemoresistant and have the capacity to repopulate the entire tumor. The non-cancer cells in the TME, such as mesenchymal stem cells (MSCs), endothelial cells (ECs), and immune cells help to maintain CSCs and influence the classification of HGSOC molecular subtypes, which have variable clinical prognoses. However, it is unclear exactly how CSCs and the other TME cells collectively promote chemoresistance and poor outcomes.

To better understand this phenomenon, practical *in vitro* model systems that more closely represent *in vivo* microenvironments are needed. We hypothesize that development of more physiologically relevant *in vitro* models will contribute novel insights into TME-mediated CSC regulation and development of chemoresistance in HGSOC.

In aim 1 we developed a *3D in vitro* serial passaging model to study chemoresistance development in the context of CSCs. This model demonstrated increased proliferation, CSC marker experssion, tumorigenicity, chemoresistance, and a malignant gene signature in patient-derived spheroids over the course of long-term passaging. Treatment responses were reflective of

patient-specific chemoresistance development *in vivo*. Finally, we used this model to show that Metformin treatment can hinder CSC driven development of chemoresistance. This model facilitates research of patient-specific chemoresistance development and could serve as a pre-clinical screening tool.

In aim 2 we developed a tumoroid culture system that enabled culture of patient-derived tumor cells with controlled ratios of MSCs, ECs, and immune cells to study how non-cancer cells in the TME drive CSC maintenance and chemoresistance. We found composition-specific changes in CSC marker expression, increased tumorigenic potential, and increased chemoresistance in tumoroids with evidence of epithelial-to-mesenchymal transition (EMT), altered CSC phenotypes, a malignant matrisome signature, and a mesenchymal subtype molecular signature. Together, this indicates that the non-cancer cells in the TME contribute to the development of advanced, chemoresistant disease.

In aim 3, we generated tumoroids with 23 different cell compositions to evaluate how TME cell composition affects response to therapy. Drug assays revealed that different composition tumoroids respond differently to therapy and that the number of monocytes included in the culture was associated with the greatest resistance to therapy. Random forest models were able to predict drug response with moderate success and showed that nuanced differences in cell composition can influence drug response. We found that the strongest predictor of response to therapy was the total quantity of non-cancer cells. Overall, this model demonstrates the potential of using the TME composition to predict patient drug response and direct clinical management.

In conclusion, we demonstrate the utility of complex and realistic, yet practical *in vitro* models to study the influence of the TME and CSCs on chemoresistance and outcomes. Overall, the models presented in this work can be used to better understand the role of CSCs and the TME

in chemoresistance and clinical outcomes. This could ultimately lead to the development of novel therapies, enhanced clinical management, and improved clinical outcomes.

Chapter 1: Introduction

1.1 Introduction to Bioengineered Cancer Models

Tumors have long been viewed as the accumulation of a mass of aberrant cancer cells. However, research has repeatedly shown the dependence of cancer progression on a variety of environmental factors, including non-cancerous cells, mechanical stimuli, and the surrounding extracellular matrix (ECM), aptly naming it as a 'cancer-organ'. Although many *in vitro* and computational models currently exist, the complex and interdependent microenvironmental regulation of the 'cancer-organ' system at the dynamic tissue and molecular scale have not been fully addressed.

Tumorigenesis and cancer formation is a complex multistep process involving genetic, epigenetic, and metabolic alterations, and interactions with the microenvironment that transform normal cells into malignant ones. As part of this process, oncogenes get activated, and tumor suppressor genes get repressed, affecting cell proliferation, apoptosis, pro-tumoral inflammation, avoiding immune surveillance and destruction, promoting genomic instability, angiogenesis, and metastasis[6,7].

As the tumors progress, new aberrant blood vessels continue to sprout due to activation of angiogenic switches in order to sustain proliferating malignant cells. The excessively proliferating autonomous neoplastic cells invade the local tissue, following which they

intravasate into nearby blood and lymphatic vessels. Through these conduits, the disseminated cancer cells transit to distant organs, ultimately homing into specific niches after extravasating the blood/lymph vessel lumina. At the secondary sites, they form micro-metastasis, which include small nodules of cancer cells, followed by growth of these lesions into macroscopic tumors, leading to metastatic colonization[6,7].

Due to diverse interactions involved, cancers are highly heterogeneous organ-like masses. Their complex microenvironments not only contain the tumor cells, but also various infiltrating endothelial, hematopoietic, stromal, immune and other cell types, ECM components, biophysical characteristics and mechanical stimuli [8–10]. Interactions within microenvironment also help create metabolic changes, such as a hypoxic environment and nutrient fluctuations, which further contribute to heterogeneity of cancer cells.

With this multifaceted network of communication between the native tissue and the tumor taken into consideration, cancer is more aptly understood as a complex organ, dependent on and working within the various colonized organs. This view of cancer provides a realistic perspective which allows us to increase our understanding of the disease, and thus identify crucial aspects for facilitating drug screening and development of efficacious, individualized cancer therapies.

Investigative approaches and interpretation of the 'cancer-organ' system heavily influences research conclusions. For example, the growth of cells on 2-dimensional (2D) surfaces versus 3-dimensional (3D) constructs alters a cancer cell's response to chemotherapeutics, thus influencing drug development and perceived effectiveness[11]. Similarly, mechanical stimuli innate to the microenvironment and exacerbated by the growth and development of the tumor can alter the stemness of the cancer cells[12] along with metastatic

tendencies[13–15]. Meanwhile, cellular interactions between the non-malignant cell populations, immune components[16,17], and cancer cells influence the advancement of the disease, as well as, the response to common treatments[18]. Additionally, acellular aspects of the microenvironment, including soluble signaling and ECM composition and architecture, play a large role in phenotypic behavior[19,20] and thus the conclusions of experimental outcomes. Each of these factors uniquely impacts cellular components within the tumor microenvironment (TME), contributing to the complexity of the 'cancer-organ' system (Figure 1.1). However, our in depth understanding of these factors and their complex interplay is limited by current model systems, which fail to corroborate findings and elicit sufficient reproducibility within the field. This dissertation focuses on the development of novel bioengineered cancer models to study ovarian cancer and its associated chemoresistance and poor outcomes. This work specifically concentrates on models to study cancer stem cells and the role of the non-cancer cells in the TME within physiological, yet controllable microenvironments. I focus on the cellular component of the TME due to the capacity of the cells to directly influence the other factors of the TME (soluble signals, ECM, cell phenotypes, etc.)[2] The next section will review ovarian cancer and some of the key features in the heterogeneous TME.

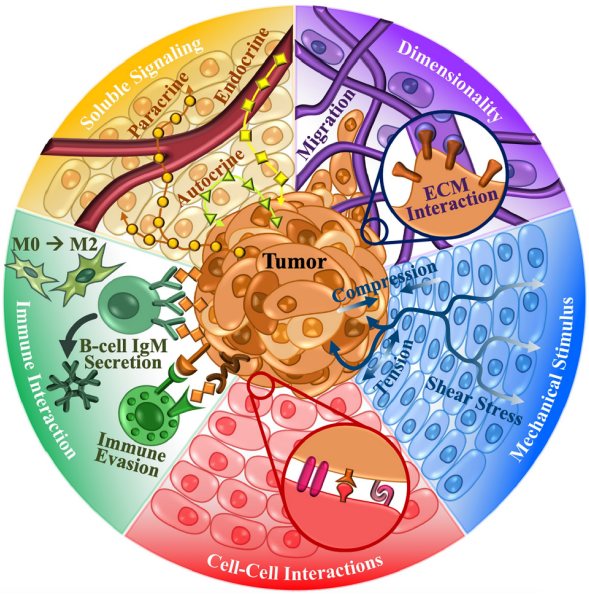

Figure 1.1: Components of the 'Cancer-Organ' model.
To develop an accurate multi-dimensional understanding of the structure, organization, and complex relationships in cancers, we need to consider the following factors. Heterogeneous cancer cells reside in a complex tumor microenvironment, which consists of mechanical stimuli, non-malignant cell-cancer cell interactions, soluble signals, and extracellular matrix (ECM). The dimensionality of cell culture influences cancer cell motility and cellular interaction with the surrounding cells and ECM. Mechanical stimuli including shear, compressive, tensile, and viscoelastic forces, dynamically influence cancer cells as the tumor grows. Similarly, cellular interactions through direct contact with surrounding non-malignant cells and soluble signals alter communication and downstream signaling. Interactions between immune cells and cancerous cells are highly complex and can lead to immune evasion and support of tumor progression. All of these characteristics play an integral role in tumor progression and are critical to forming a complete picture of the 'cancer-organ' system.

1.2 Introduction to Ovarian Cancer

Epithelial ovarian cancer (EOC) is the leading cause of gynecological mortality as well as the sixth most common cancer in women[21]. EOC is a heterogeneous disease that encompasses five major histological subtypes: low grade serous, high grade serous, mucinous, endometrioid, and clear cell. Each of these subtypes is characterized by unique molecular abnormalities and variable prognoses[22]. High grade serous (HGSOC) is the most prevalent subtype, making up about 70% of all cases and is associated with the worst prognosis[22,23]. The majority of patients are diagnosed with HGSOC in late stages with significant intraperitoneal spread due to lack of clear symptoms[22,24]. Despite high rates of successful first line of therapy, which usually involves surgical debulking followed by platinum and taxane combination therapy, about 70-80% of

women with HGSOC experience relapse within 5 years[23,24]. The recurrent tumors tend to be more chemoresistant and time to subsequent recurrence progressively decreases as chemoresistance increases until ultimately >65 % of patients succumb to the disease within 5 years[21,22].

HGSOC is characterized by high copy number variations, combined with ~96% of cases having TP53 mutations and about 10-22% with BRCA1/2 mutations[22,24]. Overall about 50% of HGSOCs are deficient in homologous recombination repair[22]. Mutations in *NF1*, *BRCA1*, *BRCA2*, *RB1*, and *CDK12* are also frequent [25,26]. However, importantly, there are only a handful of genetic mutations common between patients and they are not uniformly expressed across all HGSOC which complicates the use of targeted therapies [25,27,28]. Further complicating treatment of HGSOC is the high degree of cellular heterogeneity within and between tumors.

1.3 Introduction to Cellular Heterogeneity in Ovarian Cancer

Primary HGSOC can have highly heterogeneous genomic alterations, which are associated with high recurrent risk and poor prognosis [29]. Acquisition of genetic mutations over the course of disease progression is an example of the clonal evolution model of tumor heterogeneity wherein somatic mutations result in a heterogeneous mixture of different phenotypes that may respond differently to treatment [30]. In addition to genetic heterogeneity, cancer cells are also subject to epigenetic variation which influences cell phenotypes and thus treatment responses [31–33]. Epigenetic changes are heritable modifications to gene expression that do not change the DNA, but rather alter accessibility of genes through various mechanisms including DNA methylation, histone modifications, and microRNA. These epigenetic changes occur more often than genetic mutations and happen early on in tumor progression, highlighting their role in developing heterogeneous mixtures of tumor cells and the potential impact of drugs

targeting epigenetic dysregulation [33]. In ovarian cancer, an important example of epigenetic alterations and heterogeneity is the hypermethylation of *BRCA1*. This results in decreased *BRCA1* expression which in turn promotes genomic instability in the ovarian cancer cells and leads to heterogeneous phenotypes [34]. Importantly, epigenetic alterations are also reported to be involved in the reprogramming of cancer cells into a rare, but clinically relevant population of cancer cells called cancer stem-like cells (CSC)[35].

CSC are a clinically relevant subpopulation that is responsible for tumor initiation, metastatic disease, recurrence, and resistance to chemo/radio-therapy [36–40]. Like normal stem cells, CSC maintain a level of pluripotency, which enables self-renewal and differentiation [38,41,42]. In addition, CSC are highly plastic cells with a heterogeneous population defined by different epigenetic and metabolic states which they pass on to their progeny. CSC progeny comprise most of the tumor mass and tend to be more responsive to chemotherapy than CSC [42]. This ultimately leads to the development of a heterogeneous tumor cell population generated from distinct CSC from the heterogeneous CSC population [32,39,40,43,44].

Self-renewing tumorigenic CSC have been identified and isolated in many cancers, including, leukemia [45], breast [46], ovarian [47], colon [48,49], prostate [50,51], brain [52–54], pancreatic [55], melanoma [56], myeloma [57], and lung [58]. Importantly, while some CSC markers are shared between different cancer types, some cancers also have unique CSC markers [59]. Even among common CSC markers, recent work by Dzobo *et al.* found no consistent pattern of CSC marker expression in different cancers when evaluating the expression of CSC markers including ALDH1A1, CD44, CD24, EPCAM, ICAM1, CD90, CXCR4, NES, CD133, ABCB1, and ABCG2 in colon, pancreatic , lung, and esophageal cancers [60]. This cross-cancer heterogeneity in CSC populations may indicate that CSC targeting therapies may not share efficacy across cancer types. In ovarian

cancer, CSC are identified by an amalgam of biomarkers including, CD133, ALDH, CD44, CD24, and CD117, and their presence is an indicator of reduced progression-free survival and poor patient outcomes [61–73].

The resistance of CSC to treatment is attributed to overexpression of ABC transporters, enhanced ALDH activity, response to DNA damage, epithelial to mesenchymal transition (EMT), and dormancy [74,75]. Due to these resistance mechanisms, CSC are capable of surviving primary therapies and repopulating the tumor with a heterogeneous population of cancer cells [76]. In ovarian CSC, it has also been suggested that heterogeneity within the CSC population may increase the odds of the development of spontaneous escape variants [77]. Anoikis resistance is also a key feature of ovarian cancer CSC, which allows them to survive in non-adherent conditions like the malignant ascites fluid that accumulates in the peritoneal cavity in many ovarian cancer patients [40,76]. Despite the known presence of CSCs in ovarian cancer and their inherent chemoresistant properties, the exact mechanisms through which chemoresistance is developed is unknown. This is due in part to lack of adequate model systems that allow for practical evaluation of chemoresistance development in a cancer stem cell context, an issue that will be addressed in Chapter 2.

As described in section 1.1, tumors are not composed merely of cancer cells that cause their uncontrolled growth. Rather, they are a heterogeneous mixture of host cells and tumor cells that interact dynamically to drive tumor progression [78,79]. Specifically, the proportion of epithelial, endothelial, lymphocyte, myeloid, and stromal cell components varies significantly between tumors [80–82], serving as yet another degree of heterogeneity. The high degree of cellular heterogeneity both within and between patients' tumors can affect drug response and prognosis, causing major challenges in the clinical management of many cancers [79,83]. In section 1.4 we will

review the heterogeneity of cell compositions in various types of HGSOC microenvironments (Figure 1.2).

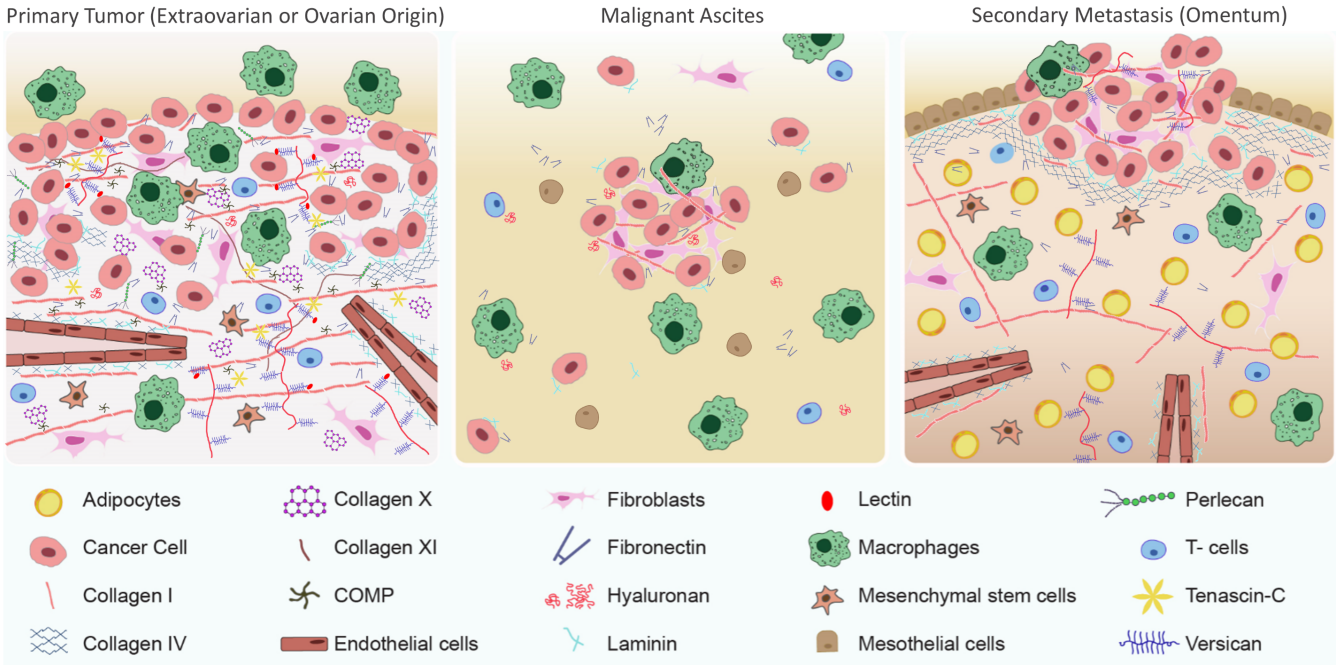

Figure 1.2: Distinct and heterogenous cellular and ECM composition and organization are present in the primary and metastatic ovarian cancers.
(Left) Production of ECM in the primary ovarian tumor gradually dysregulates over time, depositing new proteins normally not found in the ovarian germinal epithelium and tunica albuginea. The basement membrane is degraded in the primary tumor aiding in dissemination. The primary tumor is infiltrated by tumor associated macrophages, T-cells, carcinoma associated fibroblasts and endothelial cells. (Middle) The malignant ascites contains suspended single cells and cellular aggregates comprising of cancer cells, cancer stem-like cells (CSC), fibroblasts, mesothelial cells, macrophages and T-cells. ECM such as fibronectin, hyaluronan, and collagen type I are found within cellular aggregates, and in and around the fluidic ascites. (Right) Secondary omental metastases consist of colonizing cellular spheroids from the ascites. In these sites, cancers cells begin to produce new basement membrane, collagens, and hyaluronan. In all three TME, the cell and ECM sub-types are indicated with the representative schematic (not drawn to scale).

While there is overlap between the cells that are present in each microenvironment, their relative proportions vary and this can influence the signals received by the tumor cells [84]. In primary HGSOC tumors, epithelial cells have been shown to make up as much as ~68% of the population, while in a metastatic tumors, epithelial cells may only make up as few as 10% [84]. However, the immune cell composition is known to be highly variable and the stroma makes up anywhere from 10% to 60% of the tumor, indicating that a fair degree of heterogeneity exists even within the primary tumor [80–82].

CSC are enriched through dynamic interactions with cells in the surrounding TME, such as carcinoma-associated mesenchymal stem cells (CA-MSC), carcinoma-associated fibroblasts (CAF), endothelial cells (EC), and macrophages [78,79]. These interactions are exemplified by CA-MSC, which can be recruited to the primary tumor from distant locations in the body through soluble signaling or tissue resident mesenchymal stem cells (MSC) in the ovary or from the omentum. These MSC can then be converted into CA-MSC by the cancer cells [85–87]. Once converted, they have been shown to increase the number of CSC, enhance chemo-protection for CSC, and lead to tumor growth, either through paracrine signaling or indirectly by differentiation into CAF [87–95]. Importantly, CA-MSC are distinct from CAF and normal MSC, and can differentiate into several other critical components of the tumor stroma including fibroblasts, osteocytes, and adipocytes [85,95], further contributing to cellular heterogeneity. Additionally, EC in the primary tumor and secondary tumor locations can also support CSC and tumor cells [96,97]. Not only have EC been shown to induce self-renewal pathways in CSC [98], but they also protect them from cisplatin and paclitaxel treatment [99–101]. Similar to CSC recruitment of MSC to the tumor, CSC can recruit EC to the tumor through secretion of angiogenesis promoting signals, like VEGF, SDF-1. This occurs when hypoxia develops as a result of the tumor outgrowing its vasculature. Hypoxic microenvironments activate Oct-4, Sox2, Notch, VEGF, and c-MYC expression which stabilizes HIF-1α and promotes survival capacity of the CSC [59,78,102,103]. EC additionally contribute to disease progression through their role in the formation of the unique malignant ascites TME [104,105].

The malignant ascites is the buildup of fluid in the peritoneal cavity that accompanies various pathologies, including HGSOC [104]. While the exact cellular context of the ascites changes with disease progression [106], the predominant cell populations in the ascitic TME

include cancer cells [107,108], CAF [107,108], leukocytes [107,108], and mesothelial cells [109]. Within the cancer cell population, ascites harbor a high proportion of treatment-resistant CSC [108,110,111]. Cells within the ascites often aggregate, to form tumor spheroids that are highly malignant, metastatic, and resistant to chemotherapy [107,112,113]. The non-tumor cells in these spheroids influence cancer cell phenotype and promote malignant characteristics. Among them, CAF are fibroblasts that are reprogrammed into a pro-tumoral phenotype. They promote EMT, tumor cell attachment to the mesothelium, and subsequent displacement of mesothelial cells [80,107,112]. This ultimately allows tumor spheroids to initiate tumor growth at secondary locations. CAF also have immunomodulatory functions, can promote angiogenesis, inhibit cancer cell apoptosis, and produce and remodel ECM [80,107,114]. CAF also have the propensity to promote stemness, chemoresistance, and tumor growth [80,87,114].

Tumor associated macrophages (TAM), another predominant cell type found in the malignant ascites as well as the primary tumor, are similar in their ability to drive components of disease progression such as angiogenesis, angiostasis, metastasis, and the function of other immune cells in the TME [115–117]. Like CAF, ovarian cancer cells also reprogram macrophages that are recruited to the tumor, into a pro-tumoral phenotype termed alternately activated M2-like macrophages [117]. These macrophages can contribute to immunosuppression by attracting regulatory T cells, inhibiting the anti-tumor response of natural killer (NK) cells and cytotoxic T cells, and inhibiting maturation of dendritic cells (DC). They can also promote drug resistance, decrease apoptosis, and promote stemness in ovarian cancer cells [117,118]. Despite the widespread influence that M2-like macrophages have on tumor progression, their prognostic effect depends on the proportion of anti-tumoral M1 macrophages, which are also present in the TME. The M1:M2 macrophage ratio in patients can vary widely, resulting in different immune responses

and altered prognosis. Expectedly, higher M1:M2 ratios are associated with better outcomes for the patient [117,119].

In addition to macrophages, a host of other immune cells can be found in the ovarian cancer TME including NK cells, regulatory T cells, DC, CD8+ and CD4+ T cells, B cells, and myeloid derived suppressor cells (MDSC). Each of these cell types play a role in the complex immune response present in a tumor, with some cells like MDSC, regulatory T cells, and DC, serving tumor suppressive functions and others such as CD8+ and CD4+ T cells having antitumor effects [82,120,121].

Within the immune cell category there is remarkable heterogeneity, even at the same tumor site within the same patient [83,122–124]. The immune cell context of a tumor can change throughout tumor progression and can depend on factors like tumor location and treatment status [83,122,124]. For example, a recent study in HGSOC examined immunogenomic changes before and after neoadjuvant treatment in paired samples. Astoundingly, the authors observed that in treatment-naïve patients some areas of the same tumor could completely exclude immune cells, while different areas in the same tumor could be infiltrated [83]. Furthermore, they found that variation in immune cell genes, particularly those associated with T cells and NK cells, was responsible for the highest degree of variation between different treatment-naïve patient samples. This suggests the importance of immune heterogeneity in interpatient differences. Thorough characterization of these samples revealed that immune exclusion was associated with amplification of MYC targets and WNT signaling, which has previously been related to immune evasion [83,125]. The authors also noted increased NK cell infiltration and oligoclonal T cell expansion following treatment with neoadjuvant therapy, demonstrating the plasticity of the heterogeneous immune microenvironment when perturbed [83].

Another study of immune heterogeneity in HGSOC compared the immune cell infiltration in the primary tumor and its surrounding stroma to the infiltration of corresponding omental or peritoneal metastases. Interestingly, they found variances in the number of CD45+, CD3+, CD8+ and PD-1+ cells between all primary samples and matched metastatic samples. Furthermore, immune cell infiltration in the stroma of the omentum was observed to be significantly greater than in the primary tumor stroma [122]. Post treatment analysis of the same patients/samples, revealed that an increased intratumoral CD3+ infiltration in the primary tumor was associated with platinum sensitivity indicating that high pre-therapeutic CD3+ infiltration could be an indicator that platinum therapy will be effective. Similarly, higher intratumoral CD8+ infiltration in peritoneal metastases compared to the primary tumor was also associated with platinum sensitivity [122]. These results are concordant with previous work indicating the CD3+ and CD8+ T cells are prognostic indicators for ovarian cancer [123,126,127]. Contrarily, high PD-1+ expression in peritoneal metastases is linked to poor response to platinum therapy [122]. This finding is also logical as PD-1 activation is associated with decreased anti-tumor immunity [128]. Overall, this study highlights the potential utility of immune context characterization in predicting treatment responses and disease progression. The immune cell composition in HGSOC is indisputably heterogeneous and can influence treatment response and thus needs to be taken into account in development of personalized models.

Aside from the prominent cells found directly in the malignant ascites, mesothelial cells and adipocytes can both interact with the tumor at secondary tumor sites in the peritoneal cavity and from afar through soluble signaling in the ascites to exert additional influence on disease progression [112]. Mesothelial cells, for example, can secrete factors like lysophosphatidic acid (LPA) to promote tumor cell adhesion, migration, and invasion [129,130]. They can also produce

factors that inhibit drug induced apoptosis in cancer cells, following stimulation by the ascites [130,131]. Additionally, mesothelial cells are capable of transitioning into CAF via TGF-β signaling [132] to advance disease progression. Recently, mesothelial cells have even been found to induce platinum resistance in peritoneal metastasis through cell-to-cell interactions [133].

Adipocytes are prominent in the omentum, which is one of the most common sites of ovarian cancer metastasis, as well as subcutaneous tissues and the mesenteric membrane. From these locations, adipocytes can interact with tumor cells through secretion of adipokines and lipokines. Specifically, adipocytes in the omentum can attract cancer cells through IL-8 secretion and promote their proliferation through transfer of fatty acids. Importantly, adipocytes have recently been shown to confer chemoresistance to cancer cells through activation of the Akt pathway in cancer cells and secretion of a chemo-protective lipid, arachidonic acid [134]. Contrarily, adipocytes may contribute to suppression of ovarian cancer through cross-talk with ovarian cancer cells via secreted protein acidic and rich in cysteine (SPARC) [135]. These studies underscore the fact that the specific phenotype of the adipocytes and cancer cells may determine the result of adipocyte-cancer cell interactions.

As in the primary and ascites TME, ovarian cancer cells that have metastasized to secondary locations are subjected to even more diverse cellular microenvironments that can further alter the phenotype of cancer cells [136]. For example, in the omentum, adipocytes and mesothelial cells are in closer proximity to cancer cells, which is different from the TME in the ascites, where cancer cells are surrounded by mostly CAF and leukocytes. In the omentum, adipocytes are abundant with localized *milky spots* filled with immune cells, CAF, adipose-derived MSC, and vascular cells [137–140].

When discussing cellular heterogeneity, it is also important to note the role of hypoxia in producing heterogeneous cell populations. As tumors develop, they outgrow their vasculature which leads to development of hypoxic pockets of cells [141]. These pockets of cells develop altered metabolism in order to survive the harsh conditions, which influences their proliferation, migration, and invasion [40,142]. HIF-1α plays a central role in cellular response to hypoxia and its expression is associated with poor outcomes in ovarian cancer [2]. In ovarian cancer hypoxia has been implicated in CSC enrichment through HIF-1α mediated activation of NF-κb signaling and consequent upregulation of SIRT1 [102]. Not only has hypoxia been shown to enrich for cancer stem cell phenotypes in ovarian cancer, but it also promotes CSC chemoresistance via HIF-2α mediated upregulation of BCRP, a gene encoding a transporter that can expel drugs [102,143].

Hypoxic conditions also influence the non-cancer TME cells and how they interact with the cancer cells. For example, in hypoxic environments CAF stabilize HIF-1α leading to a metabolic switch to aerobic glycolysis and corresponding lactate production. This lactate can then be used by cancer cells to promote tumor growth [141,144]. Furthermore, CAF are also known for pro-tumorigenic ECM remodeling, which may be linked to hypoxia given that fibroblasts cultured in hypoxia and associated HIF-1 have been shown to promote fibrosis and elevated ECM transcripts when fibroblasts from various organs have been exposed to hypoxic conditions [141,145]. This ultimately can influence the metastatic potential of the cancer cells [141]. Intuitively, as mentioned above, hypoxia also results in the secretion of angiogenesis promoting factors such as VEGF by tumor and stromal cells. This can lead to some new vessels temporarily restoring normoxic conditions until rapidly growing tumor cells once again exceed the reach of the new vessels. This generates further heterogeneity by creating chronic and acute hypoxic regions and development of disorganized vasculature [141].

Unsurprisingly, immune cells are not exempt from the effects of hypoxia. Tumor cells in hypoxic conditions can recruit macrophages to the tumor through secretion of chemoattractants [146]. Once they arrive, hypoxia has been shown to polarize them into an M2-like phenotype to promote tumor progression [146]. Interestingly, myeloid-derived suppressor cells (MDSC), which are normally thought to be immunosuppressive have been shown to enhance immuno-suppression in hypoxia and also to obtain an immuno-stimulatory phenotype [141]. A final example of the role of hypoxia in cellular heterogeneity stems again from the metabolic change in cancer cells brought about by HIF-1α stabilization and the switch to glycolytic dominated metabolism [40,141]. This switch ultimately creates competition for nutrients between the hypoxic cancer cells and T cells, a battle that T cells are unlikely to win. Without sufficient nutrients, the anti-tumor effects of T cells are stymied. T cells in hypoxia may even differentiate into regulatory T cells, which contribute to immunosuppression [141]. Given this evidence it is clear that as hypoxia emerges throughout a tumor, pockets of cells will also emerge with differential, often tumor supporting behavior and thereby contributes to cellular heterogeneity.

Given the effects that each cell type can have on tumor progression and chemoresistance, and the wide ranging TME present in ovarian cancer, it would be unreasonable to assume that a successful therapy for the primary tumor will be similarly effective in secondary locations such as the ascites or the omentum. Consequently, it is critical that these sources of heterogeneity be carefully considered when developing precision medicine models. The effects of this potential variability between and within patients' tumors are compounded by the ECM in the TME. The various cell types within primary and metastatic tumor sites remodel the ECM in a context-specific manner, which in and of itself impacts drug response (Table 1.1).

Table 1.1: Impact of different cell types on the extracellular matrix.

Type of Cell	Impact on extracellular matrix (ECM)	References
Cancer stem-like cells (CSC)	Overexpress several collagens, periostin, mucin 1, and tenascin-C (TN-C). Highly express decorin, lumican, biglycan, versican, aggrecan. Produce high levels of hyaluronic acid.	147–165,165,166
Cancer-associated mesenchymal stem cells (CA-MSC)	Differentiate into CAFs and adipocytes. Remodel surrounding collagen matrix. Increase collagen production through JAK1 activation.	93,167–169
Cancer-associated fibroblasts (CAF)	Remodel ECM to provide ideal stiffness. Create actomyosin tracks in ECM for cancer cells to follow. Secrete versican and increased amounts of collagens. Upregulate COL1A1, COL1A2, COL3A1, COL4A1, COL4A2, COL5A1, COL5A2, COL6A1, COL6A3, and collagen support genes, secreted protein acidic and rich in Cysteine (SPARC), SERPINH1, and SERPINE1. Increased expression of MMP2, MMP11, and TIMP1.	84,170–173
Endothelial cells (EC)	Upregulation of lysyl oxidase homolog 2 (LOXL2). Secrete SPARC related modular calcium binding 2 (SMOC-2), cysteine rich with EGF like domains 2 (CRELD-2), microfibril-associated glycoprotein 2 (MAGP-2), lumican, extracellular matrix protein-1 (ECM-1). Highly express COL4A1, COL4A2, SERPINH1, and SPARC.	84,174,175
Tumor-associated macrophages (TAM)	Secrete osteopontin, osteoactivin, collagens, fibronectins, and truncated fibronectin. Secrete matrix metalloproteases, cathepsins, lysosomal and a disintegrin and metalloproteinase (ADAM) proteases, and the urokinase-type plasminogen activator (uPA). Secrete TN-C, fibronectins (FN1).	176–182
Adipocytes	Upregulation of tumor necrosis factor (TNF-α), osteopontin, MMP9, versican, and leptin. Secrete and process collagen type VI. Secrete endotropin.	183–186
Mesothelial cells	Secretes collagen type I. Secrete fibronectin.	187,188
Myeloid derived suppressor cells (MDSC)	Secrete MMPs and cathepsins. Releases TGF-β to induce LOX production. Remodel basement membrane.	189–191

Neutrophils	Secrete MMP-9 during angiogenesis.	[192,193]
Dendritic cells	Release indoleamine 2,3-dioxygenase (IDO) which catalyzes tryptophan and prompts tumor angiogenesis and metastasis.	[194]
B cells	Generate interleukin 10 (IL-10) and immunoglobulins (IgG) which form antigen-IgG complexes to recruit immunosuppressive myeloid cells.	[195]

1.5 Precision Medicine

As a result of the high degree of heterogeneity between and within patient's tumors, there is a clear need for precision medicine in HGSOC wherein therapies are specifically optimized based on molecular profile, cancer type, stage, and biomarkers for each patient. This process currently involves obtaining the genetic profile of the patient, which is then used to anticipate patient specific drug metabolism, response, and toxicities. However, importantly, there are only a handful of genetic mutations common between patients and they are not uniformly expressed across all HGSOC which complicates the use of targeted therapies [25,27,28] In addition, the efficacy of cancer cell-targeting therapies are often compromised by the non-cancerous components of the TME [2,196,197]. This includes tumor supporting cells and tumor secreted ECM which form complex multifaceted interactions with cancer cells that act to modulate chemoresistance [111,198–200]. Unfortunately, high level cell-cell and cell-ECM interactions are often omitted in contemporaneous model systems leading to underrepresented cellular, molecular, and ECM heterogeneity and substantially impacting their clinical translation potential [201–203].

Consequently, a long term goal of precision medicine entails thorough analysis of the genetic, molecular, cellular and ECM composition of patient biopsies, performed concomitantly with pathologic diagnosis, to guide construction of personalized *in vitro* models. Generating 3D microscale models based on this comprehensive analysis of each patient's tumor would be

followed by high throughput drug screening assays. This process would have numerous applications, ranging from personalized drug screening to identification of novel biomarkers. If successfully implemented, these applications have the potential to change the landscape of precision medicine and decrease mortality rates in many cancers. In this work we present models with potential in personalized medicine in a HGSOC context. However, we postulate that these same methods can be extended to different epithelial cancer types with their own unique genomic, molecular, and microenvironmental characteristics [31,204,205]. Using HGSOC as a model disease allows us to highlight specific differences in the TME, which may not be ubiquitous in all other epithelial tumors, but serves as a starting point from which pragmatic parallels can be drawn to other tumors.

1.5.1 Current Models of Cellular Heterogeneity

Conventional approaches to drug screening include the use of isogenic cell lines in 2D culture or propagated as xenografts, genetically engineered mouse models (GEMM), patient-derived xenografts (PDX), and patient derived organoids (PDOs) [2,206–208]. While 2D cell line cultures are easy to use and inexpensive, they have long been known to poorly represent *in vivo* conditions, making observed drug responses unreliable [209]. Newer 2D models might use cell lines derived from patient samples, however generation of a new cell line is prone to low success rates and fibroblast contamination. Moreover, the cell lines that are successfully established will have persevered through a strong selection pressure in 2D *in vitro* conditions making them a poor representation of the heterogeneous tumor cell population [204].

GEMM and PDX on the other hand are labor- and time-intensive, making it challenging for them to contribute to humanized drug screening and individualized therapy on a clinical scale [204,209,210]. Furthermore, GEMM are limited in their ability to consistently generate tumors on a

reliable timeline as these tumors form with heterogeneous latency periods and growth rates [211]. PDX formed from heterogeneous populations of patient cells maintain cellular heterogeneity, however are susceptible to copy number alterations with passaging and loss of human immune cells in the tumor which may result in unrepresentative drug responses compared to the patient responses [212]. The immunocompromised nature of PDX [211] also prevents evaluation of a functioning immune system in drug response. Overall, mouse models have struggled to translate into the clinic with only about 5% of the drugs tested in mouse models performing well enough in phase III trials, to be licensed for clinical usage [212]. However, a promising newer variation of mouse model, called 'humanized mice' has been developed with human immune cells, allowing for evaluation of tumor interactions with the immune system [212]. Despite this improvement, the technical challenge of developing these models remains, and hinders use as high throughput screening systems. Furthermore, these systems also offer less control over the exact cell composition in the culture, complicating their use in parsing apart the interactions of each cell type in the tumor microenvironment.

On the other side of the spectrum, 3D *in vitro* co-cultures are ideal for high throughput drug screening and have played an important role in our evaluation of interactions between two or more cell types in the TME. For example, using recently developed 3D co-culture heterospheroid of CSCs and CA-MSCs, PDGF and Hedgehog crosstalk was found to be a key signaling mechanism, involved in increasing stemness, metastatic potential, and chemoresistance in CSCs [213]. Similar heterospheroid models were utilized to show that ovarian cancer cells reprogram normal ovarian and omental MSCs into pro-tumoral CA-MSCs, presenting evidence that ovarian cancer cells catalyze the formation of their own pro-tumoral microenvironment [85]. Similarly, to dissect the signaling between immune cells and ovarian tumor cells, recent 3D

models have featured co-cultures with immune cells [104,214]. Ovarian cancer cells form spheroids in the ascitic fluid due in part to their interactions with macrophages, and these heterospheroids are thought to aid in transcoelomic metastasis [118]. Utilizing a hanging drop non-adherent 3D suspension model, ovarian CSC and activated macrophages can be brought in close association, simulating the physiologic environment of non-adherent malignant ascites. These 3D heterospheroids illustrate that pro-tumoral macrophages promote chemoresistant and invasive phenotypes in CSC, further leading to CSC enrichment. This model was used in the discovery that reciprocal paracrine signaling via WNT/β-catenin between macrophages and ovarian CSC promoted pro-tumoral environments including polarization of macrophages into M2-like phenotypes, and increased expression of the stem marker ALDH in CSC. This suggested that the WNT/β-catenin pathway could be a potentially effective target for new therapeutics to specifically eradicate the immuno-modulation of macrophages by CSC that contribute to recurrent disease [215]. These types of models have been made with tumor cells and endothelial cells [216], mesothelial cells [217], and adipocytes [135]. While co-cultures are advantageous in examining interactions between two or three cell types, they are still often over simplified by omission of key cell types and/or culture in non-physiologic microenvironments.

Lying in the middle of the spectrum between *in vitro* co-culture models and mouse models are patient-derived organoids. PDOs have been instrumental in our ability to replicate cell-cell interactions with realistic cell compositions *in vitro* and have had some success in predicting drug response [204,209]. PDOs are formed from either a single patient cell or a heterogeneous population of patient-derived cells grown into organoids that are embedded in basement membrane extract with an appropriate growth factor and small molecule cocktail to replicate the *in vivo* TME[204]. A panel of ovarian PDO have been successfully created for long

term *in vitro* culture of all subtypes of epithelial ovarian cancers. The panel of organoids was generated with cells from primary tumors, metastatic lesions, ascites, and pleural puncture. Through in-depth analysis, they demonstrated that tumor organoids maintain histological characteristics like nuclear and cellular atypia and expression of tumor biomarkers like p53 and pax8, similar to their source samples. This study showed that passaging the organoids did not result in any genomic changes compared to the original tumors. The organoids also show hallmarks of ovarian cancers, including the significant number of copy number variations, recurrent mutations and tumor heterogeneity[204]. However, a drawback of these organoids is their cell composition, as tumor organoids averaged 88 ± 23% of cancer cell content, while the actual tumors contained only 49 ± 9% tumor cell content across all samples [204]. HGSOC organoids have also been utilized for screening compounds, while maintaining the intra- and inter-patient tumor heterogeneity and mutation status, and matching the parental tumors genetically and functionally [218–220]. Another drawback to conventional organoids is the use of basement membrane extract, such as Matrigel, for organoid culture [204]. However, with undefined constituents, batch to batch variability, and poor biophysical properties, Matrigel does not accurately replicate the ovarian tumor stroma [221]. Moreover, Matrigel fails to replicate the physiology of the primary tumor, as the basement membrane is lost during disease progression. Finally, the dynamic interactions between the ECM and the cells in a tumor have a profound effect on tumor progression and clinical outcomes, which deems the use of extracts with uncontrolled ECM composition problematic [215,222–224]. While each of these model systems has their advantages, we present a unique tumoroid model system to study the interactions between cancer cells and the non-cancer cells in Chapter 3.

1.5.2 Molecular Subtyping in HGSOC

Despite the substantial heterogeneity in HGSOC, most patients receive the same treatment, meaning that some patients might respond to treatment while others will not[225]. In order to move towards a more precision medicine oriented approach, large-scale HGSOC datasets have been used to stratify ovarian cancer patients into molecular subtypes based on gene expression [25,226]. This stratification has prognostic and therapeutic relevance [227], however, no clinical use has been validated [228]. Tothill et al. were the first to define four molecular subtypes of high grade and endometriod ovarian cancer. In their work they identified that different molecular subtypes responded differently to therapy and were characterized by unique gene expression patterns determined with microarray analysis of 285 serous and endometriod tumors of the ovary, peritoneum, and fallopian tube. In particular, they identified an immunoreactive subtype that was characterized by higher numbers of intratumoral CD3+ T cells, lower stromal conent, and longer term survival. Contrarily, the high stromal response subtype had the worst survival, a trend that was mirrored to a lesser degree in the subtype with a high mesenchymal signature[229]. This finding suggests the need for patient stratification based on subtype to determine optimal clinical management. In fact a more recent retrospective study evaluated the outcomes of anti-angiogenesis inhibitor bevacizumab in each subtype be retrospectively classifying the tumors of patients in a clinical trial. This study showed that while overall survival benefits were miniscule, the benefit was greater on mesenchymal and proliferative tumors, which are typically associated with worse outcomes[230]. This serves as direct evidence for the need to stratify patients tumor in order to determine treatment course.

However, these subtypes have yet to be implemented regularly in clinical management due in part to lack of consensus about how many subtypes there are, if they have prognostic value, and lack of common biomarkers between subtypes defined by different labs[231–234].

Furthermore, recent studies by Izar et al. and others have found that certain subtype specific markers, such as those for the mesenchymal subtype, are expressed mainly in the stromal cells[82,235,236], effectively linking stroma and clinical outcomes. Although it remains unclear if there are nuanced differences in the stromal composition that have differential implication in treatment response and also how the stroma drives poor outcomes. Without this knowledge, the benefits of patient-stratification based on stroma composition may be limited. While this particular question could be investigated retrospectively using cell type deconvolution methods, the full effect of TME cell composition on drug response will likely remain unknown until sufficient single cell sequencing datasets have been generated[237]. Furthermore, the methods commonly used to predict a patient's response to therapy are based largely on expensive imaging or bulk-omics datasets with matched clinical annotations. While undeniably valuable, they are limited by low sample numbers and are not suitable to predicting response to therapies that have not been around long enough to have the required clinically annotated datasets[238]. The open question of whether or not nuanced differences in TME composition affect drug response, and the lack of suitable methods to predict drug response for new therapies motivated the development of Chapter 4.

1.5.3 Thesis overview and impact

In this work, 3D *in vitro* models to study the role of CSCs and the TME in chemoresistance in ovarian cancer were developed to address gaps in the currently available models. Chapter 2 specifically focuses on the development of a 3D *in vitro* serial passaging model and its application in studying the emergence of chemoresistance in a cancer stem cell context. We hypothesized that this *in vitro* model system would provide a clinically relevant model of the emergence of chemoresistance in ovarian cancer on a relatively short timescale.

With this model system we showed that proliferation, stemness, tumorigenicity, and chemoresistance were increased with passaging. Based on these results, we were able to derive a malignant gene signature for chemoresistance, stemness, and tumorigenicity based on changes in gene expression observed with passaging of two patient samples, which could potentially be used to identify more malignant disease. We also utilized this system to model patient-specific recurrence after treatment further suggesting its potential as a personalized medicine model. Additionally, the anti-CSC and chemoresistance effects of Metformin in ovarian cancer patients without diabetes within our model system demonstrated its promise in translational applications evaluating chemoresistance and drug efficacy on CSC populations. Consequently, our system could be used as a pre-clinical screening platform for CSC targeting therapies.

Furthermore, we developed a mathematical model to predict the emergence of ALDH+ CSCs across passages. With further development and validation, this mathematical model could potentially be utilized after just two passages in order to predict the emergence of CSCs and, by association, chemoresistant phenotypes in a patient-specific manner. If validated, this could prove to be a powerful tool to predict the degree of CSC enrichment in patients and inform clinical decision making.

Further research with this model system could provide unique insights into the primary drivers of chemoresistance in ovarian (and other) cancers. Particularly, coupling this method with -omics technologies could allow for analysis of genetic, epigenetic, protein, and metabolic changes that occur as chemoresistance is developing. This type of study could provide a comprehensive view of chemoresistance and may indicate novel pathways to study further *in vitro.* Following experimental validation, therapies targeting the key pathways in chemoresistance could be developed and validated in our serial passaging model before

proceeding through the drug development pipeline. Overall, 3D *in vitro* serial passaging is a reliable and reproducible model of clinically relevant development of chemoresistance with a myriad of potential research and translational applications making it a valuable tool for cancer research.

In chapter 3, we focus on the role of the non-cancer TME cells on CSC enrichment and chemoresistance. We hypothesized that complex multi-cellular 3D tumoroid culture would result in CSC enrichment and corresponding increase in chemoresistance and malignant characteristics. With this model, we demonstrate the flexibility of the culture method with tumoroids formed with and without Matrigel as well as each of the non-cancer TME cell types. This type of experimental flexibility is important in evaluating the role of each cell type in a complex network of interactions as it allows for a single experimental variable to be adjusted in each experiment to observe how the perturbation affects the system. Unique to our tumoroid model is this experimental flexibility combined with a greater degree of cellular complexity than traditional co-cultures and less prevalent tri-cultures.

Using this model we show that tumoroid culture results in altered CSC phenotypes, increased tumorigenicity, increased chemoresistance, enhanced EMT phenotypes, and expression of a malignant matrisome signature. Since culture with all four cell types results in these increased malignant characteristics, and tumoroid culture with different cell compositions is possible, the role that each TME cell type plays in the development of not only CSCs, but all of these characteristics is within reach. Knowledge of the intricate effects of each cell type on these malignant processes and phenotypes can ultimately inform efforts to develop novel therapies and improve outcomes.

Further development of this model system with matched patient-derived TME cells and different combinations of immune cells, for example, could improve the physiological relevance. This would provide an opportunity to model patient-specific drug response in the context of heterogeneous cellular microenvironments. Additionally, more robust analysis of a panel of CSC markers with tumoroids from different patients would enhance our understanding of TME-mediated CSC maintenance and thereby advance CSC-TME targeting drug development efforts. More generally, this model serves as an example for other cancers and diseases, which could benefit from more comprehensive, yet highly controlled culture systems. Widespread implementation of these types of model systems could inspire the development of new treatments across a broad spectrum of fields.

In the third aim, the tumoroid culture system is used to evaluate the role of the TME cell composition in response to traditional therapies (carboplatin and paclitaxel) as well as novel therapies (pacma31, N773, and SC144). We hypothesized that nuanced differences in tumoroid cell composition would influence response to different therapies and that these compositions could be used to predict drug response using machine learning. We found that, indeed, different cell compositions responded differently to therapy, indicating that there may be more nuanced cell composition effects that need to be investigated in HGSOC molecular subtyping. Furthermore, we generate random forest models to predict therapy response based on TME cell composition. We observed that the models have moderate predictive performance, and analysis of variable importance suggests that despite differences in response due to different cell compositions, the most predictive factor is the overall TME cell quantity. With further development with matched patient-derived cells, this model system could be used as a patient-specific drug screening platform to evaluate the localized response to various therapies based on

local cell composition within the tumor, thereby accounting for intratumor cell composition heterogeneity. Moreover, it can be used to better understand how different subtypes and tumor cell compositions develop resistance to certain treatments and to identify the most universally effective treatments. Finally, this model system provides an opportunity to make pre-clinical drug response predictions for new up-and-coming drugs that have yet to accumulate bulk-omics datasets with clinical annotations with which predictive models could be made to direct treatment.

Overall, these aims seek to improve research paradigms of CSC and TME-mediated chemoresistance in ovarian cancer through the development of three model systems: 1) a 3D *in vitro* serial passaging model of the development of chemoresistance in a CSC context; 2) a complex multi-cellular tumoroid model system to facilitate the study of TME-mediated CSC regulation and chemoresistance; and 3) a tumoroid drug screening model to examine the impact of the TME on drug response *in vitro*.

Chapter 2 : Engineering *In Vitro* Models of Chemoresistance Development in Ovarian Cancer

2.1 Introduction

The first line of chemotherapy (combination of platinum and paclitaxel), although successful in ovarian cancer, often leads to recurrent chemoresistant disease [239–242]. Cancer stem-like cells (CSCs) are largely implicated for relapse of ovarian tumors, and the development of chemoresistance[110,243]. Therefore, chemoresistance and CSC- enrichment are recognized as major causes of failure for chemotherapy of ovarian tumors. Although advancement in genomic profiling has been successfully used to identify subtypes of ovarian cancer[244], its application to elucidating mechanisms of chemoresistance is still evolving and can be furthered with reliable and clinically relevant in vitro models of chemoresistance[240,242].

Several models have been developed to experimentally address and reproduce the complexity and heterogeneity of cancer and the pathobiologic mechanisms that underlie the poor survival of patients with ovarian cancers [208,240–242,245]. Given their relevance to tumor metastasis and relapse, models of in situ chemoresistance development are a primary target of study, for both fundamental understanding of cancer biology and the development of effective and targeted treatments. However, the currently available in vitro models are lacking in the ability to

understand the development of chemoresistance in situ. Moreover, the existing studies rely only on cell lines in which platinum resistance is derived *in vitro*, the mechanisms of which may have little or no relevance in the clinical setting [242,246]. Additionally, these models lack a direct study of chemoresistance within a CSC-context, and therefore, in vitro models that incorporate CSCs' role in emergence of chemoresistance are critically important for developing biomarkers of chemoresistant disease, and for effectively targeting ovarian cancer. Currently available models for the study of CSCs rely on reprogramming, identifying side population or CSC populations using surface marker expression, selection of cells resistant to chemotherapy, modulation of oxygen tension, among others [247–250]. While these models derive CSCs with moderate success, CSCs are notoriously plastic in *in vitro* 2D monolayer culture conditions, making biological queries cumbersome.

Therefore, in this chapter we present an engineered 3D ovarian cancer serial passage model that addresses the development of chemoresistance and the enhancement of CSC populations simultaneously. Previously, in ovarian and other cancers, serial passaging of spheroids *in vitro* and serial transplantation of tumor cells *in vivo* has been demonstrated to lead to increased tumor growth rates, and decreasing time to form tumors with increasing passage number [251,252].We combined the power of serial passaging with 3D hanging drop array spheroids described by us extensively in previous reports[4,253,254], to create a novel engineered serially passaged 3D spheroid platform. This model combines the advantage of spheroids grown on a 3D platform, as previously described, over conventional 2D culture, with the greater ease of an *in vitro* model compared to an *in vivo* model [4,253–255]. Moreover, compared to *in vivo* PDX serial passaging, our model is low cost, takes less time and can be applied to many more patient

derived specimens. Furthermore, in contrast to our model, under the same experimental conditions, serial passaging in 2D did not yield the same results.

Our model allows us to examine changing response to chemotherapy, along with a thorough investigation of proliferation, cell surface markers, and tumor initiating ability of serially passaged spheroids within a mouse xenograft in a reliably testable format. Using these experimental outcomes, we are able to inform our mathematical model describing the evolution of the CSC populations over the course of serial passaging ovarian cancer spheroids. By coupling our experimental data with a mathematical model, we can gain insights regarding CSC enrichment not otherwise possible, generate new hypotheses, and predict the outcome of experiments [256,257]. Given the correlation of drug resistance with CSC populations shown in our data and other reports [4,61], predicting CSC evolution allows us to infer the emergence of chemoresistance in a patient-specific manner within our model system. While there are many models of CSC population development [257–260], to our knowledge, none have been applied to a serial passaging platform to predict enrichment of CSCs. The unique strength of our math model is that it is informed by experimental data, including those obtained from patient samples. Moreover, the math model can be used to predict more complex environmental conditions that include hypoxia, stem cell plasticity, extracellular matrix physical–chemical properties, etc.

The innovation in our approach stems from the use of a powerful in vitro model to simultaneously assess the emergence of chemoresistance with CSC-enrichment, combined with gene sequencing queries that demonstrate the predictive and prognostic capability of this *in vitro* platform. Coupled with the mathematical model to predict CSC enrichment, this integrated platform has utility in guiding targeted therapies for ovarian cancers, and studying the underlying mechanisms of chemoresistant and recurrent disease.

2.2 Results and Discussion

2.2.1 Proliferation increased within the 3D engineered serial passage model.

The 3D engineered model of stemness and chemoresistance was established by serial passaging of non-adherent ovarian cancer spheroids on the hanging drop array. In order to evaluate the effect of the model on cell proliferation, the kinetics of cell growth in the 3D suspension were evaluated at each passage. At every passage in the model, spheroids were initially seeded at 100 cells per spheroid. This consistency was also evaluated by checking cell viability on Day 1, and no significant differences were present (Supplemental Figure 1). Furthermore, all three patient derived cells and cell lines (OVCAR3, Pt224, Pt412) formed spheroids with tight boundaries at every passage by Day 1, just 1 day after initial seeding of the cells into the 3D hanging drop array (Figure 2.1). The fold-changes in alamarblue fluorescence after 7 days of growth compared to Day 1, increased with serial passaging.

The alamarblue results indicated a linear increase in proliferation for OVCAR3 spheroids as passage number increased (Figure 2.1A,B). At P6, the fold increase in alamarblue fluorescence was 12.2 ± 2.3, as compared to the fold-increase at P1 of just 6.5 ± 3.3. Cell counts reaffirmed this increase in proliferation, with the number of cells per spheroid increasing two-fold from P1 to P6 (54 ± 8.4 to 118 ± 7.8, Figure 2.1B). Pt224 ascites cell proliferation also increased significantly with increasing serial passage, though to a lesser degree as compared to the OVCAR3 spheroids (Figure 2.1D,E). The corresponding values of fold-change in proliferation indicate a 6.2 ± 1.7-fold increase at P0, compared to a 7.2 ± 1.2-fold increase at P6. Lastly, the Pt412 cell spheroids underwent an increase from 4.4 ± 0.97-fold proliferation at P3, to 6.7 ± 1.4-fold at P6, higher than the initial P0 value of 5.7 ± 1.6-fold. However, in Pt412 spheroids, drop in proliferation was observed in P3 (Figure 2.1G,H). For all three ovarian cancer

cell types and patient samples, the fold-change in proliferation at P6 was significantly higher than the proliferation at P0. These results demonstrate that the model caused increases in proliferation in all 3 ovarian cancer cell types.

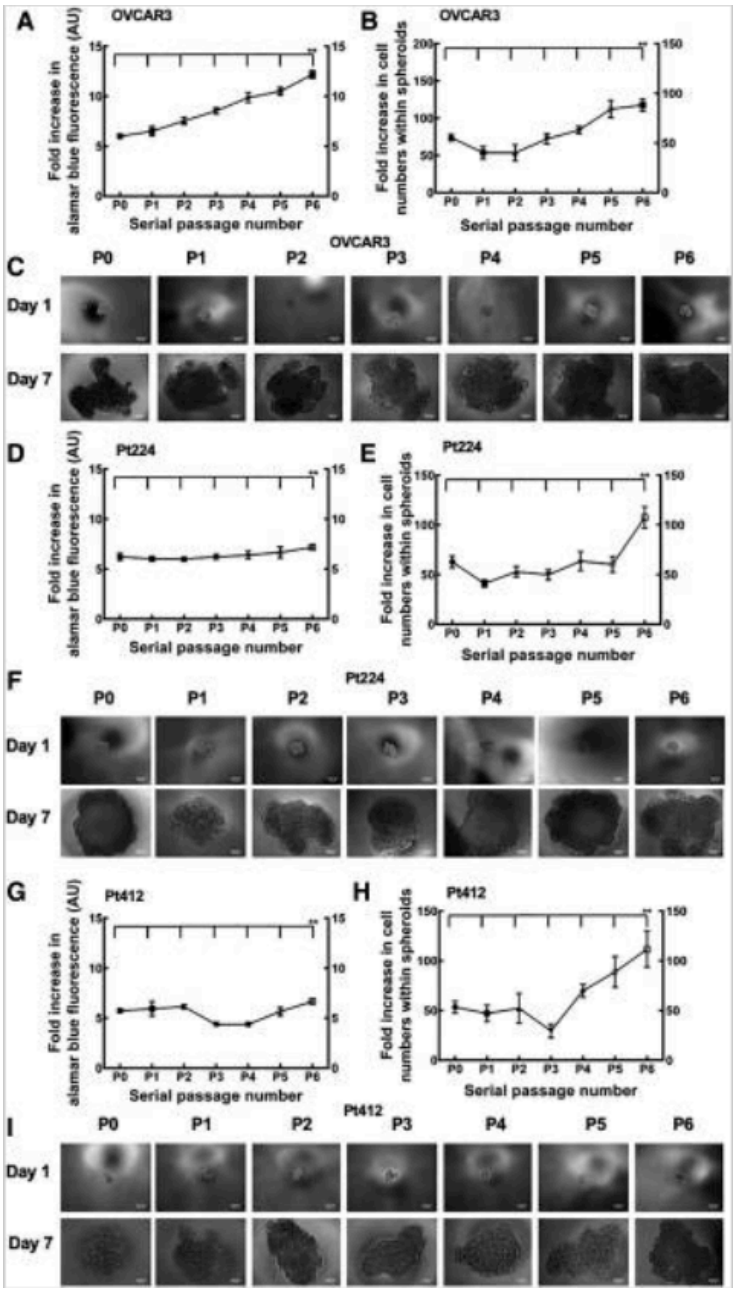

Figure 2.1: The 3D engineered serial passage hanging drop array model enhances proliferation in OVCAR3, Pt224, and Pt412OV spheroids initiated at 100 cells/drop.
*Fold increase in proliferation of **A)** OVCAR3, **D)** Pt224 cells, and **G)** Pt412 cells over 6 serial passages, based on alamarblue fluorescence at Day 7 normalized to Day 1 of each passage. Significant linear increase in proliferation*

*as serial passage number increased was observed ($n \geq 6$, with 150–200 spheroids formed for each experiment, **$P \ll .01$, one-way ANOVA, horizontal line indicates significant differences between serial passages [P0-P6] in proliferation). Number of **B)** OVCAR3, **E)** Pt224, and **H)** Pt412 cells/spheroid quantified with trypan blue at Day 7 of each passage. Significant linear increase in proliferation is observed as spheroids are passaged serially ($n \geq 6$, with 150–200 spheroids formed for each experiment, **$P \ll .01$, one-way ANOVA, horizontal line indicates significant differences between serial passages [P0-P6] in proliferation). Representative phase contrast micrographs of **C)** OVCAR3, **F)** Pt224, and **I)** Pt412 spheroids at Day 1 and Day 7 at each passage. Scale bar = 100 μm.*

2.2.2 Cancer stem cell populations were enriched in spheroids within this 3D engineered serial passage model.

In order to further examine the evolution of the CSC populations in our model, we quantified the ovarian CSCs expressing ALDH+ and CD133+ in the serially passaged spheroids. Given that chemoresistant CSCs prefer to form spheroids in suspension cultures, and can be enriched in such cultures, we assessed the effect of this model on the CSC subpopulation. Figure 2.2 shows the percentage of total cells that are ALDH+ and CD133+ in OVCAR3, Pt224, and Pt412 respectively. From P0 to P6 in the OVCAR3 serially passaged spheroids, there was 5.6-fold increase of ALDH+ cells from P0 to P6 (from 2.28 ± 0.33 to 12.7 ± 2.21 percent), and a 2.5-fold increase in CD133+ cells (1.58 ± 0.46 to 3.97 ± 0.30 percent; Figure 2.2A). A significant increase in ALDH+ and CD133+ cells were observed in the Pt224 cells as well, with nearly a 5.1-fold increase in ALDH+ cells from P0 to P6 (1.63 ± 0.08 to 8.44 ± 0.26 percent), and a 1.5-fold increase in CD133+ cells (2.27 ± 0.31 to 3.44 ± 0.5 percent; Figure 2.2B).

Although the ALDH+ cells in Pt412 spheroids started off relatively high, there was still a 2.4-fold increase in ALDH+ cells between P0 and P6 (18.7 ± 4.08 to 46.02 ± 5.16 percent; Figure 2C). The change in CD133+ population was especially high in Pt412 spheroids, with about a 7-fold increase between P0 and P6 (0.71 ± 0.09 to 5.18 ± 0.14 percent). The significant increase in ALDH+ and CD133+ cells in OVCAR3, Pt224, Pt412 spheroids serially passaged from P0 to P6 indicates that CSCs are enriched within this model. Moreover, serial passaging of

the same cells in 2D was erratic, and did not show the same increase in ALDH+ and CD133+ populations as we observed within the spheroids.

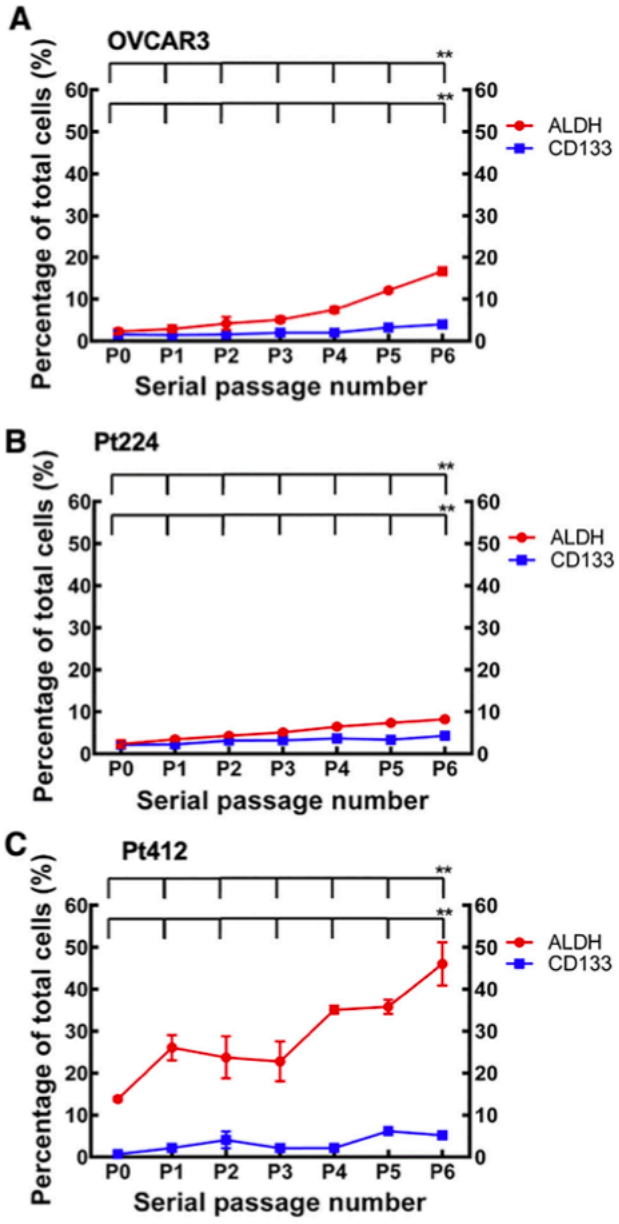

*Figure 2.2: This serial passage model increased populations of ALDH+ and CD133+ cells. Percentage of ALDH+ and CD133+ populations in **A)** OVCAR3, **B)** Pt224, and **C)** Pt412 spheroids quantified from flow cytometry. Significant linear increase in both ALDH+ and CD133+ populations from P0 - P6 ($n \geq 4$, with 150–200 spheroids formed for each experiment, **P ≪.01, one-way ANOVA, top horizontal line indicates significant differences between serial passages [P0-P6] in ALDH, and the bottom line indicates differences in CD133).*

2.2.3 Serially passaged spheroids in the 3D engineered model exhibited resistance to cisplatin and sensitivity to ALDH inhibitor.

After confirming that the CSCs were enriched in spheroids from P0 to P6, we hypothesized that resistance to cisplatin would also be observed as passage number increased within this model, and thus investigated the effectiveness of the model to enhance chemoresistance. Notably, there was an initial resistance to cisplatin in P0 following the first formation of spheroids in OVCAR3 that decreased upon passage to P1 (38% ± 2.23 viability in P0 to 27.3% ± 2.10 in P1). As hypothesized, when the spheroids were serially passaged from P1 to P6, this resistance to cisplatin increased (Figure 2.3). The viability of OVCAR3 spheroids fell to 27.3% ± 2.09 with cisplatin treatment at P1, and rose to 61.3% ± 2.36 at P6 (Figure 2.3A, C). Pt224 and Pt412 cell spheroids reacted in a similar manner as OVCAR3 spheroids, with cell viability values at P1 of 27.7% ± 1.23 and 46.9% ± 6 respectively following 50 μM cisplatin treatment, and 42.6% ± 3.19 and 69% ± 2.16 at P6 respectively (Figure 2.3, D, F, G, I).

Given that ALDH percentage increased with serially passaging, the spheroids were treated with 50 μM of Compound 673A, an ALDH inhibitor [261]. Cell viability in OVCAR3 spheroids dropped from 85.7% ± 2.6 at P1 to 69.8% ± 2.84 at P6 following treatment with the inhibitor (Figure 2.3B, C). An increase in sensitivity to Compound 673A resulted in cell viabilities of 98.2% ± 2.17 and 84.8% ± 2.63 at P1 and 63.3% ± 4.1 and 66.8% ± 3 at P6 of Pt224 and Pt412, respectively (Figure 2.3, E, F, H, I). These data corroborate increasing levels of CSCs in the spheroids as serial passage increased in this model. These data are consistent with our previous observations of ALDH inhibitor significantly reducing the viability of various

patient derived CSC spheroids [4]. Serially passaging spheroids in the hanging drop array caused the emergence of resistance to cisplatin and increased sensitivity to the ALDH inhibitor.

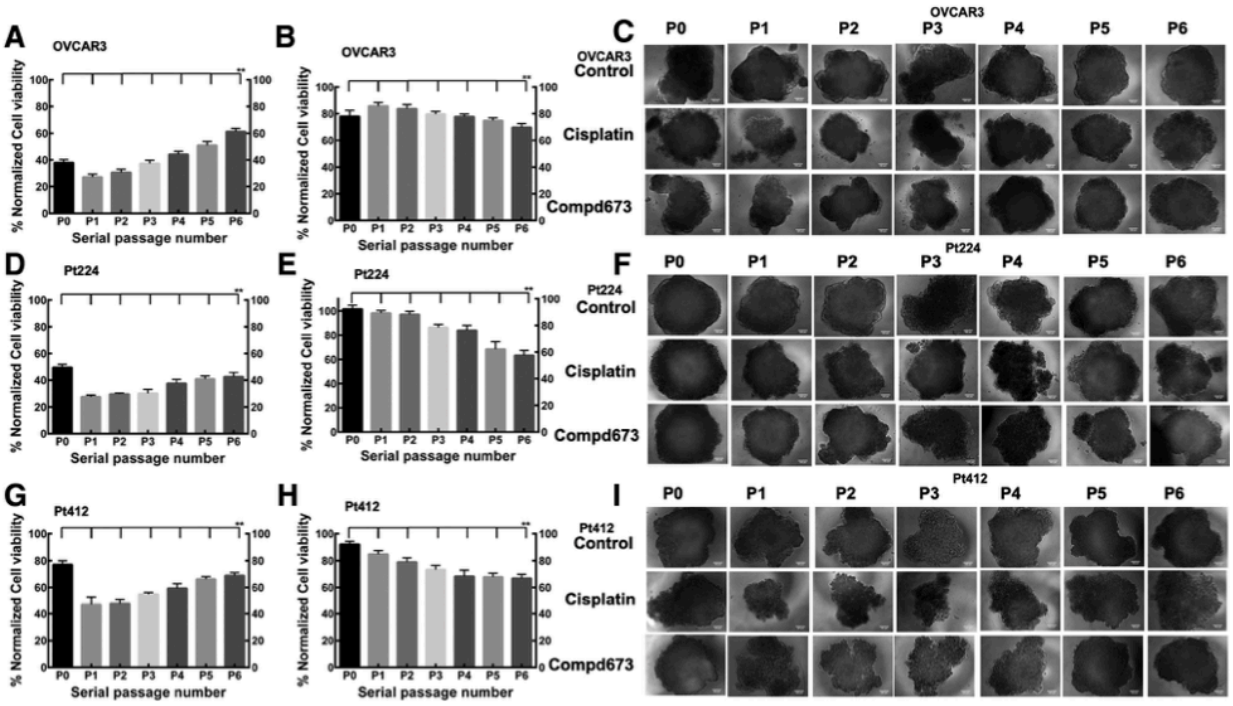

*Figure 2.3: Resistance to cisplatin and sensitivity to ALDH inhibitor Compound 673 increase within this model. Percent viability of **A)** OVCAR3, **D)** Pt224, and **G)** Pt412 spheroids 3 days following treatment with 50 μM Cisplatin. Significant increase in cell viability over serial passage was observed ($n \geq 6$, with 150–200 spheroids formed for each experiment per treatment group, **P ≪.01, one-way ANOVA, horizontal line indicates significant differences between serial passages (P0-P6) in cell viability after cisplatin treatment). Percent viability of **B)** OVCAR3, **E)** Pt224, and **H)** Pt412 spheroids 3 days following treatment with 50 μM of novel ALDH inhibitor Compound 673. Significant decrease in cell viability over serial passage was observed ($n \geq 6$, with 150–200 spheroids formed for each experiment per treatment group, **P ≪.01, one-way ANOVA, horizontal line indicates significant differences between serial passages (P0-P6) in cell viability after Compound 673 treatment). Representative phase contrast micrographs of **C)** OVCAR3, **F)** Pt224, and **I)** Pt412 spheroids at Day 10, following 3 days of treatment. Scale bar = 100 μm.*

2.2.4 ALDH expression in viable cells decreased following drug treatment of spheroids.

Further, we sought to quantify the changes in the CSC population after treatment with cisplatin or ALDH inhibitor that occur within this model. Thus, we analyzed the ALDH activity in viable cells after these treatments. The percentages of ALDH+ cells in spheroids treated with 50 μM Cisplatin or 50 μM Compound 673A decreased compared to the controls. The ALDH+

population increased significantly with increased serial passage number (Figure 2.4). However, treatment with cisplatin decreased the levels of ALDH+ cells, with the exception of P0 for OVCAR3 and Pt224 spheroids. The greatest fold difference between control and drug treatment was clear in P6 spheroids. The decrease in ALDH+ cells was most drastic following treatment with the ALDH inhibitor.

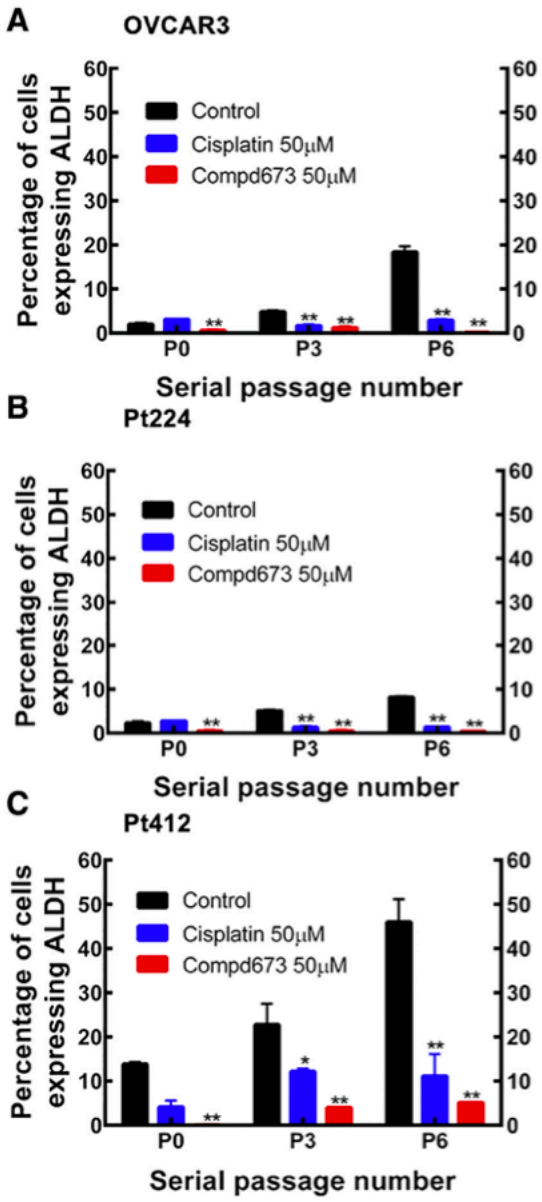

Figure 2.4: Evaluating CSC marker expression after treatment at P0,P3, and P6.
Population of ALDH+ cells decreases after treatment with Cisplatin and ALDH inhibitor Compound 673A. Percent of ALDH+ cells in ***A)*** *OVCAR3,* ***B)*** *Pt224, and* ***C)*** *Pt412 spheroids following treatment with 50 μM Cisplatin, 50 μM ALDH inhibitor Compound 673, or spheroid serum free medium. Significant difference between control and drug treatment in all cases ($n \geq 4$, with 150–200 spheroids formed for each experiment per treatment group, $^{**}P \ll .01$, $^{*}P \ll .05$, one-way ANOVA).*

2.2.5 Spheroids from the serial passage 3D engineered model initiated ovarian tumors in vivo, with later passage spheroids exhibiting higher tumorigenicity than early passage spheroids.

After confirming that our model enriched the ALDH+ population and increased chemoresistance, we observed how tumor growth could be impacted by enrichment in CSCs and chemoresistance within this model. This was done by subcutaneously injecting a limiting number of spheroids or 2D grown cells (1 million cells) as positive control into the flanks of NSG mice (Figure 2.5A,C). Tumorigenicity increased with serial passaging among tumors initiated from Pt224 P0, P3, or P6 spheroids. A similar trend was observed in tumors initiated from P6 and P3 spheroids as compared to P0 spheroids in mice injected with Pt412 derived spheroids (Figure 2.5B, Supplemental Figure 2). Following injection of 50 Pt224 spheroids, tumor growth from P6 spheroids was detectable as early as 2 weeks, with complete initiation of tumors from P3 and P6 spheroids by week 4 following injection. P0 spheroids completely initiated tumors by week 5. One million Pt224 cells from 2D culture-initiated tumors by week 4. Tumors from 2D cells reached the final tumor volume of 1500 mm^3 before the other tumor groups formed from 50 spheroids (Figure 2.5A). Following injection of 10 Pt224 spheroids, P6 spheroids had 100% initiation by week 4, and tumors from P3 spheroids achieved 100% initiation by week 5, with tumors from P0 spheroids initiated 100% by week 7 (Supplemental Figure 2). Similarly, after the injection of 4 spheroids, those from P6 initiated 100% tumors by week 4, meanwhile the lower passage spheroids did not initiate tumors before week 6. Additionally, when just one Pt224 spheroid was injected, P0 spheroids did not form tumors through 15 weeks of observation, though both P6 and P3 spheroids were able to form tumors, with P6 tumors initiating 3 weeks prior to P3 spheroids. This differential tumor initiation also corresponded with differential time-points for reaching final tumor volume, with tumors from P6 spheroids reaching the endpoint before P3 spheroids, which reached the endpoint before P0 spheroids. In mice administered with 10 Pt412 derived spheroids, P0, P3 and P6 passages initiated tumors by week 2, but P6 reached

the tumor volume endpoint earlier than the P0 and P3 passages, indicating a higher number of tumor initiating stem cells and higher tumorigenicity in P6. These results highlight the relevance of the serial passage model in modulating the tumor aggressiveness and accelerating rate of tumor formation in later passage spheroids.

Additionally, we examined the role of later passage spheroids in inducing larger tumor load and faster initiation using extreme limiting dilution analysis (ELDA)[262] (Figure 2.5D–G, Supplemental Table 1). The fitted model displayed vastly different tumorigenicity and CSCs in the three groups. Specifically, in case of Pt224, the CSC frequencies in P6 increased to 1 in 0.6, from 1 in 28.5 at P3, and from 1 in 62 for P0 spheroids (Figure 2.5D, F). Meanwhile for patient metastasis derived Pt412 sample, CSC frequency was estimated as 1 CSC per cell at P6, 1 CSC in 45 cells at P3, and 1 CSC in 92 cells at P0, which were significantly higher than CSC frequencies in patient ascites Pt224 spheroids. Therefore, Pt 412 demonstrated highly enriched cancer stem cell population in P6, as compared to P3 and P0 (Figure 2.5E, G). These findings underline the role of serial passaging in enriching and maintaining CSCs[263].

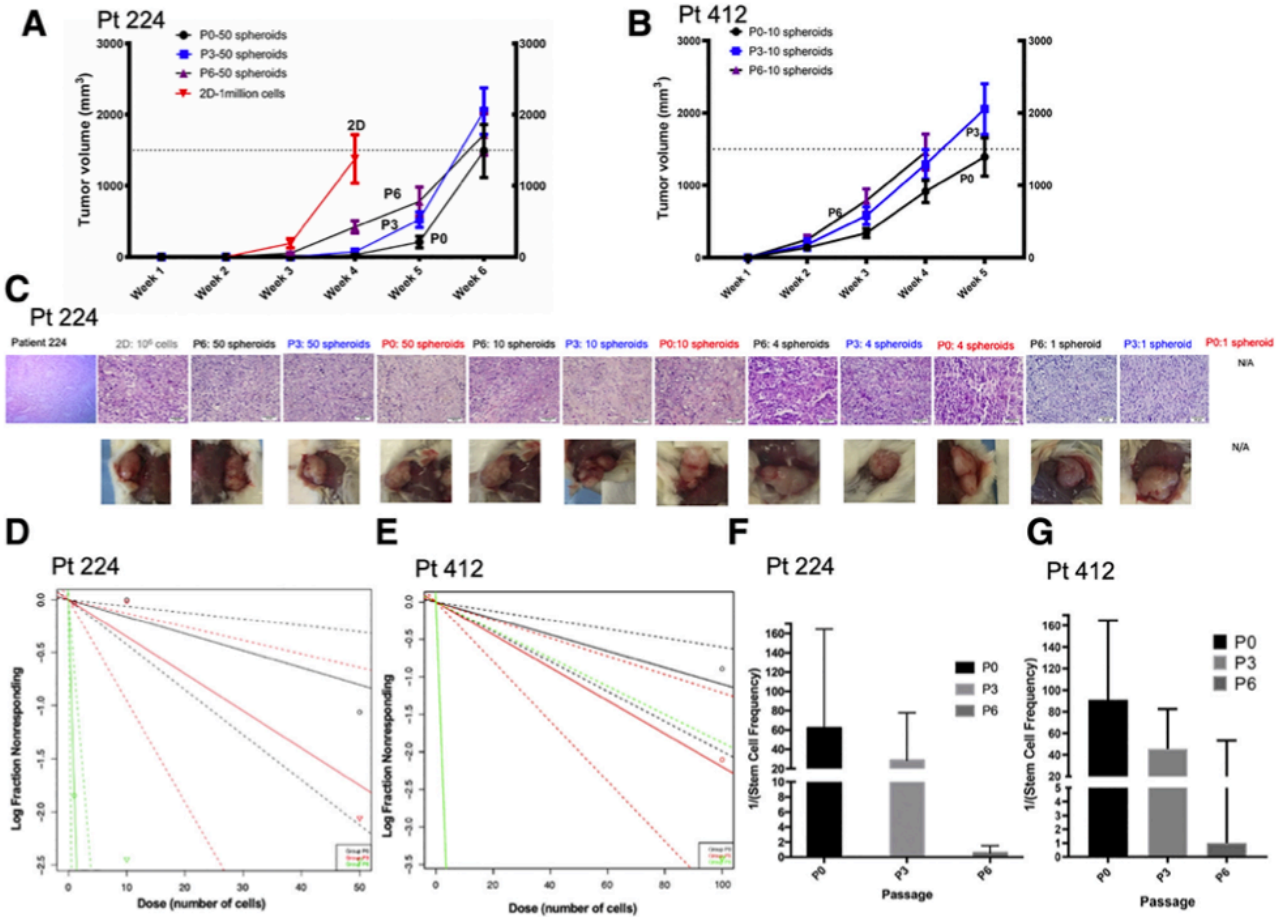

Figure 2.5: Spheroids from higher serial passage number within this model are more tumorigenic in NSG mice. ***A)*** *For Pt224, tumor volume as a function of time for 50 spheroid/s (n = 6 in each group). Fifty spheroids from P0, P3, and P6 all reached the endpoint of 1500 mm^3 by week 6, and 1 million 2D grown cells reached endpoint by week 4.* ***B)*** *For Pt412, tumor volume as a function of time for 10 spheroids (n = 6 in each group). 10, 100 cell spheroids from P0 and P3 reached the endpoint of 1500 mm^3 by week 5, while P6 group reached end point by week 4.* ***C)*** *Macroscopic pictures and photomicrographs of hematoxylin and eosin images of naïve patient tumor and xenografts observed in NSG mice with subcutaneous injections of spheroids or 2D grown cells. Scale bar = 50 µm.* ***D)*** *Plot for Pt224 of the log fraction of mice bearing no tumors in 4 weeks (Log fraction nonresponding) as a function of the number of spheroids injected in NSG mice at that serial passage (Dose). The slope of the line: log-active cell fraction; dotted lines: 95% confidence interval; down-pointing triangle: cell dose with 0 non-xenografted mice. The more vertical the line, the higher the percentage of stem cells in that passage (n = 6, ****P ≪.0001).* ***E)*** *Plot for Pt412 of the log fraction of mice bearing no tumors in 4 weeks (Log fraction nonresponding) as a function of the number of spheroids injected in NSG mice at that serial passage (Dose). The slope of the line: log-active cell fraction; dotted lines: 95% confidence interval; down-pointing triangle: cell dose with 0 non-xenografted mice. The more vertical the line, the higher the percentage of stem cells in that passage (n = 6, ****P ≪.0001).* ***F)*** *Inverse of frequency of stem cells as determined by Extreme Limiting Dilution Analysis (ELDA) between different passages for Pt224. Lower number indicates higher fraction of cancer stem cells in P6, compared to P3 or P0 (n = 6, ****P ≪.0001).* ***G)*** *Inverse of frequency of stem cells as determined by Extreme Limiting Dilution Analysis (ELDA) between different passages for Pt 412. Lower number indicates higher fraction of cancer stem cells in P6, compared to P3 or P0 (n = 6, ****P ≪.0001).*

2.2.6 Spheroids initiated with ALDH+ had greater proliferation compared to ALDH- cells.

Knowing that the serial passage hanging drop array model induced an increase in the percentage of ALDH expressing cells at later passages, we quantified the differences in the proliferation rates between spheroids initiated with ALDH+ and ALDH- cells. Spheroids initiated with ALDH+ cells had greater fold-changes in proliferation than ALDH- cells (Figure 2.6). Based on alamarblue fluorescence, a significant difference in proliferation was observed after a week of growth; with about a 5-fold difference in ALDH+ cells to near a 3-fold difference in ALDH- cells (Figure 2.6B). Moreover, there was a significantly higher percentage of cells expressing Ki67+ cells in the ALDH+ cells initiated spheroids compared to the ALDH- group (Figure 2.6C). This provides evidence that our model may be increasing the ALDH+ population over serial passage, and thereby causing the increase in proliferation that was observed.

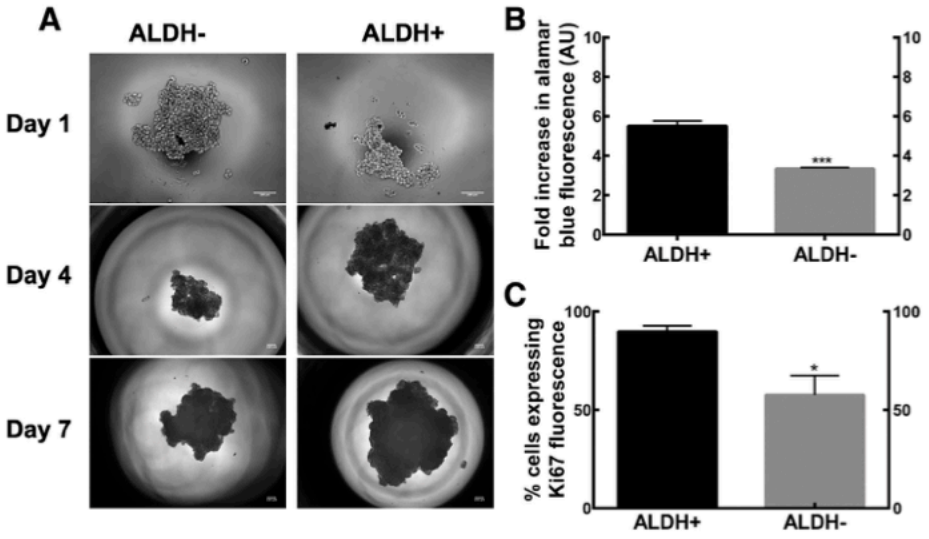

Figure 2.6: ALDH+ OVCAR3 spheroids have higher proliferation than ALDH- spheroids.
A) *Representative phase contrast micrographs of ALDH+ and ALDH- OVCAR3 spheroids at Days 1, 4, and 7 (Scale bar = 100 μm).* ***B)*** *Fold increase in proliferation of ALDH+ and ALDH- OVCAR3 cells, based on alamarblue fluorescence at Day 7 normalized to Day 1 of each passage.* ***C)*** *Percent of cells expressing Ki67 higher in ALDH+ spheroids, quantified via flow cytometry. ($n \geq 6$, with 150–200 spheroids formed for each experiment per treatment group, ***$P \ll .001$, *$P \ll .05$, one-way ANOVA).*

2.2.7 RNA sequencing reveals stemness, tumorigenic and chemoresistance signatures through in vitro passaging.

Using RNA sequencing, we assessed genome-wide changes to RNA synthesis and stability in Pt412 and Pt224 CSC spheroids that underwent early (P0), middle (P3), or late (P6) serial passaging in the 3D model. Generation of a PCA plot from our gene-expression data shows a clear difference in gene signature between each patient sample (Figure 2.7A). Similarly, we observed a definitive trend showing changes in gene signature within each patient sample with serial passaging. This trend was also evident in Pt224 and Pt412 heatmaps showing significantly up- and down-regulated genes for each patient sample across P0, P3, and P6 spheroids (Figure 2.7B).

Of the significantly up-regulated genes for Pt224 (553 genes) and Pt412 (507 genes), a total of 142 genes were commonly upregulated in both patient samples. From these 142 genes, we identified and binned 9 of the most highly upregulated genes associated with stemness (WLS[264,265], ALDH1A1 [69,266], BMP2[64,267], RSPO3[268,269]), tumorigenicity (MAGEB2 [270,271], BMP2[64], EFNB2 [272], SERPINE2 [273–277], HHIP[278–280], PTGS2[281–284]), and chemoresistance (WLS[264,265,285], ALDH1A1[286,287], BMP2[64], [281,288]PTGS2) based on the literature (Figure 2.7C, D). The upregulation of these genes between P0 and P6 for both patient samples was subsequently confirmed with qRT-PCR. While qRT- PCR confirmed the upregulation of all binned genes, ALDH1A1 was among the top two upregulated genes in both patient samples regardless of quantification metric (Figure 2.7D, E). Further analysis of 17 transcription factors previously associated with ovarian CSCs indicated that FOXA1 and LEF1 are significantly upregulated between P0 and P6 spheroids generated from Pt412 cells with the thresholds used in our analysis (Figure 2.7F)[289].

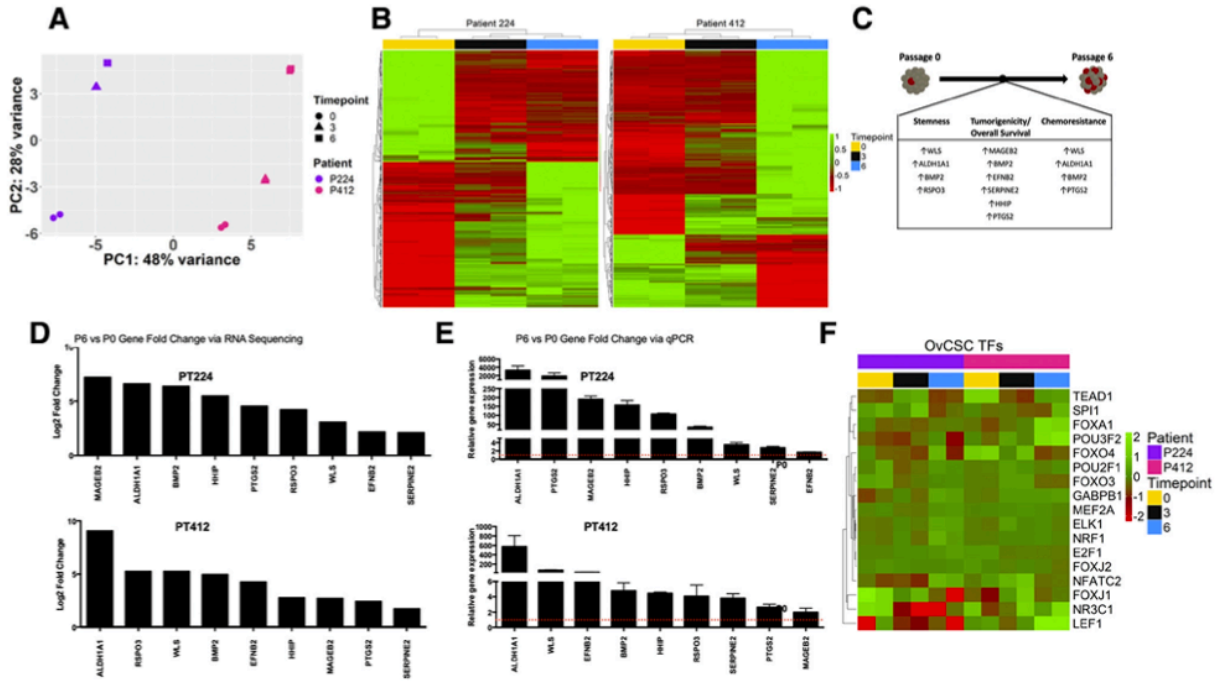

Figure 2.7: Stem-related pathways are enriched in late-passage spheroids.
A) *Principal component analysis demonstrated emerging differences in Pt224 and Pt412 samples as they proceeded through serial passages P0, P3 and P6;* ***B)*** *Heatmaps denoting changes in RNA-Seq between P0, P3 and P6 in Pt224 and Pt412 samples;* ***C)*** *Gene signature establishing the stemness, tumorigenicity and chemoresistance of serially passaged spheroids derived from common upregulated genes between both patient samples;* ***D)*** *Waterfall plots generated from RNA-Seq analysis of common upregulated genes in P0 Vs. P6 for Pt224 and Pt412;* ***E)*** *qPCR confirmation of genes from P0 Vs. P6 upregulated by RNA-Seq, included in the gene signature;* ***F)*** *Heatmap of expression levels of transcription factors commonly implicated in ovarian cancer stem cell maintenance.*

2.2.8 Mathematical modeling strongly predicts emergence of cancer stem cell populations, and tumorigenicity within serially passaged spheroids.

To further validate our experimental findings, and enhance the utility of our model as a predictive and prognostic tool, we developed a mathematical model describing the emergence of ALDH+ populations across 6 passages. In simulating the growth of a spheroid over 7 days for the OVCAR3 cell line (Figure 2.8A), as well as Pt224 (Figure 2.8B) and Pt412 cells (Figure 2.8C), we corroborate our experimental findings of increased proliferation in later passages. Spheroids formed from the Pt412 metastatic sample were predicted to exhibit the greatest

increase in proliferation (1.19-fold simulated P0- P6 increase vs. 2.1-fold experimental P0-P6 increase) compared to the OVCAR3 cell line (1.084-fold simulated P0-P6 increase vs. 1.6-fold experimental P0-P6 increase) and the Pt224 ascites sample (1.083- fold simulated P0-P6 increase vs 1.7-fold experimental P0-P6 increase). As expected, this increase in proliferation corresponded with increased ALDH+ percentages, with Pt412 spheroids exhibiting highest ALDH+ levels (35.61% simulated vs 46±5.2% experimental) after 6 passages (Figure 2.8G), followed by OVCAR3 spheroids (9.78% simulated vs 12.1±2.2% experimental) (Figure 2.8E) and lastly Pt224 spheroids (8.65% simulated vs 8.4±0.26%) (Figure 2.8F). These findings mirrored our experimental data confirming the ability of our model to reproduce biological trends. Interestingly, the model also predicts a plateau in cells per spheroid and ALDH+ cells within spheroids of each patient sample, which could not be perceived from our experimental data. This is especially evident when the model is used to simulate 20 passages, indicating that Pt412 cells per spheroid begins to plateau around passage 9 (9206 cells/spheroid), while the increased percentage of ALDH+ cells is predicted to plateau around passage 11 (~38.0%). On the other hand, Pt224 and OVCAR3 spheroids are predicted to plateau in cells per spheroid around passage 18 (5506 and 7160 cells/spheroid respectively) and in percentage of ALDH+ cells around passage 20 (~30.6% and ~28.7% respectively; Figure 8D, H).

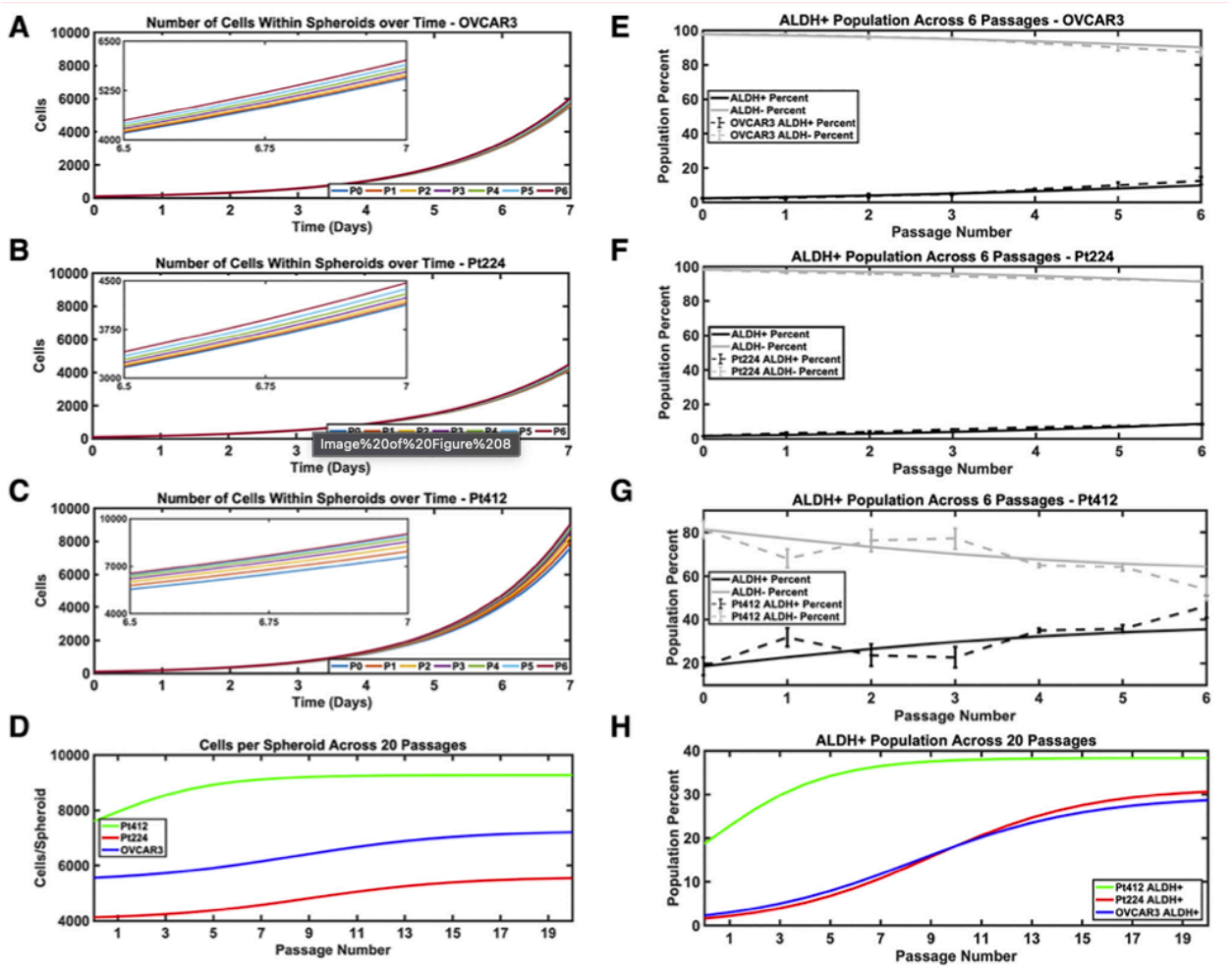

Figure 2.8: Mathematical modeling of 3D engineered serial passaging.
*Spheroid growth over the course of 7 days for each passage with the **A**) OVCAR3, **B**) Pt224, and **C**) Pt412. Insets illustrate increase in cell numbers per spheroid across passages from day 6.5 to 7. Emergence of ALDH+ population across 6 passages in the **E**) OVCAR3, **F**) Pt224, and **G**) Pt412. Experimental values are plotted as dotted lines with the standard error of the mean at each passage. **D**) Cells per spheroid and **H**) ALDH percentage simulated over 20 passages for OVCAR3 (blue), Pt224 (red), and Pt412 (green) spheroids.*

2.2.9 Serial passaging ovarian cancer stem cell spheroids to model tumor re-emergence in vitro.

Modeling tumor reemergence following cisplatin/673A treatment in vitro Following cisplatin/673A treatment, live cells from spheroids were sorted using flow cytometry to isolate cells that escaped cisplatin/673A treatment. Spheroids were reinitiated with these cells to preliminarily model tumor reemergence in vitro (Figure 2.9A). All three patient ascites samples reliably formed spheroids, indicative of the ability of residual viable cells to reform a "tumor" following cisplatin/673A treatment (Figure 2.9A). Flow analysis indicated that ALDH+ OvCSC progeny had reliably repopulated within these spheroids (Figure 2.9B), despite their initial depletion after cisplatin/673A treatment. Despite the differential response to therapy, the remnant resistant cells demonstrated similar proliferative capacity (Figure 2.9C). At the first repassage, the extent of repopulation of ALDH+ progeny did not match the original fraction present in these samples, except in Pt152 samples where the ALDH+ cells exceeded those in the original sample (5.1% in spheroids reemerged following cisplatin/673A treatment vs. 1.4% in spheroids originally initiated from the primary patient sample; Figure 2.9D). These spheroids were serially passaged over seven cycles, to demonstrate tumor reemergence over a significant time scale of 7 weeks *in vitro* (Figure 2.9E,F). Flow analysis indicated that ALDH+ OvCSC progeny had reliably repopulated within these spheroids (Figure 2.9E,F), despite their initial depletion after cisplatin/673A treatment. The extent of repopulation of ALDH+, CD133+, and ALDH+/ CD133+ progeny approached and even surpassed the original fraction present in the patient samples.

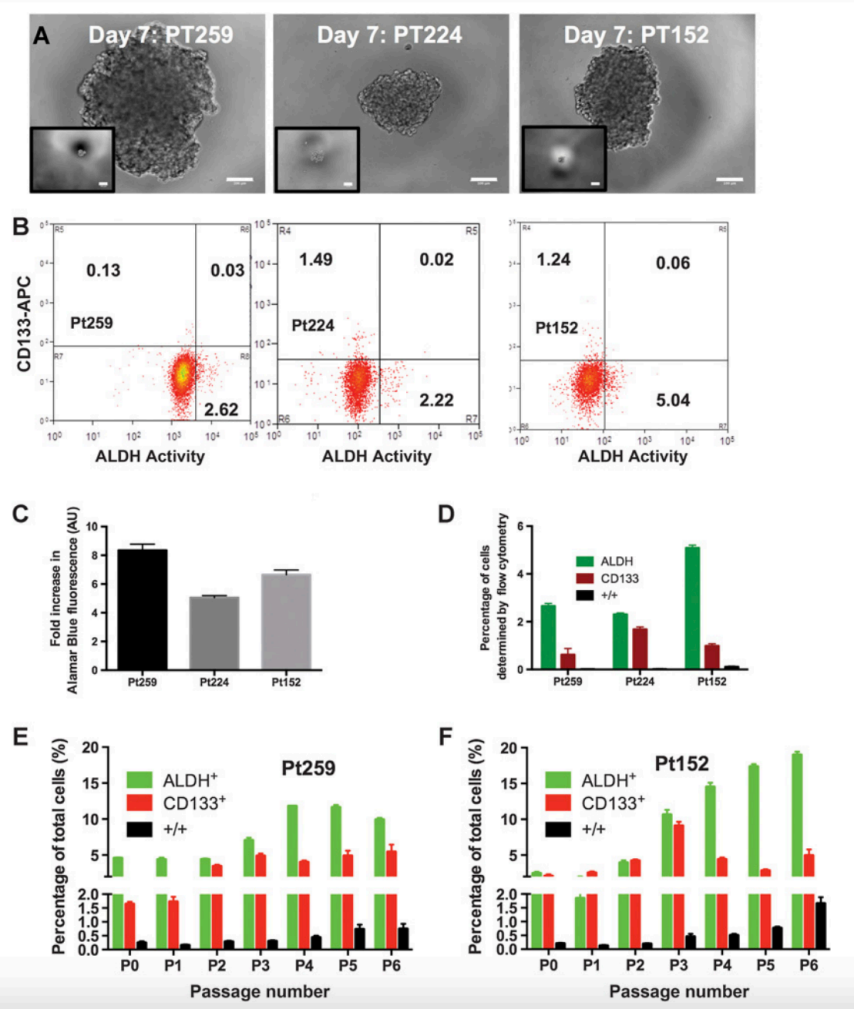

Figure 2.9: Remnant viable cells cause reemergence of ovarian tumor and CSC populations in cisplatin/673A–treated OvCSC spheroids.
A, Phase-contrast micrographs of spheroids generated from viable cells surviving cisplatin/673A treatment. Insets show spheroids at day 1 following cell seeding (scale bar, 100 mm). B, Representative flow cytometry plots of OvCSC populations in the reemerging spheroids at day 7, following cisplatin/673A treatment. C, Quantification of proliferation within spheroids over 7 days, formed from viable cells after cisplatin/673 treatment, indicating robust proliferation and recovery following cisplatin/673A therapy. No statistical significance was observed in the proliferation rates between patient samples. D, Graphical quantification of OvCSC populations derived from flow analysis, indicating the presence of ALDH+ populations, minimal to no recovery of ALDH+/CD133+ or CD133+ populations. E, Flow analysis of serially passaged recovered Pt259 OvCSC spheroids indicates an increasing expression of ALDH+, CD133+, and CD133+/ALDH+ populations, over seven generations. OvCSC populations approach and even seem to surpass original populations. F, Flow analysis of serially passaged recovered Pt152 OvCSC spheroids demonstrates an increase in ALDH+, CD133+, and CD133+/ALDH+ OvCSC progeny. CD133+ progeny do not approach original levels in Pt152 spheroids even after seven generations.

2.2.10 Serial passaging to evaluating the effect of Metformin on ovarian CSCs and the development of chemoresistance.

Prior studies suggest metformin can reduce cancer "stemness" [290–292]. We have shown that $ALDH^+CD133^+$ ovarian cancer cells are enriched for ovarian CSCs[64]. Thus, a primary endpoint of this study was to evaluate $ALDH^+CD133^+$ CSCs in the metformin-treated specimens and matched non–metformin-treated control patients. For homogeneity, we only evaluated samples from 22 patients with stage III/IV high-grade serous cancer. Controls met the eligibility criteria set forth for the trial and were consented for tissue collection via an IRB-approved tumor banking protocol. Selecting from a bank of more than 200 patient samples, 22 controls were matched to have identical stage, histology, and chemotherapy (including adjuvant vs. neoadjuvant). Average age of controls at the time of surgery was similar at 61.1 years (range 42–76). Among control patients, 75% underwent optimal debulking (15 of 20; debulking status unavailable for 2). Flow cytometry revealed metformin-treated patients exhibited an average 2.4-fold reduction in percentage of $ALDH^+CD133^+$ cells compared with non–metformin-treated ovarian cancer controls ($P < 0.0001$, Figure 2.10A).

To further evaluate the stemness of these tumors, tumor cells from 6 metformin-treated patients and 7 controls were grown in hanging-drop suspensions in serum-free media and serially passaged. Spheroids were then analyzed for response to cisplatin therapy over time and expression of ALDH or CD133. In line with a potential reduction in stemness, metformin-treated cells were more sensitive to platinum treatment, unlike controls, and appeared not to develop therapeutic resistance with passaging ($P < 0.001$, Figure 2.10B). Consistent with the initial analysis, spheroids from metformin-treated patients initially demonstrated reduced levels of both ALDH and CD133 (Figure 2.10C). Furthermore, these levels stayed lower over time and, in the case of ALDH, appeared to increase less over time.

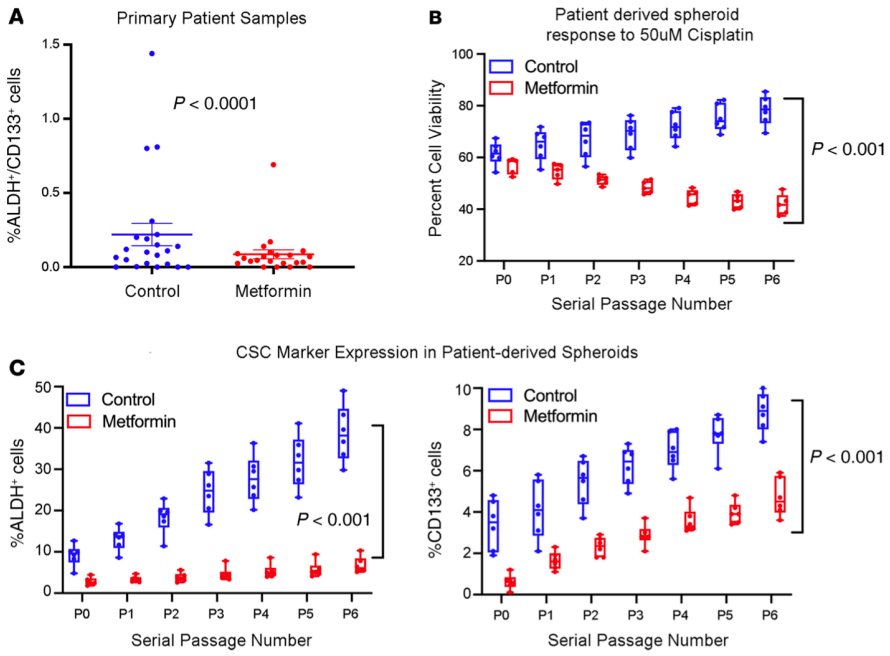

Figure 2.10: Tumors treated with metformin have decreased cancer stemness.
(A) Summary of FACS analysis of ALDH+CD133+ CSCs in metformin-treated (n = 22) and matched control ovarian cancers (n = 22) demonstrating a 2.4-fold decrease in CSCs in metformin-treated tumors. (B) Cell viability of tumor cells from metformin-treated patients (n = 6) or control patients (n = 7) grown in suspension, passaged weekly, and treated with cisplatin (5 replicates each). Tumor cells from metformin-treated patients maintain platinum sensitivity with serial passage, while control tumor cells increase platinum resistance over time. (C) Evaluation of ALDH and CD133 expression in metformin-treated and control tumor cells grown in suspension and after serial passages. Metformin-treated samples start at a lower baseline and increase less over time relative to controls. Lines in boxes represent averages. The whiskers depict the minimum and maximum values, and the length of the box represents the interquartile range. Statistical significance between passages was assessed with 2-sided Student's t tests and comparisons made between metformin and non-metformin samples at each passage, using 1-/2-way ANOVA and Tukey's post hoc analysis to determine specific significant differences ($P < 0.05$). All data are expressed as mean ± SEM.

2.2.11 Serial passaging discussion.

Ovarian CSCs are putative mediators of chemoresistance and recurrent disease, escaping conventional chemotherapy and contributing to relapse and tumor progression [293,294]. Therefore, in this study, we engineered an *in vitro* model that probes development of chemoresistance within a CSC-context. Further, we applied this model system in two clinically relevant scenarios, the first using this system to evaluate recurrence and the emergence of chemoresistance with patient-derived ovarian CSC spheroids and the second evaluating stemness and therapy response

with passaging of spheroids made from metformin treated and untreated patient samples from a phase II clinical trial[4,5].

Traditional monolayer models of chemoresistance neither recapitulate 3D cell–cell interactions, nor are they comparable to chemoresistance observed in the clinic [242,295]. A variety of traditional chemoresistance models also do not address the CSC context. Since the CSC phenotype is notoriously heterogeneous and unstable in 2D monolayer cultures, serial passages in xenografts are performed to study tumor initiating traits and CSC characteristics in serous ovarian cancer [65,293,296]. Genetically engineered mouse models and patient-derived xenografts, although more representative of primary disease, are expensive to establish and perform routinely[207,297,298]. For these reasons, 3D spheroid and organoid models are used for preclinical drug screening *in vitro* to bridge the gap between 2D monolayer cell culture and xenografts[253,254,299,300]. In our current serially passaged spheroid model, we demonstrate the combined evolution of chemoresistance along with CSC traits in vitro - mimicking the progression of recurrent malignant ovarian carcinoma. We address the challenge that *in vitro* models of recurrence must mimic the complexity and heterogeneity of *in vivo* tumors and provide the longevity needed to capture tumor dormancy following chemotherapy. We observe that cells placed in the 3D spheroid culture and taken through serial passaging, enriches for CSCs, evidenced by the increasing expression of ALDH through the passages. Our observation of 3D enrichment of the CSC marker, ALDH, is corroborated by increased expression of ALDH1A1 as per RNA-Seq and qRT-PCR, which also showed increased stemness, chemoresistance, and tumorigenicity signatures. This is in line with other reports in various cancers including breast cancers, where enrichment of CSC traits are observed in non-adherent 3D culture systems [301,302]. The increasing ALDH expression with increasing serial passage is

correlated with increased proliferative rates of ALDH+ cells, compared to ALDH- cells. Similar to this phenomenon observed by us, Alvero et al. also reported that serially passaging CD44+epithelial ovarian cancer CSCs triggered a "repair/proliferation" signal, where the process of proliferation by non-stem CD44- cells derived from a quicker differentiation of CD44+ cells was heightened [251]. Increasing growth rates for serial passaged xenografts were also reported in colorectal tumors, where later generations had higher growth rates compared to earlier generations of xenografted tumors[252]. Moreover, the inconsistent expression of CSC markers in 2D passaging validates the use of our 3D serial passaging model, which produces more consistent and predictable increases in expression of CSC markers with serial passaging. In this model, we also report that with increasing ALDH+ populations with serial passage, we observe an increasing chemoresistance to conventional platinum-based therapy, and an increased sensitization to Compound 673A, an ALDH targeting compound. We have previously reported that Compound 673A targets the ALDH positive population in patient derived CSC spheroids, and reduces ALDH expression and activity in these spheroids[4]. The increase in chemoresistance to cisplatin is not surprising, given that several reports suggest the strong correlation of the presence of ALDH to chemoresistance in clinical cohorts, as well as, in *in vitro* models and patient derived xenografts in ovarian and other cancers [61,62,303,304]. Clinically, chemoresistance develops despite initial chemosensitivity in ovarian cancer. Excluding the transition from 2D to P0 3D spheroids, subsequent 3D passaging from P1 onwards resulting in increasing chemoresistance is thereby not surprising and putatively mirrors clinical observations in ovarian cancer.

This was additionally corroborated in our tumor recurrence experiment with patient-derived ovarian CSC spheroids. In this experiment both the platinum sensitive and platinum

resistant patient samples responded to treatment, but CSC populations re-emerged with serial passaging. However, both patient samples exceeded their initial percentage of CSCs indicating development of chemoresistance. Also of note, the platinum resistant sample recovered and surpassed its original CSC quantities faster than the platinum sensitive sample. This is in line with time-based clinical definitions of platinum resistant tumors recurring in less than six months while platinum sensitive tumors recur longer than 6 months after treatment is stopped[5,305]. Since the platinum sensitive sample eventually exceeded its original CSC marker expression, this suggests that even though it remained sensitive to platinum resistance was developing. For this reason, it is especially interesting that we found that Metformin treated samples were 1) sensitized to platinum therapy, 2) maintained platinum sensitivity with serial passaging, and 3) had attenuated enrichment of CSC markers with serial passaging. These findings agree with previous reports that Metformin can sensitize tumors to platinum therapy, increase recurrence free survival, and overall survival[5,291,292,306] and highlight its potential as an anti-cancer therapy. Importantly, these findings also demonstrate the ability of our model system to recapitulate clinically relevant emergence of chemoresistance.

Similar to reports by Hu et al. [307] where increased tumor burden was observed when side population CSCs were injected into mice, compared to non-side population cells, we observe that injection of spheroids from P6 or P3 (which are significantly more enriched in CSCs) demonstrate a higher tumor burden when compared to spheroids injected from P0, in line with several reports of higher tumor initiating abilities in ALDH+ cells compared to ALDH- cells in murine xenograft models [61,62,308]. Thus, our model was successfully able to enhance tumorigenicity as well. In fact, at late passage (P6) we observed significantly higher estimated cancer stem cell frequency as compared to early passage (P0). This increase in the CSC

frequency at late passage was also correlated with earlier tumor establishment and greater tumor burden. Moreover, in comparison with serial passaging in PDXs, our model demonstrates higher efficiency, low cost, low latency, low time commitment, as well as, ability to test numerous patient derived tumors for personalized diagnostics and therapeutics.

When considering the clinical utility of this model, it is important to note that while the model in this work is presented over 6 passages, the early passages could be utilized to direct initial therapies, with treatment adjustments being made later based on subsequent passages. Furthermore, with more clinical validation, our mathematical model could be used to predict emergence of CSC phenotypes based only on data from P0 and P1, which could then be used to inform treatment strategies on a much shorter time frame than PDX models. The validity of our results showing increased stemness, chemoresistance, and tumorigenicity using our model is validated by our RNA-sequencing and qRT-PCR results from P0, P3, and P6spheroids. In addition to clear changes in gene expression with passaging, we also report a new gene signature of upregulated genes binned into stemness (WLS, ALDH1A1, BMP2, RSPO3), tumorigenicity (MAGEB2, BMP2, EFNB2, SERPINE2, HHIP, PTGS2), and chemoresistance (WLS, ALDA1A1, BMP2, PTGS2) based on current reports in the cancer literature. Interestingly, ALDH1A1was among the top two commonly upregulated genes in both patient samples regardless of quantification metric. This likely indicates high involvement of ALDH1A1 in stem cell enrichment and increased platinum resistance observed with serial passaging. Furthermore, this finding helps to explain the increased sensitivity to ALHD inhibitor observed with passaging, and lends credence to the use of Compound673A to treat platinum refractory ovarian cancer. Our sequencing data also revealed upregulation of two transcription factors, FOXA1and LEF1, that had previously been associated with ovarian CSCs [289]. Interestingly, these two factors

were only found to be significantly upregulated in the Pt412 sample. This difference between Pt224 and Pt412 may be due to the different stage and history of each sample (ascites vs abdominal metastasis) as well as the greater increase in ALDH+ OvCSCs in Pt412 spheroids compared to Pt224 spheroids. As a whole, given the results from our model and previous findings in the literature, we believe that the gene signatures presented by serially passaged P6 spheroids *in vitro* are extremely representative of a clinically malignant, chemoresistant disease portending poor prognosis. It is important to note that while some genes upregulated in our P6 spheroids, such as BMP2 [64,267,309] and SERPINE2 [273,278] can be associated with pro- or anti-malignant features in different cancers, their upregulation in our P6 spheroids implicates them in malignant features of ovarian cancer. That said, future studies should further investigate the role of these gene signatures in ovarian cancer and development of chemoresistance with more patient samples and functional assessments of each gene.

Concurrent with our *in vitro* data, the mathematical model demonstrates increased CSC proportions and proliferative capacity in a patient-specific manner over six passages, mimicking the increased tumorigenicity of CSCs. Our model additionally demonstrates CSC-driven tumor development consistent with the CSC hypothesis[64,258]. While our model mimics increased cells per spheroid over 6passages, the simulated fold increase is significantly lower than that determined experimentally. This discrepancy can be attributed to the simplicity of the model, which will be made increasingly more robust with additional biological considerations, such as dedifferentiation[310], successive decrease in progenitor proliferation capacity [257],or the stratified proliferative, quiescent, and necrotic regions that may form within spheroids[311], for example. However, over longer term passaging our model predicts a plateau in cells per spheroid which could represent the development of quiescent and necrotic regions within a spheroid as it grows

larger and the inner cores become deprived of nutrients and oxygen[312]. While this cannot be confirmed with our data, it serves as a solid basis for future experimentation. Interestingly, our model also predicts the eventual plateau of CSC populations within spheroids of each sample over the course of 20 passages, which could not be discerned from our experimental data within the six serial passages. This finding supports reports of negative feedback control on CSC populations by non-CSCs when space is limited [313]. In the 20-passage simulation, Pt412 spheroids were shown to reach cell/spheroid and CSC population plateaus much faster than the other two samples. This finding perhaps indicates that Pt412 would be quicker to develop ALDH conferred chemoresistance and relapse as their corresponding spheroids were simulated to reach their putative nutrient and space limitations fastest. Given that Pt412 contains the highest proportion of ALDH+ cells, which are generally more proliferative and chemoresistant [261,314,315], this observation is plausible. Additionally, this interpretation supports our in vivo evidence showing that xenograft tumors generated from Pt412 spheroids reached the tumor size endpoint 1week faster for P0 and P3 and 2 weeks faster for P6 than tumors generated from Pt224 spheroids. These findings may be indicative of the need for differential treatment strategies for Pt412 and Pt224.While other mathematical models have been developed to describe tumor growth dynamics and chemoresistance relative to CSC proportion, none have modeled CSC emergence in serial passaging of epithelial ovarian cancer spheroids [256–259,316–318], which can provide easily discernable, experimentally derived parameter-values to enhance biological relevance of the model.

Similar to our model, Fornari et al. [257] proposed an experimentally informed system of equations to investigate CSC-driven tumorigenesis and analyze tumor growth dynamics based on CSC population proportions at passage 1,2, and 3. Analysis of this model was contained within

each passage and did not attempt to predict increased CSC populations across passages. Fornari's model, as well as others, solely attempt to model population development within a single growth iteration and do not attempt to predict emergence of increasing CSC populations across iterations[257,258,260] limiting their utility in modeling emergence of CSC-related chemoresistance upon relapse. Lastly, many other mathematical models of tumor recurrence do not take into account the role of cancer stem cells in relapsed tumors and resulting increased chemoresistance[319–321].Therefore, while simple, our model demonstrates a novel mathematical application by which the development of chemoresistance within epithelial ovarian cancer can be inferred in a patient-specific manner using only data from P0 and P1. Moreover, our math model can be easily adapted to include other experimental parameters that influence CSC evolution, including hypoxia, extracellular matrix biophysical properties, stem cell plasticity, and paracrine interactions with other cell types in the TME. Through these studies, we report an *in vitro* spheroid model that generates reproducible spheroids and results, takes a relatively short period of time to develop, more accurately addresses *in situ* chemoresistance development, and could be further used to examine the development of chemoresistance in the setting of enhanced cancer stem cell populations.

This serial passage hanging drop model also incorporates the study of ovarian CSCs, thereby modeling the evolution and emergence of chemoresistance within a micro-tumor with a CSC-context. Since chemoresistance is observed in many ovarian cancer patients after first line chemotherapy, and we observe increased resistance to conventional chemotherapy in serially passaged spheroids, this model is well suited to study the in situ emergence of chemoresistance. Using the serial passage spheroid model, widely available -omics approaches can be used to analyze changes at genetic, epigenetic, metabolic and secretome levels, and compare them

between parental tumors, chemosensitive and subsequent chemoresistant passages. The evolution of chemoresistance could be related to molecular mechanisms, and the mechanistic roles attributed to key players within the molecular pathways could be further explored in vitro. This model has a wide variety of applications in both biomarker discovery, as well as preclinical screening from an evolved chemoresistant tumor standpoint. Apart from the obvious advantage of being physiologically relevant, the serial passage spheroid model recapitulates the existence of CSCs in malignant ascites that aggregate into spheroids to escape anoikis and maintains cellular heterogeneity of patient derived ovarian tumors, which can be utilized to study cellular interactions and their resultant biology in a systematic manner. Lastly, this model could be used as a way to enrich CSCs and chemoresistance within patient derived cells, and ultimately examine better treatment options for these patients.

2.3 Conclusions

In this work we present a newly engineered 3D ovarian cancer model to discern the underpinnings of chemoresistance development and role of ovarian CSCs in this process. We demonstrated the capacity of this model system to recapitulate *in vivo* chemoresistance development over long term culture with concordant increase in stemness, chemoresistance, tumorigenicity, and expression of a malignant gene signature. Furthermore, we present two applications of our model system that highlight its relevance to *in vivo* development of chemoresistance. We first demonstrated the utility of this model in precision medicine applications by modeling patient-specific tumor re-emergence with serial passaging of platinum sensitive and resistant patient-derived ovarian CSC spheroids after drug treatment. Finally, we used our model in a phase II clinical trial to demonstrate the effect of Metformin on CSCs and their ability to promote chemoresistance and recurrence, which reflected clinical observations

and previous literature. The applications of this system range from investigations into the mechanisms behind the development of chemoresistance and the enrichment of CSCs to personalized drug screening to inform clinical management or a translational tool to evaluate the effectiveness of new CSC or chemoresistance targeting therapies. As a result of its wide-reaching applications, this serial passage model has the potential to transform our understanding of CSCs and chemoresistance and expedite the development of new treatments.

2.4 Materials and Methods

2.4.1 Cell Culture.

All reagents used in the experiments were purchased from Life Technologies (Carlsbad, CA), unless otherwise specified. The high grade serous ovarian adenocarcinoma cell line OVCAR3 was obtained from ATCC (Manassas, VA). Patient cells were recovered from primary patient ascites and primary or metastatic tumors after informed consent under approved IRB protocol, following procedures established previously[61]. Briefly, primary patient malignant ascites infusions were centrifuged to recover a cell pellet, and red blood cells were lysed following manufacturer's protocol of a commercial ACK lysis buffer. Cells were obtained from primary or metastatic tumors using the tumor cell dissociation kit (Miltenyi Biotech, San Diego, CA) following manufacturer's protocols. Following 40 μm filtration to obtain single cell suspensions, cells were recovered by centrifugation and resuspended in a serum free medium. The patient samples utilized in this report were: tumor (Pt412, stage III, abdominal metastasis of high grade serous ovarian cancer) and ascites (Pt224, stage IV, platinum resistant ovarian adenocarcinoma).

OVCAR3 cells were cultured in 2D in 1640 RPMI supplemented with 10% fetal bovine serum and 1.5X antibiotics/antimycotics. Within the 3D hanging drop, OVCAR3 and Pt224 spheroids were cultured in serum-free medium, composed of 1:1 DMEM:Ham's F- 12, supplemented with 1X B27 supplement without vitamin A, 1X MEM Non-Essential Amino Acids, 1X insulin-transferrin-selenium, 5 ng/mL Epidermal growth factor (EGF), and 5 ng/mL basic fibroblast growth factor (bFGF)[4,322]. Pt412 spheroids were plated in a serum free medium that was the same as above, except for 10 ng/ ml EGF and bFGF. These cells were maintained in a humidified 37°C incubator with 5% carbon dioxide.

2.4.2 Generating spheroids on the hanging drop array.

Spheroids were formed in hanging drop plates, purchased from XCentric Mold and Engineering (Clinton Twp, MI). For initial spheroid formation, cells were counted using a hemacytometer and diluted to contain 100 cells per 20 μL, and plated in 20 μL drops, following the procedure described previously [4,253,254]. Serum free medium (3 μL) was added to the spheroids every 2–3 days.

2.4.3 Serial passaging of ovarian cancer spheroids.

At their first plating in the hanging drop array, the spheroids were labeled as passage 0 (P0). At each passage, spheroids were maintained for 7 days on the array. On day 7, spheroids were harvested by pipetting out the drop, and disassembled through mechanical disruption caused by repeated pipetting of the spheroid in quick succession followed by accutase treatment. These single cells were counted and plated on a new hanging drop plate with density of 100 cells per 20 μL to generate passage 1 (P1) spheroids. This entire process was repeated 5 more times, to

reach a passage number of 6 (P6) by day 42. Phase images of the spheroids were collected using live cell microscopy on a calibrated phase contrast microscope (Olympus IX81, Japan equipped with ORCA R2 Cooled CCD camera and CellSens software) on days 1, 7, and 10 of spheroid growth for each passage. At least 3 representative images were collected for each hanging drop plate, and at least 5 serial passage experimental plates were prepared for each sample.

2.4.4 Drug treatment of serially passaged ovarian cancer spheroids

On day 7 of every passage, spheroids were treated with one of the following: 50 μM Cisplatin, 50 μM Compound 673A (a novel inhibitor that targets ALDH1A1, ALDH1A2, ALDH1A3 [261]), or no drug control (blank serum free medium). Three days after this treatment (day 10), phase images of the drug-treated and control spheroids were imaged and harvested for counting.

In order to examine proliferation and viability after drug treatment, alamarblue dye was used in a 1:10 dilution within the hanging drops, and fluorescence values were collected at 530 nm excitation and 590 nm emission within a microplate reader (Synergy HT, BioTek Instruments, Winooski, VT). Alamarblue from day 7 was normalized to day 1 for proliferation, and viability values from day 10 drug groups were normalized to non-drug treated values from day 10. Lastly, 10 spheroids were harvested from each drug treatment group, disassembled via mechanical disruption, and counted with trypan blue using a hemacytometer to assess viability and proliferation.

2.4.5 Fluorescence-activated cell sorting (FACS) on serially passaged ovarian cancer spheroids.

On day 7 of each passage, spheroids were collected and disassembled to single cells for FACS analysis according to previously established protocols [4,322]. The Aldefluor Kit was purchased from StemCell Technologies (Vancouver, BC, Canada), and used to analyze the activity of ALDH in viable cells within spheroids. $CD133^+$ cells were detected using an Anti-CD133 antibody purchased from Miltenyi Biotec (San Diego, CA). Furthermore, spheroids at P0, P3, and P6 treated on day 7 with 50 μM Cisplatin, 50 μM Compound 673, or no drug treatment, were examined on day 10 using FACS.

2.4.6 FACS sorting for ALDH+ and ALDH- cells.

OVCAR3 cells were sorted as ALDH+ and ALDH- cells, as described previously[4,322]. Briefly, cells were divided into equal volumes and concentrations across tubes, with at least 10,000 cells in each tube. Aldefluor assay was performed following the manufacturer's protocols, using DEAB as an established negative control, and activated Aldefluor reagent for positive staining of ALDH activity. Cells were incubated in the 37C incubator for 30 to 45 minutes, recovered by centrifugation, and resuspended in FACS buffer with 300 μmol/L 4′,6-diamidino-2-phenylindole (DAPI) to assess viability. Cells were processed through a flow cytometer, and forward and side scatter were used to isolate single cells, that were viable and DAPI negative. Gates were established using DEAB (less than 0.2% false positive), and stained tubes were used to sort for cells that represented ALDH+ and ALDH- populations.

2.4.7 RNA-seq.

RNA was isolated from uncultured or cultured (P0, P3, or P6) spheroids derived from Pt224 and Pt412 using the Qiagen RNeasy Miniprep kit following manufacturer's protocol. RNA

quality was verified using the Nanodrop, agarose Gel electrophoresis to test RNA degradation and potential contamination, as well as, RNA Integrity using Agilent 2100. After quality control, mRNA was enriched using oligo(dT) beads, and cDNA was synthesized by using mRNA template and random hexamer primers. cDNA library preparation was performed using a custom second-strand synthesis buffer (Illumina), and completed through size selection and PCR enrichment followed by quality control. Libraries were sequenced on the HiSeq 4000 (Illumina) by Novogene (Sacramento, CA).

The RNA-seq reads were aligned to the hg19 transcriptome using the pseudo-alignment tool Kallisto. The aligned reads were then imported and analyzed for differential expression using DESeq2[323]. The transcript counts were summarized to gene-level counts using ensembl GRCh37 build using the biomaRt R package [324]. A principle component analysis (PCA) plot of the samples was generated after variance-stabilizing transformation of the counts data. For each patient, genes differentially expressed between the P0 and P6 passages at a false discovery rate (FDR) threshold of 0.1 and absolute $\log_2$ fold change threshold of 0.5 were identified. Heatmaps of the differentially expressed genes were plotted using the complex Heatmap package [263] in R after standardizing (centering and scaling) the expression data. Heatmaps of expression of 22 transcription factors (TFs) predicted to be activated in ovarian cancer stem cells in the literature are plotted to show the time-evolution of the serially passaged patient derived spheroids at P0, P3, or P6[289].

2.4.8 Xenografts from serially passaged ovarian cancer spheroids.

NOD SCID gamma female mice were purchased from Jackson Laboratories (Bar Harbor, ME), and injected with ovarian cancer spheroids at a starting age of 8–12 weeks. Injections were

prepared by carefully harvesting Pt224 and Pt412 spheroids using a pipette and supporting them within Growth-Factor-Reduced Matrigel from Corning (Corning, NY). Mice received subcutaneous injections of 1, 10 or 50 Pt224 spheroids generated from 100 cells after 7 days of growth, from spheroids at P0, P3, or P6 (n = 6 in each group) and 10 spheroids (100 cells/drop) at P0, P3 and P6 generated using Pt412 sample (n = 6 in each group). Tumor size was measured once weekly using calipers. Mice were euthanized after tumors reached 1500mm^3 in volume, when tumors were then dissected, and placed within biopsy cassettes for histology, followed by Hematoxylin and Eosin staining.

2.4.9 Mathematical modeling.

Our two-compartment mathematical model was based on a simplistic set of differential equations proposed by Moliña et al.[258] and those proposed by Fornari et al[257]. All simulations were performed in MATLAB version R2017b (Mathworks, Natick, MA, USA). Briefly, two equations were formulated; one describing change in the ALDH+ population, and the other describing changes in the ALDH- population (Supplemental Figure 3). Changes in the ALDH+ population are described by symmetric division, asymmetric division, symmetric differentiation, and death rates of ALDH+ cells. Contrarily, ALDH- cells are assumed to be capable of only symmetric division and death, and depend on asymmetric division and symmetric differentiation of ALDH+ cells. Rate constants with the units of cells per day were derived mainly from experimental data and supplemented with the literature. Briefly, the symmetric division rate of ALDH+ cells is chosen based on the value that minimizes the collective difference between simulated cells per spheroid at the end of P0 and P1 and the observed cells per spheroid at the end of P0 and P1 (Supplemental Table 2). The symmetric division rate of ALDH- cells was

chosen to maintain an approximate ALDH+:ALDH- proliferation rate calculated from FACS data and cell counts at the end of P0 and P1. Cell death rate of ALDH+ and ALDH- cells were determined via FACS. The asymmetric division rate was determined from Tomasetti et al. [325], while the rate of symmetric differentiation by ALDH+ cells, has been found to be low through the observation of single cell divisions of ovarian cancer cell lines and primary samples, and is therefore taken to be 0 in this model [64,325].

First, exponential growth curves were generated for ALDH+ and ALDH- populations respectively for the OVCAR3 cell line, and the two patient samples, Pt224 and Pt412 individually. The curves were based off of the number of each cell phenotype expected at the beginning of P1 out of 100 initial cells, determined by flow cytometry. After finding the best fit for each exponential curve, the best fit equation was set equal to the expected number of ALDH+ or ALDH- cells at the end of P1, determined by cell counts and flow cytometry, and the approximate number of generations needed to reach the expected final ALDH+ or ALDH- cell number was calculated. Subsequently, the calculated number of generations of ALDH+ and ALDH- cells over the course of 7 days was then used to calculate the approximate proliferation rate in the exponential growth phase. A ratio of ALDH+ proliferation and ALDH- proliferation rate was assumed to reflect the ratio of ALDH+ symmetric division and ALDH- symmetric division. This ratio was used to calculate ALDH symmetric division rate given ALDH+ symmetric division rate (Supplemental Figure 3). ALDH+ symmetric division rate was chosen to minimize the collective difference between simulated and experimental cells per spheroid at the end of P0 and P1 (Supplemental Figure 3). Death rates for ALDH+ and ALDH- populations were similarly determined by flow cytometry following culture of P0 spheroids, assuming that the cells used to form the spheroids began with 100% viability. The asymmetric division rate was

determined from Tomasetti et al., whose predicted CSC growth curve with low asymmetric division matched that shown by our experimental data[325]. Finally, the rate of symmetric differentiation by ALDH+ cells, which we assume to be CSCs, has been found to be low through the observation of single cell divisions of ovarian cancer cell lines and primary samples, and is therefore taken to be 0 in this model [64,325] (Supplemental Table 3).

2.4.10 Isolation of OvCSCs from primary patient ascites.

Cells were recovered from primary patient ascites following protocols established previously[61]. Briefly, primary patient malignant ascites infusions were centrifuged to recover a cell pellet, and red blood cells were lysed following manufacturer's protocol of a commercial ACK lysis buffer (Life Technologies). Cells were obtained from xenografted tumors using the Tumor Cell Dissociation Kit (Miltenyi Biotec) following the manufacturer's protocols. After a 40-mm filtration to obtain single-cell suspensions, cells were recovered by centrifugation and resuspended in a flow cytometry appropriate buffer (FACS Buffer; PBS supplemented with 2% FBS). OvCSCs were isolated on the basis of concurrent elevated ALDH activity and expression of CD133, following protocols established previously[61]. Cells were counted using a hemocytometer and adjusted to $1x10^6$ cells/mL. The ALDEFLUOR Assay was carried out as per manufacturer's protocol, using diethylaminobenzaldehyde (DEAB) as a negative control for ALDH staining. Simultaneously, cells were incubated with activated ALDEFLUOR reagent or allophycocyanin (APC)-conjugated CD133 antibody (Miltenyi Biotec) to isolate CD133+ cells based on surface antigen expression and ALDH+ cells on the basis on ALDH activity. A negative control for CD133- APC staining was established using an isotype-matched APC-conjugated antibody, to identify background staining. Cells were incubated in staining solutions for 30 to 45 minutes at 37C, washed with PBS, and resuspended in FACS buffer with 300

mmol/L 40 ,6-diamidino-2-phenylindole (DAPI). Cells were sorted on a flow cytometer, and discrete single-cell viable populations were identified. Appropriate gates were set for ALDH and CD133- APC using DEAB-stained tubes, and APC-isotype antibody tubes. OvCSCs were isolated as the small fraction of cells positive for both ALDH activity and the expression of CD133-APC. For this study, OvCSCs were FACS sorted and obtained from three different patient samples: Pt259 (stage IV progressive primary peritoneal carcinoma), Pt224 (stage IV, platinum-resistant ovarian adenocarcinoma), and Pt152 (stage IIIc, recurrent platinum-resistant high-grade ovarian adenocarcinoma).

2.4.11 Drug treatment on OvCSC spheroids in hanging drop array culture.

OvCSC spheroids were initiated in 384-well hanging drop arrays using 10 OvCSCs per spheroid. Spheroids were allowed to aggregate and form a 3D microtissue over a period of 7 days, at which point, flow cytometry–defined populations of OvCSC progeny were established. For drug treatment, a 10 stock of drug was prepared independently, and 2 mL of drug was added to the 20 mL hanging drop containing spheroids to result in a final concentration of 1. Several drug-dosing regimens were carried out, including cisplatin (50 mmol/L), the ALDH inhibitor compound 673A (50 mmol/L), cisplatin (50 mmol/L) + 673A (50 mmol/L), the JAK1/2 inhibitor, ruxolitinib (500 nmol/L), and/or cisplatin (50 mmol/L) + ruxolitinib (500 nmol/L). The concentrations for drug dosing were arrived at following dose–response curves, where the effect of the drug was maximal for the different patient samples, while simultaneously demonstrating platinum resistance in OvCSC spheroids. The effect of drug was assayed on spheroids at 72 hours, using the AlamarBlue assay to determine viability after drug treatment. Control untreated spheroids were maintained for the same duration in culture. At least 20 spheroids (technical replicates) were assayed per experiment, with 3 to 5 biological replicates. Drug-treated spheroids

were imaged using phase-contrast microscopy to observe morphologic differences in spheroids exposed to drug compared with control untreated OvCSC spheroids. Flow cytometry was used to analyze OvCSC progeny following 72-hour drug treatment to identify whether chemotherapy targeted specific populations of OvCSC progeny. Finally, spheroids were either treated with 500 nmol/L ruxolitinib or left untreated and collected and lysed in RIPA buffer (Invitrogen) with complete proteinase inhibitor and phosphatase inhibitor (Roche). Insoluble material was removed by centrifugation. Protein concentrations were determined using the Bradford Protein Assay Kit (Bio-Rad). Lysates were separated by gel electrophoresis and transferred onto a nitrocellulose membrane. Primary antibodies for immunoblotting include anti– phospho-STAT3 (tyrosine705, #9131, Cell Signaling Technology), anti–total-STAT3 (#9139, Cell Signaling Technology), and anti-GAPDH (Thermo Fisher Scientific). Following incubation with the appropriate secondary antibody, bands were visualized using the ECL Kit (Thermo Fisher Scientific).

2.4.12 Recovery of drug-treated spheroids to model tumor re-emergence and serial passaging.

Recovery of drug-treated spheroids to model tumor reemergence and serial passaging Following 72 hours of maximal dose drug treatment (cisplatin/ 673A), OvCSC spheroids were harvested and suspended in FACS buffer with 300 mmol/L DAPI. Cells were flow sorted based on DAPI negativity, therefore isolating cells that remained viable following drug treatment. Spheroids were reinitiated in hanging drop array plates with cells suspended in SFM media and imaged with phase-contrast microscopy to visualize spheroid formation. To preliminarily model tumor reemergence in the most platinums ensitive (Pt259) and most platinum-resistant (Pt152) ascites samples, spheroids were collected from these two patient samples, mechanically dissociated to generate single-cell suspensions, and re-counted to initiate 100 cells per drop

spheroids for the next passage. Spheroids were serially passaged for 7 cycles (P0–P6) over a period of 7 weeks. Flow analysis was performed as outlined previously at the end of each cycle to characterize OvCSC markers (ALDH and CD133). This allowed us to identify OvCSC populations within serially passaged spheroids, while cells from the same population were allowed to re-form spheroids, serving as a preliminary model of tumor reemergence in vitro.

2.4.13 Evaluating the effect of Metformin on ovarian CSCs in vitro.

CSC studies. Tumor samples were processed into live single-cell suspensions[326] and frozen for batch analysis. The proportion of $ALDH1^{+}CD133^{+}$ CSCs was evaluated via flow cytometry as previously described [4,253,254].

Hanging-drop spheroids. Tumor cell suspensions from 6 neoadjuvant metformin-treated patients and 7 control patients were gown as previously described in 5 replicate plates [254]. After 7 days, spheroids were harvested and disaggregated and single cells counted and replated on a new hanging-drop plate as drops of 100 cells, to form passage 1. This process was repeated weekly for 6 passages. Live-cell phase microscopy images of the spheroids were collected (Olympus IX81 and CellSense software) on days 1, 3, and 7 of culture for each passage to monitor spheroid formation/proliferation [4,253,254,322]. At the time of disaggregation, a portion of cells was used for flow cytometry analysis of ALDH and CD133 as above. Seven-day- old spheroids were treated with cisplatin at a concentration of 50 μM. The effect of drug treatment was determined at 72 hours, using the Alamar blue assay as described[4,253,254].

2.4.14 Statistical Analysis.

3D in vitro Serial passage model characterization statistics: All serial passages were repeated with at least 5 biological replicates, with n ≥ 10 for each replicate for alamarblue analysis, and 3 cell counts for trypan blue. Analysis of flow cytometry data was performed on Summit Software (Beckman Coulter, Brea, CA). At least 10,000 live cells were analyzed for each experimental condition and used to determine percentage of ALDH or CD133 positive cells. For xenografts, longitudinal tumor growth was compared between different groups (naïve Pt224 or P0, P3, P6 spheroids, naïve Pt412 or P0, P3, P6 spheroids) using repeated measures ANOVA techniques and/or mixed-effect longitudinal models. Tumor weights were compared between different groups and controls using a student's two-sample t-test. Statistical data was analyzed in Graphpad Prism 7.0 (www.graphpad.com, San Diego, CA). One-way ANOVA was performed where necessary, with secondary post-hoc analysis. All data is presented as mean ± standard error of the mean. Significance was considered for $P \leq .05$. Asterisks on the figure panels and legends indicate statistical significance.

Patient-derived OvCSC serial passage model of tumor re-emergence statistics: Statistical analysis Flow cytometry data were analyzed using Summit software (Beckman Coulter). Percentage of cells determined positive by flow cytometry was expressed after analyzing at least 10,000 events per experimental condition. Three to five independent flow cytometry analyses were performed, to identify an average percentage of OvCSC populations. Statistical analysis was performed using GraphPad Prism 5 (GraphPad Software Inc.). All data are expressed as mean SEM and are an average of at least 3 to 8 independent experiments. Drug viability data were determined and quantified using the AlamarBlue assay, as outlined previously[254,322]. Briefly, normalized viability was calculated by comparing the AlamarBlue fluorescence of drug-treated spheroids to control untreated spheroids and expressed as a percentage. Statistical

analysis was performed using one- or two-way ANOVAs where appropriate, and levels of statistical significance are indicated in the figures. All data are expressed as mean SEM and are an average of at least 3 to 8 independent experiments.

Translational Metformin studies statistics: Spheroid studies were repeated 5 times, with at least 40 spheroids (tech- nical replicates) interrogated for each analysis at each time point and at least 6 patient samples. Spheroid proliferation at day 7 was normalized to day 1 for each specimen. Normalized viability is expressed as percentage of untreated controls. Statistical significance between passages was assessed with 2-sided Student's *t* tests and comparisons made between metformin and nonmetformin samples at each passage, using 1-/2-way ANOVA and Tukey's post hoc analysis to determine specific significant differences ($P < 0.05$). Three independent flow cytometry analyses were performed to identify an average percentage of $ALDH^+$ or $CD133^+$ populations. All data are expressed as mean ± SEM. Statistical analyses were performed using Prism 7 (GraphPad) and SAS version 9.4.

Chapter 3 : 3-Dimensional Patient-Derived Tumoroids to Study the Role of the Tumor Microenvironment in Cancer Stem Cell Regulation and Chemoresistance in Ovarian Cancer

3.1 Introduction

In 2021, 21,410 women are estimated to be diagnosed with ovarian cancer and 13,770 are estimated to succumb to the disease in the United States alone. 75% of these patients won't be diagnosed until stage III/IV due to lack of symptoms, at which point the survival rates are dismal[327–329]. Even with the success of standard treatments involving surgery and chemotherapy as well as the development of immune, hormone receptor modulator, and combination therapies most patients develop chemoresistant, recurrent disease[327,330,331]. This trend results in the fifth highest cancer-related mortality rate in women in the United States[332].

Importantly, these dismal outcomes are not due solely to the uncontrolled proliferation of malignant cancer cells. Rather, they are the product of the complex interactions that take place between the cancer cells and the non-cancer cells in the tumor microenvironment (TME), as well as the acellular factors such as dimensionality, extracellular matrix (ECM), mechanical forces, and oxygen availability[1,2]. Each of these factors can influence cell phenotypes and disease progression, making the TME characteristics an important determinant of disease course. The cell composition in particular has recently been shown to have clinical implications in the different molecular subtype of high-grade serous ovarian cancer (HGSOC).

Specifically, in 2008, Tothill et al. identified 4 molecular subtypes that correspond with different clinical outcomes[229]. These subtypes were verified by The Cancer Genome Atlas in 2011, and termed "proliferative", "immunoreactive", "differentiated", and "mesenchymal"[333]. While outcomes in the TCGA dataset were not found to be significantly different between the subtypes Tothill and others have found that the proliferative and mesenchymal subtypes are associated with the worst outcomes while the immunoreactive subtype is associated with the best outcomes[82,229,230,237]. Furthermore, recent advances in single cell sequencing have showed that the presence of stromal and immune cells in the tumor heavily influences stratification into different molecular subtypes[82]. In particular, the mesenchymal and immunoreactive subtypes, are characterized by high proportions of myofibroblasts and immune cells respectively[82].

As a result, efforts have been made to retroactively examine the role of the stromal cell contribution to clinical outcomes associated with bulk sequencing data, however a complete understanding of how nuanced differences in stromal and immune cell composition influence outcomes is lacking[235,237]. This lack of understanding has contributed to a lack in clinical implementation, highlighting the need to better understand how the cell composition of the TME influences outcomes.

The role of the non-cancer cells in the TME is further complicated by their interactions with cancer stem-like cells (CSCs), which have been clearly linked to recurrence, chemoresistance, and outcomes in ovarian cancer. CSCs are a rare population of the chemoresistant cancer cells that can survive initial treatment. Their stem-like properties, such as their ability to self-renew, repopulate the tumor, and resist apoptosis, serve as the basis of development of a more aggressive, metastatic, recurrent disease[334]. These cells have increased detoxification capacity and chemoresistance due to altered drug transporters, and an altered DNA repair mechanism.

Additionally, CSC's can switch bidirectionally between stem and non-stem phenotypes, contributing to the heterogeneity of the disease and complexity in treating primary and recurrent tumors.

The non-cancer cells in the TME such as the mesenchymal stem cells (MSCs), endothelial cells (ECs), and macrophages (MPs) among others can enriched this CSC population[118,213,335–340]. For example, Mclean et al. demonstrated that cancer associated MSCs (CA-MSCs) isolated from a tumor can increase tumorigenesis and stemness through IL-6 and LIF mediated STAT3 signaling and BMP signaling[338,340]. Additionally, related stromal cell types, such as adipocytes and fibroblasts have similarly been shown to induce pro-tumorigenic properties in ovarian cancer[341]. Intercellular signaling resulting in CSC enrichment is further complicated through involvement of endothelial cells and immune cells. Macrophages in particular have also emerged as a driver of stemness and metastasis in ovarian cancer when present in their immunosuppressive phenotype [118,342,343]. Comparably, endothelial cells have been shown to promote CSC phenotypes in colorectal cancer through secretion of a soluble form of Jagged-1 resulting in NOTCH activation [336]. Due to the clear role of CSCs in chemoresistance and recurrence in ovarian cancer there is a definite need for more targeted treatments. Due to the role of the TME cells in CSC maintenance, CSC-TME interactions are a promising avenue for the development of targeted treatments, as with molecular subtyping, there is currently a lack of understanding of how the non-cancer cells work together in complex multi-cellular microenvironments to regulate CSCs and promote chemoresistance.

Current models used to study the complex multi-cellular interactions in the TME are lacking in their ability to provide a clear understanding of the role that each component plays in CSC maintenance and ultimately in determining clinical outcomes. While 2D cultures have been

shown to translate poorly into clinical environments due to their limited replication of in vivo tumor microenvironments, 3D culture represents a significant improvement given their improved ability to replicate 3D cell-cell and cell-ECM interactions and nutrient and drug diffusion gradients that are found *in vivo*[344,345]. 3D suspension cultures are especially ideal for CSC research given the resistance of CSCs to anoikis and subsequent enrichment in suspension culture[3,346]. Due to these benefits, co-culture models have been successfully implemented in 3D to provide insights into the interactions between CSCs and the other cells in the CSC niche[118,213]. For example, Raghavan et al. cultured ovarian CSCs with MSCs in hanging drop plates to study the interactions between CSCs and MSCs. Using this model, they were able to identify the PDGF signaling as a mechanistic pathway through which MSCs promote stemness and chemoresistance in ovarian cancer[213]. Raghavan et al. utilized a similar model to demonstrate that macrophages promote chemoresistance and invasiveness in ovarian cancer through macrophage initiated Wnt signaling with CSCs[118].

While most experiments investigating the molecular subtypes of HGSOC focus on analysis of molecular signatures from publicly available sequencing data[227,229,232,235,237,333], similar co-culture models have been implemented to study mechanisms behind differential HGSOC subtype outcomes[347,348]. For example, a 2D culture system was used to suggest that the exosomes secreted by plasma cells in the tumor microenvironment induce mesenchymal phenotypes in ovarian cancer cell lines through the miR-330-3p/junctional adhesion molecule 2 (JAM2) pathway. Moreover, in this work, the authors used an immune cell composition deconvolution algorithm, CIBERSORT, to identify enrichment of plasma cells in the mesenchymal subtype of ovarian cancer and increased quantities of M1 macrophages in the immunoreactive subtype[347]. Another model used a 3D co-culture of fibroblasts with tumor cells

to examine the capacity of SNAI2 to drive transformation of normal fibroblasts into their tumor supporting phenotype, thereby promoting the transcriptional signature of the mesenchymal subtype that contributed to desmoplasia[348]. These co-culture studies provide impetus to investigate therapies targeting Wnt and PDGF pathways to target CSCs or miR-330-3p and SNAI2 expression to counteract the poor outcomes associated with the c1 mesenchymal subtype. However, it remains unknown if the same signaling pathways would be the driving factors behind malignancy in more complex cellular microenvironments.

The drastic changes that can occur in signaling with increased cellular complexity was highlighted in work by Regier et al. who compared mono-, co-, and tri-culture of breast cancer cell lines in a microfluidic device designed to keep each cell type separate. In this work, they found non-linear changes in gene expression in tri-culture compared to co-culture. For example, they found that culture of SKBR3 breast cancer cells with HS5 cells led to a 72.4X increase in FGF2 expression in the tumor cells while culture with THP1-M2 cells resulted in no increase in FGF2 expression in the tumor cells respectively. Despite the fact that THP1-M2 cells alone did not increase FGF2 expression in tumor cells, culture of of SKBR3 breast cancer cells with both HS5 cells and THP1-M2 cells resulted in a 154X increase in FGF2 gene expression[349]. This is a clear example of the impact that increased cellular heterogeneity can have in the TME. Therefore, the lack of cellular complexity in typical co-culture models may attenuate the translational value of their results.

On the other hand, patient-derived organoids (PDOs), ex vivo tumor cultures, and patient-derived xenografts (PDXs) are better at maintaining the complex cellular microenvironments found *in vivo*[204,350–353].However, these models can be difficult to use to evaluate the role of the non-cancer cells in the TME due to gradual loss, or intentional exclusion,

of stromal components over time in culture or the invasion of mouse stroma in the case of PDX models[204] . These models are also susceptible to mouse-specific tumor progression[210]. Furthermore, these complex patient-derived systems do not provide fine control over the cell composition, which hinders careful experimental design to evaluate how each individual cell type contributes to the complex system of cell interactions to support CSCs and drive chemoresistance in ovarian cancer. Although these types of *in vivo* models allow for evaluation of stromal influence on tumor growth *in vivo*, they are inherently low throughput, technically challenging, time consuming, and costly. Therefore, there is a need for a more comprehensive *in vitro* model to study the complex multi-cellular interactions the tumor microenvironment, while maintaining fine control over cell composition.

In this work, we present a novel 3D *in vitro* tumoroid model, which improves upon the physiological relevance of current *in vitro* models by incorporating controlled ratios of mesenchymal stem cells (MSCs), endothelial cells (ECs), and immune cells (PBMCs) in the same 3D culture with patient-derived tumor cells in 384-well hanging drop plates. Through incorporation of four cell types we anticipate more comprehensive cell-cell signaling and thus a more representative model of interactions with the TME. Based on previous work in our lab and others showing that each individual TME cell type can enrich CSC populations[118,213,335–337,339,354], we hypothesized that tumoroids will enrich CSCs to a greater extent than mono-culture or co-culture patient-derived spheroids. Accordingly, we expected tumoroids to possess malignant characteristics associated with stemness including increased tumorigenicity, and chemoresistance compared to mono-culture spheroid controls. Furthermore, we hypothesized that these heterotypic tumoroids will reflect realistic molecular signatures associated with HGSOC molecular subtypes and clinical outcomes due to the influence of non-cancer cells on molecular

subtyping[82]. To evaluate these hypotheses we evaluate tumoroid stemness, tumor formation capacity, and chemoresistance in tumoroids compared to spheroids made with only patient tumor cells. Subsequently, we examine molecular differences in tumoroids compared to controls and probe the expression of molecular signatures associated with different clinical outcomes.

We found that tumoroids were amenable to flexible culture conditions, with and without an added ECM component, and could be successfully cultured with different cell compositions. Using this system, we observed that the effect of TME cells on stemness was not equivalent in co-cultures compared to more heterogeneous tumoroids, highlighting the importance of incorporating more than one TME cell type in models designed to test CSC enrichment by the TME. Additionally, the influence of the TME cells on expression of CSC markers in tumoroids was variable, depending on the patient sample, pointing to patient-specific cell-cell signaling with the non-cancer cells in the TME. Tumoroids were also able to form tumors faster than control spheroids *in vivo* and contained more proliferative cells enriched in ALDH expression after harvesting from xenograft tumors. Moreover, tumoroids were more resistant to treatment with traditional and novel targeted therapies.

These observations were accompanied by evidence of epithelial-to-mesenchymal transition and expression of malignant matrisome signatures as well as the c1 mesenchymal subtype signature associated with poor clinical outcomes. Together these findings demonstrate the ability of heterotypic tumoroids to evaluate the role of the TME cell composition in CSC maintenance and physiologically relevant disease states that are associated with chemoresistance and poor clinical outcomes. By leveraging the flexibility of this system the impact of key TME components on disease progression and clinical outcomes can be elucidated in the context of a complex multi-cellular environment. With a better understanding of the interactions within the

TME, new targeted therapies can be developed and patient management based on molecular subtyping can be improved, ultimately resulting in a better outlook for ovarian cancer patients.

3.2 Results

3.2.1 Heterogeneous patient-derived tumoroids are amenable to different culture compositions.

Patient-derived tumor cells were successfully cultured with human adipose-derived MSCs, human umbilical vein endothelial cells (HUVECs), and peripheral blood mononuclear cells (PBMCs) in 384-well hanging drop plates with Matrigel (Figure 3.1A,B, Supplemental Figure 4A) and without Matrigel (Figure 3.1A,C). Tumoroids generated without Matrigel were cultured for up to 22 days, with culture terminated due to large droplet size and corresponding sample instability (Figure 3.1D). As such, remaining experiments were conducted with a day 7 endpoint at the latest. Following 7 days of culture, tumoroid histology appeared consistent with *in vivo* tumors (Figure 3.1E). To further verify the capacity of our culture system to maintain each cell type in culture and visualize cell localization, tumoroids were generated with each cell type expressing a different fluorescent protein (Pt4 cells: dtTomato; MSC: GFP; EC: AmCyan; U937: mCherry). Visualization of tumoroids using fluorescence confocal microscopy and spectral unmixing post-processing revealed that the majority of each tumoroid is made up of patient tumor cells, with other cell types dispersed throughout the culture with no particular organization. This experiment also confirmed the presence of all four cell types at the end of 7 days (Figure 3.1F).

Additionally, expression of markers for each cell type was detected in tumoroids made with all 5 patient samples (Supplemental Figure 4B,C), further supporting the presence of all

four cell types at the end of the 7 day culture period. Pt6 was the only sample with significant differences in expression of CSC markers with significantly greater expression of $CD133^+ALDH^+$ and $CD133^+ALDH^-$ compared to all other samples. Pt6 also had significantly greater expression of CD73 compared to all other patient samples (Supplemental Figure 4B,C). This was later found to be due to baseline high CD73 expression in Pt6 only controls, suggesting maintenance of patient specific features in tumoroid cultures (Supplemental Figure 4D). However, this also highlighted the potential of tumor cells to express TME cell markers, like CD73.

Due to this potential, we next generated Pt1 tumoroids and control spheroids with GFP^+ tagged tumor cells in order to separate the marker detection in the patient tumor cells from the expression in the added TME cells. This experiment confirmed presence of GFP^+CD133^+ and GFP^+ALDH^+ tumor cells and GFP^-CD73^+, GFP^-CD31^+, and GFP^-CD11b^+ TME cells (Figure 3.1G). Finally, viability of tumoroids compared to control spheroids is significantly lower on day 3, but not day 0 or day 7 ($p < 0.05$) (Supplemental Figure 4E).

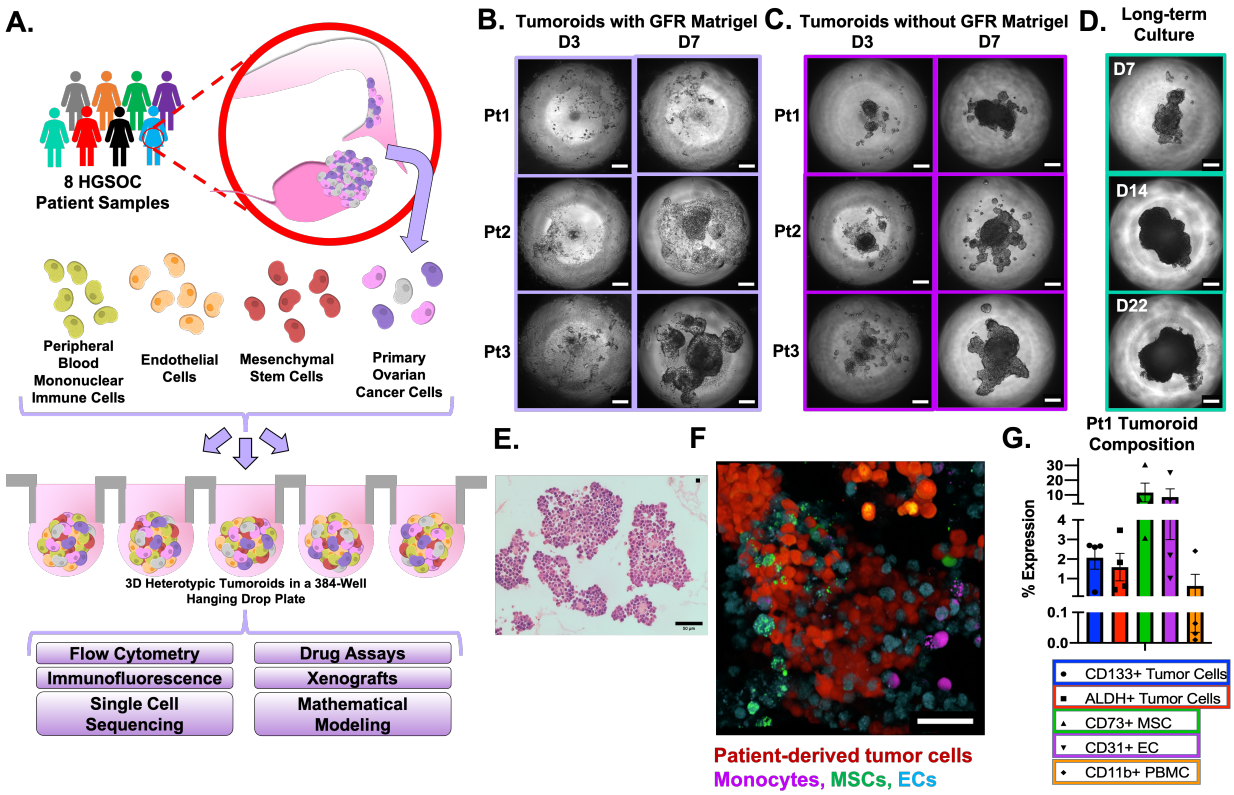

Figure 3.1: Generation of heterogenous tumoroids.
A) Primary ovarian tumor cells were combined with endothelial cells, mesenchymal stem cells, and peripheral blood mononuclear cells in 384-well hanging drop plates to form heterotypic tumoroids. Phase contrast images of tumoroids generated B) with growth factor reduced Matrigel and C) without growth factor reduced matrigel for three patient samples. D) Phase contrast images of tumoroids maintained in culture for up to 22 days. Scale bars = 200 um. E) H&E tumoroid section demonstrating expected hisological features (scale bar = 50 um). F) Tumoroid formed from patient-derived cancer cells (dtTomato – red) , mesenchymal stem cells (GFP – green), endothelial cells (AmCyan – blue), and U937 monocytes (mCherry – pink) on day 7. Scale bar = 50 um. G) Percentage of CD11b+, CD73+, CD31+, ALDH+, CD133+, and ALDH+CD133+ cells measured via flow cytometry on day 7 for tumoroids made with 5 different patient samples (n = 3 for each patient sample).

3.2.2 CSC markers are differentially expressed in tumoroids compared to co-cultures.

A key feature of our model system is the ability to culture tumoroids with different cell compositions to determine the role of each individual cell type in the TME on CSC populations in the context of a complex cellular microenvironment. As such we demonstrated successful co-culture of GFP^+ Pt 1 cells with MSCs alone, ECs alone, and PBMCs alone (Figure 3.2A). To evaluate differences in expression of CSC markers in different culture types, we performed flow

cytometry to analyze expression of GFP^+ALDH^+ or GFP^+CD133^+ patient tumor cells from control mono-culture spheroids, Pt1 + MSC co-culture, Pt1 + EC co-culture, Pt1 + PBMC co-culture, and Pt1 tumoroids with all four cell types. Interestingly, Pt1 + EC co-cultures significantly increased ALDH expression compared to Pt1 + PBMC co-cultures, but no other significant differences between CD133 or ALDH expression were found. When the percentage of cells expressing CD133 was added to the percentage of cells expressing high ALDH, a significant increase in total stemness was observed in the Pt1 + EC co-cultures compared to all other culture types indicating that ECs may be having the largest impact on CSC maintenance in this model system. Notably, the tumoroids had lower total expression of CD133 and ALDH than the EC only co-culture, despite being plated with an equivalent number of ECs (Figure 3.2B). This indicates the importance of including multiple cell types in cultures evaluating the role of TME cells on stemness as inclusion of additional cell types attenuated the increase in stemness shown in the EC only co-culture.

Evaluating the percentage of GFP^+ cells in each culture type provided further evidence of the presence of TME cells in tumoroid cultures. The expected distribution was observed across culture types, with tumoroids having the lowest average percentage of GFP^+ cells due to the inclusion of all three other cell types. EC and MSC only co-cultures showed similar expected decrease in percentage of GFP^+ cells (Supplemental Figure 4F). On the other hand, PBMC co-cultures did not appear to affect the proportion of GFP^+ cells to a noticeable degree. This could be due to the low level of PBMC proliferation in TM (Supplemental Figure 4G) leading to a relatively low expression of leukocyte marker CD11b compared to the markers for the other cell types (Figure 3.1G). Using the average GFP^+ tumor cell percentage from these GFP^+ Pt1 spheroids and tumoroids, we derived a scaling factor (1.3687) to account for dilution of CSC

marker expression in Pt1 tumoroids (due to the presence of the non-cancer cells) that were made without GFP tagged tumor cells.

With adjustment for the TME composition, we found significantly increased $CD133^{-}ALDH^{+}$ ($p<0.01$) and $CD133^{+}ALDH^{+}$ ($p<0.05$) expression (Figure 3.2C). No significant differences were observed in the non-scaled version of this GFP^{-} Pt1 CSC data, however the mean $ALDH^{+}$ and $CD133^{+}ALDH^{+}$ percentages in the tumoroids were greater than the spheroids ($ALDH^{+}$: 27.07 +/- 15.62 vs 20.61 +/- 14.03 and $CD133^{+}ALDH^{+}$: 0.9121 +/- 0.8113 vs 0.6203 +/- 0.5406) (Supplemental Figure 5A). Given the presence of the TME cells in tumoroids and their absence in spheroids, it follows that in reality the difference in CSC marker expression should be greater as reflected by the scaled data in Figure 3.2C.

Due to the potential biases introduced with scaling, as well as the lack of scaling factors for each patient sample, we next evaluated the composition of CSC markers in tumoroids and spheroids from 5 different patient samples, considering $CD133^{+}ALDH^{+}$, $CD133^{+}ALDH^{-}$, and $CD133^{-}ALDH^{+}$ phenotypes. Breaking the analysis apart based on patient sample suggests patient-specific differences in response to the TME cells with Pt1, Pt2, and Pt5 showing a trend towards increased $CD133^{-}ALDH^{+}$ proportions in tumoroids compared to spheroids while Pt4 and Pt6 appeared to have a higher proportion of $CD133^{+}ALDH^{+}$ cells and $CD133^{+}ALDH^{-}$ cells respectively (Figure 3.2D). This suggests that tumoroids have the capacity to alter the composition of CSC phenotypes, however there may be a patient-specific characteristic that affect how tumor cells from different patients response to the presence of the added TME cells.

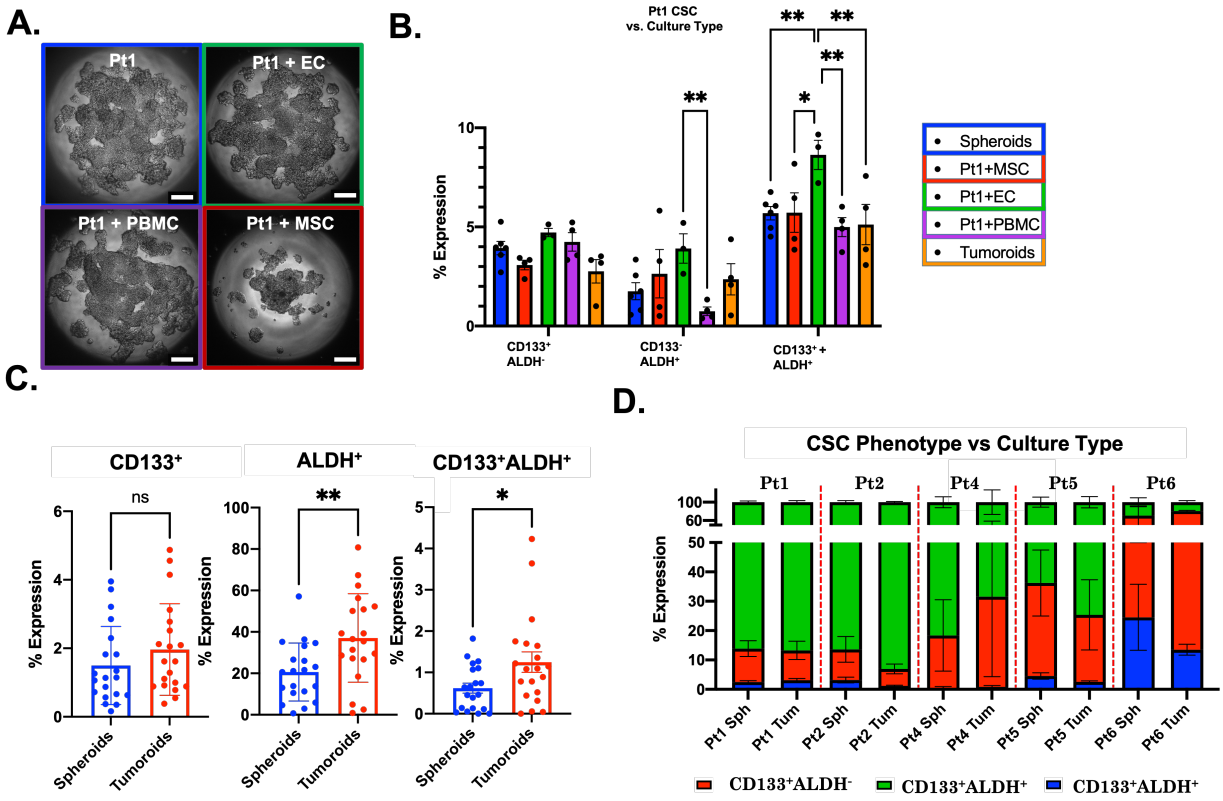

Figure 3.2: Evaluation of stemness in 3D heterotypic hanging drop systems.
*A) Phase contrast images of Pt1 co-cultures with MSCs, ECs, or PBMCs. B) Expression of CD133, ALDH, or the sum of CD133 and ALDH expression in GFP+ patient cells from each culture type. C) ALDH+CD133+, CD133+, and ALDH+ population percentages (with tumoroids scaled according to the ratio of GFP+ tumor cells found in spheroids compared to tumoroids.) D) Proportion of each CSC phenotype ($CD133^{+/-}ALDH^{+/-}$) in the CSC compartment of each sample split by patient sample. Error bars = SEM, ** $p<0.01$. Scale bars = 200 um.*

3.2.3 Machine learning to facilitate investigations of how the TME cell composition influences CSC populations.

Finally, we supplemented our tumoroid system with a random forest model to make predictions about the level of CSC marker expression based on cell composition (determined by FACS on day 7). The goal of this model was to further reinforce the relationship between the TME cells and stemness with the added benefit of helping to understand the importance of various cell-cell relationships in CSC maintenance and by extension how they may be related to

clinical outcomes. First, we obtained and processed FACS data from 52 tumoroid FACS experiments that measured $CD133^{-}ALDH^{+}$, $CD133^{+}ALDH^{-}$, $CD133^{+}ALDH^{+}$, $CD73^{+}$, $CD31^{+}$, and $CD68^{+}$ percentages. After pre-processing and generating new features to obtain a total of 17 tumor mircroenvironment based parameters, the data was randomly broken up into a 37 sample training set and a 15 sample test set. A random forest classifier was trained to predict 'high' versus 'low' expression of $CD133^{-}ALDH^{+}$, $CD133^{+}ALDH^{-}$, or $CD133^{+}ALDH^{+}$, based on the TME-based parameters (Figure 3.3A). After running a tuning algorithm to identify the optimal number of trees and parameters to consider at each node, we found that this model was able to predict high versus low expression of $CD133^{-}ALDH^{+}$ with moderate success in the training and test data sets which had AUC values of 0.66 and 0.69 respectively (Figure 3.3B). The model trained to predict $CD133^{+}ALDH^{-}$ percentages was similarly effective with training and test AUC values of 0.65 and 0.88 (Figure 3.3C). Contrarily, the model trained to predict $CD133^{+}ALDH^{+}$ percentages performed worse with a training AUC value of 0.39 and a test AUC value of 0.73. These results suggest that within our tumoroid model system, the TME composition played a bigger role in the expression of single CSC markers compared to the double positive CSCs. That these models attained moderate predictive performance despite the limited sample size used to train each model highlights the potential of using TME cell composition to predict CSC levels.

Coupling machine learning models with complex multi-cellular cultures can help to reveal critical cellular relationships. Particularly, when there are many different cell types present in the culture, it is difficult to ascertain which cells or which combinations of cells are most influential in determining the characteristics of the model (in this case CSC marker expression). To evaluate which parameters in our models are most important in predicting the level of $CD133^{-}ALDH^{+}$ and $CD133^{+}ALDH^{-}$, the mean decrease in gini impurity was calculated for the

ALDH and CD133 models. This analysis suggested that the proportion of the cells expressing CD31, CD73, or CD68 that is made up of $CD73^+$ cells is was the most important parameter in predicting ALDH levels (Figure 3.3E) while the ratio of cells expressing CD31 to the cells expressing CD73 was the most important parameter in predicting CD133 levels (Figure 3.3F). Plotting the relationship between these parameters indicates that when CD73 expression makes up high proportions of the total expression of CD31, CD73, and CD68, there is a corresponding drop in ALDH expression (Figure 3.3G). The relationship between the ratio of CD31 and CD73 and the expression level of CD133 is less clear, with most datapoints centered in the middle of the plot with the exception of four datapoints with exceptionally low ratios of CD31 to CD73 (CD73 >> CD31) which also had the highest CD133 expression (Figure 3.3H).

To test the effectiveness of this type of model on clinically relevant data, new random forest models were trained on all 52 datapoints from our tumoroids resulting in an AUC value of 0.62 for ALDH prediction (Figure 3.3I) and 0.74 for CD133 prediction (Figure 3.3J). The test set for these models was cell compositions derived from single-cell RNA sequencing of 42 HGSOC patient samples. The ALDH prediction model performed worse on the test set than the training set with an AUC of 0.51, essentially as good as a null predictor. The CD133 prediction model also performed worse in the test set compared to the training set with an AUC of 0.63. These discrepancies could be due to the fact that the models were trained on protein based data whereas the test data was based on mRNA expression, which has been shown to correlate poorly with protein level expression[125]. These findings leave open the possibility of predicting stemness based on cell composition in clinically relevant datasets. Overall, despite the moderate performance of our machine learning models, we demonstrated the utility in coupling machine learning techniques with experimental model systems to facilitate comprehension of multi-

variate systems and the importance of complex cellular relationships that are difficult to discern otherwise.

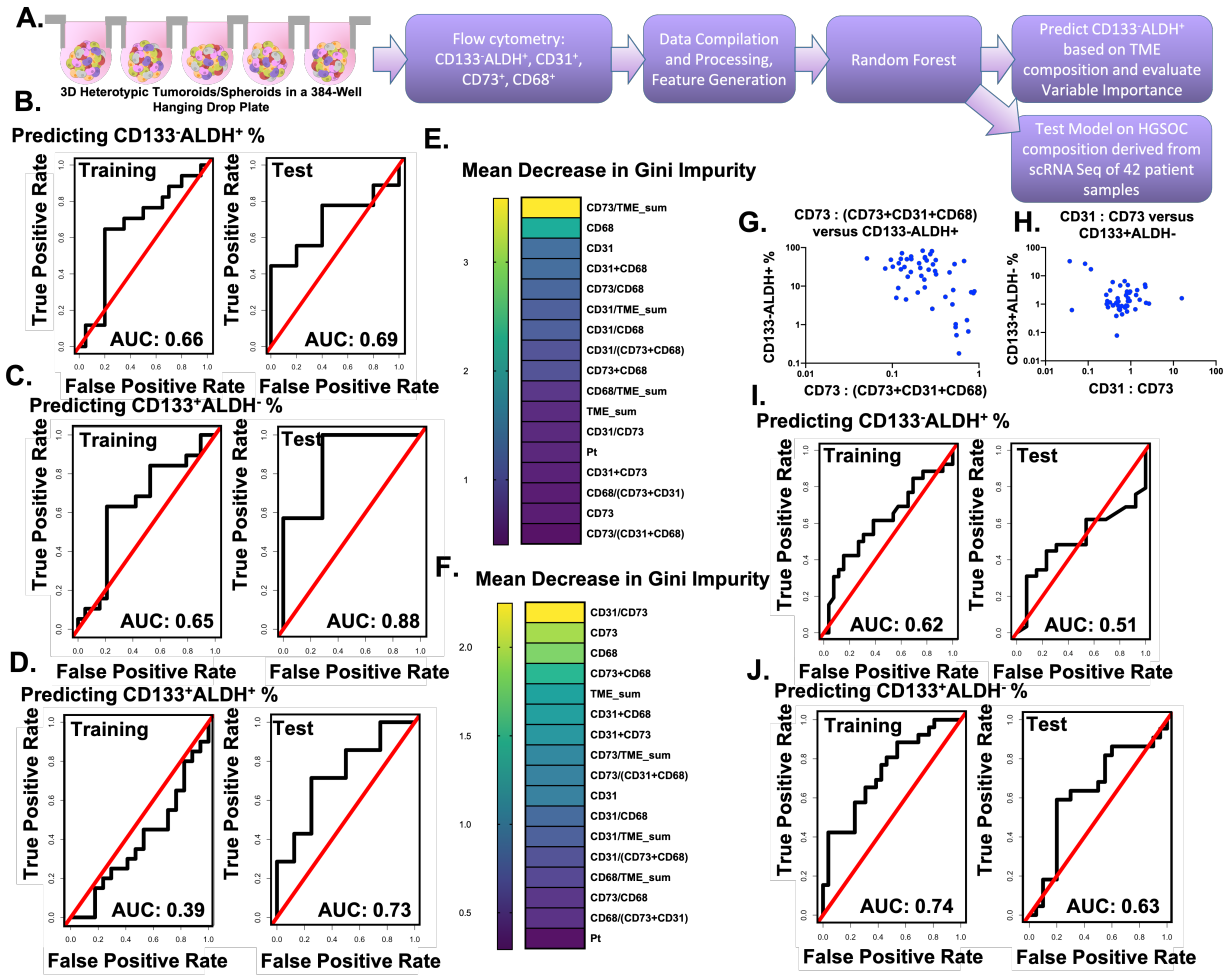

Figure 3.3: Machine learning provides insight into complex cell-cell interactions and their role in CSC maintenance.
A) Model schematic. ROC curves for the FACS training set and test set for B) CD133-ALDH+, C) CD133+ALDH-, and D) CD133+ALDH+ prediction models. Heatmap of the mean decrease in gini impurity from the E) CD133-ALDH+ and F) CD133+ALDH- training sets. G) Scatter plot showing the relationship between the ratio of CD73 expression to the total CD73 + CD31 + CD68 expression and ALDH percentages. H) Scatter plot showing the relationship between the ratio of CD31 to CD73 and CD133 expression. ROC curves for random forest models trained on all 52 FACS samples to predict I) CD133-ALDH+ and J) CD133+ALDH- levels. Models in I) and J) were tested on compositional data from 42 single cell sequencing HGSOC samples.

3.2.4 Tumoroids have elevated tumorigenic potential.

Due to the capacity of CSCs to drive tumorigenesis, we next evaluated the tumor formation capacity of tumoroids compared to spheroid controls. To accomplish this we collected tumoroids and spheroids from hanging drops and injected them into NOD SCID mice subcutaneously with Matrigel (Figure 3.4A). To evaluate tumorigenic potential, we observed injection sites with palpable tumors at a four week timepoint and found that 4/10 sites spheroid injection sites showed tumor growth while at the same time point 6/10 tumoroid injection sites showed tumor growth. We used this data to estimate the fraction of true stem cells in the tumoroid condition using an extreme limiting dilution analysis (ELDA) tool[262] and found a greater expected stem cell population in tumoroids compared to spheroids (Supplemental Figure 6A,B). Moreover, tumoroid-derived xenografts (TDXs) reached their endpoint volume significantly faster compared to spheroid-derived xenografts (SDXs) (Figure 3.4B,C). Body weight measurements did not show a significant difference across the two groups. H&E stains from xenograft sections show pleomorphic cells with prominent nuclear atypia (Supplemental Figure 6C).

To further evaluate differences in tumoroid and spheroid xenografts, cells harvested from each tumor type were used to form spheroids and cultured for 7 days in hanging drop plates. Following 7 days, TDX spheroids had a significantly greater area than SDX spheroids, suggesting increased proliferation capacity (Figure 3.4D,E). No significant differences in tumoroid cell composition was found following flow cytometry on each spheroid type (Supplemental Figure 6D). However, given the larger size of TDX spheroids, the roughly equivalent CSC percentages theoretically should translate to a greater number of CSCs per spheroid corroborating our ELDA analysis. Moreover, by analyzing the CSC phenotype proportions in the CSC compartment of both spheroid types, we find significantly greater

proportions of CD133^{-}ALDH^{+} CSCs in the TDX spheroids compared to the controls further agreeing with our ELDA analysis.

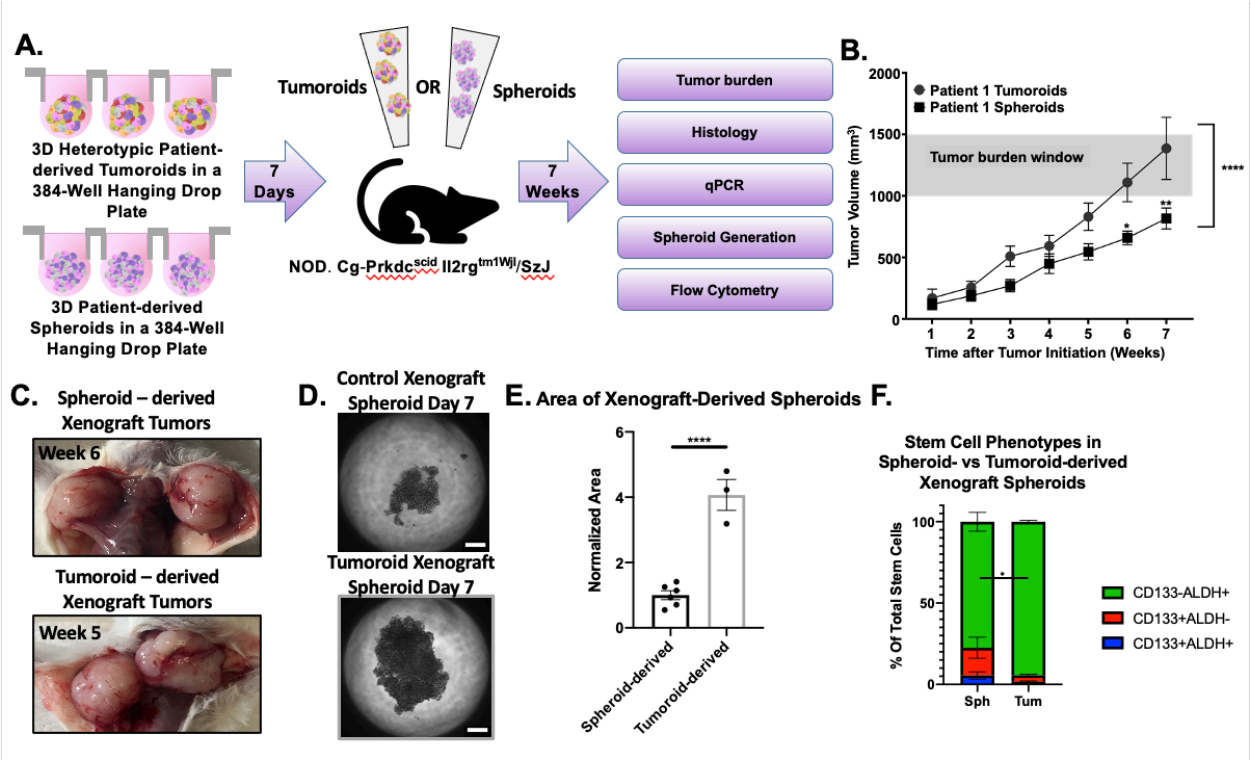

Figure 3.4: Generation of xenograft tumors.
A) Tumoroids and control spheroids were generated in hanging drop plates and injected into NSG mice on day 7. Tumors were harvested once they reached their endpoint size, digested, and frozen until later use in xenograft-derived spheroids. B) Xenograft tumor growth over 7 weeks showing that tumoroids produced tumors that reached the endpoint faster than spheroid generated tumors. C) Images of endpoint tumoroid and spheroid-derived tumors. D) Phase contrast images of spheroids generated from 200 tumoroid-derived xenograft tumor cells or 200 spheroid-derived xenograft tumor cells. Scale bar = 200 µm. E) Average area of spheroid versus tumoroid xenograft-derived spheroids after 7 days in hanging drop culture. $p<0.0001$. F) Proportion of each CSC phenotype (CD133$^{+/-}$ALDH$^{+/-}$) in the CSC compartment of spheroid xenograft derived-spheroids versus tumoroid xenograft derived spheroids. $p<0.05$.

3.2.5 Tumoroids promote epithelial-to-mesenchymal transition and changes in CSC phenotype.

To investigate potential mechanisms behind the increased tumorigenic potential and changes in stemness observed in our tumoroids compared to spheroids, we performed single cell RNA sequencing. Pt7 was used to compare differences in gene expression between 2D cultured

patient cells, spheroids made with patient cells, and tumoroids made with Pt7 cells as the tumor cell component with MSCs, ECs, and PBMCs (Figure 3.5A). We first observed the presence of all expected cell types in our tumoroid cultures, albeit with relatively small myeloid, B cell, endothelial, and epithelial clusters (Figure 3.5B). Interestingly, 2D and spheroid cultures had a clear epithelial tumor cell composition (represented in orange), which almost completely disappeared in Pt7 tumoroids. To investigate the drop in epithelial tumor cells in tumoroids compared to 2D and spheroid cultures Ingenuity Pathway Analysis (IPA) of the patient cells in each culture was performed to examine the predicted canonical pathways and upstream regulators. We found predicted activation of canonical pathways related to EMT, motility, and metastasis in tumoroids compared to spheroids (EMT*: Regulation of the Epithelial Mesenchymal Transition by Growth Factors Pathway* and *IL-8 Signaling*[355]; Motility: *PAK signaling*[356]; Metastasis: *Neuregulin Signaling*[357]) (Figure 3.5C). Similarly, 7/9 upstream regulators that were predicted to be activated in tumoroids compared to spheroids had direct links to the EMT process (MEK[358], TGFB1[359–362], FOXM1[361,363], PPP1R13L[364], MAPK1[365], CCL5[366,367], TCF4[368]) (Supplemental Table 4).

Consequently, we next investigated the possibility that the epithelial cells in tumoroid cultures underwent EMT and were subsequently identified as mesenchymal cells. First, a baseline was established for epithelial cancer cells by evaluating the expression of PAX8 and EPCAM, two traditional epithelial cancer cell markers in ovarian cancer (Figure 3.5D). Notably, spheroid cluster 2 and tumoroid cluster 6, which were previously assigned identified as epithelial cancer cells, highly expressed PAX8 and EPCAM, which were not highly expressed in any of the more mesenchymal clusters. Next we evaluated expression levels of TP53 with the rational that most HGSOC tumors have a TP53 mutation, which could alter its expression and make it

easy to identify cancer cells with a mesenchymal phenotype. We found that the spheroid epithelial cluster in particular had the lowest average expression of TP53. This makes sense as Pt7 was determined to have an H179R TP53 mutation associated with no expression of TP53 mRNA[369]. As such, it follows that a previously epithelial mesenchymal cluster would also express low levels of TP53 mRNA. Interestingly, tumoroid cluster 4, which was previously assigned as a mesenchymal cluster, had the lowest expression of TP53 in the tumoroids (average expression of 0.258 compared to the next lowest average TP53 expression of 0.445), indicating that it may contain cells that had undergone EMT.

This suspected EMT cluster also highly expressed two additional epithelial cell markers, KRT18 (average expression of 1.670 compared to the cluster with the next highest expression of 0.878) and KRT19 (2.708 compared to the cluster with the next highest expression of 0.042), which were also highly expressed in our established epithelial clusters and not expressed highly in the other mesenchymal clusters. This suggested that the suspected EMT cluster maintained remnant expression of epithelial markers. Finally, examining the classical EMT transcription factors (*TWIST1, TWIST2, SNAI1, SNAI2, ZEB1,* and *ZEB2*) showed low expression in the epithelial clusters, but high expression of *TWIST2*, *SNAI1*, and *SNAI2* in the suspected EMT cluster. Consequently, tumoroid cluster 4 is henceforth referred to as the 'EMT cluster'.

To examine the overall similarity of the EMT cluster to the epithelial tumor cells identified in Pt7 spheroids, scRNA seq datasets from spheroids and tumoroids were integrated to align common cell types across each culture type using a methodology first described by Stuart et al.[370] After alignment, a t-SNE plot showed that the EMT cluster and the epithelial cluster remained separate clusters (Figure 3.5E, Supplemental Figure 7A). However, a principle component analysis of the aligned dataset showed that the EMT cluster and the epithelial cluster

directly overlap due to their high degree of similarity despite differences in expression of epithelial and mesenchymal markers (Figure 3.5E). As external validation that the tumor cell population becomes more mesenchymal within tumoroids expression of mesenchymal marker CD73 was evaluated in GFP^+ Pt1 cells from spheroids or tumoroids using flow cytometry. This experiment showed significantly greater $CD73^+$ expression in patient-derived tumor cells from tumoroid cultures compared to spheroid cultures, reflecting the trend observed in the epithelial cluster and the EMT cluster (Supplemental Figure 7B).

Having identified an EMT cluster, we then examined changes in CSC marker expression in the epithelial tumor cells from spheroids compared to the EMT cluster in tumoroids. The differences in average expression of each CSC marker in the EMT cluster compared to the epithelial cluster showed loss of *CD24* and *EPCAM* expression in the EMT cluster concordant with an increase in *THY1* expression (Figure 3.5F). Differential expression analysis found these differences to be statistically significant (*CD24* average $\log_2$FC: -2.442, p-adjusted: 1.771E-74; *EPCAM* average $\log_2$FC: -2.587, p-adjusted: 6.716E-81; *THY1* average $\log_2$FC: 1.172, p-adjusted: 1.777E-18) (Figure 3.5G). While not significant, small increases in average expression of *ALDH1A3* (+0.348), *ALDH2* (+0.494), and *ALDH3A2* (+0.227) with a decrease in *PROM1* (*CD133*; -0.162) was also observed in the EMT cluster compared to the epithelial cluster, though average expression of these markers was generally low overall (Supplemental Figure 7C). Contrarily, average *CD44* expression in both clusters was substantial and appeared to remain consistent between the EMT cluster and the epithelial cluster. Increased *THY1* expression in tumoroid tumor cells was confirmed with qPCR of isolated GFP^+ tumoroid tumor cells compared to sorted GFP^+ cells from spheroid controls. However, in this experiment, *CD24* was not significantly decreased, in fact it was increased, while *CD133*, was again decreased. *ALDH1A3*

was also significantly increased, corroborating increased ALDH expression in tumoroids compared to spheroids (Supplemental Figure 7D). Several other CSC markers (*ALDH1A1*, *ALDH1A2*, *POU5F1*) and EMT markers (*CDH2*, *SNAI1*, *ZEB1*, and *VIM*) were also slightly elevated in GFP tagged tumor cells from tumoroids compared to spheroids.

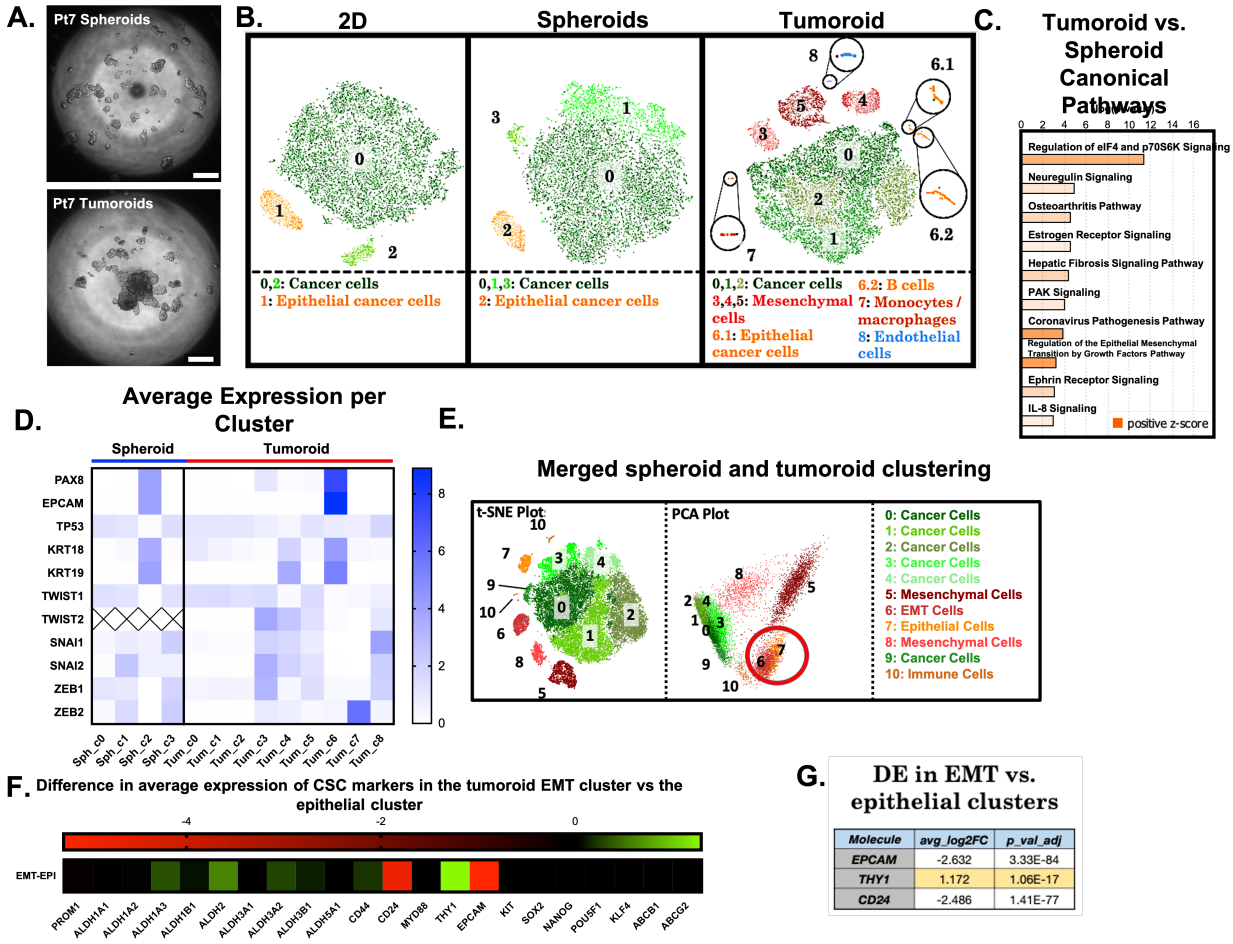

Figure 3.5: Single Cell RNA Sequencing of patient-derived tumoroids, spheroids, and 2D cultures. A) Phase contrast images of pt7 tumoroids and corresponding spheroids.B) t-SNE plots of Pt7 2D cultured cells (left), spheroid cultured cells (middle), and tumoroid cultured cells (right). C) Canonical pathways predicted to be upregulated in tumoroid cancer cells compared to spheroid cancer cells that are unique to the tumoroid-spheroid comparison. D) Heatmap of the average expression of epithelial (PAX8, EPCAM, KRT18, KRT19) and EMT (TWIST1, TWIST2, SNAI1, SNAI2, ZEB1, ZEB2) markers identifying tumoroid c4 as a mesenchymal cluster with partial epithelial expression (KRT18, KRT19). E) t-SNE (left) and PCA (right) plots of aligned spheroid and tumoroid datasets showing overlap of EMT cluster 6 and epithelial cluster 7 in the PCA plot. F) Heatmap showing the difference between the average expression of CSC related genes in the EMT cluster and the epithelial cluster. G) Statistically significant differential expression of EPCAM, THY1, and CD24 in the EMT cluster compared to the epithelial cluster.

3.2.6 Tumoroids are more resistant to chemotherapy compared to control spheroids.

As CSC marker expression, EMT, and the presence of stromal cells are associated with poor clinical outcomes, we next sought to evaluate tumoroid and spheroid viability following 48 hour treatment with traditional chemotherapies, like carboplatin and paclitaxel, which function primarily by causing DNA damage and stabilizing microtubules respectively. Tumoroids and control spheroids were also treated with more novel therapies SC144, PACMA31, and N773 for targeting ovarian cancer. SC144, is a GP130 inhibitor that prevents IL-6 mediated STAT3 activation, which is associated with stemness and EMT[339,340,371,372]. On the other hand, PACMA31 (a protein disulphide isomerase inhibitor) and N773 target chemoresistant ovarian cancers through downregulation of DNA damage repair pathways which are highly active in CSCs[373,374].

To test the efficacy of these treatments, patient-derived tumoroids and spheroids were generated from five randomly selected primary patient samples with TM medium and 1:20 ratio of growth factor reduced Matrigel to medium and treated with each of the 5 drugs for 48 hours starting on day 5. Phase contrast images show disrupted tumoroid and spheroid boundaries caused by each drug treatment, with the exception of Pt5 cultures, which show few visible effects (Figure 3.6A, Supplemental Figure 8A). Overall, drug treatments elicited a differential response between spheroids and tumoroids made with the same patient samples (Figure 3.6B-F). For example, 200 μM Carboplatin led to 23.1% viability in Pt5 spheroids and 54.85 % viability in tumoroids from the same patient sample ($p<0.0001$). Similarly, Pt2 spheroids had 15.81% viability in response to carboplatin compared to 59.3% viability in the corresponding tumoroids ($p<0.0001$). Following a similar trend, Pt3 spheroids were 23% viable while tumoroids maintained a viability of 60.92% in response to 200 μM carboplatin (Figure 3.6B; $p<0.0001$; two

way ANOVA spheroid vs tumoroid in response to 200 μM Carboplatin across all three patient samples). Tumoroids from the three patients seem to be less sensitive to a 10 μM dose of paclitaxel compared to the spheroids from the same patient (Figure 3.6C). Pacma31, SC144, and N773 treatment elicits a similar response in that tumoroids are more resistant than their spheroid controls (Figure 3.6D-F)**.** Increased viability in tumoroids across the patient samples points to the role of the TME cells in chemoresistance. However, treatment of Pt5 with PACMA31 and Pt3 with paclitaxel did not elicit significantly different responses between spheroids and tumoroids (Figure 3.6C,D). These observations also indicate that tumoroids maintain chemoresistant properties inherent to a patient-sample, and that the tumor microenvironment affects response to treatment differently for different drugs and patient samples. Given that the majority of our functional analyses of tumoroids were performed on tumoroids without GFR Matrigel, increased chemoresistance in tumoroids compared to spheroids was confirmed in Pt1 tumoroids made without GFR Matrigel (Supplemental Figure 8B).

We then sought to evaluate the effect of carboplatin, pacma31, and sc-144 on each cell type in tumoroid cultures without GFR matrigel via flow cytometry. We observed little to no effect of each drug on quantity of viable $CD31^+$, $CD73^+$, or $CD68^+$ cells, often with slight increases in expression following drug treatment (Supplemental Figure 8C-E). $CD133^+ALDH^+$ and $CD133^+ALDH^-$ populations tended to decrease following treatment, albeit not to a statistically significant degree. $CD133^-ALDH^+$ populations contrarily appeared to increase following treatment with Pacma31 or SC144 with significantly more $CD133^-ALDH^+$ cells in tumoroids treated with Pacma31 compared to spheroids with the same treatment ($p<0.05$). On the other hand, carboplatin treatment significantly reduced $CD133^-ALDH^+$ expression in tumoroids, but not spheroids, perhaps owing to its effect on rapidly dividing cells and potential

increased proliferation of this population in tumoroids compared to spheroids (Supplemental Figure 8C-E). We also found that spheroids and tumoroids had similar viability measured as $DAPI^-$ cells via flow cytometry in response to carboplatin and SC144 when cultured without Matrigel. Contrarily, Pacma31 treatment yielded significantly higher viability in tumoroids after drug treatment (Supplemental Figure 8F). These results show the impact of the non-cancer cells on drug response and the potential for tumoroids in personalized screening applications.

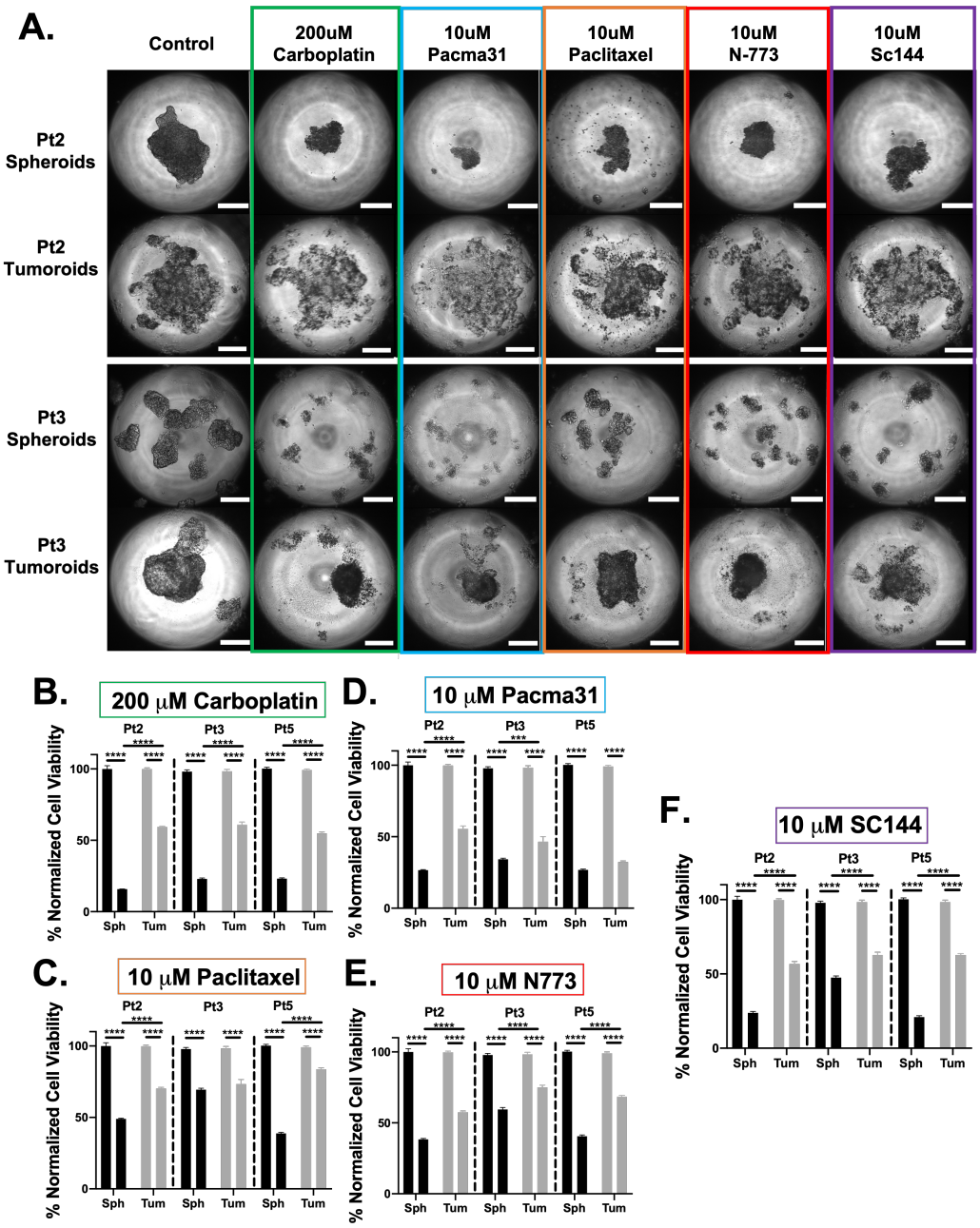

Figure 3.6: Evaluation of chemoresistance in tumoroids compared to spheroids.
*A) Phase contrast images of tumoroids and corresponding spheroid controls after 48 hours incubation with either 200 uM carboplatin, 10 uM of pacma31, 10 uM of paclitaxcel, 10 uM of N-773, or 10 uM of SC-144. Normalized cell viability obtained via MTS assays of pt2,3, and 5 following treatment with B) carboplatin, C) pacma31, D) paclitaxel, E) N-773, and F) SC144. *** = p<0.001; **** = p<0.0001.*

3.2.7 Tumoroids express a matrisome signature associated with poor clinical outcomes.

To investigate the molecular features that may be causing increased in tumor growth, EMT, and chemoresistance in tumoroids, we next evaluated the top differentially expressed genes between the EMT cluster and the epithelial cluster. We observed high upregulation of ECM related transcripts in the EMT cluster (Table 3.1) and theorized that differences in ECM between tumoroids and spheroids may be contributing to more malignant characteristics in tumoroids. Moreover, mesenchymal cells were the most abundant non-cancer cell type in our tumoroids and were also characterized by high expression of ECM related genes (Table 3.2). This idea was further supported by examination of the most highly variable genes in tumoroids and spheroids, which included MGP, MMP1, FN1, COL1A1, DCN, COL6A1, and COL6A3 among others (Supplemental Figure 9A).

This association with ECM and ECM remodeling prompted analysis of a matrisome gene expression signature previously associated with advanced disease states and chemoresistance in ovarian and other cancers[81]. We found increased expression of these matrisome genes in tumoroid cultures compared to spheroid and 2D cultures (Figure 3.7A). This finding was validated with qRT-PCR comparing the expression of these genes in spheroids and tumoroids from four patient samples (Figure 3.7B). While we expected to find elevated expression in tumoroids for all patient samples, we observed some heterogeneity between Pt1, Pt2, Pt5, and Pt6 with 17/22, 11/22, 19/22, and 10/22 genes respectively elevated compared to spheroid controls. 21 out of the 22 genes were more highly expressed in tumoroids compared to spheroids in at least one patient sample, with *ANXA6* being the lone exception. All four patient sample tumoroids had elevated expression of *AB13BP, COL11A1, COL15A1, COL1A1*, *COMP, FBLN2,* and *FN1* suggesting potential patient-independent changes in matrisome. Interestingly, *FN1* was the most elevated matrisome gene in Pt1, Pt2, and Pt5 while *COL1A1* was the most elevated in

Pt6 tumoroids. Strikingly, 4 out of the 6 matrisome genes (*COL11A1, COMP, FN1, VCAN*) most closely associated with higher disease malignancy were upregulated in tumoroids from all four patient samples (Figure 3.7E). Interestingly, looking at these markers in the EMT cluster in tumoroids compared to the epithelial cluster in spheroids, only 9/22 matrisome genes were upregulated (*FN1, VCAN, COL1A1, FBLN2, ANXA5, CTSB, ACTB, LAMB1, LAMC1*) suggesting involvement of the other cell types found in tumoroids. Breaking matrisome gene expression down by cell type in Pt7 tumoroids confirmed that the mesenchymal cells were the primary cells expressing matrisome markers, however the EMT cluster was also a significant contributor (Figure 3.7C). Looking closer at the smaller cell populations in tumoroids, endothelial cells and myeloid cells also contribute to the matrisome signature (Supplemental Figure 10A-C).

As changes in transcripts don't necessarily translate to the protein level, we sectioned and stained tumoroid or spheroid-derived xenograft tumors for collagen (Sirius red) and non-collagen (fast green) proteins (Figure 3.7D). While there was no significant difference in collagen protein found between tumoroid and spheroid derived xenograft tumors, tumoroids generated tumors with significantly greater non-collagen protein ($p<0.001$). This corresponded to a significantly lower ratio of collagen to non-collagen proteins compared to tumors generated by spheroids

($p<0.05$; Figure 3.7E). This confirms altered ECM production in tumoroids compared to spheroids on the protein level, and within *in vivo* microenvironments.

Table 3.1: Top 10 upregulated genes in the tumoroid EMT cluster compared to the spheroid epithelial cluster.

	avg_log2FC	p_val_adj
TIMP1	5.481	1.87E-287
COL1A1	5.010	5.40E-261
COL3A1	4.967	1.22E-243
IGFBP2	4.667	1.25E-209
IGFBP7	4.592	4.00E-241
COL1A2	4.070	1.65E-220
CHI3L1	3.984	1.56E-86
DCN	3.835	2.23E-128
SPARC	3.802	3.61E-173
MGP	3.784	9.60E-55

Table 3.2: Top 10 upregulated genes in the tumoroid mesenchymal cells.

Molecule	avg_log2FC	p_val_adj
COL6A1	4.932	<2.23E-308
COL6A2	4.658	<2.23E-308
COL6A3	4.636	<2.23E-308
FN1	4.402	<2.23E-308
COL1A1	4.047	<2.23E-308
DCN	3.708	<2.23E-308
COL3A1	3.476	<2.23E-308
NEAT1	3.221	<2.23E-308
BGN	3.090	<2.23E-308
IGFBP5	3.019	<2.23E-308

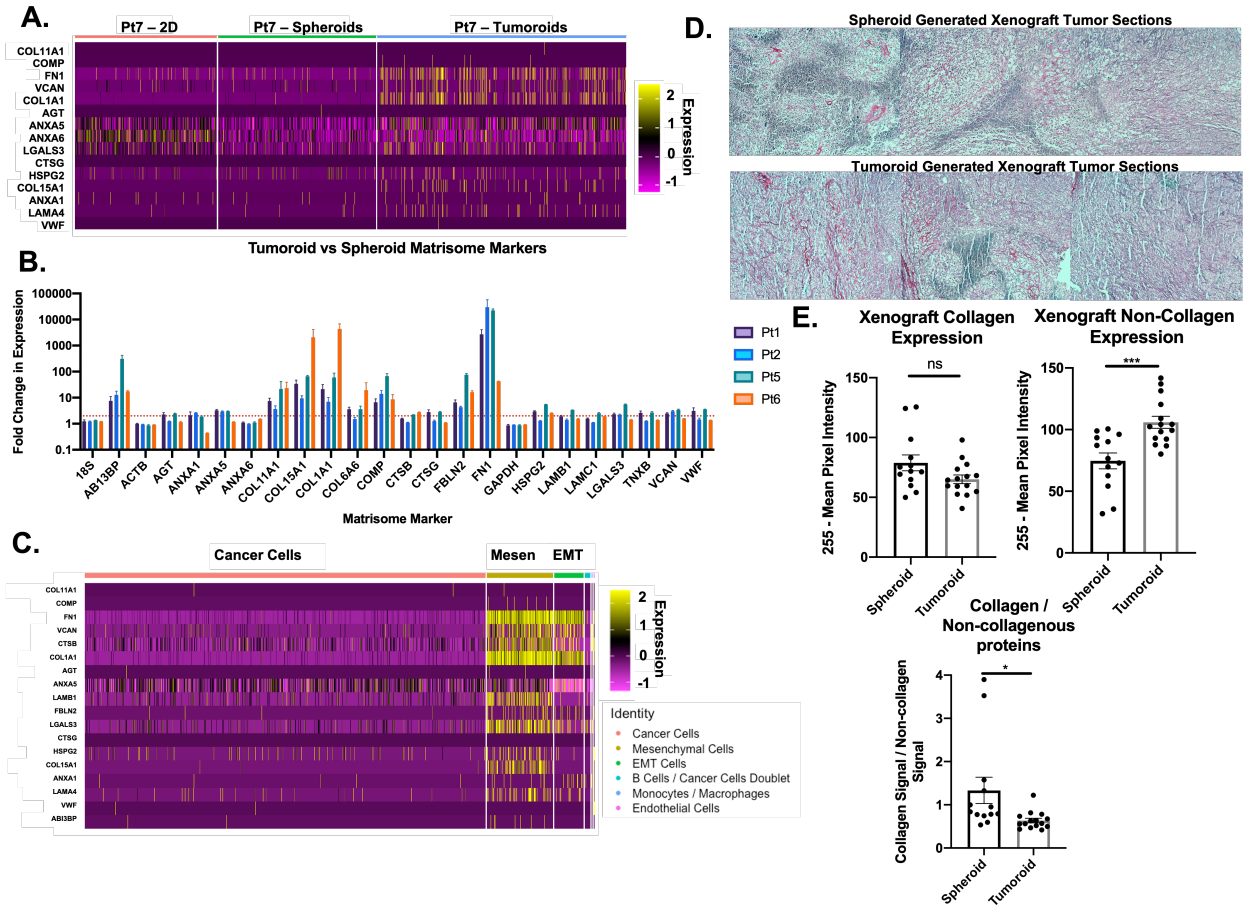

Figure 3.7: Tumoroids express a malignant matrisome signature associated with advanced disease states. A) Heatmap showing increased expression of malignant matrisome signature in tumoroids compared to spheroids and 2D culture. B) qPCR showing increased expression of malignant ECM matrisome in tumoroids made from four different patient samples compared to their patient-sample only controls. C) Heatmap showing expression of malignant matrisome signature in tumoroids split by cell type. D) Spheroid or Tumoroid-derived xenografts stained for collagen (Sirius red) or non-collagen (fast green) proteins. E) Quantified area of collagen and non-collagen protein in spheroid- versus tumoroid-derived xenografts.

3.2.8 Tumoroids have a molecular signature reflective of the mesenchymal subtype of ovarian cancer.

Finally, due to the known influence of the stromal and immune cells on classification into molecular subtypes of ovarian cancer, and the association of the mesenchymal subtype of HGSOC with increased ECM deposition, we evaluated expression of the four TCGA molecular signatures ("proliferative", "differentiated", "immunoreactive", and "mesenchymal") in our single cell RNA sequencing data. Comparison of spheroids and tumoroids revealed that

tumoroids were enriched in the molecular signature of the mesenchymal subtype and appeared to have roughly equivalent expression of the differentiated, immunoreactive and proliferative molecular signatures compared to spheroids (Figure 3.8A). Notably, with the absence of mesenchymal cells Pt7 spheroids solely expressed a C5 proliferative signature. Tumoroids appeared to maintain this proliferative signature, but with the addition of a more prevalent mesenchymal subtype expression pattern. Evaluating expression of molecular signature by cell type indicated that the majority of the mesenchymal signature is derived from the mesenchymal cells, as has been found previously in the literature[82]. Interestingly, the EMT cluster also contributed to the mesenchymal signature, potentially linking EMT and the poor outcomes associated with the mesenchymal subtype. Contrarily, the cancer cells expressed the majority of the proliferative subtype signature, perhaps suggesting that the difference between the proliferative subtype and mesenchymal subtype lies primarily in the presence of activated mesenchymal cells.

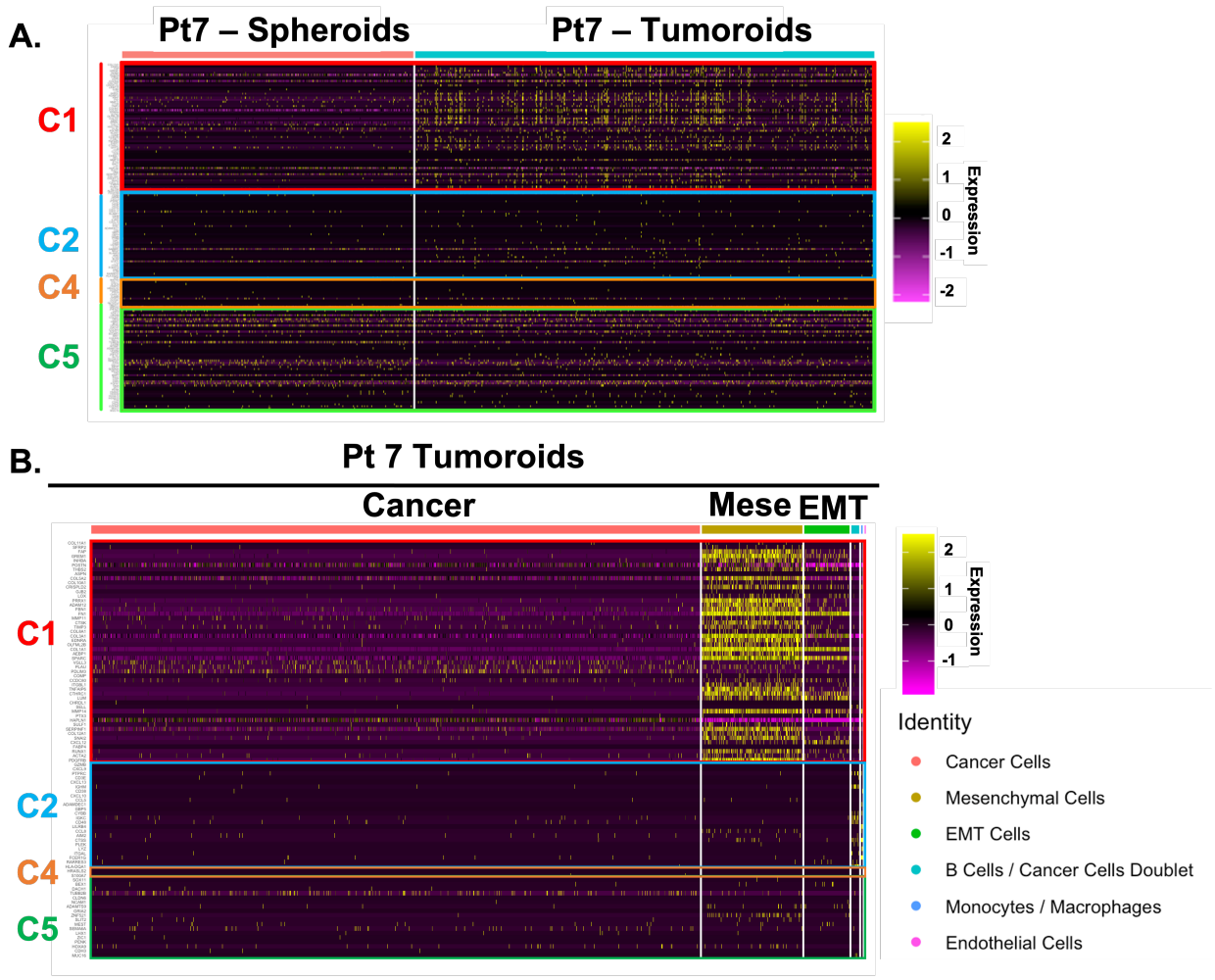

Figure 3.8: Tumoroids express the C1 mesenchymal molecular subtype signature.
A) Heatmap showing expression of genes highly expressed in each molecular subtype of HGSOC (C1: Mesenchymal – red; C2: Immunoreactive – blue; C4: Differentiated – orange; C5: Proliferative – green). B) Heatmap showing molecular subtype marker expression in Pt7 tumoroids divided by cell type.

3.3 Discussion

The non-cancer cells in the tumor microenvironment play a critical role in the disease course and outcomes of ovarian and other cancers. These cells can interact dynamically with ovarian cancer stem cells to maintain stemness, and thereby drive development of chemoresistance and recurrence[118,213,335,336,338,339,354,375–377]. The importance of the non-cancer cells in the TME is further reflected by their influence on molecular stratifications associated

with differential clinical outcomes. However, despite the clear importance of these cells, there remains a lack of flexible systems that can be used to truly understand how each cell type works together to maintain CSC phenotypes and poor clinical outcomes.

2D cell line models often translate poorly to the clinic due to the unrealistic environment that is inherent in 2D cultures such as lack of 3D cell-cell contacts and abnormal oxygen and nutrient diffusion[2,378–380]. They are also subject to gradual loss of stemness over time, although it can be partially rescued in 3D serum free culture[69]. Furthermore, cell lines provide a generalized and heavily pre-selected population of cells that may not accurately reflect the characteristics of each patient's cancer cells[353,381]. Moreover, 3D cultures with cell lines or even patient cells are limited by lack of cellular heterogeneity, which is required in understanding the complex interactions in a tumor. Some 2D and 3D models incorporate one or two additional cell types to study these interactions and have provided important insights into CSC regulation and the impact of non-cancer cells thus far[213,349,382,383]. However, the more cell types that are omitted from a model, the less comprehensive the interaction network, potentially leading to misinterpretation of results or results that won't translate into the clinic.

On the other hand, patient-derived organoids, ex vivo tumor cultures, and patient-derived xenograft models due a better job of maintaining the complex cellular microenvironment. Even so, these cultures are subject to the loss of stromal cells over time or infiltration of mouse stroma over time in the case of xenografts[204,350,351,384]. Patient-derived xenografts are also limited by variable engraftment rates and long periods of time needed for tumor growth[380]. While these models have demonstrated good replication of patient response to chemotherapy, they are difficult systems to use for the study of multicellular TME interactions due to lack of control over the cell composition[204,218,350,352,353,380]. This complicates the design of experiments to test the

effect of a single cell type on complex multicellular interactions in the TME, and ultimately limits our ability to effectively develop new treatments that will have a substantial impact on clinical outcomes.

As a result of these challenges, the goal of this work was to bridge the gap between 3D co-cultures used to study multicellular TME interactions and the complex cell cultures like PDO's and PDX's. To accomplish this goal, we developed a tumoroid culture system with patient derived tumor cells cultured with controlled ratios of MSCs, ECs, and PBMCs within 384-well hanging drop plates. This system allowed for high throughput experiments to study the effect of TME cells on CSCs and the outcomes associated with different molecular subtypes in the context of complex cellular microenvironment while maintaining fine control over the cell composition. Our ability to understand the complex interactions in this culture system was supplemented with the development of a machine learning model to predict stem cell enrichment and evaluate the importance of the relationships between different cell types.

In the initial stages of developing our tumoroid culture system, we used a 1:10 ratio of growth factor reduced Matrigel to support growth of each cell type, as this is common practice in organoid culture[204,380]. While this technique was successful, we ultimately performed the majority of our tumoroid cultures without Matrigel to minimize the potential impact of exogenous ECM on cell functions and to facilitate cell recovery from spheroids for downstream analyses. After establishing our culture technique, we demonstrated that tumoroids could be cultured for up to 22 days in a hanging drop plate, with termination of the experiment due to large droplet size leading to droplet instability. This culture period could potentially be extended with the use of serial passaging, which is commonly performed to culture PDO's over long periods of time[204], however it is unclear if all of the cell types would remain viable through

passaging and fine control over cell composition would be lost unless tumoroids were FACS sorted with each passage. That said, within a culture period of 7 days, tumoroids were formed successfully and highly amenable to downstream analyses.

Since MSCs, ECs, and macrophages have each been shown to individually influence stemness in a tumor[213,337,338,354], we hypothesized that expression of ovarian CSC markers CD133 and ALDH would be enriched in tumoroid cultures compared to co-culture and mono-culture spheroid controls. Interestingly, when patient tumor cells were tagged with GFP (allowing us to isolate CSC marker expression in the patient cells) we found the endothelial cell co-culture resulted in the greatest sum of cells expressing CD133 or high ALDH compared to spheroid controls ($p<0.01$), co-culture with MSCs ($p<0.05$), co-culture with PBMCs ($p < 0.01$), and tumoroids with all four cell types ($p<0.01$). While endothelial cells have been shown to enhance stemness previously [335–337], this is particularly intriguing as immune cells and mesenchymal stem cells have previously been shown to enhance stemness as well, suggesting that incorporation of all four cell types did not have an additive effect on stemness. This could be due to the fact that co-culture with MSCs alone did not appear to enhance stemness while co-culture with PBMC appeared to have a deleterious effect on $CD133^{-}ALDH^{+}$ expression. Lack of CSC enrichment in co-culture with MSCs could be because they were healthy adipose derived MSCs at the start of the culture as opposed to CA-MSCs previously transformed by tumor cells into a tumor promoting phenotype[85,338]. That said, single cell sequencing did indicate possible transformation of MSCs into CA-MSCs indicated by relatively high expression of BMP2, IL-6, LIF, and CXCL8 (IL-8) (Supplemental Figure 11A), which have previously been linked to tumor supporting MSCs[338,340].

Contrarily, PBMCs could potentially be killing some CSCs in tumoroids and PBMC co-cultures, though an experiment comparing MUC16 expression with and without PBMCs in hanging drop culture with TM indicated lack of epithelial tumor cell death with PBMC culture (Supplemental Figure 11B). Importantly, $CD133^{+}ALDH^{+}$ CSCs were not measured in these experiments, leaving open the possibility of increased $CD133^{+}ALDH^{+}$ CSC populations in tumoroids compared to controls. Perhaps more intriguing is the fact that the tumoroid culture seemed to negate the CSC promoting effect of the endothelial cells in the EC co-culture. This could be due to differentiation triggering signals from the PBMCs and/or MSCs counteracting EC effects on CSCs, or perhaps interactions between ECs and PBMCs / MSCs in a manner that prevented the ECs from promoting CSC growth. While more work is required to elucidate the reason for this finding, this demonstrates the non-linear relationship between TME cell composition and CSC enrichment, highlighting the need for complex heterogeneous cultures to study the interactions in the CSC niche.

However, when Pt1 tumoroid experiments with GFP^{-} tumor cells were compiled, tumoroids had a greater average percentage of $CD133^{-}ALDH^{+}$ cells compared to spheroids. The same was true for $CD133^{+}ALDH^{+}$ percentages. While these differences were not significant, given the dilution of tumor cells by TME cells in tumoroids it is likely that this difference is greater in reality. Scaling these tumoroid percentages based on the average percentage of GFP^{+} tumor cells in spheroids compared to tumoroids from our GFP^{+} experiments yielded significant increases in $CD133^{-}ALDH^{+}$ and $CD133^{+}ALDH^{+}$ compared to tumoroids. This crude scaling method may under or overestimate the true CSC percentages in our tumoroids, however it may yield results closer to reality than the unscaled percentages which were diluted by the presence of TME cells.

To circumvent the potential biases introduced by scaling, we next evaluated potential changes in the distribution of CSC phenotypes. Specifically, we examined the percentage of each CSC phenotype ($CD133^{+/-}ALDH^{+/-}$) relative to the total percentage of cells expressing one or both CSC markers. This analysis represents differences in CSC composition in tumoroids compared to spheroids independent of TME cell dilution. While differences between spheroids and tumoroids were not significant, this analysis suggested a patient-specific response to the presence of the TME cells, potentially due to patient-specific factors such as differences in disease stage, genetic background, and epigenetic signatures between and within patients[204,328]. Differential effects of TME signaling with tumor cells from different patients potentially reflects the variable outcomes in clinical trials of therapies targeting established CSC maintenance pathways, such as NOTCH, WNT, and HH, indicating the need for more comprehensive characterization of patient-tumors prior to treatment[385]. Since our tumoroid system captures these patient-specific differences, it has the potential to serve as a screening platform for drugs targeting interactions in the TME.

Our machine learning model demonstrated the utility of coupling our *in vitro* tumoroid model with *in silico* techniques to gain insight into variable importance. This is especially beneficial for complex models like the tumoroid system as it is difficult to ascertain the complex relationships between different parameters otherwise. While the prediction models had only moderate performances, they were limited by the small size of the dataset and therefore show promise for predicting CSC levels based on the cell composition of the TME, which would be indicative of prognosis. The predictive performance of these models would likely improve with more datapoints and more rigorous feature selection. That said, even the moderate predictive performance still serves as evidence that CSC levels are influenced by the TME composition.

As a result of the relationship between the non-cancer TME cells, CSCs, and prognosis, we examined the tumorigenicity of tumoroids compared to spheroids. Our xenograft experiment revealed increased tumor forming capacity and a significantly greater fraction of $CD133^{-}ALDH^{+}$ CSCs in TDX spheroids compared to SDX spheroids. TDX spheroids also seemed to be more proliferative based on their size after 7 days of hanging drop culture aligning with work from our lab and others showing increased proliferative capacity of $ALDH^{+}$ cells compared to $ALDH^{-}$ cells[3,386]. This also supports our finding of an increased $CD133^{-}ALDH^{+}$ CSC fractions in TDX spheroids compared to SDX.

On a molecular level, single cell sequencing of tumoroids compared to spheroids and 2D cultures from the same patient sample revealed evidence for EMT and altered stemness in tumoroids. That tumoroid cultures induced EMT is unsurprising, given the previously reported ability of MSCs, ECs, and macrophages to do so through a variety of mechanisms[213,387–390]. Despite the well-documented association of EMT with increased stemness, we found minimal changes in expression of most CSC markers in the EMT cluster in tumoroids compared to the epithelial cancer cell cluster in spheroids[267,391–394]. However, we did see small increases in average expression of various ALDH isoforms that are detectable with the ALDEFLUOR assay (which we used to measure ALDH expression via flow cytometry) potentially corroborating the modest increase in $CD133^{-}ALDH^{+}$ CSC fractions in tumoroids[395]. Notably, average expression of *ALDH1A3*, which has been linked to EMT was slightly greater in the EMT cluster in tumoroids compared to the epithelial tumor cell cluster[396–398]. That said, the most significant differences in CSC marker expression were the loss of *CD24* and *EPCAM* expression with concordant increase in *THY1* in the EMT cluster. A relationship between decreased expression of *CD24* and increased expression of *THY1* mediated by $\beta 3$ integrin was previously shown[399] and

implicated in suppression of ovarian tumor growth. Contrarily, *CD24* expression and *THY1* expression have independently been associated with poor outcomes in ovarian cancer[400–402]. Importantly, *CD44* expression remained high in the EMT cluster meaning that there were *CD44*$^{+}$*CD24*$^{-}$ cells which have been linked to not only EMT, but also to stemness and poor survival in ovarian cancer[391,403]. While there is still some ambiguity in the role *of CD24* and *THY1* in disease progression in ovarian cancer[391,399–401,403–407], our work showing increased proliferation, tumor forming capacity, and chemoresistance in tumoroids supports a pro-tumorigenic role of *THY1* and *CD44*$^{+}$*CD24*$^{-}$ cells in ovarian cancer.

Contrarily, in validating our findings with qPCR of tumor cells sorted from Pt1 tumoroids, we found increased *THY1* and *CD24* expression compared to tumor cells from spheroids, suggesting that some patient-specific differences in the tumor cells between Pt1 and Pt7 may be influencing the effect of the TME cells on *CD24* expression. Ultimately, more work is needed to fully understand the relationship between these markers and disease progression in ovarian cancer, however it stands to reason that the exact role of *THY1* and *CD24* may be dependent on the conditions of the microenvironment and / or the patient sample. Owing to the fine control over microenvironment composition, our patient-derived tumoroid model system could help elucidate the relationships between each of these markers and the microenvironmental conditions that are conducive to their pro- or anti-tumorigenic functions.

Expectedly, as EMT and chemoresistance are closely linked[408], we found that tumoroids in our system demonstrated significantly higher chemoresistance against various conventional and experimental therapies compared to spheroids alone. This difference was almost ubiquitous across the four patients with paclitaxel treatment of Pt3, pacma31 treatment of Pt5, and N773 treatment of Pt1 being the lone exceptions, demonstrating that patient-specific responses are

present. Importantly, these differences did not necessarily reflect the inherent chemoresistance of each patient sample (for example, Pt5 spheroids were most sensitive to paclitaxel out of the three patient samples whereas the Pt5 tumoroids were the least sensitive to paclitaxel out of the tumoroids from each patient sample). This intriguing finding indicates that culture of patient-derived cancer cells with TME cells may be a critical factor in accurately predicting response to specific drugs. While this finding needs to be compared against clinical responses before we can know if the tumoroid drug responses are more representative of clinical scenarios than patient cell only spheroids, at minimum this finding shows that aside from molecular and genetic differences within a tumor, different regions may respond differently to treatment based on the local cell composition. This is important as intra-tumor heterogeneity is thought to be a critical factor in drug resistance[409]. As our tumoroid system is amenable to culture with different cell compositions, it could serve as a promising screening platform wherein drugs could be screened for each patient on tumoroids made with an array of different compositions. Then, the optimal treatment could be chosen to minimize chances of resistance due to cellular heterogeneity.

Interestingly, tumoroids were even generally more chemoresistant than spheroids after treatment with targeted therapies. For example, they were more resistant to PACMA31 and N773, which can downregulate the DNA damage repair systems that are activated in CSCs, in ¾ patient samples[373,374,410]. All four patient samples also demonstrated increased resistance to SC144 which inhibits IL-6 / LIF induced STAT3 phosphorylation and consequent increased stemness and EMT[339,340,371,372,411–413]. These results suggest alternative means of chemoresistance conferred by the tumoroids. For example, BMP-2, which is more highly expressed by mesenchymal cells in tumoroids than IL-6, can promote stemness independent of STAT3[64,338,394].

Examining the most highly differentially expressed genes in the tumoroid EMT cluster compared to the spheroid epithelial cluster and the most variable genes in the tumoroids and spheroids showed greatly increased expression of ECM proteins in tumoroids. Not only did the EMT cluster express significantly more matrix related transcripts compared to the spheroid epithelial cluster, but Pt7 tumoroids had a high proportion of mesenchymal cells, which are also known to remodel the ECM in tumors[171,414,415]. This observation suggests a potential ECM related chemoresistance mechanism in tumoroids. In fact, the ECM has long been known to impact chemoresistance. Specifically, the top 10 most significantly upregulated genes in the tumoroid EMT cluster compared to the spheroid epithelial cluster (tissue inhibitor of metalloproteinases 1 (TIMP-1)[416], collagen 1A1 (COL1A1)[417], collagen 3A1 (COL3A1)[161], insulin growth factor binding protein 2 (IGFBP2)[418], insulin growth factor binding protein 7 (IGFBP7)[419], collagen 2A1 (COL2A1)[420], CHI3L1[421], DCN[422], SPARC[423], and MGP[424]) all have associations with chemoresistance.

The relationship between tumoroids, chemoresistance, and malignant characteristics of advanced disease is further linked to the ECM through expression of a 22 gene matrisome signature associated with advanced stage disease and poor clinical prognosis was further supported by tumoroid expression of a malignant matrisome signature of ovarian cancer (that also translates to other cancers)[81]. In particular, four out of six matrisome genes (*COL1A1, COL11A1, COMP, FN1*) most closely associated with advanced disease score were upregulated in our tumoroids compared to spheroids in all four patient samples in our qPCR analysis. Importantly however, even among the four genes upregulated in all four patient samples, there was substantial variability, which may contribute to patient-specific differences in drug response. Pt5 tumoroids had greater expression of *COL1A1*, *COL11A1*, and *COMP* than Pt2 tumoroids and

also had significantly greater viability after treatment with N773 and Paclitaxel. Contrarily, Pt2 tumoroids had significantly greater resistance to Pacma31 treatment.

These matrisome genes were most highly expressed in tumoroids by the mesenchymal cells as well as the EMT cluster, with COL11A1 being unique to the mesenchymal cells (Supplemental Figure 11C). Notably, common transcription factors for the 22 gene matrisome signature (including *RUNX2, STAT3, SMAD4, WT1, JUN*, and *TP53*) were also most highly expressed in the EMT and mesenchymal clusters (Supplemental Figure 11D)[81]. This finding highlights the role of the TME cells, most notably the mesenchymal cells in our model system, in matrix remodeling within our tumoroids, which parallels the remodeling identified in omental metastases of HGSOC and other cancers. The prominent role of the mesenchymal cells in matrix remodeling is also in line with the literature[171,414,415,425,426]. While the number of myeloid cells and endothelial cells in this particular patient tumoroid were low, they also had relatively high expression of matrisome genes (Supplemental Figure 11A-C).

Comparing this 22 gene matrisome signature against the four HGSOC molecular subtypes defined by Tothill et al. revealed substantial overlap with the C1 mesenchymal subtype. In fact, the C1 subtype was the only subtype that was characterized by increased expression of any of the 22 genes[81,229]. In particular, 7 of the 22 matrisome signature genes (*COL11A1, COMP, FN1, COL1A1, LAMB1, FBLN2,* and *LAMA4*) were upregulated in the C1 mesenchymal subtype, suggesting that this could be a 7 gene signature of poor outcomes in HGSOC. Notably, this included the same four matrisome genes upregulated in all four tumoroid qPCR patient samples, which were most closely associated with advanced disease[81,229].

Our tumoroids were further linked to clinically relevant chemoresistance through our finding that tumoroids expressed a C1 mesenchymal subtype signature compared to spheroids

due primarily to the presence of the mesenchymal cells and the EMT cluster. This corresponds not only with the worse outcomes associated with the C1 mesenchymal subtype, but also with the association of EMT, matrix remodeling, and desmoplasia with poor outcomes[229,348,408,414]. As the molecular subtype of a tumor is closely linked to the presence of stromal cells, and our tumoroids are amenable to culture with four or more cell types in many different compositions, it follows that our model will be advantageous in studying how the non-cancer cells in the TME contribute to different clinical outcomes of the different molecular subtypes.

3.4 Conclusions

In this chapter we show that the flexibility of our tumoroid system opens the door for in depth study of the role of the complex tumor microenvironment in the most critical facets of HGSOC. The non-cancer cells in the tumor microenvironment are inextricably linked to clinical outcomes through their role supporting cancer stem cells, promoting EMT, tumorigenesis, chemoresistance, and ECM remodeling. However, many questions remain surrounding the key mechanisms through which the TME contributes to poor outcomes leading to limited success of current targeted therapies. Moreover, despite the knowledge that cell composition influences molecular subtypes of HGSOC, our lack of comprehensive understanding of how each cell type influences outcomes is a barrier to clinical adoption of currently defined subtypes. Our model combines the increased cellular complexity of a four cell type culture while maintaining fine control over experimental conditions that is lacking in PDO's and PDX's in order to address these challenges.

Using this platform, demonstrated flexible culture of patient-derived tumor cells with three non-cancer cell types. We show that patient tumor cells cultured with controlled ratios of

MSCs, ECs, and PBMCs have patient specific and culture composition specific changes in stemness. These cultures also demonstrate increased tumorigenicity, changes in CSC phenotype with EMT, and increased chemoresistance along with a physiologically relevant increased expression of malignant matrisome genes and the C1 mesenchymal subtype signature.

With our tumoroid model system we can being to understand the role of each component of the TME within the context of a complex multi-cellular microenvironment in a step-wise manner. The knowledge gleaned from this model has the potential to inspire new therapies targeting the critical components of the TME and facilitate the implementation of HGSOC subtyping in clinical management to improve outcomes for ovarian cancer patients around the world.

3.5 Materials and Methods

3.5.1 Cell Culture and Materials.

All tissue culture reagents, and media supplements were purchased from Life Technologies (Carlsbad, CA) unless specified otherwise. Primary tumor samples were collected from patients with informed signed consent under an institutionally approved IRB protocol. Peripheral blood mononuclear cells (PBMCs) were purified from buffy coats from healthy donors through Ficoll-Paque gradient centrifugation, using Histopaque from Millipore sigma (Burlington, MA). Human adipose derived mesenchymal stem cells (haMSCs) were purchased from Lonza Walkersville Inc. (Walkersville, MD). Human Dermal Microvascular Endothelial Cells, Microvascular Endothelial Cell Growth Medium and Adipose Derived Stem Cell Growth Bullet Kit medium were purchased from Lonza Walkersville Inc. (Walkersville, MD). Human umbilical vein endothelial cells (HUVECs) were a donation from Dr. Lola Eniola-Adefeso's lab. Human monocyte U937's were purchased from ATCC. Carboplatin and Paclitaxel were

purchased from LKT Laboratories (St Paul, MN) and Apexbio (Houston, TX) respectively. The PDI inhibitor Pacma31 and novel compound N773 and SC144 were a gift from Prof. Nouri Neamati's lab. Antibodies and isotype controls for FACS were bought from Miltenyi Biotech (CD31, CD133/2, CD68) (Bergisch Gladbach, Germany) and BD Pharmingen (PE isotype control, CD73, CD31) (San Diego, CA). EGF was bought from Peprotech Inc. (Rocky Hill, NJ). MTS reagent was purchased from Abcam (Cambridge, UK). The ALDEFLUOR Assay Kit, bFGF, RHO/ROCK pathway inhibitor (Y-27632) were purchased from StemCell Technologies (Vancouver BC). Chromium Single Cell 3' Reagent Kit for single cell sequencing was purchased from 10X Genomics (Pleasenton, California). ECM Gel from Engelbreth-Holm-Swarm murine sarcoma was purchased from Millipore Sigma (Burlington, MA). pUltra-Smurf AmCyan, mCherry, GFP, and dtTomato was purchased from Addgene. Perfecta hanging drop plates were purchased from Xcentric Molds & Engineering.

3.5.2 Generation of tumor spheroids and tumoroids in 3D.

Control mono-culture spheroids were generated in a hanging drop array plate using patient-derived, unsorted bulk tumor cells, adapting protocols described previously[3]. Patient-derived tumor cells were harvested from culture and concentrated using high-speed centrifugation. Cells were resuspended in RPMI 1640 supplemented with 10% fetal bovine serum and 1% antibiotics and antimycotics. Cell counts were obtained using a hemacytometer and volume of cell suspension needed to obtain the appropriate number of total patient cells for the experiment was partitioned into a new microcentrifuge or conical tube. The partitioned cells were then centrifuged and resuspended in tumoroid medium (TM) at a density of 60 patient-derived tumor cells per 20 μL for deposition into hanging drop wells. TM is composed of 5 parts 2x SFM to one part EBM-2 and 20 μM ROCK inhibitor (Y-27632) (Supplemental Table 5) (2X

serum-free growth media [2X SFM; DMEM/F12 supplemented with 10 ng/ml basic fibroblast growth factor, 10 ng/ml epidermal growth factor, 1X B27 supplement, 1X insulin-transferrin-selenium supplement, 1X non-essential amino acids and 1X antibiotics and antimycotics]. For tumoroid generation, MSCs were harvested using 0.05% trypsin and resuspended in Adipose-derived Stem Cell Basal Medium (ADSCBM) and counted. Similarly, ECs were harvested using 0.25% trypsin and resuspended in EBM-2. PBMCs were thawed from -80 degrees Celsius on the day of the experiment, resuspended in 10% RPMI, and counted. U937 monocytes were cultured in RPMI with 10% heat inactivated FBS and 1X antibiotics and antimycotics. Each tumoroid cell type was added to a single cell suspension, centrifuged, and resuspended in TM such that a 20 µL volume contained 60 heterogeneous tumor cells, 300 ECs, 300 MSCs and 300 PBMCs (or U937s for the fluorescent tumoroid experiment) so the ratio of tumor cells to each of the other cell types in the tumoroid was at 1:5 at the start of the culture. To maintain homogeneity of experimental conditions, media composition was not changed between the tumoroid and spheroid cultures. Spheroids and tumoroids were maintained in TM for a period of 7 days and imaged using live phase contrast microscopy to follow spheroid and tumoroid formation. Cultures were fed with 2 µL of fresh TM medium on day 3 and 5. Growth factor reduced ECM gel was used in some experiments to form spheroids and tumoroids such that a 20 µL suspension had 2 µL of growth factor reduced Matrigel, to provide a heterogeneous base of ECM proteins to facilitate growth.

3.5.3 Response of spheroids and tumoroids to traditional and novel anti-cancer compounds.

Patient-derived spheroids and tumoroids were treated with traditional chemotherapeutics carboplatin and paclitaxel for 48 h with final concentrations of 200 µM and 10 µM respectively within 20 µL droplets. Other novel anticancer compounds Pacma 31, N773, and Sc144 were also administered to a final concentration of 10 µM each, within 20 µl drops for 48 h. At the end of

48 h, MTS reagent was added to each drop at a 1/10 dilution, and allowed to incubate at 37 °C for 2.5 h. At the end of the incubation period, absorbance was read on the spheroids and tumoroids at 490 nm, according to manufacturer's protocols using a BioTek plate reader (Winooski, VT). Drug treated conditions were normalized to either untreated spheroids or tumoroids, which were used as controls and statistical significance was determined by comparing control and treated conditions within and across spheroid and tumoroid aggregates derived from the same primary patient sample. Experiments were repeated with 3–5 biological replicates for statistical analysis.

3.5.4 Gene expression via qPCR.

RNA was extracted from harvested spheroids and tumoroids using the RNeasy extraction kit (Qiagen). Extracted RNA was assessed for concentration and purity using a Nanodrop 2000 (Thermo Fisher Scientific) spectrophotometer. RNA was transcribed to cDNA using the High-fidelity cDNA Transcription kit (Life Technologies), and qPCR was carried out in the 384 well format using the 7900HT platform (Applied Biosystems). Gene expression differences were quantified using the 2ΔΔCT method, using GAPDH, 18S, β-actin as the housekeeping controls, and reported as fold change compared to a control sample. To compare stemness and EMT signatures in patient tumor cells only, flow cytometry was used to collect GFP expressing patient tumor cells from spheroids and tumoroids prior to RNA extraction. Controls were patient-derived tumor cell spheroids. qPCR experiments were run in triplicates, with 2–3 independent samples.

3.5.5 In vivo tumorigenicity of spheroids and tumoroids in NSG mice.

NOD SCID gamma female mice were purchased from Taconic Biosciences (Rensselaer, NY). Spheroids and tumoroids from patient tumor cells were generated as mentioned earlier and injections were prepared by carefully harvesting spheroids or tumoroids using a pipette and supporting them within Growth-Factor-Reduced Matrigel from Corning (Corning, NY). The injections were administered subcutaneously into the mice. Each injection contained 10 spheroids or tumoroids. Tumor size was measured once weekly using calipers. Tumors were allowed to grow until an end-point of 1500mm^2 was reached for maximum tumor burden, and mice were euthanized according to IRB approved protocols. Tumors were dissected, and routine paraffin histology and H&E staining was performed to understand any changes in histology as well as Sirius Red and Fast Green staining to quantify collagenous and non-collagenous proteins. Tumor pieces were frozen and stored at -80 degrees C for future analysis and spheroid generation. Slides stained for collagen and non-collagen proteins were analyzed in ImageJ using a defined threshold to isolate the red pixels (collagen proteins) and the green pixels (non-collagen proteins). The area of each color in each picture was quantified.

Cells isolated from tumoroid-derived xenografts and control spheroid-derived xenografts were used to plate spheroids in our hanging drop system at a density of 200 cells per well. After 7 days, spheroids were harvested and evaluated for expression of ALDH, CD133, ALDH+CD133, CD73, CD31, and CD68. Day 7 images of these spheroids were traced manually in ImageJ and used to calculate average spheroid area for each culture condition.

3.5.6 Evaluation of cell phenotypes with flow cytometry.

Following 7 days of culture in the 384-well hanging drop platform, tumoroids were harvested with a 1 mL pipet and either digested with 1-2 mL of Accutase for 10 minutes at 37 degrees and / or mechanically separated via repeated pipetting. When large cell clusters were

visible, cell suspensions were passed through a 70 μm filter. The cell suspensions were then spun down and resuspended in ALDEFLUOR Buffer such that the total resuspension volume for each experimental group (i.e. control, tumoroid, control drug, tumoroid drug) allowed for 100 μL of cell suspension to be allotted per antibody condition. Each group included the following conditions: DAPI only control, APC-isotype, DEAB control, CD133-APC + ALDH, FITC-isotype + PE-isotype, CD31-FITC, CD73-PE, and CD68-APC or CD11b-APC. To determine the viability over time, this protocol was repeated on day 3 and day 7, while on day 0, FACs was performed on leftover 2D cells that were used to plate the tumoroids and spheroids for that experiment. FACs on drug treated samples was performed as described following 48 hours of drug treatment. Each FACs experiment was performed on a CytoFLEX Flow Cytometer (Beckman Coulter) or a MoFlo Astrios Cytometer (Beckman Coulter) and analyzed on FlowJo as described previously[427]. Briefly, double positive CSCs were identified as ALDH+ CD133+ cells with a quadrant gate set with 0.5% non-specific CD133 signal in the APC-isotype condition and 0.15% non-specific ALDH signal in the DEAB control condition. CD31+, CD68+, and CD73+ cells were identified as endothelial cells, macrophages, and MSCs respectively based on corresponding isotype control gates set with 0.5% non-specific staining. Experiments with GFP^+ patient tumor cells were stained with ALDERed and ALDEFLUOR Buffer supplemented with verapamil in order to distinguish between the GFP signal and the ALDH signal.

For experiments plated with GFP^+ Pt1 tumor cells, the perecentage of GFP^+ expressing cells in each culture type was evaluated. The mean GFP^+ percentage at the end of 7 days for spheroids and tumoroids were used to derive the scaling factor for GFP^- experiments. Specifically, the average percentage of GFP tumor cells in the spheroids was divided by the

average percentage of GFP tumor cells in the tumoroids yielding a scaling factor of 1.3687 to account for the dilution of CSC percentages in tumoroids.

3.5.7 Lentiviral transduction to visualize cell localization within tumoroids.

To visualize localization of each cell type within tumoroids, endothelial cells were transduced with AmCyan (1X), MSCs were transduced with GFP (0.5X), U937 monocytes were transduced with mCherry (1X), and patient-derived cancer cells were transduced with dtTomato (1X). MSCs, ECs, and patient-derived cancer cells were plated in 6-well plates and allowed to adhere to the dish overnight. The following day, medium was aspirated and the cells were washed with 1X PBS. Viral titer was diluted to the final concentration with the appropriate cell medium. Polybrene was added to the cells for incubation overnight. Following incubation, medium was aspirated, cells were washed with 1X PBS, and medium was added to allow cells to grow prior to plating. U937 monocytes were spun at 800g for 30 minutes at 32 degrees Celsius with a concentration of $1x10^6$ cells per mL with polybrene and virus.

Fluorescent cells were plated with dtTomato Pt4, GFP MSCs, AmCyan HUVECs and mCherry U937s and imaged on day 7 with a Nikon A1Si Confocal Microscope. Tumoroids and single-color controls were harvested and embedded in a thin layer of agarose for imaging. Single color controls were imaged first to establish fluorescence spectra for each color. Then tumoroids were imaged and the single-color control spectra were used to deconvolve the fluorescence signals into the appropriate colors using spectral deconvolution. A stack of deconvolved images was converted into a 3D rendering on the microscope software for visualization.

3.5.8 Evaluation of single cell gene expression.

A fresh patient-derived tumor sample (Pt7) was obtained as a generous donation from Dmitriy Zamarin at the Memorial Sloan Kettering Cancer Center and used to generate tumoroids and control spheroids as described previously. Tumoroids and control spheroids were collected on day 4 of culture for single cell isolation and library preparation. A 2D cultured control was included in lieu of a raw uncultured control due to poor viability of the raw uncultured sample. 3D samples were collected from hanging drop plates using a 1000 uL pipet and deposited into 15 mL centrifuge tubes and given to the Rogel Cancer Center Single Cell Resource where the viability of each sample was evaluated, dead cells were removed with Miltenyi's dead cell removal kit, and single cells were isolated using 10x Genomics single cell isolation platform. Sequencing was performed by collaborators at Yale and data was then analyzed in R using a Seurat v 3.0 (available on CRAN [https://CRAN.R-project.org/package=Seurat] and GitHub [https://github.com/satijalab/Seurat]) pipeline that can be found on https://satijalab.org/seurat/.

Briefly, cells were filtered to include those with more than 200 features, but less than 6500 features as well as all cells with less than 25% mitochondrial content. Then the feature expression measurements for each cell was normalized by the total expression, scaled by a factor of 10,000, and passed through a log transformation. Subsequently, the data was scaled such that the mean expression across all cells is 0 and the variance across all cells is 1. Dimensionality of the dataset was determined to be approximately 15 dimensions with elbow plots prior to cell clustering. Clusters were generated with a resolution of 0.1-0.2 and plotted in t-SNE plots. Cluster identities were determined through manual evaluation of the expression of known cell type markers in each cluster. To determine the cell type identity of ambiguous cell populations, samples were aligned to a publicly available set of ovarian cancer single cell sequencing data using the Seurat integration pipeline. Aligned tumoroid cells were assigned cell

types based on overlap with the previously published cluster identities from the public dataset (Supplemental Figure 12A-C)[428]. Differential expression analysis was performed between cancer cells from different culture conditions. Finally, differential expression portrayed as log fold change along with p-value and adjusted p-value were imported into IPA for core analysis of canonical pathway activation and prediction of upstream regulators.

3.5.9 Predicting the stemness of a sample based on the cellular makeup of the TME.

52 tumoroids cultures were generated with 60 patient-derived tumor cells, 300 MSCs, 300 ECs, and 300 PBMCs and evaluated for $CD133^{-}ALDH^{+}$, $CD31^{+}$, $CD68^{+}$, and $CD73^{+}$ expression on day 7 via flow cytometry. Data was analyzed on FlowJo and recorded in Excel. Each percentage was increased by 0.001 % to eliminate zero values while maintaining relative relationships between parameters and data points. Additional features were generated by adding or dividing different combinations of experimental data (Supplemental Table 6). In *Rstudio,* the median $CD133^{-}ALDH^{+}$, $CD133^{+}ALDH^{-}$, or $CD133^{+}ALDH^{+}$ value was obtained and used as the threshold determining which samples had 'high' versus 'low' expression of each CSC phenotype. High or low labels were applied to each tumoroid and stored in a 'response' column appended to the input dataset. Parameter data types were checked, and the 'response' column was redefined as a factor for use as the prediction variable. CSC marker columns were then removed from the dataset. A seed was applied ('set.seed(123)') to ensure reproducible outputs. The dataset was then split such that 75% of the samples, 37 in this case, were randomly assigned to the training set and the remaining 25% (15 samples) were randomly assigned to the test set. A tune function ('tune.randomForest') was applied to optimize the number of parameters evaluated at each node of the decision trees ('mtry') and the number of trees to make the model with ('ntrees'). Results were assessed based on out-of-bag error rate.

The best random forest settings for mtry and ntrees were then used as the settings for the 'randomForest()' with the training set as the input with which to train the model to predict the response variable based on all of the parameters. The test set and the corresponding test response variable was included in the function to test the performance of the model. After running the model, receiver operating characteristic curves were generated and the area under the curve calculated to assess the performance of the models on the training and test sets. Mean decrease in gini impurity (calculated in the 'randomForest() function) was used as a measure of variable importance for $CD133^{-}ALDH^{+}$ and $CD133^{+}ALDH^{-}$ models, but not for the $CD133^{+}ALDH^{+}$ model due to poor performance on the training set.

To test the performance of the model in predicting the CSC levels in clinically relevant data, single cell sequencing was performed on 42 HGSOC tumors by collaborators. Cell clusters were annotated by our collaborator and the percentage of cells expressing ALDH isoforms, *CD68*, *NT5E* (CD73), *PECAM1* (CD31), and *PROM1* (CD133) in each cluster was evaluated (Supplemental Table 7). Based on the total number of cells in each cluster and the percentage of cells expressing a given marker, the number of cells expressing each marker in each patient sample could be back-calculated. The number of cells expressing each marker could then be used to calculate the percentage of the total cells for a given patient sample that express a marker, serving as an approximation of the cell compositions obtained from FACS analysis. The expression of the ALDH isoforms was summed to obtain a cumulative value. This processing yielded a percentage of *ALDH*, *PROM1*, *PECAM1*, *CD68*, and *NT5E* for each patient sample which were then used to generate the same features used to train our random forest model. Finally, each parameter column was scaled such that the median value was equivalent to the median value of the training flow cytometry data. This ensured that the protein level FACS

expression data and the scRNA seq expression data were on the same scale. The 42 scRNA seq patient sample was then assigned ‘high’ or ‘low’ designations based on the threshold determined for the flow cytometry data. The CSC parameters were then removed, the response column was appended to the new test set and converted to a factor variable type. All 52 FACS datapoints were used as the training set and the new test set replaced the old test set.

Chapter 4 : Engineered Tumoroid Models Coupled with Machine Learning to Study the Role of the Tumor Microenvironment in Chemoresistance.

4.1 Introduction

Most ovarian cancer patients are treated with a standard non-personalized treatment regimen of surgical debulking followed by combination treatment with platinum and taxane therapy. While this treatment regimen is often initially effective, most patients experience relapse with the development of chemoresistance leading to high mortality[429,430]. Personalized medicine is a promising concept to improve patient outcomes by directing clinical management based on the specific characteristics of each individual tumor and patient. However, HGSOC has highly heterogeneous clinical response and a paucity of prognostic factors with which patients can be stratified. The current most informative prognostic factors are disease stage, success of surgical debulking, BRCA1/2 germline mutations, and infiltrating lymphocyte scores[430]. Factors like BRCA1/2 mutations can aid in directing clinical management (BRCA1/2 mutations suggest increased sensitivity to PARP inhibitor therapies), but ovarian cancer patients are still plagued by frequent development of drug resistant disease[430]. As a result, there is considerable effort to define molecular subtypes of HGSOC that can improve prognosis predictions and more effectively determine clinical management course to improve outcomes.

4.1.1 Molecular Subtyping of HGSOC indicates the role of the tumor microenvironment cell composition in clinical outcomes.

In 2008, Tothill et al. identified a set of four molecular subtypes of HGSOC (mesenchymal, immunoreactive, proliferative, and differentiated), via microarray analysis of 285 serous and endometriod tumors. They found that the four subtypes had implications in clinical outcomes with the C1 (high stromal response) and C5 (mesenchymal, low immune signature) subtypes corresponding with the worst outcomes. Contrarily, C2 and C4, which were characterized by a high immune signature and a low stromal response respectively were associated with more favorable outcomes[229]. Since then, these subtypes have been validated by some studies while other labs have developed unique molecular classifications of HGSOC into similar, yet different subtypes[234]. Despite validation in multiple studies, the original four HGSOC subtypes have not been implemented clinically in part because the individual markers in the193 gene signature were not statistically significant across all studies[430]. That said, a recent study demonstrated the promise of using molecular subtyping in HGSOC in their retrospective study of of the effectiveness of anti-angiogenic therapy bevacizumab[230]. In their work, they stratified each patient's tumor into one of the four original molecular subtypes and examined the response to bevacizumab. By doing so, they identified that bevacizumab conferred a greater overall benefit in the two subtypes with worst prognosis (mesenchymal and proliferative). Overall adoption of bevacizumab therapy has been limited due to its lack of effect on overall survival, however by examining the effectiveness of this therapy in each proposed molecular subtype of HGSOC, the authors were able to identify a subset of patients that may gain additional clinical benefits[230]. This highlights the potential of personalized patient stratification to direct clinical management. Importantly, recent work has also shown that subtype

classifications are highly influenced by the presence of stromal cells in and around the tumor[82], lending to the idea that the tumor microenvironment composition could potentially be used to stratify patient responses. In fact, several studies have begun to evaluate this possibility based on stromal gene signatures[235] or the immune cell composition inferred from deconvolution of bulk sequencing datasets[237]. Despite the likely role of the tumor microenvironment in directing patient responses, this information is of limited value without a better understanding of how the TME composition translates to drug response. Additionally, current patient stratification studies tend to rely on bulk-omics measurements or expensive imaging techniques to generate features with matched clinical response information to make predictions about response to previously studied therapies[238,431–433]. While the value of making predictions with these types of data are obvious, there is little benefit in terms of newly developed therapies that have not been around long enough to generate the large clinically annotated datasets required to make predictions. A better understanding of the role of the nuanced stromal composition in patient drug response to various drugs may elevate the clinical value of HGSOC molecular subtyping efforts by providing additional context with which to develop new treatments and direct administration of current treatments.

4.1.2 Machine learning models for prediction of drug response and identification of biological mechanisms.

Machine learning models are uniquely suited to study the role of nuanced cell compositions in drug response due to their ability to identify meaningful patterns in complex multi-dimensional datasets[238,434,435]. For example, Yu et al. developed a machine learning model trained on proteomic profiles of 130 ovarian serous carcinoma patients to predict response to platinum therapy using various supervised machine learning algorithms (including random

forests, support vector machines, naïve bayes classifiers, and bootstrap aggregating)[433]. Using these models, they were able to show the relevance of proteomic data in predicting a patient's platinum response and propose the key pathways involved in platinum resistance with further bioinformatics analysis[433]. This work provides an example of the value of machine learning in identifying and confirming prognostic value of biological parameters. Another study published in 2021 combined explicit mathematical models with a machine learning framework in order to identify candidate combinations of existing therapies. Their algorithm, termed "CellBox", involves non-linear ordinary differential equation (ODE) based models of biological networks of 99 components to simulate cell behavior in response to perturbation. The connections in their biological network are "learned" from a dataset of 89 experiments with pre-and post-perterbation measurements. The authors used gradient descent with automatic differentiation (a machine learning technique) to infer interaction parameters in their ODE network. Using this model, the authors were able to simulate interpretable cell responses to various arbitrary treatment combinations (perturbations) and thereby develop new therapeutic hypotheses for testing. Due to the interpretability of this model, mechanistic hypotheses could be developed facilitating potential implementation or improvement of therapeutic approaches[436]. This model serves as an example of how machine learning can be used to gain biological insights that can shape the development of new hypotheses and prompt further experimentation. Together these two examples of machine learning techniques in drug response prediction applications highlight the value of interpretable machine learning models in clinical and research applications.

As a result, in this aim we seek to address the current need for improved molecular stratification in HGSOC and the unclear role of the tumor microenvironment composition in response to treatment with a combination of experimental drug screening of heterogeneous

tumoroids and easily interpretable machine learning techniques. We hypothesize that tumoroids engineered with different cell compositions will respond differentially to treatment. Furthermore, we expect that the cell composition of each tumoroid culture can be used to make accurate predictions of drug response and be used to gain insights into key cell-cell relationships in chemoresistance. Finally, we predict that cell compositions related to chemoresistance in our tumoroid model system will translate to effective molecular stratification of patient drug response in publicly available HGSOC datasets.

4.2 Results and Discussion

4.2.1 Tumoroids derived from different tumor microenvironment cell compositions respond differentially to 5 different chemotherapies.

In order to test the effects of different TME cells on response to traditional chemotherapies (carboplatin, paclitaxel) as well as novel treatments (pacma31, N773, and SC144), tumoroids were generated with 23 different cell compositions (Figure 4.1A-C, Table 4.1) and assayed for viability following 48 hours of treatment. Within each drug treatment, significant differences in viability depending on cell composition were numerous (Figure 4.2A-G). In Figure 4.2G, the most significant differences were clustered in the left half of the heatmap, which was made up of the comparisons of compositions 1,2, and 3 (the cancer cell only conditions) with the other 20 compositions, supporting the notion of TME cell mediated chemoresistance. Paclitaxel, PACMA31, and N773 treatment yielded the most significant differences in viability, suggesting that their mechanisms of action are more attenuated by TME cells than the mechanisms of carboplatin or SC144. Although, the highest proportion of significant differences with carboplatin or SC144 treatment were still in comparison to the cancer cell only compositions.

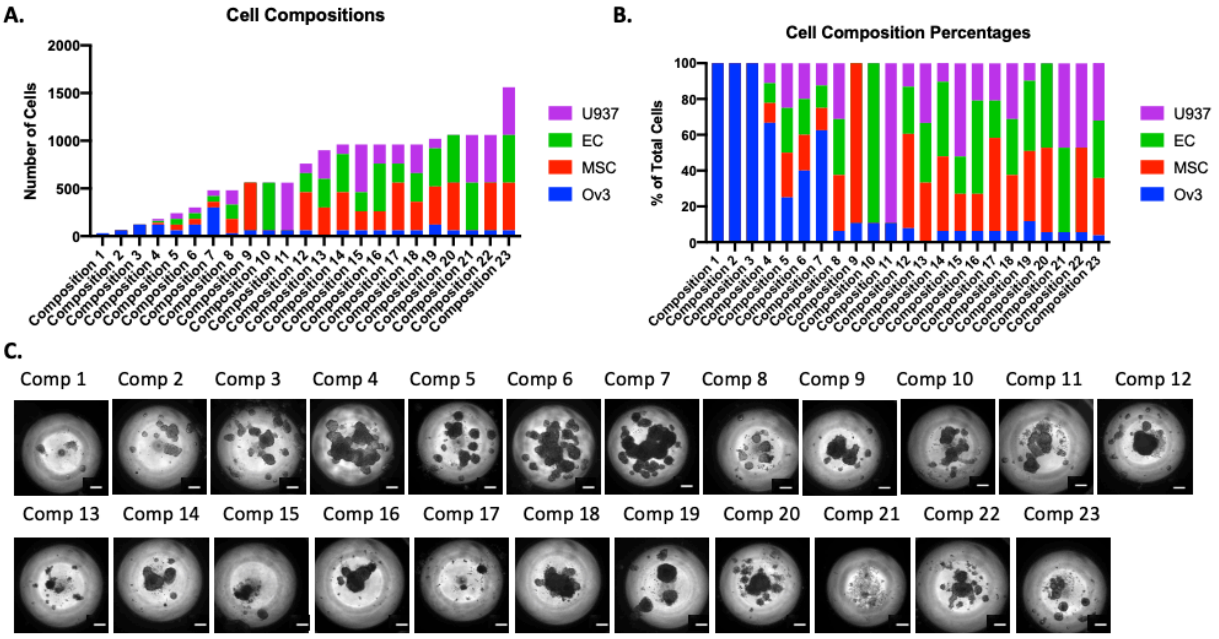

Figure 4.1: Heterogeneous tumoroids were cultured with 23 different cell compositions.
A) Bar graph showing the total cell number in each composition distributed between Ovcar3's (blue), MSCs (red), ECs (green), and U937 monocytes (purple). B) Bar graph showing the percentage of each cell type in each composition with Ovcar3's represented in blue, MSCs in red, ECs in green, and U937 monocytes in purple. C) Phase contrast image of tumoroids made with each cell composition showing heterogeneous size and morphology.

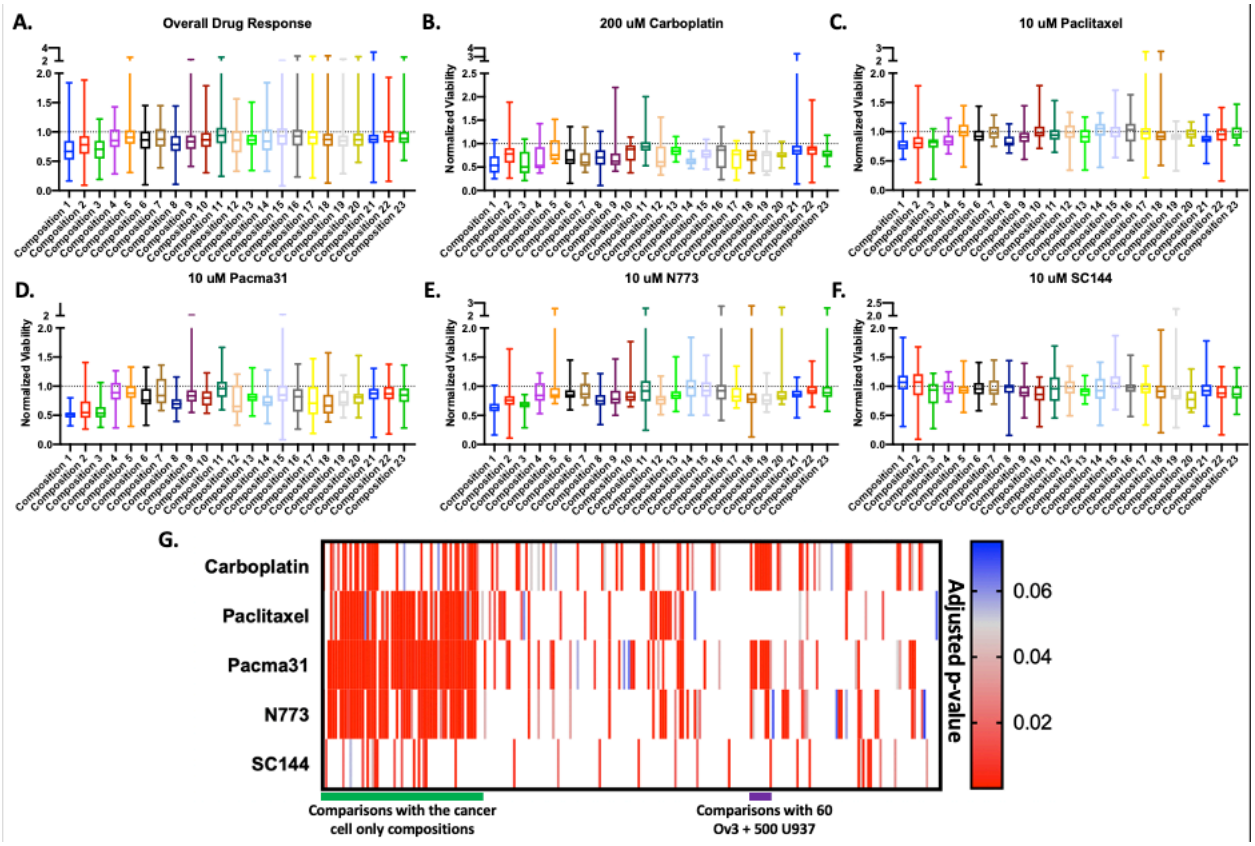

Figure 4.2: Tumoroids with different cell composition had statistically significant differences in treatment response. A) Box and whisker plot of averaged normalized viability for each cell composition across all treatment conditions showing overall resistance to treatment. Box and whisker plots showing resistance of each composition to B) carboplatin, C) paclitaxel, D) pacma31, E) N773, and F) SC144. G) heatmap of adjusted p-values for comparisons between all conditions determined via One-way ANOVA and Tukey's Post Hoc Analysis. Red indicates most significant ($p<0.05$), grey indicates borderline significance ($p=0.05$), and blue and white indicate not significant ($p>0.05$).

Arguably more interesting are the differences in drug response between the compositions with different numbers of TME cells, which might indicate composition dependent chemoresistance effects and would thus be most useful in determining the effects of nuanced cell composition differences. Myriad scattered significant differences can be observed between tumoroids with different TME compositions throughout the right most 75% of the heatmap in Figure 4.2G. In several instances, a cluster of significant differences can be observed. For example, a similar cluster of significant differences exists in both the carboplatin and pacma31 treatment group. Upon examination, these clusters correspond to the increased chemoresistance

of composition 11 (60 Ov3 + 500 U937) compared to compositions 12 – 20 which contain cancer cell numbers varying from 0-120 Ov3's and MSCs and ECs that vary between 200-500, and U937s that vary between 100 and 500. That this same cluster of differences exists in both the carboplatin treatments and pacma31 treatments suggest that there may be an overlapping mechanism of chemoresistance to each drug in the 60 Ov3 + 500 U937 condition. However, the presence of the 60 Ov3 + 200 MSC + 200 EC + 500 U937 group in this cluster complicates the idea that the high number of U937s is behind the resistance. It is possible that carboplatin and PACMA31 are negatively influencing viability through effects on the MSCs and / or ECs, thereby causing the conditions with all TME cells to have lower viability compared to conditions with only cancer cells and U937s. Alternatively, it is possible that the MSCs and / or ECs are interacting with the cancer cells and / or U937s to attenuate the chemoresistant effect observed in the Ov3 + U937 co-culture. Exactly what is driving this finding requires further experimentation, but poses some interesting questions with potential translational implications.

Notably, the top five compositions with the highest average pooled viability after drug treatments were compositions 11 (60 Ov3 + 500 U937), 15 (60 Ov3 + 200 MSC + 200 EC + 500 U937), 5 (60 Ov3 + 60 MSC + 60 EC + 60 U937), 22 (60 Ov3 + 500 MSC + 500 U937), and 23 (60 Ov3 + 500 MSC + 500 EC + 500 U937) in order of most viable to least (Table 4.2). Interestingly, of the top five most resistant compositions on average were 4 out of the 5 compositions that included 500 U937, again potentially implicating U937s as a key factor in chemoresistance in this model. Since compositions that contain high numbers of U937s and variable numbers of MSCs and ECs are included in this chemoresistant group of compositions, it is possible that previously observed significant differences in viability between the Ov3 + U937 co-culture were not due solely to drug induced MSC and / or EC death in the more effected

compositions. This is surprising as U937s included in each culture were undifferentiated, yet is potentially supported by the literature which indicates that chemotherapy can induce the differentiation of monocytes into their M2-like tumor supporting phenotype[437–440] . While this needs further experimental validation to confirm, it suggests an interesting biologically relevant possibility.

The bottom five compositions with the lowest average viability after all drug treatments were compositions 19 (120 Ov3 + 400 MSC + 400 EC + 100 U937), 8 (30 Ov3 + 150 MSC + 150 EC + 150 U937), 2 (60 Ov3), 1 (30 Ov3), and 3 (120 Ov3) in order of most viable to least (Table 4.2). Also of note, the three most sensitive compositions on average were the only three conditions generated with cancer cells only, suggesting the role of the tumor microenvironment cells in conferring chemoresistance as is expected based on the literature[117,134,213,441].

However, the compositions with the greatest resistance and sensitivity to treatment were treatment dependent (Table 4.2). Briefly, compositions 11, 21, 22, 5, and 13 were the most resistant to carboplatin treatment while compositions 19, 7, 14, 3, and 1 were the most sensitive to carboplatin. Composition 13 contained no cancer cells (300 MSC + 300 EC + 300 U937 only) which makes sense as one mechanism of carboplatin mediated cell death is through blockage of replication machinery and growth arrest, making it particularly effective against rapidly dividing cells[442,443].

Contrarily, paclitaxel was least effective against compositions 14, 5, 10, 16, and 15, two of which contained 500 ECs, potentially indicating a connection between ECs and resistance to paclitaxel (Table 4.3). This is contrary to previous reports of anti-angiogenic and endothelial-specific effects of paclitaxel[444–446]. However it is possible that ECs are conferring chemoresistance through indirect mechanisms such as the modulation of tumoroid ECM[447].

Compositions 4,8,2,1, and 3 were the least resistant to paclitaxel, again including the three cancer cell only cultures. PACMA31 was least effective against compositions 11, 7, 4, 5, and 15 which includes two out of the five compositions with 500 U937s and two conditions that started with more cancer cells than TME cells. Pacma31 was most effective against composition 18, 8, 2, 3, and 1. Compositions 19, 8, 2, 3, and 1 were most sensitive to N773 treatment and compositions 14, 11, 16, 15, and 22 were most resistant, including again, three conditions with 500 U937. Finally, SC144 was most effective against compositions 19, 23, 3, 10, and 20 and least effective against compositions 15, 1, 2, 12, and 7. Interestingly, among the least effected compositions for SC144 were cancer cell only compositions with 30 and 60 Ov3 cells respectively. SC144 inhibits gp130 through binding resulting in gp130 phosphorylation and deglycosylation and ultimately abrogates STAT3 phosphorylation and subsequent downstream gene activation[371]. Through these mechanisms, SC144 was previously shown to be effective against ovarian cancer cell lines *in vitro* and *in vivo*[371], however in our culture system overall response across all conditions was low as indicated by sparse significant differences between culture compositions in Figure 4.2G. This low overall response (lowest viability of ~78.63%) perhaps suggests the need for increased doses in our system to identify true responses. Further supporting the idea that cancer cells cultured alone are not definitively more resistant to SC144, composition 3 with 120 cancer cells alone was among the top five most sensitive to SC144 (Table 4.2).

It has been reported in the literature that mesenchymal subtypes are more sensitive to taxane therapy and more resistant to platinum based therapies[448]. Mesenchymal subtype signatures have also been linked to the presence of mesenchymal cells, as opposed to more mesenchymal cancer cell populations[82]. Therefore, to attempt to draw a clinical parallel with our

tumoroid model, we compared the drug response of 7 “mesenchymal” tumoroid compositions (compositions 9, 12, 14, 17, 20, 22, and 23) characterized by ≥400 MSCs, to carboplatin treatment versus paclitaxel treatment (Figure 4.3A-G). This comparison yielded the opposite relationship with carboplatin being more effective in the selected “mesenchymal” tumoroids compared to paclitaxel treatment. Although, like SC144, paclitaxel had low overall response with the lowest viability composition following treatment being ~78.12% viable, suggesting the potential need for higher doses or longer treatments to ensure that treatment effects are not being obscured.

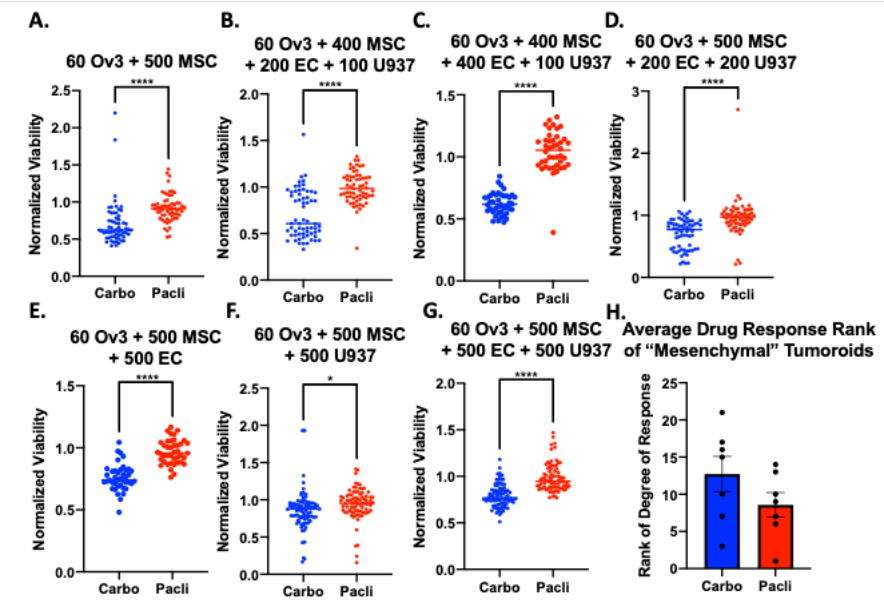

Figure 4.3: Comparison of platinum and taxane response among tumoroids with the highest number of MSCs, termed “mesenchymal” tumoroids.
A-G) Average normalized viability of each mesenchymal tumoroid following treatment with carboplatin or paclitaxel. H) Average resistance rank of each mesenchymal tumoroid to carboplatin (blue) or paclitaxel (red) compared to all other tumoroid compositions.

To combat the relative effectiveness of carboplatin versus paclitaxel dosing, we next examined the relative ranking of the “mesenchymal” tumoroids compared to all other compositions treated with carboplatin or paclitaxel (Figure 4.3H). We expected that they should rank in the most resistant compositions among the carboplatin treatment group and the least

resistant compositions among the paclitaxel treatment group. Surprisingly, the average ranking of the tumoroids with the most MSC in carboplatin was 12.7 (in the bottom half of all compositions, in other words more sensitive to carboplatin) while the average rank of mesenchymal tumoroids in response to paclitaxel was 8.6 (in the top half of all compositions or more resistant), including the most resistant composition (composition 14). This finding could be due to a number of factors including the crude nature with which we defined "mesenchymal" tumoroids, as it is possible that some other tumoroid compositions would be clustered into a mesenchymal subtype if they were to be sequenced even with lower numbers of MSC at the start of the culture. Additionally, it is possible that some tumoroid compositions generated in this study are not physiologically relevant and are more or less resistant than would be expected in a clinical environment and therefore interfering with the response rank of the designated mesenchymal clusters. Furthermore, while mesenchymal subtypes have been attributed to the presence of mesenchymal cells, the subtype signature may also be influenced by other cell types in the stroma making our crude definition of a "mesenchymal" tumoroids less meaningful. Finally, these tumoroids were generated with non-matched cell lines suggesting that their response to treatment might not be reflective of responses observed *in vivo*. Of note, composition 22 (60 Ov3 + 500 MSC + 500 U937) was the only dubbed "mesenchymal" tumoroid that showed the expected trend (third most resistant composition to carboplatin and the thirteenth most resistant to paclitaxel), potentially indicating that this composition is the most representative (out of the 7 designated mesenchymal tumoroids) of the mesenchymal molecular subtype. It was also interesting to see that the composition without cancer cells (composition 13: 300 MSC + 300 EC + 300 U937) also followed the expected mesenchymal subtype trend being the fifth most resistant to carboplatin and the fifteenth most resistant to paclitaxel. This suggests that the

unexpected effects that we observe are due to differences in the cancer cell response to these treatments.

Table 4.1: Tumoroid Cell Compositions.

	Cancer Cells	Mesenchymal Stem Cells	Endothelial Cells	Monocytes
Composition 1	30	0	0	0
Composition 2	60	0	0	0
Composition 3	120	0	0	0
Composition 4	120	20	20	20
Composition 5	60	60	60	60
Composition 6	120	60	60	60
Composition 7	300	60	60	60
Composition 8	30	150	150	150
Composition 9	60	500	0	0
Composition 10	60	0	500	0
Composition 11	60	0	0	500
Composition 12	60	400	200	100
Composition 13	0	300	300	300
Composition 14	60	400	400	100
Composition 15	60	200	200	500
Composition 16	60	200	500	200
Composition 17	60	500	200	200
Composition 18	60	300	300	300
Composition 19	120	400	400	100
Composition 20	60	500	500	0
Composition 21	60	0	500	500
Composition 22	60	500	0	500
Composition 23	60	500	500	500

Table 4.2: Top 5 Most Resistant and Sensitive Tumoroid Compositions for Each Treatment.

Most Resistant Compositions for Each Treatment											
Overall drug response		***Carboplatin drug response***		***Paclitaxel drug response***		***Pacma31 drug response***		***N773 drug response***		***SC144 drug response***	
Composition	***Normalized Viability***	***Composition***	***Normalized Viability***	***Composition***	***Normalized Viability***	***Composition***	***Normalized Viability***	***Composition***	***Normalized Viability***	***Composition***	***Normalized Viability***
60 Ov3 + 500 U937	0.9605	60 Ov3 + 500 U937	0.9543	60 Ov3 + 400 MSC + 400 EC + 100 U937	1.043	60 Ov3 + 500 U937	0.9558	60 Ov3 + 400 MSC + 400 EC + 100 U937	1.002	60 Ov3 + 200 MSC + 200 EC + 500 U937	1.064
60 Ov3 + 200 MSC + 200 EC + 500 U937	0.9318	60 Ov3 + 500 EC + 500 U937	0.8873	60 Ov3 + 60 MSC + 60 EC + 60 U937	1.008	300 Ov3 + 60 MSC + 60 EC + 60 U937	0.9	60 Ov3 + 500 U937	0.9755	30 Ov3	1.039
60 Ov3 + 60 MSC + 60 EC + 60 U937	0.9271	60 Ov3 + 500 MSC + 500 U937	0.8583	60 Ov3 + 500 EC	1.007	120 Ov3 + 20 MSC + 20 EC + 20 U937	0.8932	16	0.9563	60 Ov3	1.016
60 Ov3 + 500 MSC + 500 U937	0.9176	60 Ov3 + 60 MSC + 60 EC + 60 U937	0.8525	60 Ov3 + 200 MSC + 500 EC + 200 U937	1.003	60 Ov3 + 60 MSC + 60 EC + 60 U937	0.893	60 Ov3 + 200 MSC + 200 EC + 500 U937	0.9486	60 Ov3 + 400 MSC + 200 EC + 100 U937	0.976
60 Ov3 + 500 MSC + 500 EC + 500 U937	0.9114	300 MSC + 300 EC + 300 U937	0.8486	60 Ov3 + 200 MSC + 200 EC + 500 U937	0.9971	60 Ov3 + 200 MSC + 200 EC + 500 U937	0.8736	60 Ov3 + 500 MSC + 500 U937	0.9364	300 Ov3 + 60 MSC + 60 EC + 60 U937	0.9731
Most Sensitive Compositions for Each Treatment											
Overall drug response		***Carboplatin drug response***		***Paclitaxel drug response***		***Pacma31 drug response***		***N773 drug response***		***SC144 drug response***	
Composition	***Normalized Viability***	***Composition***	***Normalized Viability***	***Composition***	***Normalized Viability***	***Composition***	***Normalized Viability***	***Composition***	***Normalized Viability***	***Composition***	***Normalized Viability***
120 Ov3 + 400 MSC + 400 EC + 100 U937	0.8369	120 Ov3 + 400 MSC + 400 EC + 100 U937	0.6836	120 Ov3 + 20 MSC + 20 EC + 20 U937	0.8677	60 Ov3 + 300 MSC + 300 EC + 300 U937	0.7033	120 Ov3 + 400 MSC + 400 EC + 100 U937	0.7796	120 Ov3 + 400 MSC + 400 EC + 100 U937	0.9032
30 Ov3 + 150 MSC + 150 EC + 150 U937	0.7926	300 Ov3 + 60 MSC + 60 EC + 60 U937	0.6731	30 Ov3 + 150 MSC + 150 EC + 150 U937	0.8366	30 Ov3 + 150 MSC + 150 EC + 150 U937	0.6981	30 Ov3 + 150 MSC + 150 EC + 150 U937	0.761	60 Ov3 + 500 MSC + 500 EC + 500 U937	0.8829
60 Ov3	0.7875	60 Ov3 + 400 MSC + 400 EC + 100 U937	0.6232	60 Ov3	0.8039	60 Ov3	0.6137	60 Ov3	0.7536	120 Ov3	0.881
30 Ov3	0.7086	120 Ov3	0.5803	30 Ov3	0.782	120 Ov3	0.5683	120 Ov3	0.6799	60 Ov3 + 500 EC	0.8647
120 Ov3	0.6981	30 Ov3	0.5633	120 Ov3	0.7812	30 Ov3	0.5172	30 Ov3	0.641	60 Ov3 + 500 MSC + 500 EC	0.7863

4.2.2 Machine Learning to Predict Drug Response Based on Cell Composition.

To evaluate the effectiveness of the tumor microenvironment cell composition in predicting treatment response and to glean additional potentially biologically relevant insights from our tumoroid MTS assays, random forest models were created to predict tumoroid response to each drug based on cell composition. The generated random forests had variable effectiveness at predicting response to different drugs. The worst model (predicting SC144 response) had an AUC of 0.5883 for the training set and 0.6264 for the test set, still better than a random prediction model, which would have an AUC of 0.5 (Figure 4.4E). This particular model potentially had the worst performance due to the paucity of statistically significant differences between cell compositions (Figure 4.2G) and low overall effect of treatment with 10 uM SC144 in our model system, potentially obscuring significant differences in response between the different compositions (least viable condition was ~78.63% viable after treatment).

Contrarily, the most effective random forest model had an AUC of 0.6915 for the training set and an AUC of 0.6832 on the test set when trained to predict Pacma31 response (Figure 4.4C). Paclitaxel (training AUC: 0.6825; test AUC: 0.6898; Figure 4.3B) and N773 (training AUC: 0.6415; test AUC: 0.6833; Figure 4.4D) predictions were the second and third most accurate. The carboplatin model was the second to last most effective with a training AUC of 0.6089 and a test AUC of 0.6695 (Figure 4.4A). Each model performed better than a random predictor and was relatively consistent between the training and test sets indicating lack of overfitting. Training set AUCs ranged from 0.5883 to 0.6915, indicating moderate performance, however these values are in line with those of previous drug prediction models generated based on protein (AUC: ~0.58-0.64 for various machine learning algorithms)[433] or molecular features (AUC: ~0.56-0.76 for a Deep Neural Network model)[449] demonstrating the potential of predictions made based solely on cell composition. Interestingly, the three most effective

prediction models were predicting response to the three drugs that showed the greatest significant difference in viability in cultures with TME cells compared to those without TME cells (Figure 4.2G), potentially indicative of a greater role of TME cells in conferring chemoresistance to PACMA31, paclitaxel, and N773. From a clinical application perspective, this could indicate that those three drugs would be relatively less effective in tumors with high stromal content. That said, it could also be indicative of the need for more robust drug responses to avoid obscuring potential composition specific differences due to lack of overall drug response (as may have been the case with SC144). More robust drug responses obtained with higher concentration treatment or longer duration treatment could also reduce overlap in response values between compositions, potentially leading to more accurate model predictions.

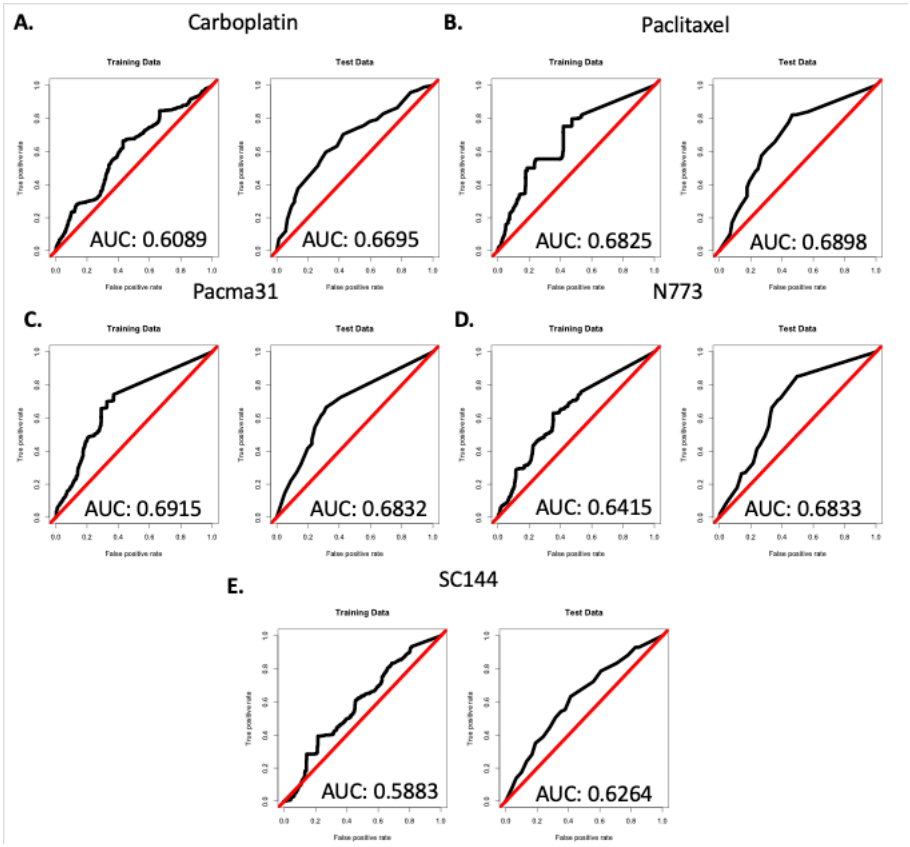

Figure 4.4: Evaluating random forest model performance.
Random forest models performed better than random predictors at predicting response to each treatment. Receiver operating characteristic curves (ROCs) for the training (left) and test (right) set for random forest model generated to predict response to A) carboplatin, B) paclitaxel, C) pacma31, D) N773, and E) SC144.

Finally, we evaluated the importance of each parameter in making predictions for each drug. None of the none of the random forest models utilized a single cell type in the top five most important parameters, indicating the complex relationships between cell types and how they may work together to determine the degree of chemoresistance. The carboplatin model placed relatively equivalent importance on most of its parameters, though put the most weight on the proportion of the culture made up of U937s. The proportion of the culture made up of ECs and MSCs respectively were also in the top 5 most important parameters (Figure 4.5A). The paclitaxel response predictor placed the most importance by far on the total number of cells and

the total number of TME cells plated at the start of culture (Figure 4.5B). As the total number of TME cells is highly influential in the total number of cells, these parameters are heavily overlapping. PACMA31 predictions placed the most importance on the ratio of cancer cells to TME cells and total cells respectively (Figure 4.5C). N773 places a similar weight on the proportion of cancer cells and the total cells. Finally, SC144 placed the greatest importance on the cancer cell type (Ov3's sorted for CSC markers ALDH and CD133 compared to unsorted Ov3's), as one experiment was plated with sorted OvCSCs as opposed to unsorted Ov3's. The SC144 model also placed high importance on the proportion of U937s in the culture (Figure 4.5E). Figure 4.5F shows a heatmap of the importance value of each parameter for each drug response prediction model, revealing a clear pattern of the importance of the proportion of cancer cells and TME cells in each tumoroid. The heatmap also reveals moderate importance placed on various cell – cell relationships whereas the individual cell type numbers were among the least important for all models, highlighting the importance of including complex cellular compositions in analysis of drug response.

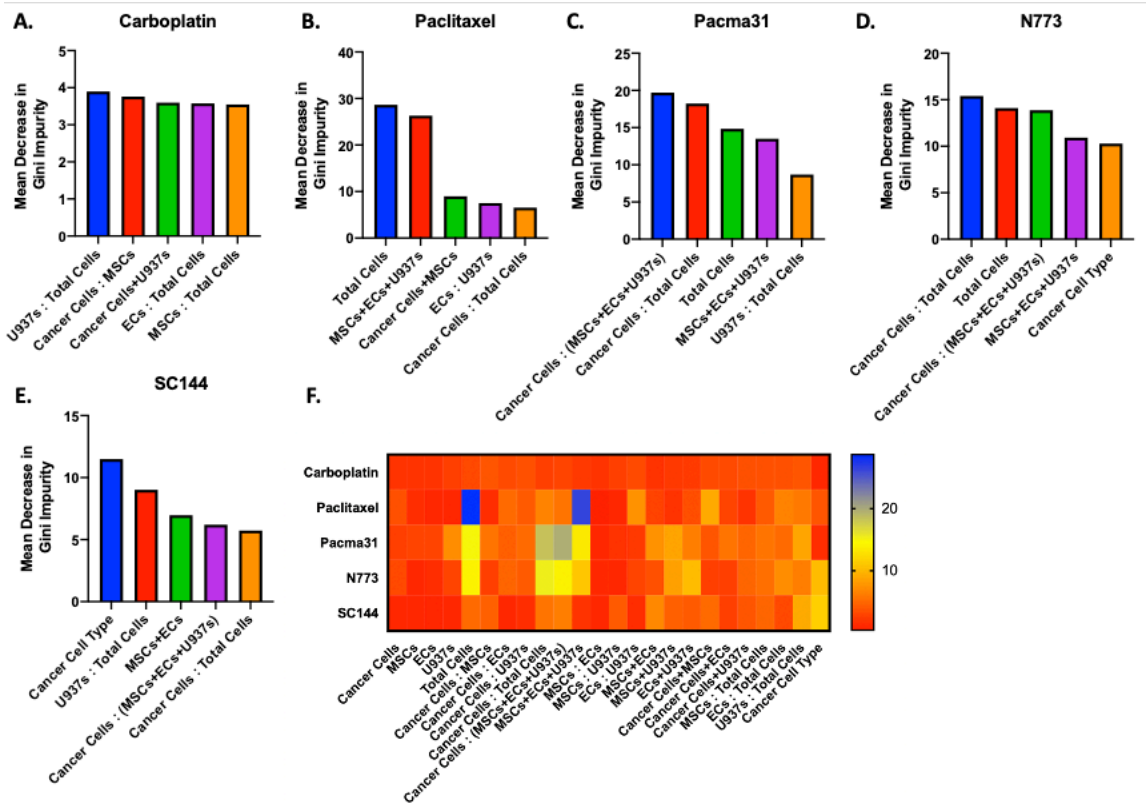

Figure 4.5: Random forest models can provide easily interpretable variable importance measures to facilitate interpretation of results.
Top 5 most influential parameters in predicting drug response to A) carboplatin, B) paclitaxel, C) pacma31, D) N773, and E) SC144. F) Heatmap showing the importance measures of all paramters for each drug prediction model.

Breaking down the most important parameters for each model and plotting the important parameter versus the treatment response shows the relationship between each variable and the treatment response (Figure 4.6A-E). In general, there appears to be an inverse relationship between drug response and TME cell total, which is highly correlated with the total cell number (more TME cells / total cells results in decreased drug response). For example, PACMA31 appears to be most effective when the ratio of cancer cells to MSCs + ECs + U937s is high (i.e. there are no added TME cells) (Figure 4.6C). This relationship makes sense given the chemoprotective effects previously attributed to MSCs, ECs, and macrophages. Interestingly, the SC144 prediction model placed the most importance on the type of Ov3 cells used in culture as

tumoroids made with sorted Ov3 CSCs were more susceptible to SC144, potentially due to SC144's ability to prevent STAT3 activation which is known to be involved in CSC maintenance (Figure 4.6E)[308,411,450]. Moreover, when examining the second most important parameter in predicting response to carboplatin we can see that low ratios of Ov3s to MSCs (a higher proportion of MSCs than cancer cells) results in generally greater resistance to carboplatin treatment (Figure 4.6F). Despite the fact that the tumoroids with the highest number of MSCs did not rank among the most resistant to carboplatin in Figure 4.3, this analysis supports the expected trend of increased carboplatin resistance in more mesenchymal tumors. This highlights the importance of cell-cell relationships in stratifying durg responses as considering MSCs alone did not reflect clinical trends while considering the ratio of cancer cells to MSCs did. Overall, these machine learning models demonstrate the potential of predicting therapy response based on cell composition and evaluating the importance of each parameters in order to attempt to make biological interpretations to drive future experimentation. Although these models had moderate prediction accuracy, they could potentially be improved through the generation of more physiologically relevant tumoroids (with matched cancer-associated stromal and immune cells). These models could also possibly be improved with higher concentration or longer duration drug treatments to obtain more robust drug responses.

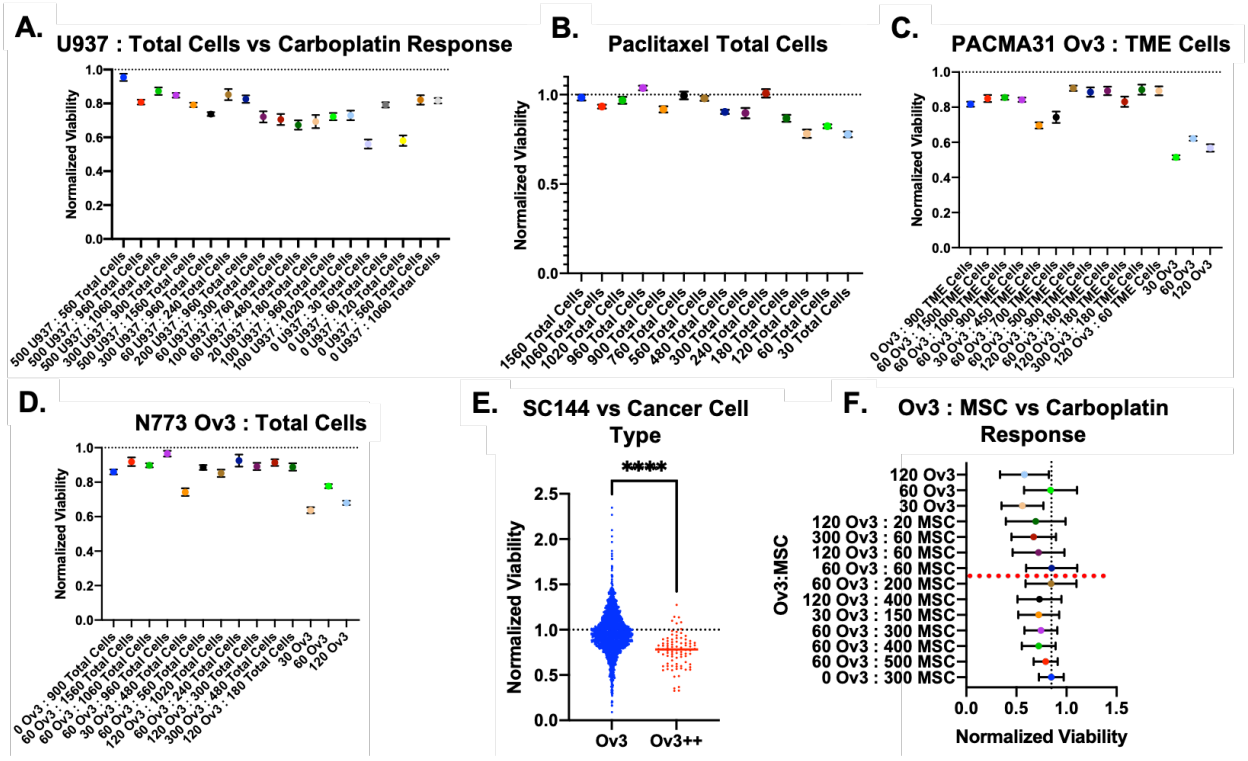

Figure 4.6: Plotting normalized viability versus the important features for each model reveals potential relationships.
The most important features in predicting response to A) carboplatin, B) paclitaxel, C) PACMA31, D) N773, and E) SC144 versus normalized viability. F) Plotting the second most important feature in predicting carboplatin response versus normalized viability reveals the expected relationship between presence of mesenchymal cells and resistance to carboplatin (higher ratios of MSCs to Ov3's is associated with greater resistance to carboplatin).

4.3 Conclusions

Recent work has suggested that the stromal cells can impact molecular subtyping classifications and thus may have prognostic significance[82,235], however the exact role of nuanced differences in stromal composition in drug response is still unclear. Furthermore, current treatment drug prediction models rely on bulk-omics measurements or expensive imaging techniques, which are often limited in sample size and only exist for previously administered therapies[238,404,431–433,451,452], limiting their utility in predicting response to novel therapies. Here we have developed an *in vitro* model system wherein tumoroids are generated

with different cell compositions and assayed for drug response in a high throughput hanging drop plate. Drug response data can then be used to make predictions of drug response based on tumoroid cell composition using random forest models. Using this system, we found an amalgam of significantly different responses depending on tumoroid composition with the highest frequency of significant differences comparing tumoroids to cancer cell only controls. This finding supports the current literature showing that the TME cells can confer chemoresistance[95,138,213,337,453,454], yet may be obscuring the importance of nuanced differences in cell composition in drug response.

Interestingly, we observed that the most resistant populations to each drug tended to include high numbers of U937s, suggesting their potential role in chemoresistance within tumoroids. We also found that the tumoroids generated with the highest numbers of MSCs did not reflect the expected chemoresistance pattern that has been attributed to the mesenchymal molecular subtype (increased resistance to platinum therapy and increased sensitivity to taxane therapy[448]), with the exception of the 60 Ov3 + 500 MSC + 500 U937 composition. While more experimentation is needed, this suggests that there could be an interaction between the MSCs and macrophages within the mesenchymal subtype that is leading to the observed responses. However, the mesenchymal subtype is typically characterized as having a low immune component, so this could be a model specific effect such as the adipose-derived MSCs needing signals from the U937s in order to shift into a more malignant phenotype. Our machine learning models were able to predict response to treatment with moderate accuracy, albeit with AUC's within the range of some existing response prediction models. Evaluation of parameters used to make these predictions suggested that the proportion of TME cells to cancer cells was among the

most influential factors in predicting response, likely due to the high number of comparisons between cultures with and without any non-cancer TME cells.

Overall this work provides evidence that the cellular composition of the TME has potential in predicting therapy response and provides a proof of concept model for engineering different composition tumoroids in order to investigate the role that each TME cell type plays in resistance to traditional and novel therapies. Future model development with more robust drug responses, matched patient-derived tumoroid cultures, and incorporation of additional parameters such as tumoroid size, average cluster number, circularity, and matrisome gene expression could improve physiological relevance and predictive performance of these models. This work ultimately paves the way for understanding the nuanced role of the cell composition in the tumor microenvironment in chemoresistance, potentially resulting in development of new therapies and more effective clinical management.

4.4 Materials and Methods

4.4.1 Cell Culture and Materials.

Epithelial ovarian cancer cells (OVCAR3: American Type Culture Collection), were cultured in RPMI 1640 (Gibco) supplemented with 10% fetal bovine serum (FBS:) and 1% antibiotics and antimycotics. Human adipose-derived mesenchymal stem cells (haMSCs: Lonza PT-5006) were cultured in Adipose-derived Stem Cell Basal Medium (Lonza) supplemented with 10 % FBS and 1% antibiotics and antimycotics as well as 2 mM L-glutamine (Gibco). Human umbilical vein endothelial cells (HUVECs) were a donation from Dr. Eniola-Adefeso and were cultured in Endothelial Basal Medium-2 (EBM-2 [AKA EGM-2], Lonza). U937 monocytes were cultured in 1640 RPMI supplemented with 10% heat inactivated FBS and 1% antibiotics and antimycotics. Tumoroid cultures were formed in 384-well hanging drop plates in

Tumoroid Medium (TM) (2X SFM:EBM-2 (5:1) + 20 uM ROCK inhibitor). See Supplemental Table 5 for detailed composition.

To plate tumoroids in 384-well hanging drop plates, each cell type is collected from 2D culture and resuspended in their respective 2D culture medium for counting on a hemacytometer. The cell density of each cell type is calculated and then used to calculate the total volume of that cell suspension will be needed to obtain the required number of that cell type per condition. The calculated volume of each cell suspension is then added into a single tube per tumoroid composition, spun down at 800g and resuspended in the appropriate volume of TM so that every well plated on the hanging drop plate will receive 20 uL the desired number of each cell type.

Tumoroids were imaged on day 3, 5, and 7 using an epifluorescent Olympus microscope to obtain phase contrast images (4X). On day 3 tumoroids are supplemented with 2 uL of TM per well. On day 5, each tumoroid composition was fed with 2 uL of TM with no drug as a control, 200 uM carboplatin, 10 uM paclitaxel, 10 uM pacma31, 10 uM N773, and 10 uM SC144. Each treatment condition contained 20-40 wells as technical replicates. Plates were incubated for 48 hours and imaged on day 7.

To quantify viability, an MTS assay was used. 2 uL of MTS reagent was added to each well and plates were incubated at 37 degrees C. Absorbance was then measured in each well at 2 hour and 4 hour incubation time points. Normalized viability was quantified by averaging all control wells and dividing the absorbance in each well by the control average to obtain viability measurements for each drug in reference to the viability of the control. Drug assays for each tumoroid composition were repeated in at 2-12 separate experiments (most compostions were 2-4 replicates, but composition 2 and 18 had 12 and 7 replicates each because they served as frequent control compositions).

4.4.2 Data Processing and Model Generation.

Normalized MTS viability data was compiled into an excel spreadsheet and coupled with the corresponding input cell composition for a given experiment. To avoid 'zero values' that would lead to "N/As" that need to be excluded or imputed in random forest models, a value of 0.001 was added to all cell numbers. Features were generated by calculating various relationships between the four cell numbers obtained at the inception of the experiment.

Compiled data was then grouped by drug treatment and saved in different files that were then read into Rstudio v1.4.1093 with R version 4.1 for use in model generation. The median absorbance value for each drug treatment was calculated and used as a threshold to assign each replicate a 'high' or 'low' response label. After appending the response label to the dataset, it was converted into the 'Factor' datatype for use as the prediction variable. The normalized absorbance values (and any other parameters that were not needed) were then trimmed from the dataset.

The trimmed dataset was then split into a training set (75% of the samples) and a test set (25% of the samples). At this point, the seed was set at '123', in order to facilitate repeatable runs of the model. First the training set was used to optimize the number of trees for the random forest to generate and the number of parameters to consider at each node split. Those optimal values were then used as inputs in the 'randomForest()' function with the training set as the dataset to build the model and the test set in the test set slot. After running the model, the variable importance (quantified as mean decrease in gini impurity) was saved, ROC curves were generated, and AUC values were calculated to quantify model performance on the training and test sets for each drug.

Chapter 5 : Conclusions and Future Directions.

Tumors are not merely cancerous cells that undergo mindless proliferation. Rather, they are highly organized and interconnected organ systems. Tumor cells reside in complex microenvironments in which they are subjected to a variety of physical and chemical stimuli that influence cell behavior and ultimately the progression and maintenance of the tumor. As cancer bioengineers, it is our responsibility to create physiologic models that enable accurate understanding of the multi-dimensional structure, organization, and complex relationships in diverse tumor microenvironments. Such models can greatly expedite clinical discovery and translation by closely replicating the physiological conditions while maintaining high tunability and control of extrinsic factors. Moreover, the development of robust, user-friendly models that integrate important stimuli will allow for the in-depth study of tumors and the complex ways in which cancer cells interact with their surroundings. This has direct implications for individualized therapies and achieving better patient survival.

The work in this dissertation focused on developing *in vitro* model systems to study the role of the tumor microenvironment and cancer stem cells in the development of chemoresistance in ovarian cancer. The development of an *in vitro* serial passage model to study the long-term development of chemoresistance in ovarian cancer, sought to improve upon previous models used to study chemoresistance development which involved either cyclic treatment of cells in 2D culture or cyclic dosing of xenograft tumors over a time period of

months. With our 3D serial passaging system, the emergence of chemoresistance could be modeled without cyclic dosing over a period of 7 weeks in a physiologically relevant microenvironment with patient cells. We demonstrated the ability of this system to model tumor re-emergence following drug treatment, and the clinical relevance through evaluation of Metformin's effects on CSC re-emergence after treatment in a phase II clinical trial. These results reflected clinical observations and previous reports and thereby highlighting the clinical relevance of our model. Overall this system has applications in personalized medicine and with additional validation could be used to screen patient specific drug responses on a consistent basis. Furthermore, 3D *in vitro* serial passaging can be utilized to identify critical molecular changes that occur during emergence of chemoresistance and thereby provide novel targets for new therapies. Finally, this system can be used as a preclinical model to screen the effectiveness of CSC targeting therapies and /or to supplement clinical trials and examine specific effects of novel therapies on the emergence of chemoresistance and CSCs.

Having developed a model to study the emergence of chemoresistance in a CSC context in Chapter 2, we next sought to engineer complex multicellular tumoroids with highly controlled cell compositions, providing unique advantages to study the role of the tumor microenvironment in chemoresistance and overall outcomes from a molecular signature and CSC context. With this model system, cellular complexity is enhanced beyond typical mono- or co-cultures thereby allowing for evaluation of CSC maintenance and chemoresistance in a more complex and physiologically relevant microenvironment. Furthermore, this model provides fine control over cell composition that is not easily accomplished in patient-derived organoids or patient-derived xenograft cultures. This allows for practical design of experiments where the effect of a single variable (i.e. cell type) on the complex signaling networks can be easily isolated. With this model

we found patient-specific changes in in CSC phenotype in tumoroids that included MSCs, ECs, and PBMCs. Importantly, CSC marker expression was inconsistent between tumoroids with all three non-cancer cell types and co-cultures with either MSCs, ECs, or PBMCs. This demonstrated the importance of complex multi-cellular models of the TME in CSC research. Tumoroids also possessed malignant characteristics such as increased chemoresistance, increased tumorigenic potential, promotion of epithelial-to-mesenchymal transition, a malignant matrisome signature, and a mesenchymal subtype signature associated with poor outcomes. Due to the modularity of our tumoroid system, each of these phenomena can be evaluated in the presence of different cell compositions to discern the role that each cell type plays in driving malignant disease with or without contributions to CSC maintenance. Using this model to unravel the complex multi-cellular interactions in the TME can lead to the development of improved therapies targeting interactions between the cancer and non-cancer cells in the TME. Alternatively, this tumoroid platform could serve as a pre-clinical model to evaluate the effectiveness of therapies that seek to leverage the cellular interactions in the TME to improve outcomes.

Chapter 4 serves as an additional application of our tumoroid model system, wherein tumoroids made with different cell compositions are used to evaluate response to traditional and novel therapies. Coupled with machine learning, this system can provide insights into the role of more nuanced cell compositions in chemoresistance. With this system we found significant differences in drug response between culture compositions, though the addition of TME cells to cancer cells conferred resistance to some drugs more than others. We interestingly observed a trend wherein cultures with high numbers of U937 monocytes tended to have the greatest resistance to therapy. Not directly in contradiction to this is the finding that our machine learning

models suggested that the total number of MSCs, ECs, and U937s was the strongest predictor of drug response. Using this system, it is possible to engineer tumoroids with a myriad of compositions to understand the role of the TME composition on drug response. This knowledge could also facilitate implementation of HGSOC subtyping in patient stratification in clinical settings. As molecular subtypes are highly influenced by the presence of non-cancer cells in the TME, drug screening with tumoroids engineered with different cell compositions could provide insight into which subtypes may respond well to new and existing therapies. Additionally, previously undiscovered cell-cell communication networks that are important in drug response could be elucidated using this system and ultimately inspire development of new therapies. Finally, with rigorous validation and use of more physiologic matched patient sample cells, the developed models could eventually be used to predict patient specific therapeutic outcomes.

Together, these aims represent advances in *in vitro* model systems to study chemoresistance and the complex tumor microenvironment of ovarian cancer. It is immensely difficult to recapitulate the dimensionality, the mechanical environment, the cell-cell interactions, the soluble signals, and the immune compartment of the TME in a single model that is amenable to precise analysis. Each of these factors of the TME is integral in directing tumor progression and thus should be considered in the design of experimental models. When many of these factors are not considered in a given model, there is an increased risk of producing unreliable results. Herein lies one of the main challenges facing cancer research: the lack of physiologically representative *in vitro* models due to the abundance of variables that exist within the complex, 3D, multicellular, organ-like TME. To overcome this limitation, cancer tissue-engineered models that present a slightly more comprehensive representation of the tumor while maintaining reasonable degrees of simplicity need to be developed to ensure that experimental

results truly reflect the *in vivo* system. The work presented in this dissertation has moved the field closer to that goal. With further development, each of the models presented in this work has the potential to improve our understanding of ovarian cancer physiology, inspire development of new therapies, and inform clinical management, ultimately culminating in improved patient outcomes. The future directions to achieve this endpoint and specific limitations for each chapter are discussed below.

5.1 Overarching challenges

Each model presented in this work has its own unique future directions and limitations, which will be discussed in the following sections. However, each system shares a similar challenge. Namely, despite the need for patient samples in order to produce the most physiologically relevant and patient-specific results, tumor samples are often hard to come by and when obtained, there often isn't an abundance of material to work with. While this conundrum is still a challenge with our systems, it is important to note that the 384-well hanging drop system utilized in each chapter is uniquely suited to maximize throughput with scarce patient samples as 3D spheroids and tumoroids can be made with small cell numbers[4,213,254]. Furthermore, advances in single-cell "-omics" technologies are beginning to expand the quantity of information that can be obtained from small cell numbers, thereby leaving more of each patient sample for other forms of downstream analyses and use within *in vitro* model systems like those presented in this dissertation. Moreover, recent HGSOC organoid culture models have demonstrated the ability to expand patient-samples *in vitro* within 3D cultures while maintaining key patient-specific characteristics, albeit with a loss of stromal cells[204]. By expanding patient-samples *in vitro* to build stocks, characterizing them with minimal numbers of single cells, and performing drug screening and other assays in high throughput *in vitro* models like 384-well

hanging drop plates will help to maximize the utility of scarce patient samples while also enhancing the physiological relevance and predictive capacity of *in vitro* models, like those presented in this work.

Each aim in this dissertation stands to benefit from more patient samples and / or the use of matched patient-derived cancer cells and non-cancer cells, as discussed in later sections. However it is important to note that accumulation of data for these models using patient samples may be a long term endeavor as a result of the inherent limitations in quantity of source material. Consequently, the proposed pre-clinical predictive models may require periodic updates as more patient-samples are obtained and used with our model systems to generate data for model development. While patient samples can be obtained from tumor banks, predictive mathematical models usually require hundreds to thousands of datapoints to develop models that can make reliable and accurate predictions. Availability of such a large quantity of samples to screen *in vitro* is unlikely at any single point in time, however spread over a longer period of time a sufficient number of datapoints could be obtained. In the interim, while patient samples are being obtained and studied, cell lines and currently available patient-derived samples can be utilized to begin experiments and inform initial model development to determine the important features for making predictions, as we demonstrated in each of the aims in this dissertation. Furthermore, using systems like our 384-well hanging drop platform high throughput assays can be performed, with each well serving as a datapoint making it easier to reach the quantities of data typically required for robust prediction models.

Ultimately, using our model systems over time with highly characterized samples could result in a robust databank of tumor characteristics associated with favorable and unfavorable responses to novel and experimental therapies in addition to well-trained predictive models that

could potentially make predictions about drug response without the need to perform additional *in vitro* or *in vivo* experiments. This long-term goal would prove invaluable in the clinical management of ovarian cancer patients and thereby lead to improved outcomes. As society transitions further into the era of personalized medicine we predict that similar efforts will be enacted across a wide range of malignancies and effectively transform healthcare. More specific details regarding the future directions and limitations for each chapter are outlined below.

5.2 Serial passage future directions.

In this work, we thoroughly characterized our 3D serial passaging model to study the emergence of chemoresistance in ovarian cancer from a CSC context, and demonstrated the physiological relevance of the model. We showed that this system has potential as a research tool, to study the mechanisms of the emergence of chemoresistance as well as a pre-clinical tool that could be used to predict patient responses to treatment and thereby inform clinical management. A mechanistic investigation behind the chemoresistance, tumorigenicity, and stemness gene signature defined in the characterization of our model system may help to achieve these goals. More specifically, this would involve silencing or knockdown of individual genes within the malignant gene signature and subsequent characterization of changes in stemness, chemoresistance, and tumorigenicity. This process be facilitated with the use of genome wide CRISPR screening[455], wherein many genes that potentially play key roles in stemness, chemoresistance development, and tumorigenicity could be knocked out in patient cancer cells prior to passaging. By identifying which gene knockouts prevent increases in stemness and /or the development of chemoresistance in our passaging model it would suggest that targeting of that gene has potential therapeutic value. Coupling this process with our serial passaging system

could greatly expedite the discovery of novel therapeutic targets behind the emergence of chemoresistance and poor outcomes in ovarian cancer.

Importantly, to move towards the goal of pre-clinical drug screening with this model system, additional clinical validation will be required. This could be in the form of treating fresh patient sample spheroids with the same therapies that the patient receives, sorting for live cells, and then performing passaging to evaluate how quickly chemoresistance emerges for each patient sample following treatment, similar to the experiment shown in Figure 2.9E,F. If spheroids from different patient samples consistently reflect the accurate emergence of chemoresistance following treatment, it would lend further credence to the use of this model system in pre-clinical screening. Moreover, after successful patient-specific prediction of the emergence of chemoresistance drug screening could be performed on re-emerged spheroids to identify the most effective treatment for each patient sample after the emergence of chemoresistance. With enough validation that the models can predict or mimic patient response and their potential to develop chemoresistant disease our model could then be used as a preliminary screening tool to inform clinical decision making. This particular application would be facilitated with further development of our mathematical model predicting emergence of CSC populations, by incorporating more complex physiologically relevant equations that take into account phenomena such as the development of hypoxia, tumor cell dedifferentiation, and response to drug treatment.

5.3 Serial passage limitations.

While the serial passaging model is well established in Chapter 2, as with all model systems, there are limitations. One of the drawbacks of our serial passage system is the lack of cellular heterogeneity, which might influence behavior of CSCs and how they promote

chemoresistance. While our results in Chapter 2 indicate good agreement between drug response in passaged patient-derived spheroids and the expected response based on the platinum status or metformin status of the sample, it is also well known that the non-cancer cells in the tumor microenvironment can influence response to treatment, as we showed in Chapter 3 and 4. That said, it remains to be seen if the physiological relevance of our serial passaging model could be further improved by incorporation of non-cancer cells. The cellular complexity of the TME *in vivo* may prove to be a critical component of predicting drug response in our serial passaging model and warrants investigation. To successfully incorporate non-cancer cells in this model the culture medium may need to be altered to promote survival of the non-cancer cells. For example, to successfully culture all four cell types in our tumoroids using a single medium composition in Chapter 3, the serum free medium that was used in our serial passaging model was supplemented with endothelial cell medium and a ROCK inhibitor, to aide in survival and growth of non-cancer cells susceptible to anoikis in non-adherent environments.

Aside from adjusting the media composition, an additional hurdle would be maintaining viability of the non-tumor cells throughout the passaging process, which would require cyclic spheroid / tumoroid dispersion either with rapid pipetting and / or chemical digestion techniques. If viability of the non-cancer cells was identified as an issue, it could potentially be circumvented by harvesting cells from spheroids at each passage and allocating a portion of them to start the next passage and a portion of them to culture in 3D with non-cancer cells that were not passaged. This would help elucidate how interactions with the non-cancer cells change as tumor cells acquire a chemoresistant / malignant phenotype. Moreover, evaluating chemoresistance development in the context of a more complex multi-cellular microenvironment has the capacity

to improve the physiological relevance of drug response and emergence of chemoresistance predictions.

5.4 Tumoroid future directions

Our tumoroid model system allows for patient-derived cancer cells to be cultured with mesenchymal cells, endothelial cells, and immune cells with different compositions. In Chapter 3 we showed that this system results in differential expression of CSC markers compared to co-cultures as well as increased malignant properties such as tumor forming capacity, chemoresistance, EMT phenotypes, and molecular signatures associated with poor outcomes in ovarian cancer. As such, this model system can facilitate the evaluation of the role of the non-cancer TME cells in patient-specific changes in stemness, EMT, TME-mediated chemoresistance, and the key TME pathways underlying outcomes in HGSOC molecular subtypes. To improve the ability of our tumoroid model to elucidate clinically relevant knowledge and reflect physiological drug responses, there are a number of critical next steps.

The primary next step for this model system is to incorporate more specific immune cell phenotypes and physiologically representative cell compositions to match various microenvironments such as the malignant ascites or omental metastases[1]. Our current FACS data suggests that a small number of PBMCs are present in the culture by the end of the culture period (based on low % of CD11b+ cells in Figure 3.1F). In chapter 4, U937 monocytes are used in lieu of PBMCs, and there was visible presence of U937s by the end of the 7 day cultures, which was also observed with U937s in the 3D rendering of 4-color tumoroids in Figure 3.1G. This suggests that perhaps the small number of monocytes in tumoroids made with PBMCs was related to the health of the PBMCs, which were thawed on the day of plating. While PBMCs are advantageous in that they contain multiple immune cell types, it may be beneficial to use more standardized

immune cell lines like U937s, if not using matched patient immune cells. This would allow for more fine control over the immune cell composition in tumoroids and may facilitate inclusion of a greater proportion of immune cells.

This is important because while some tumors can have little or no immune infiltration[229], others have substantial immune components[82,428] including the immunoreactive molecular subtype of HGSOC, which is associated with favorable outcomes[229,237]. Some microenvironments in particular are also known to have high immune components, such as the spheroids found in the malignant ascites[82]. Therefore, to better replicate these environments and understand the role of specific immune cells in determining outcomes it will be important to incorporate more pre-differentiated immune cells. While there is some scRNA sequencing evidence that the macrophages in our tumoroid cultures have some M1-like and M2-like characteristics (Supplemental Figure 13A)[456], pre-differentiating them into these phenotypes will be important to be able to examine the effect of specific proportions of each phenotype, which has been implicated as a clinically relevant measurement[119,453].

Along the same lines, incorporating other immune cell types such as T cells, NK cells, and B cells will also be important as a long term goal with this platform due to the clinical implications of the immune cell composition[237]. This will likely require altering the culture medium (for example by adding IL-2 to facilitate T cell growth and differentiation)[457], as our single cell sequencing revealed the presence of only macrophages and B cells from the PBMCs. Importantly, more robust incorporation of specific immune cell subsets may require matched patient-derived cells for each cell type as unmatched immune cells may react to the other cells in the culture if the HLA subtype of the immune cells is not compatible with any of the other cell types. Use of matched patient-derived samples will also impact physiological relevance of the

model as the non-cancer cells interact differently with cancer cells when they are associated with a tumor[5,95,458].

With improved incorporation of specific immune cell subsets, tumoroids could then be engineered to replicate specific microenvironments, such as the immunoreactive HGSOC molecular subtype[82,237] or ascites specific models (made up of mainly macrophages, fibroblasts, and cancer cells)[82]. Engineering these specific environments could help elucidate how the roles different cell types change in a wide range of different cell contexts.

Accomplishing this with matched patient-derived cells would require isolation of each cell type from the same tissue sample, which could prove challenging. To successfully isolate each cell type, flow cytometry or magnetic cell sorting of the primary tumor and then expansion of each cell type separately would be required to build sufficient cell stocks to perform experiments. While difficult, use of our 384-well hanging drop plate-based tumoroid platform, which is capable of generating 3D cultures with minimal cell numbers[4,213,254] is an advantage as fewer cells are needed to perform high throughput experiments. Another technique that may prove useful is the *in vitro* expansion of tumor cells in with long term passaging of HGSOC organoids, which has been shown to be successful over 30+ passages with conservation of histological and genomic features, albeit with enrichment of the cancer cell component[204]. With these changes, our tumoroid system has the potential to serve as not only a research tool to study cell-cell interactions in the complex multi-cellular TME, but also as a pre-clinical screening platform that could be used to inform clinical management, if found to replicate patient-specific responses. Furthermore, the ability to engineer tumoroids with specific cell compositions allows for the recreation of HGSOC molecular subtypes *in vitro*, which could be used to screen the

effectiveness of traditional and novel therapies in each subtype, thereby facilitating clinical decision making based on molecular subtyping.

5.5 Tumoroid limitations

That said, one of the primary limitations of the model presented in Chapter 3 was the paucity of patient samples, which complicated our ability to understand the degree of patient-specific differences in the response to the presence of non-cancer TME cells. Specifically, it will be important to obtain more robust data to determine the degree of patient-specific differences in CSC enrichment. Our current FACS data suggests that some patient samples trend towards enrichment ALDH+ CSCs in tumoroids while other patients do not. However, these differences are not significant and thus will require further experimentation to understand. Our single cell sequencing data also supports minor enrichment of ALDH in tumoroids compared to spheroids via increased expression of ALDH1A3 (which also happens to be related to EMT and metastasis related processes)[396,398,459], however the difference is small and not significant. Contrarily, Pt 7 instead shows high expression of CD24, CD44, and THY1 as CSC markers (depending on the culture type), and clear shifts in expression between spheroids and tumoroids. This suggests that the TME cells in this culture system may be influencing expression of those CSC markers to a stronger degree than ALDH and CD133 (although it is possible that Pt 7 just has low baseline expression of ALDH and CD133). Some differences between the FACS data and scRNA seq data could be due to patient-specific differences, or differences between protein and gene expression data[125]. However qPCR validation of the single cell sequencing trends suggests that similar trends may be occurring in Pt 1 tumoroids (which made up the bulk of our FACS samples). That said, it is possible that robust enrichment of CD44+CD24- CSCs is occurring in

our tumoroids regardless of patient sample, even though those markers weren't examined with FACS.

Additional investigation with more patient samples and replicates would help to understand to what degree patient specific differences may affect which CSC markers are enriched, or if all patient samples will respond to tumoroid culture with increased THY1 and CD44+CD24- expression. The results of this investigation could also inform which CSC markers we train our mathematical model to predict (although we would have to generate all new training data). These experiments could be coupled with more variations in cell composition to begin ascertaining the role of each cell type in tumoroid CSC phenotypes as well as critical malignant features of ovarian cancer such as EMT, chemoresistance, and molecular subtype signatures.

In addition, our proposed machine learning model would be improved with evaluation of a variety of different machine learning algorithms, such as support vector machines, which are typically better at dealing with lower sample sizes[435]. Moreover, inclusion of additional clinically relevant features, such as molecular subtype signatures, copy number variations, and epigenetic signatures, and mutation status could improve the performance of the model and help to identify the parameters that most influence degree or type of CSC enrichment. The primary challenge associated with inclusion of these parameters is availability of sufficient quantity of patient sample to not only harvest each cell type to use in tumoroids, but also to sequence and identify copy number variations and mutation status for example. However, this may be possible with recent improvements in single-cell -omics techniques combined with the aforementioned long term passaging of HGSOC organoids, which can be used to expand patient samples *in vitro* over long periods of time while maintaining genomic features of the original tumor sample[204,428,460–462].

5.6 Predicting chemoresistance based on cell composition future directions

In Chapter 4, we demonstrated the potential of the tumor microenvironment cell composition in predicting drug response of traditional and novel therapies. However, several primary next steps are needed to improve the performance and predictive capability of the platform. Specifically, this model system could be improved with screening of additional cell compositions to provide more information from which the algorithm can learn from. The current training data consists of 23 different cell compositions, however that translates to fewer unique values for certain features. For example, the ratio of OVCAR3's to MSCs only had 10 unique values as there was overlap between different compositions (i.e. compositions 17, 20, 22, and 23 all contained 60 ovcar3's and 500 MSCs). In reality, the ratio of cancer cells to MSCs would likely be a continuous variable with more than 10 discrete possibilities. With more variation between cell compositions, more unique feature values will be available to learn from while also better representing the range of possible ratios that could be found *in vivo*. While the compositions presented in Chapter 4 were loosely based on physiologically relevant cell compositions (such as a mesenchymal tumor containing a high proportion of mesenchymal cells and an immunoreactive tumor containing a high proportion of immune cells), additional added compositions should reflect more specific cell compositions identified from patient tumors with single cell sequencing data as these compositions are likely to provide the most physiologically relevant information and because it will be important to be able to make predictions based on more realistic cell compositions[82,428].

Similar to our general tumoroid model established in Chapter 3, performing these screening assays with tumoroids made with matched patient derived cells and pre-differentiated immune cells from many different patients could greatly improve the biological relevance of the

predictions. Including patient samples in training our prediction models will also be important to help reveal how patient-specific responses to therapy may be influenced by the presence or absence of non-cancer cells.

Subsequently, it will be important to draw clinical associations with this predictive model, to assess its potential in clinical scenarios. Aside from comparing tumoroid drug responses to those in other experimental models (like xenografts or ex vivo tumor cultures) this could be done by downloading publicly available single-cell sequencing datasets or using a cell type deconvolution algorithm (such as CIBERSORT)[463] on bulk sequencing datasets if single cell data is not available to estimate the cell composition. These patient samples could then be used as a test set for our model to see if the carboplatin and / or paclitaxel response predicted by the models matches the clinical outcomes linked to each patient. Alternatively, if our models predict a relationship between a certain cell composition and carboplatin resistance, a gene signature could be assigned to reflect that cell composition and used to predict response in the publicly available datasets. Overall, these steps serve to improve the predictive capability and physiological relevance of our machine learning models and to validate them in clinically relevant datasets.

5.7 Predicting chemoresistance based on cell composition limitations.

One of the main limitations of the drug response prediction models presented in Chapter 4 is low baseline drug effectiveness. Specifically, in the case of paclitaxel and SC144, the most effected composition had greater than 70% viability. This low response in the most sensitive composition suggests that differences in response between other less responsive compositions may be obscured as few of them experience significant death. This could easily be remedied with longer treatment times (i.e. 72 hours instead of 48 hours), or by re-establishing IC50 values for

this culture system. With more robust drug responses across all conditions, we may see more significant differences in response across compositions, and that in turn could improve model performance. Oddly, our paclitaxel prediction model was still the second best performing model, potentially due to the relatively high impact that it had on the cancer cell only conditions compared to the compositions with other TME cells. SC144 on the other hand had little to no effect on viability of cancer cells alone as well as cultures with TME cells, and resulted in the worst prediction model.

To better understand the effects of nuanced differences in cell composition, it would also be beneficial to develop the models without the cancer cell only controls as they tend to be the most sensitive to therapy which automatically makes the models place high importance on total number of TME cells (since ~1/4 of the comparisons end up being between the cancer cell only conditions and the conditions with TME cells). This could decrease model performance, but it could also provide more valuable information about the chemoresistance associated with TME cell compositions.

Another limitation of our predictive models was the high degree of correlation between our features and the lack of feature selection. In our models many features are correlated as most are generated from a core set of four input variables (the number of OVCAR3s, MSCs, HUVECs, and U937s). For example, the number of MSCs alone will inevitably be highly correlated to the ratio of OVCAR3s to MSCs. When features are correlated, it has been shown that their importance can be diluted, thereby potentially obscuring relevant parameters in importance analysis[464]. This limitation is compounded by the lack of feature selection in our models. Feature selection is the process whereby the number of features used to train a model is minimized to only the most relevant features. This process can reduce computational complexity

(and time) and improve classification accuracy[465]. To address these limitations and improve model performance, a recursive feature selection algorithm could be used, which has been proposed to minimize prediction error in the presence of correlated features and reduce the effect of correlation on variable importance while selecting relevant variables for model building[464].

That said, other features that could be of potential interest could also be added prior to feature selection. Some potentially important features to add include average tumoroid area, number of independent spheres per image, and average circularity. Additional likely relevant features that would be limited by sample availability or depth of patient sample characterization include copy number variation, epigenetic, and genetic signatures. With more relevant features and less irrelevant features, these models might produce higher quality biological insights and improved predictive performance.

Finally, predictive performance may also benefit from evaluation of additional machine learning algorithms, such as deep neural networks, support vector machines, and gradient boost models or even multiple runs of the same model to evaluate average performance[238,433]. Oftentimes, in development of a predictive model multiple algorithms are tested in order to choose the one with the highest performance. In addition, each model can be generated multiple times in order to ensure robustness and to enable statistical comparisons between average model performances and variable importance measures[433,464]. In this case, only evaluated random forest models because they are easily interpretable and have straight forward measures of variable importance, although different algorithms could have better predictive performance and thus their parameter importance values may be more meaningful.

5.8 Overarching conclusion

Each of these models seeks to recapitulate the complex 3D multi-cellular tumor microenvironment while maintaining sufficient experimental control to gain meaningful biological insights. While each model system has its own limitations, they all have the potential to inspire new treatments predicated on the novel biological insights that they reveal. Incorporating patient-derived samples in each model also serves to move the field further into the era of personalized medicine. Based on the promise of the models presented in this work and advances in '-omics' technology, we envision a future wherein each patient's tumor will be harvested and thoroughly characterized on the gene and protein level, and used in pre-clinical screening models such as those presented in this work (Figure 5.1)[1]. With further development and validation, our models have the potential to predict a wide variety of critical clinical outcomes such as development of chemoresistance, tumor re-emergence, optimal treatment strategies for primary and metastatic tumors from different molecular subtypes. Moreover, effective strategies to treat minimal residual disease and malignant cells within specific microenvironments such as the malignant ascites could be

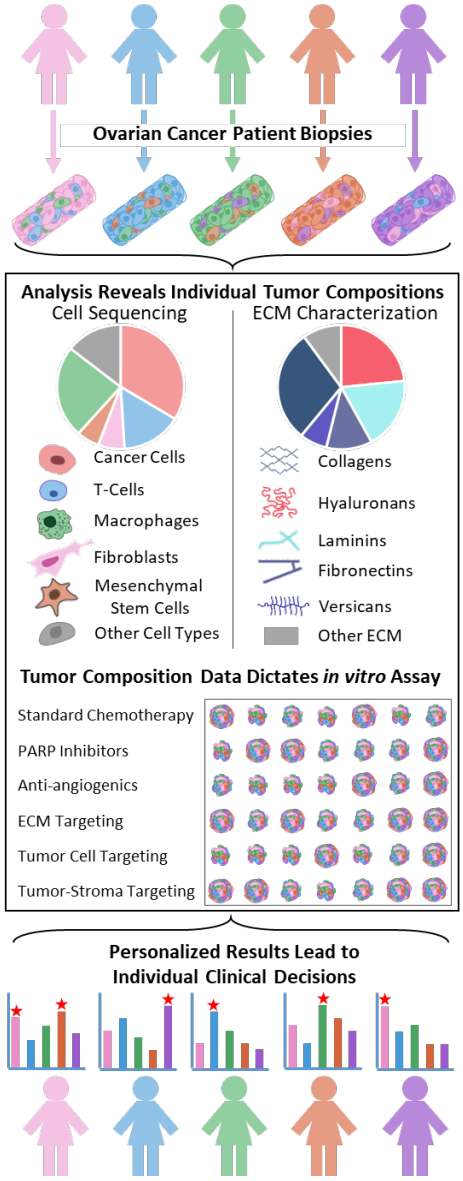

Figure 5.1: Proposed clinical workflow for patient-derived tumor-specific 3D models which can predict therapy response and identify the most effective yet non-toxic therapies or combinations, leading to sustained and durable responses.

determined. Realization of each of these applications would culminate in truly personalized care and improved outcomes for ovarian cancer patients around the world.

Appendix

Appendix A: Supplemental Tables

Supplemental Table 1: ELDA analysis of stemness across passaging.
3D serial passaging increases CSC fraction. Range and estimate of CSC frequency as determined by Extreme Limiting Dilution Analysis (ELDA) between early and later passages of spheroid initiated xenografts. The p value for the overall differences in stem cell frequencies between any of the groups is 2.6 X 10-10 for Pt224. The p value for the overall differences in stem cell frequencies between any of the groups is 0.00733 for Pt412.

Pt224

Group	Lower	Estimate	Upper
P0	164.42	62.185	23.519
P3	77.88	28.551	10.467
P6	1.51	0.558	0.206

Pt412

Group	Lower	Estimate	Upper
P0	165	91	50
P3	82.5	45.5	25.1
P6	53.3	1	1

Supplemental Table 2: K1 values for the mathematical model.
K1 values (ALDH+ symmetric division rate) chosen to minimize the absolute difference between simulated and experimentally measured cells per spheroid for P0 and P1 spheroids.

Ovcar3							
k1:	**P0 Cell Count**	**Simulated P0 Cell Count**	**Abs Diff**	**P1 Cell Count**	**Simulated P1 Cell Count**	**Abs Diff**	**Abs Diff Sum**
0.7	7398	9714	2316	5372	9792	4420	6736
0.69	7398	9058	1660	5372	9131	3759	5419
0.68	7398	8447	1049	5372	8515	3143	4192
0.67	7398	7877	479	5372	7940	2568	3047
0.66	7398	7346	52	5372	7404	2032	2084
0.65	7398	6850	548	5372	6905	1533	2081
0.64	7398	6388	1010	5372	6439	1067	2077
0.63	7398	5957	1441	5372	6004	632	2073
0.62	**7398**	**5555**	**1843**	**5372**	**5599**	**227**	**2070**
0.61	7398	5180	2218	5372	5221	151	2369
0.6	7398	4830	2568	5372	4869	503	3071
Minimum:							**2070**
Pt224							
k1:	**P0 Cell Count**	**Simulated P0 Cell Count**	**Abs Diff**	**P1 Cell Count**	**Simulated P1 Cell Count**	**Abs Diff**	**Abs Diff Sum**
0.7	6277	8811	2534	4107	8875	4768	7302
0.69	6277	8224	1947	4107	8284	4177	6124
0.68	6277	7676	1399	4107	7731	3624	5023
0.67	6277	7165	888	4107	7216	3109	3997
0.66	6277	6687	410	4107	6735	2628	3038
0.65	6277	6241	36	4107	6286	2179	2215
0.64	6277	5825	452	4107	5866	1759	2211
0.63	6277	5437	840	4107	5475	1368	2208
0.62	6277	5075	1202	4107	5110	1003	2205
0.61	6277	4737	1540	4107	4769	662	2202
0.6	6277	4421	1856	4107	4451	344	2200
0.59	**6277**	**4126**	**2151**	**4107**	**4155**	**48**	**2199**
0.58	6277	3851	2426	4107	3878	229	2655
Minimum:							**2199**
Pt412							
k1:	**P0 Cell Count**	**Simulated P0 Cell Count**	**Abs Diff**	**P1 Cell Count**	**Simulated P1 Cell Count**	**Abs Diff**	**Abs Diff Sum**
0.7	5341	10746	5405	8084	11255	3171	8576
0.69	5341	10025	4684	8084	10499	2415	7099
0.68	5341	9353	4012	8084	9793	1709	5721
0.67	5341	8726	3385	8084	9135	1051	4436
0.66	5341	8141	2800	8084	8521	437	3237
0.65	**5341**	**7595**	**2254**	**8084**	**7948**	**136**	**2390**
0.64	5341	7086	1745	8084	7414	670	2415
0.63	5341	6611	1270	8084	6915	1169	2439
0.62	5341	6168	827	8084	6451	1633	2460
0.61	5341	5754	413	8084	6017	2067	2480
0.6	5341	5369	28	8084	5612	2472	2500
Minimum:							**2390**

Supplemental Table 3: Final parameter choices for the mathematical model.
Final parameter choices for serial passaging simulation of Ovcar3, Pt224, and Pt412 spheroids. Parameter choices were based on a mixture of experimental data and the literature.

Ovcar3			
Parameter	**Symbol**	**Value**	**Source**
Symmetric Division Rate of ALDH+	k1	0.6200	Cell counts + FACS
Asymmetric Division Rate of ALDH+	k2	0.1000	Tomasetti et al. 2010
Symmetric Differentiation Rate of ALDH+	k3	0.0000	Choi et al. 2015, Tomasetti et al. 2010
Death Rate of ALDH+	k4	0.0078	FACS
Symmetric Division Rate of ALDH-	k5	0.6187	Cell counts + FACS
Death Rate of ALDH-	k6	0.0486	FACS
Pt224			
Parameter	**Symbol**	**Value**	**Source**
Symmetric Division Rate of ALDH+	k1	0.5900	Cell counts + FACS
Asymmetric Division Rate of ALDH+	k2	0.1000	Tomasetti et al. 2010
Symmetric Differentiation Rate of ALDH+	k3	0.0000	Choi et al. 2015, Tomasetti et al. 2010
Death Rate of ALDH+	k4	0.0153	FACS
Symmetric Division Rate of ALDH-	k5	0.5810	Cell counts + FACS
Death Rate of ALDH-	k6	0.0524	FACS
Pt412			
Parameter	**Symbol**	**Value**	**Source**
Symmetric Division Rate of ALDH+	k1	0.6500	Cell counts + FACS
Asymmetric Division Rate of ALDH+	k2	0.1000	Tomasetti et al. 2010
Symmetric Differentiation Rate of ALDH+	k3	0.0000	Choi et al. 2015, Tomasetti et al. 2010
Death Rate of ALDH+	k4	0.0029	FACS
Symmetric Division Rate of ALDH-	k5	0.6420	Cell counts + FACS
Death Rate of ALDH-	k6	0.0570	FACS

Supplemental Table 4: Full list of predicted upstream regulators in tumoroids vs. spheroids.

Tumoroid vs Spheroid Upstream Regulators		
Predicted Activation		
Molecule	*Activation Z-Score*	*p-value of overlap*
Mek	2.470	2.74E-08
TGFB1	2.399	7.47E-07
FOXM1	2.062	1.09E-05
DAP3	2.000	1.47E-05
PPP1R13L	2.000	2.75E-05
MAPK1	2.952	4.03E-04
CAB39L	2.000	1.19E-03
CCL5	2.000	1.58E-03
TCF4	2.000	2.43E-01
Predicted Inhibition		
Molecule	*Activation Z-Score*	*p-value of overlap*
miR-450a-5p (and other miRNAs with...)	-2.449	3.93E-06
ATF4	-2.391	1.65E-05
CLOCK	-2.000	5.24E-02

Supplemental Table 5: Tumoroid Medium Composition (TM)

Tumoroid Culture Medium (TM)	
5 Parts 2X Serum Free Medium (2X)	
DMEM/F12	1/1
B27 (without vitamin A)	1X
Anti-anti	1X
ITS-X	1X
NEAA	1X
bFGF	10 ng/mL
EGF	10 ng/mL
1 Part Endothelial Cell Growth Basal	
Hydrocortisone	0.2 mL*
hFGF-B	2 mL*
VEGF	0.5 mL*
R3-IGF-1	0.5 mL*
Ascorbic Acid	0.5 mL*
hEGF	0.5 mL*
GA-1000	0.5 mL*
Heparin	0.5 mL*
FBS	2%
20 µM ROCK inhibitor	
+/- Growth Factor Reduced Matrigel (1:20	
* = per 500 mL of EBM-2	

Supplemental Table 6: Random forest parameters.

Random Forest Parameters
CD133-ALDH+
CD31
CD31 : CD68
CD31 : CD73
CD31 : CD73+CD31+CD68
CD31 : CD73+CD68
CD31+CD68
CD31+CD73
CD68
CD68 : CD73+CD31
CD68 : CD73+CD31+CD68
CD73
CD73 : CD31+CD68
CD73 : CD68
CD73 : CD73+CD31+CD68
CD73+CD31+CD68
CD73+CD68
Patient

Supplemental Table 7: Genes analyzed in each cluster of 42 HGSOC scRNA Seq datasets for random forest validation.

scRNA Sequencing Genes Evaluated in Each Cluster
ALDH16A1
ALDH18A1
ALDH1A1
ALDH1A2
ALDH1A3
ALDH1B1
ALDH1L1
ALDH1L2
ALDH2
ALDH3A1
ALDH3A2
ALDH3B1
ALDH3B2
ALDH4A1
ALDH5A1
ALDH6A1
ALDH7A1
ALDH8A1
ALDH9A1
CD68
NT5E
PECAM1
PROM1

Appendix B: Supplemental Figures

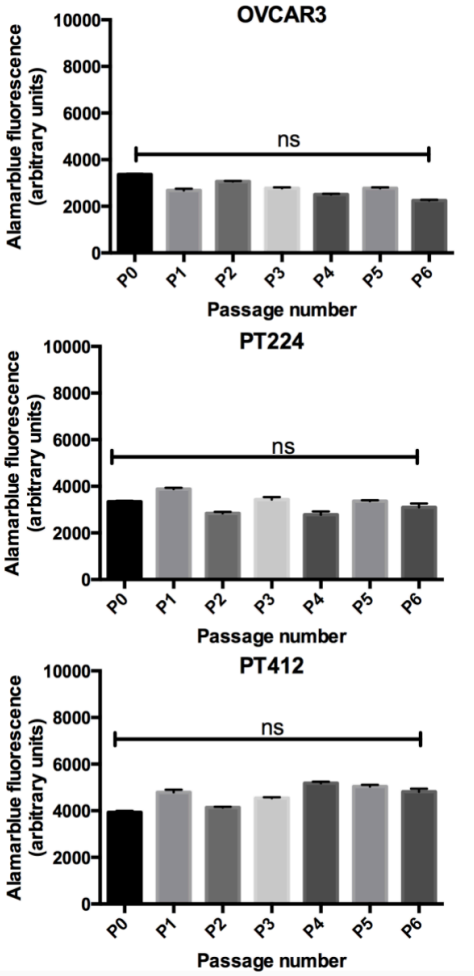

Supplemental Figure 1: Viability measurements at Day 1 of spheroid formation.
Viability was quantified using alamarblue fluorescence at Day 1 of spheroid formation from the OVCAR3 cell line, Pt224 or Pt412 primary samples. Quantification of viability at Day 1 from all passages (P0-P6) indicates no significant differences in viability at the initiation of spheroid formation with 100 cells/drop in each passage.

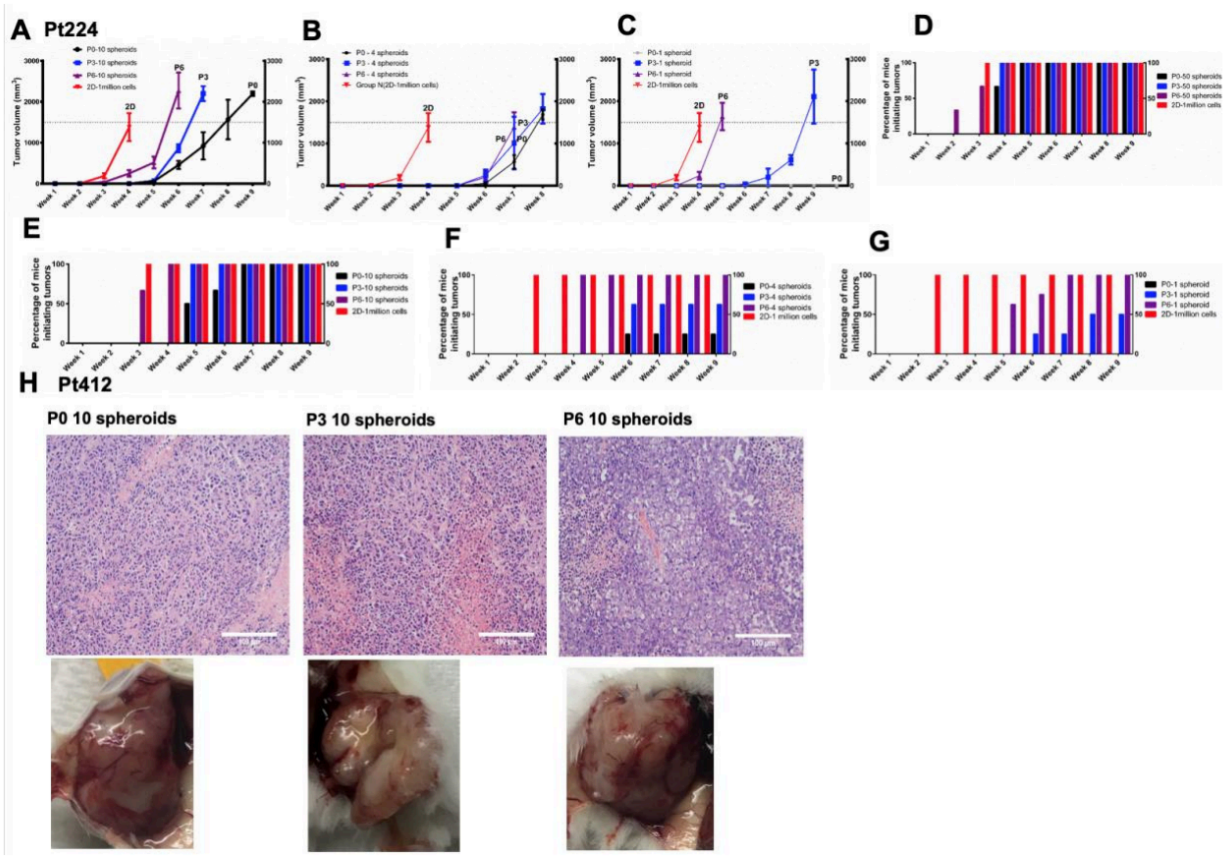

Supplemental Figure 2: Tumorigenicity of Pt224 spheroids after passaging.
(A-G) Pt224 Spheroids from higher serial passage number within this model are more tumorigenic in NSG mice. Tumor volume as a function of time for A) 10 spheroids, B) 4 spheroids, and C) 1 spheroid (n=6 in each group). 50 spheroids from P0, P3, and P6 all reached the endpoint of 1500 mm3 by week 6, and 1 million 2D grown cells reached endpoint by week 4. 10 P0 spheroids all reached endpoint by week 9, P3 by week 7, and P6 by week 5. 1 P0 spheroid never developed, meanwhile, 1 injected spheroid reached endpoint by week 8 for P3, and week 5 for P6. Percentage of mice initiating tumors after subcutaneous injection of D) 50, E) 10, F) 4, and G) 1 spheroid/s (n=6 in each group). 50 P0 spheroids initiated tumors by weeks 4 and 5, P3 by week 4, and P6 by weeks 2, 3, and 4. 10 P0 spheroids initiated tumors by weeks 5, 6, and 7, P3 by week 5, and P6 by weeks 3, and 4. 1 spheroid from P0 never initiated a tumor, even after 15 weeks. Half of the P3 spheroids formed tumors, initiating in weeks 6 and 8. All of P6 spheroids formed tumors, initiating by weeks 5, 6, and 7. H) Pt412 Macroscopic pictures and photomicrographs of hematoxylin and eosin images of xenografts observed in NSG mice with subcutaneous injections of 10 spheroids from P0, P3 and P6. Scale bar=100μm.

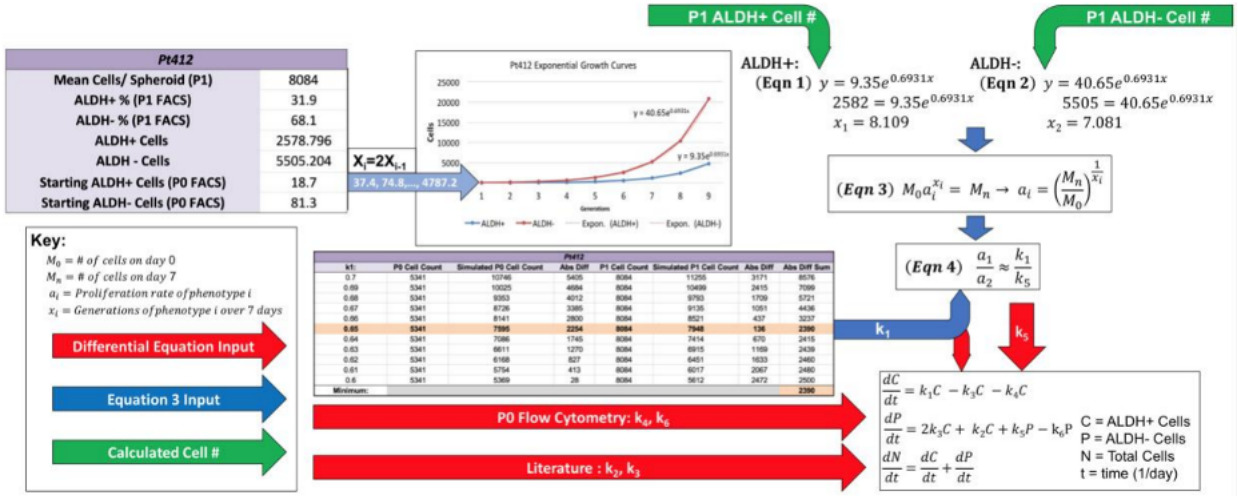

Supplemental Figure 3: Serial passaging mathematical modeling workflow.
Flow cytometry and cell count data from P0 and P1 were used to inform our simple ODE system. ALDH+ and ALDH- death rates were determined via flow cytometry following 7 days of 3D culture. Symmetric differentiation rate is derived from the Choi et al. and Tomasetti et al., while asymmetric division rate is inferred from Tomasetti et al. and unpublished data of single ovarian CSC divisions within a microfluidic device. Cell counts and flow cytometry data are used to approximate the number of ALDH+ and ALDH- generations produced over 7 days and used to constrain the ratio of symmetric ALDH+ division and symmetric ALDH- division based on the assumption of an exponential growth phase. ALDH+ symmetric division rate is chosen to minimize the collective difference between simulated cell numbers per spheroid after P0 and P1 and the experimentally derived cell numbers per spheroid.

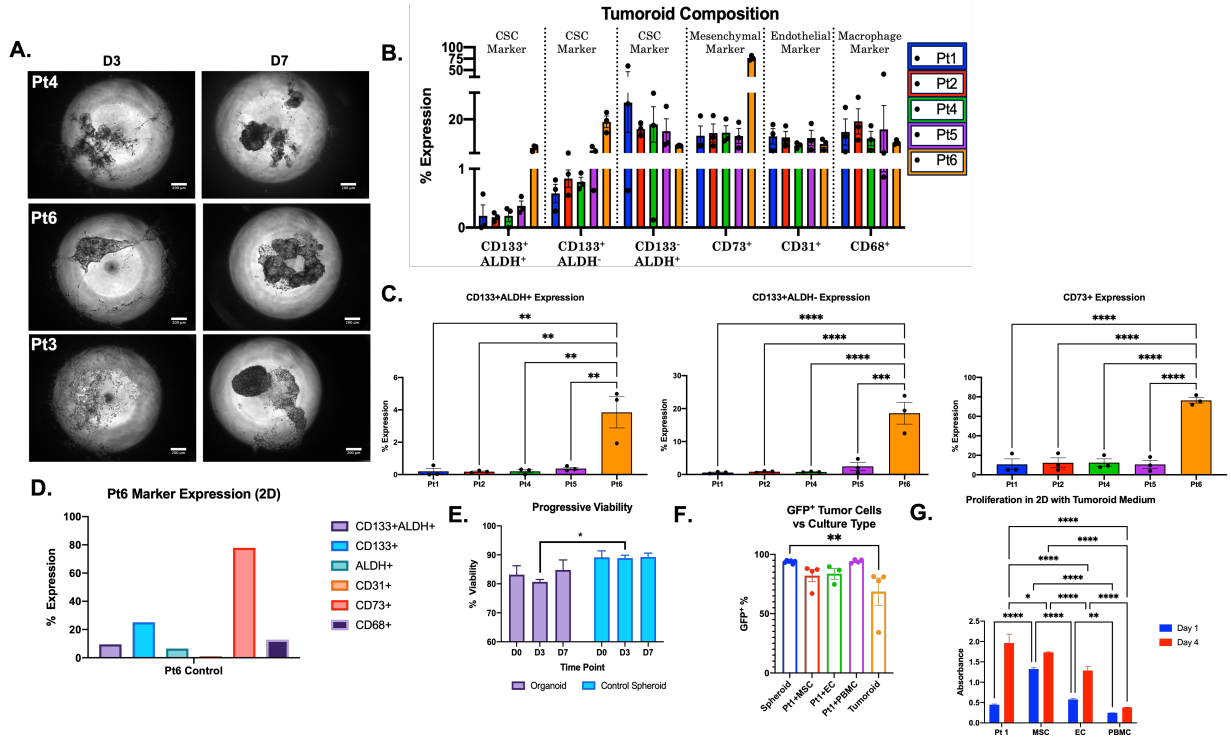

Supplemental Figure 4: Characterization of heterogeneous tumoroid cultures and culture medium. A) Phase contrast images of additional pt-derived tumoroids. B) Expression of CSC and TME markers for 5 patient samples determined with FACS. C) FACS expression of CD133+ALDH+, CD133+ALDH-, and CD73 displayed in individual graphs showing significant differences between Pt6 and the other patient samples. D) FACS expression of CSCs and TME markers for patient 6 sample cultured in 2D. E) Viability in tumoroids (purple) vs spheroids over time, measured by MTS. F) GFP expression in spheroids, co-cultures, and tumoroids generated with GFP tagged patient cells. G) Proliferation of patient cells, MSCs, ECs, or PBMCs cultured in 2D on day 1 and day 4.

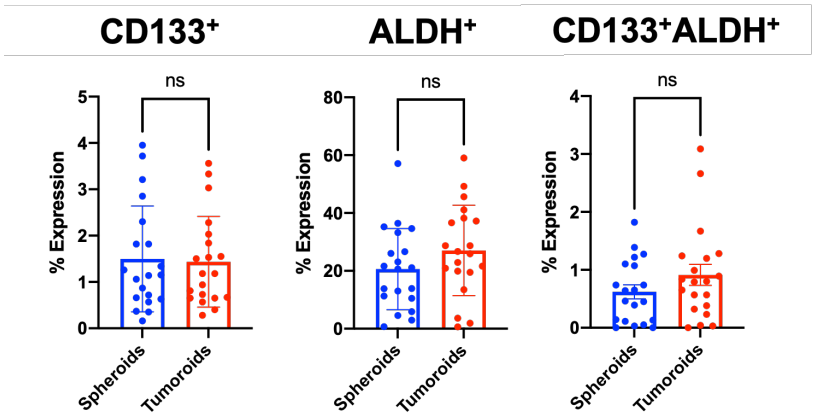

Supplemental Figure 5: Unscaled FACS quantification of Pt1 stemness in tumoroids and spheroids.
A) *Unscaled comparison of GFP$^-$ Pt1 spheroid and tumoroid CSC markers.*

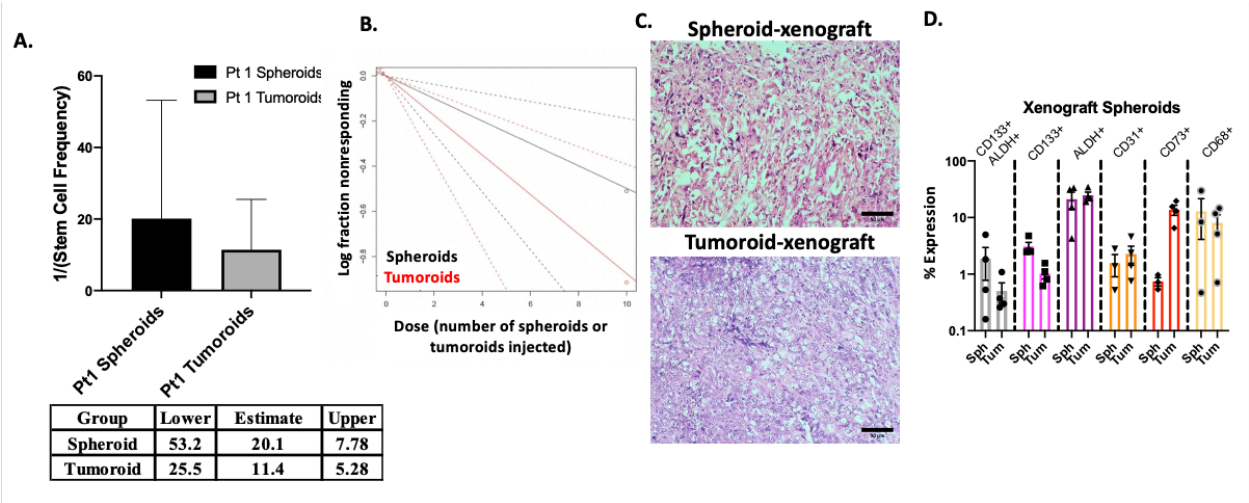

Group	Lower	Estimate	Upper
Spheroid	53.2	20.1	7.78
Tumoroid	25.5	11.4	5.28

Supplemental Figure 6: Evaluation of histological features and stemnss in tumoroid versus spheroid-derived xenografts.
A) *Bar graph indicating 1/estimated stem cell frequency in tumoroids versus spheroids.* ***B)*** *ELDA plot showing 95% confidence intervals of the log fraction non-responding versus the number of spheroids or tumoroids injected into mice.* ***C)*** *H&E sections from a spheroid-derived xenograft (top) and a tumoroid-derived xenograft (bottom).* ***D)*** *FACS analysis of CSC and TME markers in spheroids made from spheroid or tumoroid xenograft cells.*

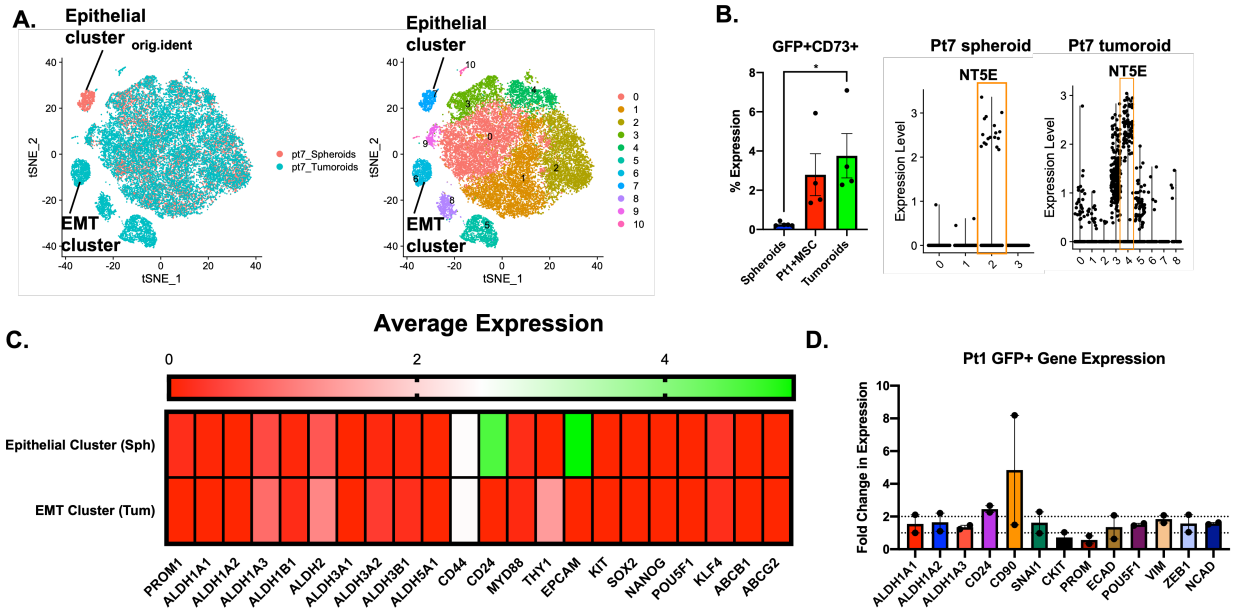

Supplemental Figure 7: Single cell RNA sequencing reveals an EMT signature and altered CSC phenotypes. A) t-SNE of aligned spheroid and tumoroid Pt7 single cell RNA sequencing clusters showing the culture origin of each cell (left) and the alignted clusters (right). B) Expression of CD73 measured with FACS in patient cells from spheroids versus MSC-co-culture and tumoroids. NT5E (CD73 gene) expression in the spheroid epithelial cluster (c2) compared to the tumoroid EMT cluster (c4) for comparison with FACS data. C) Heatmap of the average expression of a panel of CSC markers. D) qPCR of EMT and CSC markers in sorted GFP+ patient tumor cells from tumoroid culture compared to spheroid culture.

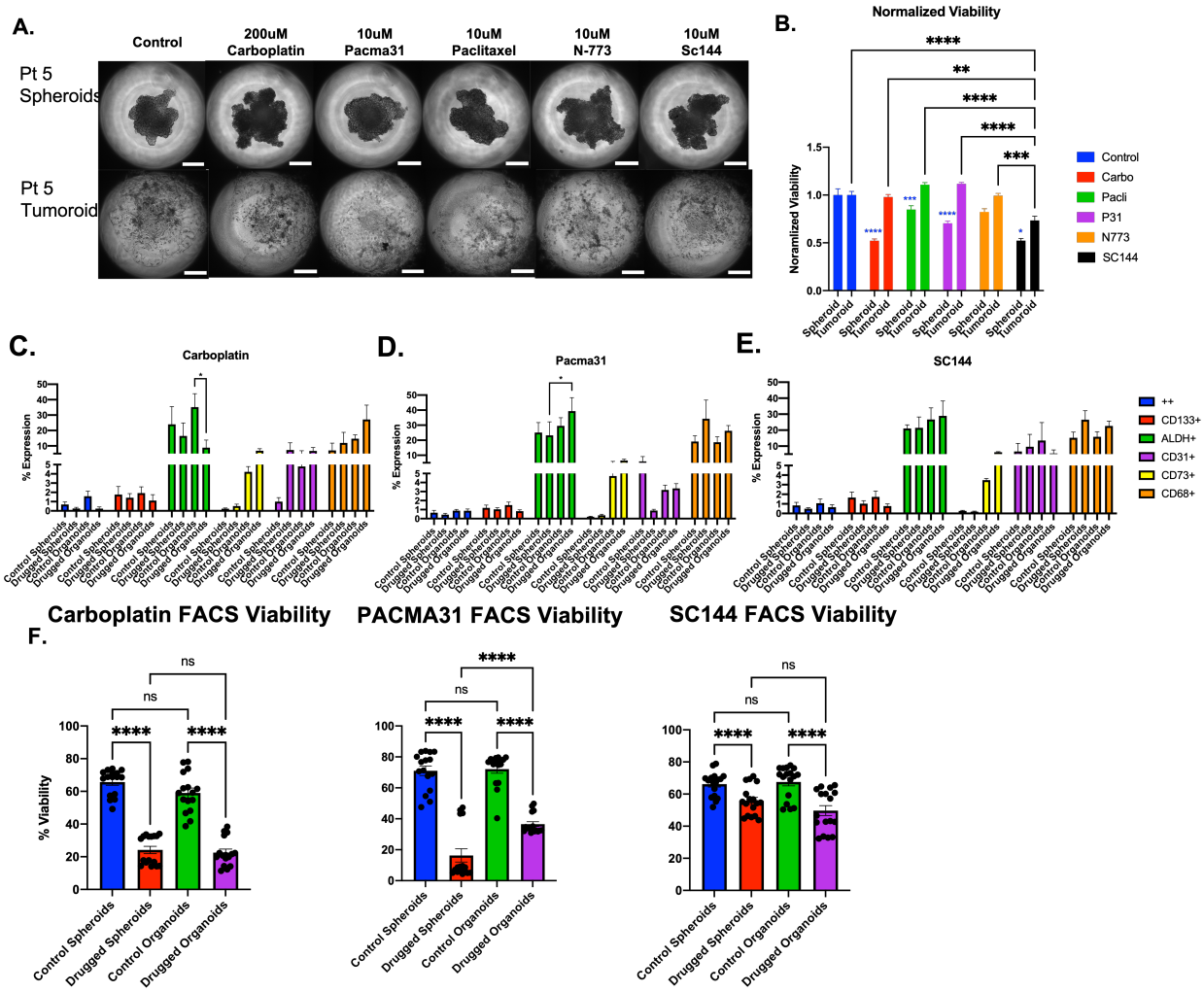

Supplemental Figure 8: Tumoroid response to drug treatment.
A) Phase contrast images of drug response in an additional patient sample. B) MTS viability of tumoroids versus spheroids made without GFR Matrigel. C-E) FACS expression of CSC and TME markers following 48 hour drug treatment with 200 uM carboplatin, 10 uM pacma31, or 10 uM SC144. F) FACS viability after drug treatment.

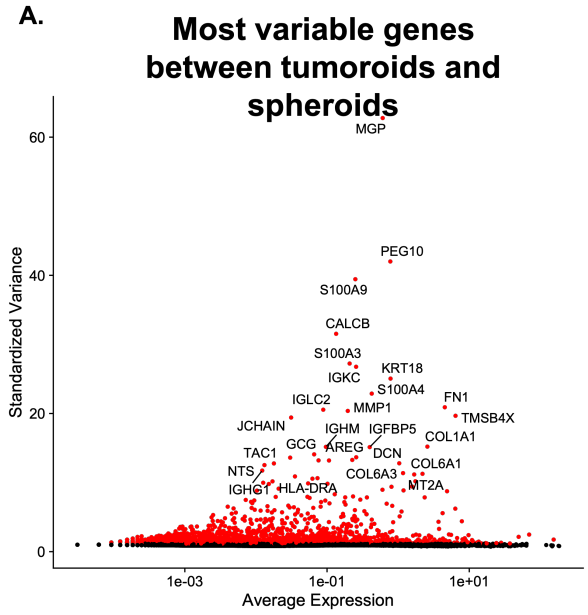

Supplemental Figure 9: Tumoroid and spheroid variable features plot.
A) Scatter plot of the top 25 most variable features in tumoroids and spheroids.

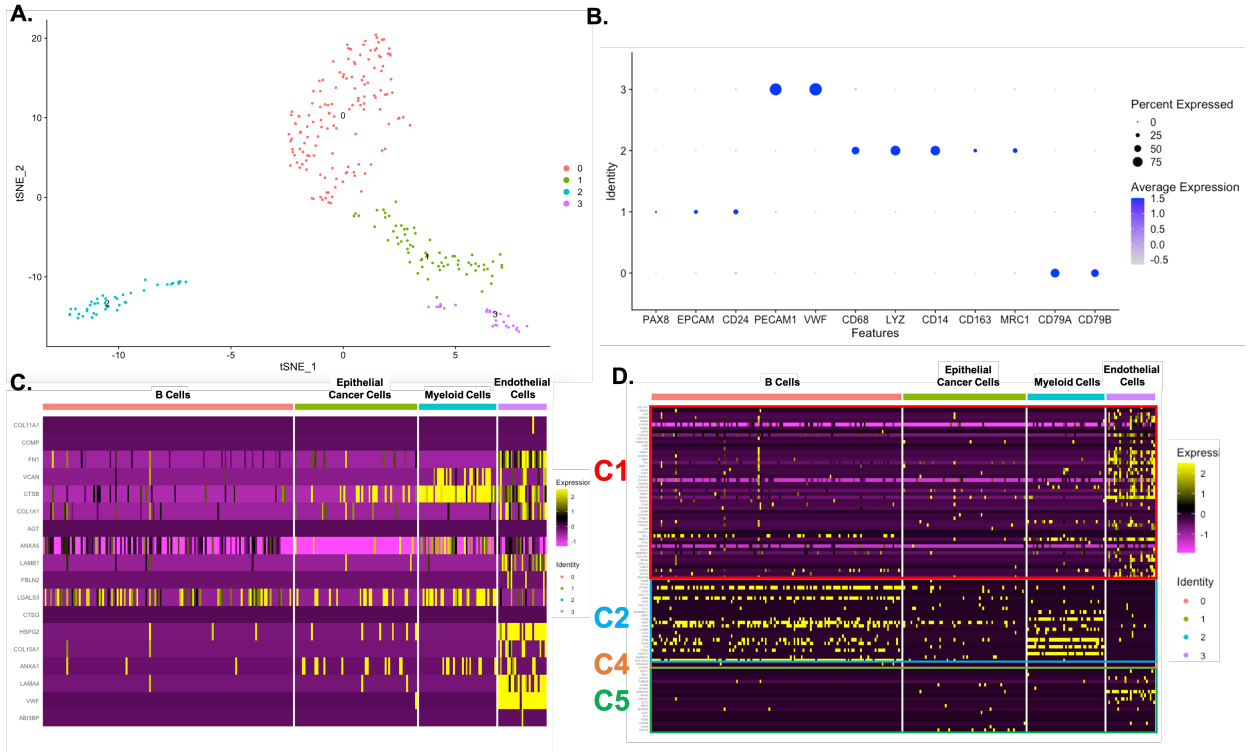

Supplemental Figure 10: Clinically relevant gene expression in the small tumoroid cell populations. A) Re-clustered t-SNE plot of the endothelial, myeloid, B cell, and epithelial cancer cell clusters from Pt7 tumoroids. B) Dotplot showing expression of cell type specific genes to identify cell types for each cluster. C) Heatmap showing the expression of malignant matrisome genes by the small cell populations in tumoroids. D) Heatmap showing the expression of HGSOC molecular subtype signatures by the small cell populations in tumoroids.

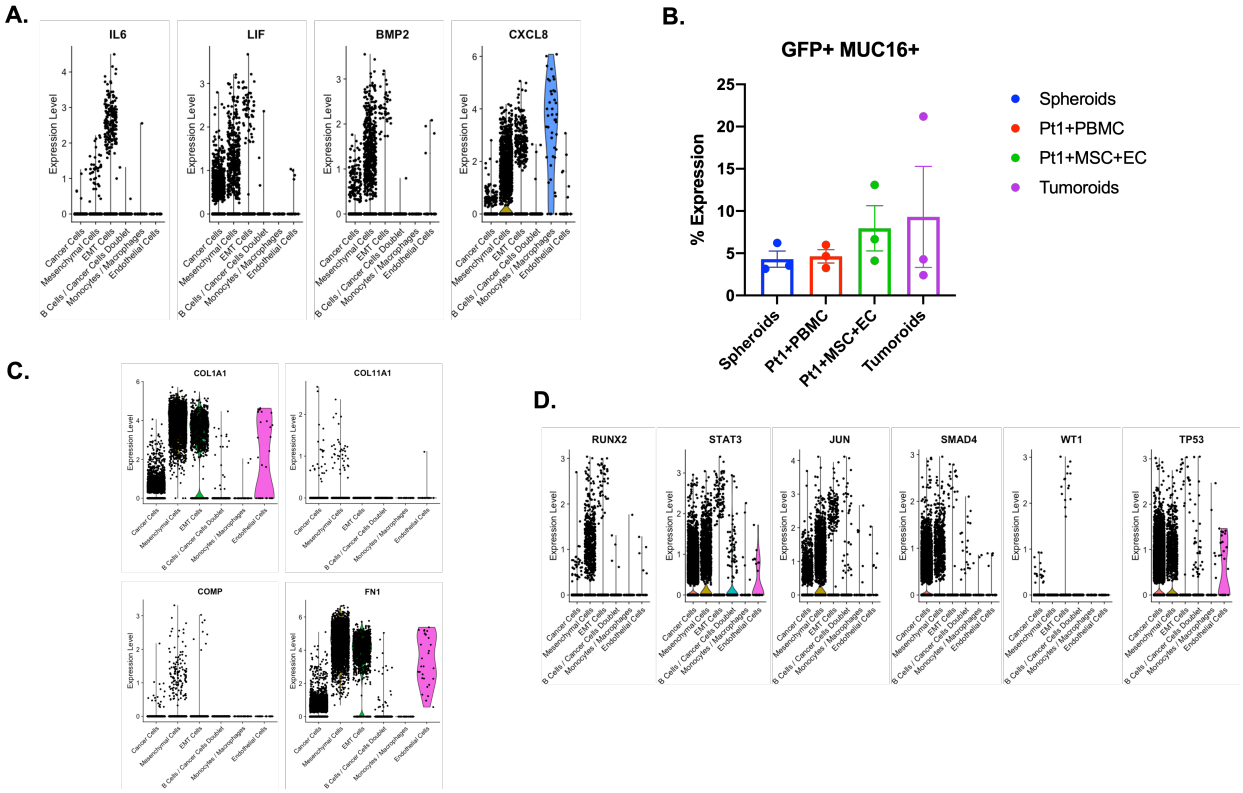

Supplemental Figure 11: scRNA sequencing investigation of tumoroid marker expression and epithelial cell populations in PBMC cultures investigation..
A) Violin plots showing expression of CA-MSC signaling molecules showing high expression in the mesenchymal tumoroid clusters and the EMT cluster. B) FACS obtained MUC16 expression in GFP+ patient tumor cells after culture with different cell combinations. C) Violin plots showing high expression of 4 malignant matrisome genes (most associated with poor outcomes) in mesenchymal tumoroid clusters and EMT tumoroid cluster. D) Violin plots showing high expression of common transcription factors for all 22 malignant matrisome markers.

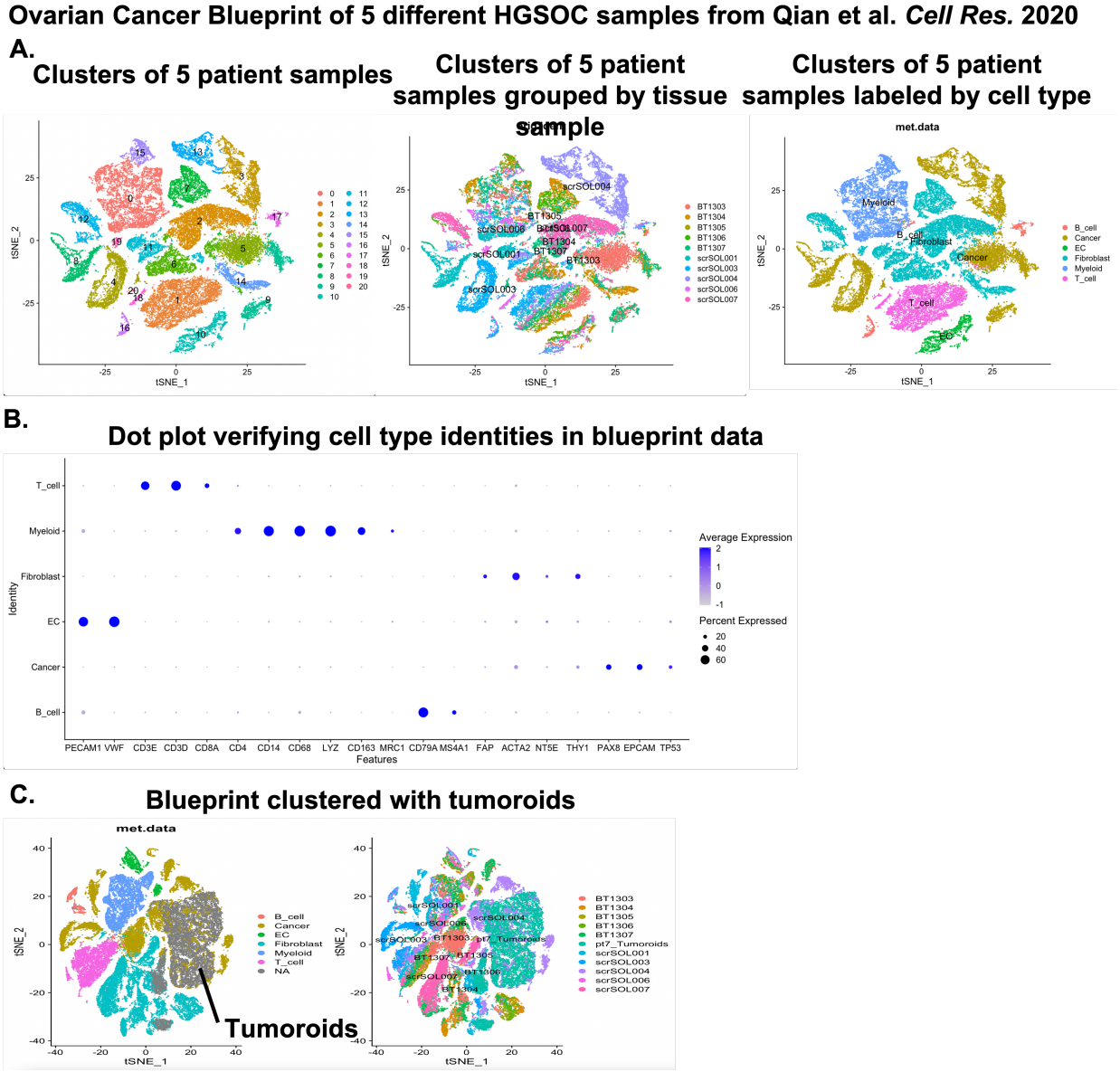

Supplemental Figure 12: Identifying cell type identities with ovarian cancer Blueprint data.
A) t-SNE plots of 5 HGSOC scRNA seq samples grouped by cluster (left), patient-sample (middle), and cell type (right). B) Dotplot verifying the cell type identities assigned to each cluster. C) Aligned blueprint data with Pt7 tumoroids showing overlap of cancer cells from the blueprint with the largest ambiguous grey population from Pt7 tumoroids.

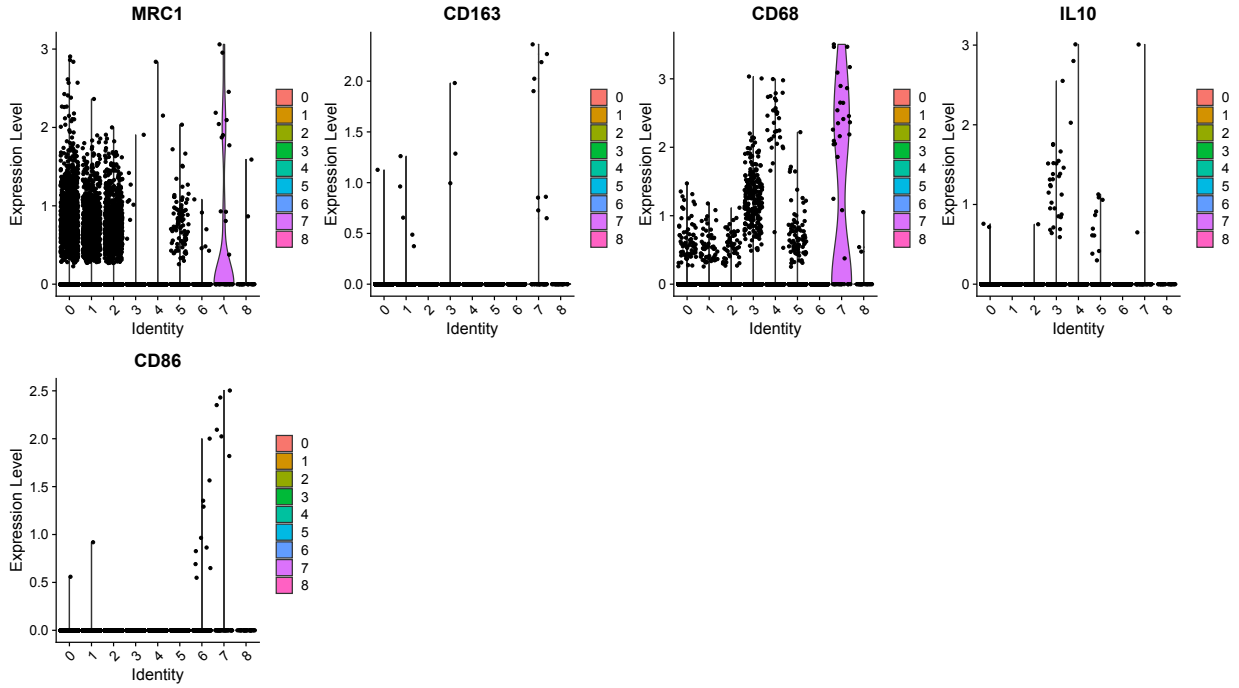

Supplemental Figure 13: Tumoroid cluster 7 (macrophages) express M1 and M2-like markers.
Single cell RNA sequencing expression levels of M2-like macrophage markers (MRC1, CD163, IL10), and M1-like macrophage marker (CD86) as well as macrophage marker CD68 in the macrophage cluster (cluster 7) within pt7 tumoroids.

Bibliography

1. Horst, E. N. *et al.* Personalized models of heterogeneous 3D epithelial tumor microenvironments: Ovarian cancer as a model. *Acta Biomater.* (2021) doi:10.1016/j.actbio.2021.04.041.
2. Bregenzer, M. E. *et al.* Integrated cancer tissue engineering models for precision medicine. *PloS One* **14**, e0216564 (2019).
3. Ward Rashidi, M. R. *et al.* Engineered 3D Model of Cancer Stem Cell Enrichment and Chemoresistance. *Neoplasia N. Y. N* **21**, 822–836 (2019).
4. Raghavan, S. *et al.* Personalized Medicine Based Approach to Model Patterns of Chemoresistance and Tumor Recurrence Using Ovarian Cancer Stem Cell Spheroids. *Clin. Cancer Res.* clincanres.0133.2017 (2017) doi:10.1158/1078-0432.CCR-17-0133.
5. Brown, J. R. *et al.* Phase II clinical trial of metformin as a cancer stem cell–targeting agent in ovarian cancer. *JCI Insight* **5**, (2020).
6. Hanahan, D. & Weinberg, R. A. Hallmarks of Cancer: The Next Generation. *Cell* **144**, 646–674 (2011).
7. Hanahan, D. & Weinberg, R. A. The Hallmarks of Cancer. *Cell* **100**, 57–70 (2000).
8. Heppner, G. H. & Miller, B. E. Tumor heterogeneity: biological implications and therapeutic consequences. *Cancer Metastasis Rev.* **2**, 5–23 (1983).
9. Holzel, M., Bovier, A. & Tuting, T. Plasticity of tumour and immune cells: a source of heterogeneity and a cause for therapy resistance? *Nat Rev Cancer* **13**, 365–76 (2013).

10. Egeblad, M., Nakasone, E. S. & Werb, Z. Tumors as organs: complex tissues that interface with the entire organism. *Dev. Cell* **18**, 884–901 (2010).
11. Loessner, D. *et al.* Bioengineered 3D platform to explore cell–ECM interactions and drug resistance of epithelial ovarian cancer cells. *Biomaterials* **31**, 8494–8506 (2010).
12. Ip, C. K. M. *et al.* Stemness and chemoresistance in epithelial ovarian carcinoma cells under shear stress. *Sci. Rep.* **6**, (2016).
13. Bougault, C., Paumier, A., Aubert-Foucher, E. & Mallein-Gerin, F. Molecular analysis of chondrocytes cultured in agarose in response to dynamic compression. *BMC Biotechnol.* **8**, 71 (2008).
14. Tse, J. M. *et al.* Mechanical compression drives cancer cells toward invasive phenotype. *Proc. Natl. Acad. Sci.* **109**, 911–916 (2012).
15. Chin, L., Xia, Y., Discher, D. E. & Janmey, P. A. Mechanotransduction in cancer. *Curr. Opin. Chem. Eng.* **11**, 77–84 (2016).
16. Takaishi, K. *et al.* Involvement of M2-polarized macrophages in the ascites from advanced epithelial ovarian carcinoma in tumor progression via Stat3 activation. *Cancer Sci.* **101**, 2128–2136 (2010).
17. Yin, M. *et al.* Tumor-associated macrophages drive spheroid formation during early transcoelomic metastasis of ovarian cancer. *J. Clin. Invest.* **126**, 4157–4173 (2016).
18. Colvin, E. K. Tumor-Associated Macrophages Contribute to Tumor Progression in Ovarian Cancer. *Front. Oncol.* **4**, (2014).
19. Cassereau, L., Miroshnikova, Y. A., Ou, G., Lakins, J. & Weaver, V. M. A 3D tension bioreactor platform to study the interplay between ECM stiffness and tumor phenotype. *J. Biotechnol.* **193**, 66–69 (2015).

20. Nargis, N. N., Aldredge, R. C. & Guy, R. D. The influence of soluble fragments of extracellular matrix (ECM) on tumor growth and morphology. *Math. Biosci.* **296**, 1–16 (2018).

21. Hanker, L. C. *et al.* The impact of second to sixth line therapy on survival of relapsed ovarian cancer after primary taxane/platinum-based therapy. *Ann. Oncol. Off. J. Eur. Soc. Med. Oncol.* **23**, 2605–2612 (2012).

22. Kossaï, M., Leary, A., Scoazec, J.-Y. & Genestie, C. Ovarian Cancer: A Heterogeneous Disease. *Pathobiology* **85**, 41–49 (2018).

23. Mitra, A. K. *et al.* In vivo tumor growth of high-grade serous ovarian cancer cell lines. *Gynecol. Oncol.* **138**, 372–377 (2015).

24. Ghoneum, A., Afify, H., Salih, Z., Kelly, M. & Said, N. Role of tumor microenvironment in ovarian cancer pathobiology. *Oncotarget* **9**, 22832–22849 (2018).

25. Cancer Genome Atlas Research, N. Integrated genomic analyses of ovarian carcinoma. *Nature* **474**, 609–615 (2011).

26. Kanchi, K. L. *et al.* Integrated analysis of germline and somatic variants in ovarian cancer. *Nat Commun* **5**, 3156 (2014).

27. Schwartz, M. *et al.* Applying Precision Medicine to Ovarian Cancer. *Int. J. Gynecol. Cancer* **28**, 479–485 (2018).

28. Govindarajan, M., Wohlmuth, C., Waas, M., Bernardini, M. Q. & Kislinger, T. High-throughput approaches for precision medicine in high-grade serous ovarian cancer. *J. Hematol. Oncol.J Hematol Oncol* **13**, 134 (2020).

29. Takaya, H. *et al.* Intratumor heterogeneity and homologous recombination deficiency of high-grade serous ovarian cancer are associated with prognosis and molecular subtype and change in treatment course. *Gynecol Oncol* **156**, 415–422 (2020).
30. Nowell, P. C. The clonal evolution of tumor cell populations. *Science* **194**, 23–28 (1976).
31. Bai, H. *et al.* Genetic and epigenetic heterogeneity of epithelial ovarian cancer and the clinical implications for molecular targeted therapy. *J. Cell. Mol. Med.* **20**, 581–593 (2016).
32. Roberts, C. M., Cardenas, C. & Tedja, R. The Role of Intra-Tumoral Heterogeneity and Its Clinical Relevance in Epithelial Ovarian Cancer Recurrence and Metastasis. *Cancers* **11**, (2019).
33. Guo, M., Peng, Y., Gao, A., Du, C. & Herman, J. G. Epigenetic heterogeneity in cancer. *Biomark. Res.* **7**, 23 (2019).
34. Moufarrij, S. *et al.* Epigenetic therapy for ovarian cancer: promise and progress. *Clin. Epigenetics* **11**, 7 (2019).
35. Muñoz, P., Iliou, M. S. & Esteller, M. Epigenetic alterations involved in cancer stem cell reprogramming. *Mol. Oncol.* **6**, 620–636 (2012).
36. Burgos-Ojeda, D., Rueda, B. R. & Buckanovich, R. J. Ovarian cancer stem cell markers: Prognostic and therapeutic implications. *Cancer Lett.* **322**, 1–7 (2012).
37. Kreso, A. & Dick, J. E. Evolution of the cancer stem cell model. *Cell Stem Cell* **14**, 275–91 (2014).
38. Magee, J. A., Piskounova, E. & Morrison, S. J. Cancer Stem Cells: Impact, Heterogeneity, and Uncertainty. *Cancer Cell* **21**, 283–296 (2012).
39. Eun, K., Ham, S. W. & Kim, and H. Cancer stem cell heterogeneity: origin and new perspectives on CSC targeting. *BMB Rep.* **50**, 117–125 (2017).

40. Ahmed, N., Escalona, R., Leung, D., Chan, E. & Kannourakis, G. Tumour microenvironment and metabolic plasticity in cancer and cancer stem cells: Perspectives on metabolic and immune regulatory signatures in chemoresistant ovarian cancer stem cells. *Semin. Cancer Biol.* **53**, 265–281 (2018).
41. Korkaya, H. & Wicha, M. S. Cancer stem cells: nature versus nurture. *Nat. Cell Biol.* **12**, 419–421 (2010).
42. Wang, T. *et al.* Cancer stem cell targeted therapy: progress amid controversies. *Oncotarget* **6**, 44191–206 (2015).
43. Boesch, M. *et al.* The side population of ovarian cancer cells defines a heterogeneous compartment exhibiting stem cell characteristics. *Oncotarget* **5**, 7027–7039 (2014).
44. Batlle, E. & Clevers, H. Cancer stem cells revisited. *Nat. Med.* **23**, 1124–1134 (2017).
45. Bonnet, D. & Dick, J. E. Human acute myeloid leukemia is organized as a hierarchy that originates from a primitive hematopoietic cell. *Nat. Med.* **3**, 730–737 (1997).
46. Al-Hajj, M., Wicha, M. S., Benito-Hernandez, A., Morrison, S. J. & Clarke, M. F. Prospective identification of tumorigenic breast cancer cells. *Proc. Natl. Acad. Sci. U. S. A.* **100**, 3983–3988 (2003).
47. Zhang, S. *et al.* Identification and characterization of ovarian cancer-initiating cells from primary human tumors. *Cancer Res.* **68**, 4311–4320 (2008).
48. O'Brien, C. A., Pollett, A., Gallinger, S. & Dick, J. E. A human colon cancer cell capable of initiating tumour growth in immunodeficient mice. *Nature* **445**, 106–110 (2007).
49. Ricci-Vitiani, L. *et al.* Identification and expansion of human colon-cancer-initiating cells. *Nature* **445**, 111–115 (2007).

50. Collins, A. T., Berry, P. A., Hyde, C., Stower, M. J. & Maitland, N. J. Prospective identification of tumorigenic prostate cancer stem cells. *Cancer Res.* **65**, 10946–10951 (2005).

51. Patrawala, L. *et al.* Highly purified CD44+ prostate cancer cells from xenograft human tumors are enriched in tumorigenic and metastatic progenitor cells. *Oncogene* **25**, 1696–1708 (2006).

52. Galli, R. *et al.* Isolation and characterization of tumorigenic, stem-like neural precursors from human glioblastoma. *Cancer Res.* **64**, 7011–7021 (2004).

53. Singh, S. K., Clarke, I. D., Hide, T. & Dirks, P. B. Cancer stem cells in nervous system tumors. *Oncogene* **23**, 7267–7273 (2004).

54. Singh, S. K. *et al.* Identification of human brain tumour initiating cells. *Nature* **432**, 396–401 (2004).

55. Li, C. *et al.* Identification of pancreatic cancer stem cells. *Cancer Res.* **67**, 1030–1037 (2007).

56. Schatton, T. *et al.* Identification of cells initiating human melanomas. *Nature* **451**, 345–349 (2008).

57. Matsui, W. *et al.* Clonogenic multiple myeloma progenitors, stem cell properties, and drug resistance. *Cancer Res.* **68**, 190–197 (2008).

58. Eramo, A. *et al.* Identification and expansion of the tumorigenic lung cancer stem cell population. *Cell Death Differ.* **15**, 504–514 (2008).

59. Dzobo, K. *et al.* Advances in Therapeutic Targeting of Cancer Stem Cells within the Tumor Microenvironment: An Updated Review. *Cells* **9**, (2020).

60. Dzobo, K., Ganz, C., Thomford, N. E. & Senthebane, D. A. Cancer Stem Cell Markers in Relation to Patient Survival Outcomes: Lessons for Integrative Diagnostics and Next-Generation Anticancer Drug Development. *Omics J. Integr. Biol.* **25**, 81–92 (2021).

61. Silva, I. A. *et al.* Aldehyde dehydrogenase in combination with CD133 defines angiogenic ovarian cancer stem cells that portend poor patient survival. *Cancer Res.* **71**, 3991–4001 (2011).

62. Landen, C. N. *et al.* Targeting aldehyde dehydrogenase cancer stem cells in ovarian cancer. *Mol Cancer Ther* **9**, 3186–99 (2010).

63. Zhang, J. *et al.* CD133 expression associated with poor prognosis in ovarian cancer. *Mod Pathol* **25**, 456–64 (2012).

64. Choi, Y.-J. *et al.* Identifying an ovarian cancer cell hierarchy regulated by bone morphogenetic protein 2. *Proc. Natl. Acad. Sci. U. S. A.* **112**, E6882-6888 (2015).

65. Curley, M. D. *et al.* CD133 expression defines a tumor initiating cell population in primary human ovarian cancer. *Stem Cells* **27**, 2875–83 (2009).

66. Sharrow, A. C. *et al.* Characterization of aldehyde dehydrogenase 1 high ovarian cancer cells: Towards targeted stem cell therapy. *Gynecol. Oncol.* **142**, 341–348 (2016).

67. Zhou, Q. *et al.* Prognostic value of cancer stem cell marker CD133 in ovarian cancer: a meta-analysis. *Int J Clin Exp Med* **8**, 3080–8 (2015).

68. Baba, T. *et al.* Epigenetic regulation of CD133 and tumorigenicity of CD133+ ovarian cancer cells. *Oncogene* **28**, 209–218 (2009).

69. Kryczek, I. *et al.* Expression of aldehyde dehydrogenase and CD133 defines ovarian cancer stem cells. *Int. J. Cancer* **130**, 29–39 (2012).

70. Murphy, S. K. Targeting ovarian cancer-initiating cells. *Anticancer Agents Med. Chem.* **10**, 157–163 (2010).

71. Steg, A. D. *et al.* Stem cell pathways contribute to clinical chemoresistance in ovarian cancer. *Clin. Cancer Res.* **18**, 869–881 (2012).

72. Charafe-Jauffret, E. *et al.* Aldehyde dehydrogenase 1-positive cancer stem cells mediate metastasis and poor clinical outcome in inflammatory breast cancer. *Clin Cancer Res* **16**, 45–55 (2010).

73. Condello, S. *et al.* beta-Catenin-regulated ALDH1A1 is a target in ovarian cancer spheroids. *Oncogene* **34**, 2297–308 (2015).

74. Alison, M. R., Lin, W.-R., Lim, S. M. L. & Nicholson, L. J. Cancer stem cells: In the line of fire. *Cancer Treat. Rev.* **38**, 589–598 (2012).

75. Singh, A. & Settleman, J. EMT, cancer stem cells and drug resistance: an emerging axis of evil in the war on cancer. *Oncogene* **29**, 4741–51 (2010).

76. Keyvani, V. *et al.* Ovarian cancer stem cells and targeted therapy. *J. Ovarian Res.* **12**, 120 (2019).

77. Hatina, J. *et al.* Ovarian Cancer Stem Cell Heterogeneity. in *Stem Cells Heterogeneity in Cancer* (ed. Birbrair, A.) 201–221 (Springer International Publishing, 2019). doi:10.1007/978-3-030-14366-4_12.

78. Pieterse, Z. *et al.* Ovarian cancer stem cells and their role in drug resistance. *Int. J. Biochem. Cell Biol.* **106**, 117–126 (2019).

79. Dzobo, K. & Dandara, C. Broadening Drug Design and Targets to Tumor Microenvironment? Cancer-Associated Fibroblast Marker Expression in Cancers and Relevance for Survival Outcomes. *Omics J. Integr. Biol.* **24**, 340–351 (2020).

80. Dasari, S., Fang, Y. & K. Mitra, A. Cancer Associated Fibroblasts: Naughty Neighbors That Drive Ovarian Cancer Progression. *Cancers* **10**, (2018).

81. Pearce, O. M. T. *et al.* Deconstruction of a Metastatic Tumor Microenvironment Reveals a Common Matrix Response in Human Cancers. *Cancer Discov.* **8**, 304–319 (2018).

82. Izar, B. *et al.* A single-cell landscape of high-grade serous ovarian cancer. *Nat. Med.* **26**, 1271–1279 (2020).

83. Jiménez-Sánchez, A. *et al.* Unraveling tumor–immune heterogeneity in advanced ovarian cancer uncovers immunogenic effect of chemotherapy. *Nat. Genet.* **52**, 582–593 (2020).

84. Shih, A. J. *et al.* Identification of grade and origin specific cell populations in serous epithelial ovarian cancer by single cell RNA-seq. *PloS One* **13**, e0206785 (2018).

85. Coffman, L. G. *et al.* Ovarian Carcinoma-Associated Mesenchymal Stem Cells Arise from Tissue-Specific Normal Stroma. *Stem Cells Dayt. Ohio* **37**, 257–269 (2019).

86. Verardo, R. *et al.* Specific mesothelial signature marks the heterogeneity of mesenchymal stem cells from high-grade serous ovarian cancer. *Stem Cells Dayt. Ohio* **32**, 2998–3011 (2014).

87. Chan, T.-S., Shaked, Y. & Tsai, K. K. Targeting the Interplay Between Cancer Fibroblasts, Mesenchymal Stem Cells, and Cancer Stem Cells in Desmoplastic Cancers. *Front. Oncol.* **9**, (2019).

88. McLean, K. *et al.* Human ovarian carcinoma–associated mesenchymal stem cells regulate cancer stem cells and tumorigenesis via altered BMP production. *J. Clin. Invest.* **121**, 3206–3219 (2011).

89. Lis, R. *et al.* Mesenchymal cell interaction with ovarian cancer cells triggers pro-metastatic properties. *PloS One* **7**, e38340 (2012).

90. Klopp, A. H., Gupta, A., Spaeth, E., Andreeff, M. & Marini, F. Concise review: Dissecting a discrepancy in the literature: do mesenchymal stem cells support or suppress tumor growth? *Stem Cells Dayt. Ohio* **29**, 11–19 (2011).

91. Sun, T. *et al.* Pilot study on the interaction between B16 melanoma cell-line and bone-marrow derived mesenchymal stem cells. *Cancer Lett.* **263**, 35–43 (2008).

92. Beckermann, B. M. *et al.* VEGF expression by mesenchymal stem cells contributes to angiogenesis in pancreatic carcinoma. *Br. J. Cancer* **99**, 622–631 (2008).

93. Mishra, P. J. *et al.* Carcinoma-associated fibroblast-like differentiation of human mesenchymal stem cells. *Cancer Res.* **68**, 4331–4339 (2008).

94. Zhu, W. *et al.* Mesenchymal stem cells derived from bone marrow favor tumor cell growth in vivo. *Exp. Mol. Pathol.* **80**, 267–274 (2006).

95. Coffman, L. G. *et al.* Human carcinoma-associated mesenchymal stem cells promote ovarian cancer chemotherapy resistance via a BMP4/HH signaling loop. *Oncotarget* **7**, 6916–6932 (2016).

96. Wang, X. *et al.* Crosstalk between TEMs and endothelial cells modulates angiogenesis and metastasis via IGF1-IGF1R signalling in epithelial ovarian cancer. *Br. J. Cancer* **117**, 1371–1382 (2017).

97. Winiarski, B. K. *et al.* Epithelial ovarian cancer-induced angiogenic phenotype of human omental microvascular endothelial cells may occur independently of VEGF signaling. *Transl. Oncol.* **6**, 703–714 (2013).

98. Thibault, B., Castells, M., Delord, J.-P. & Couderc, B. Ovarian cancer microenvironment: implications for cancer dissemination and chemoresistance acquisition. *Cancer Metastasis Rev.* **33**, 17–39 (2014).

99. Prieto-Vila, M., Takahashi, R.-U., Usuba, W., Kohama, I. & Ochiya, T. Drug Resistance Driven by Cancer Stem Cells and Their Niche. *Int. J. Mol. Sci.* **18**, (2017).

100. Varas-Godoy, M., Rice, G. & Illanes, S. E. The Crosstalk between Ovarian Cancer Stem Cell Niche and the Tumor Microenvironment. *Stem Cells Int.* **2017**, 5263974 (2017).

101. Xiang, T. *et al.* Interleukin-17 produced by tumor microenvironment promotes self-renewal of CD133+ cancer stem-like cells in ovarian cancer. *Oncogene* **34**, 165–176 (2015).

102. Qin, J. *et al.* Hypoxia-inducible factor 1 alpha promotes cancer stem cells-like properties in human ovarian cancer cells by upregulating SIRT1 expression. *Sci. Rep.* **7**, 10592 (2017).

103. Emami Nejad, A. *et al.* The role of hypoxia in the tumor microenvironment and development of cancer stem cell: a novel approach to developing treatment. *Cancer Cell Int.* **21**, 62 (2021).

104. Kipps, E., Tan, D. S. P. & Kaye, S. B. Meeting the challenge of ascites in ovarian cancer: new avenues for therapy and research. *Nat. Rev. Cancer* **13**, 273–282 (2013).

105. Nagy, J. A., Herzberg, K. T., Dvorak, J. M. & Dvorak, H. F. Pathogenesis of Malignant Ascites Formation: Initiating Events That Lead to Fluid Accumulation. *Cancer Res.* **53**, 2631–2643 (1993).

106. Kim, S., Kim, B. & Song, Y. S. Ascites modulates cancer cell behavior, contributing to tumor heterogeneity in ovarian cancer. *Cancer Sci.* **107**, 1173–1178 (2016).

107. Kan, T. *et al.* Single-cell EMT-related transcriptional analysis revealed intra-cluster heterogeneity of tumor cell clusters in epithelial ovarian cancer ascites. *Oncogene* **39**, 4227–4240 (2020).

108. Gao, Q. *et al.* Heterotypic CAF-tumor spheroids promote early peritoneal metastatis of ovarian cancer. *J. Exp. Med.* **216**, 688–703 (2019).

109. Hashimoto, K., Honda, K., Matsui, H., Nagashima, Y. & Oda, H. Flow Cytometric Analysis of Ovarian Cancer Ascites: Response of Mesothelial Cells and Macrophages to Cancer. *Anticancer Res.* **36**, 3579–3584 (2016).

110. Kenda Suster, N. & Virant-Klun, I. Presence and role of stem cells in ovarian cancer. *World J. Stem Cells* **11**, 383–397 (2019).

111. Bregenzer, M. E. *et al.* The Role of Cancer Stem Cells and Mechanical Forces in Ovarian Cancer Metastasis. *Cancers Basel* (2019).

112. Han, Q. *et al.* Tumor cell-fibroblast heterotypic aggregates in malignant ascites of patients with ovarian cancer. *Int. J. Mol. Med.* (2019) doi:10.3892/ijmm.2019.4361.

113. Al Habyan, S., Kalos, C., Szymborski, J. & McCaffrey, L. Multicellular detachment generates metastatic spheroids during intra-abdominal dissemination in epithelial ovarian cancer. *Oncogene* **37**, 5127–5135 (2018).

114. Hussain, A. *et al.* Distinct fibroblast functional states drive clinical outcomes in ovarian cancer and are regulated by TCF21. *J. Exp. Med.* **217**, (2020).

115. Yin, M. *et al.* Tumor-Associated Macrophages (TAMs): A Critical Activator In Ovarian Cancer Metastasis. *OncoTargets Ther.* **12**, 8687–8699 (2019).

116. Zhou, K. *et al.* Targeting tumor-associated macrophages in the tumor microenvironment. *Oncol. Lett.* **20**, 234 (2020).

117. Nowak, M. & Klink, M. The Role of Tumor-Associated Macrophages in the Progression and Chemoresistance of Ovarian Cancer. *Cells* **9**, (2020).

118. Raghavan, S., Mehta, P., Xie, Y., Lei, Y. L. & Mehta, G. Ovarian cancer stem cells and macrophages reciprocally interact through the WNT pathway to promote pro-tumoral and

malignant phenotypes in 3D engineered microenvironments. *J. Immunother. Cancer* **7**, 190 (2019).

119. Zhang, M. *et al.* A high M1/M2 ratio of tumor-associated macrophages is associated with extended survival in ovarian cancer patients. *J Ovarian Res* **7**, 19 (2014).
120. Cai, D. L. & Jin, L.-P. Immune Cell Population in Ovarian Tumor Microenvironment. *J. Cancer* **8**, 2915–2923 (2017).
121. Bellora, F. *et al.* TLR activation of tumor-associated macrophages from ovarian cancer patients triggers cytolytic activity of NK cells. *Eur. J. Immunol.* **44**, 1814–1822 (2014).
122. Dötzer, K. *et al.* Immune Heterogeneity Between Primary Tumors and Corresponding Metastatic Lesions and Response to Platinum Therapy in Primary Ovarian Cancer. *Cancers* **11**, 1250 (2019).
123. Jiménez-Sánchez, A. *et al.* Heterogeneous Tumor-Immune Microenvironments among Differentially Growing Metastases in an Ovarian Cancer Patient. *Cell* **170**, 927-938.e20 (2017).
124. Fridman, W. H., Zitvogel, L., Sautès–Fridman, C. & Kroemer, G. The immune contexture in cancer prognosis and treatment. *Nat. Rev. Clin. Oncol.* **14**, 717–734 (2017).
125. Petralia, F. *et al.* Integrated Proteogenomic Characterization across Major Histological Types of Pediatric Brain Cancer. *Cell* **183**, 1962-1985.e31 (2020).
126. Li, J., Wang, J., Chen, R., Bai, Y. & Lu, X. The prognostic value of tumor-infiltrating T lymphocytes in ovarian cancer. *Oncotarget* **8**, 15621–15631 (2017).
127. Ovarian Tumor Tissue Analysis (OTTA) Consortium *et al.* Dose-Response Association of CD8+ Tumor-Infiltrating Lymphocytes and Survival Time in High-Grade Serous Ovarian Cancer. *JAMA Oncol.* **3**, e173290 (2017).

128. Patsoukis, N., Wang, Q., Strauss, L. & Boussiotis, V. A. Revisiting the PD-1 pathway. *Sci. Adv.* **6**, eabd2712 (2020).

129. Carroll, M. J. *et al.* Alternatively-Activated Macrophages Upregulate Mesothelial Expression of P-Selectin to Enhance Adhesion of Ovarian Cancer Cells. *Cancer Res.* **78**, 3560–3573 (2018).

130. Matte, I. *et al.* Ovarian cancer ascites enhance the migration of patient-derived peritoneal mesothelial cells via cMet pathway through HGF-dependent and -independent mechanisms. *Int. J. Cancer* **137**, 289–298 (2015).

131. Matte, I., Lane, D., Bachvarov, D., Rancourt, C. & Piché, A. Role of malignant ascites on human mesothelial cells and their gene expression profiles. *BMC Cancer* **14**, 288 (2014).

132. Rynne-Vidal, A. *et al.* Mesothelial-to-mesenchymal transition as a possible therapeutic target in peritoneal metastasis of ovarian cancer. *J. Pathol.* **242**, 140–151 (2017).

133. Yoshihara, M. *et al.* Ovarian cancer-associated mesothelial cells induce acquired platinum-resistance in peritoneal metastasis via the FN1/Akt signaling pathway. *Int. J. Cancer* **146**, 2268–2280 (2020).

134. Yang, J. *et al.* Adipocytes promote ovarian cancer chemoresistance. *Sci. Rep.* **9**, (2019).

135. John, B. *et al.* Regulation of the bi-directional cross-talk between ovarian cancer cells and adipocytes by SPARC. *Oncogene* **38**, 4366–4383 (2019).

136. Heindl, A., Lan, C., Rodrigues, D. N., Koelble, K. & Yuan, Y. Similarity and diversity of the tumor microenvironment in multiple metastases: critical implications for overall and progression-free survival of high-grade serous ovarian cancer. *Oncotarget* **7**, 71123–71135 (2016).

137. Motohara, T. *et al.* An evolving story of the metastatic voyage of ovarian cancer cells: cellular and molecular orchestration of the adipose-rich metastatic microenvironment. *Oncogene* **38**, 2885–2898 (2019).

138. Wen, Y., Guo, Y., Huang, Z., Cai, J. & Wang, Z. Adipose-derived mesenchymal stem cells attenuate cisplatin-induced apoptosis in epithelial ovarian cancer cells. *Mol. Med. Rep.* **16**, 9587–9592 (2017).

139. Zhang, Y. *et al.* Ovarian cancer-associated fibroblasts contribute to epithelial ovarian carcinoma metastasis by promoting angiogenesis, lymphangiogenesis and tumor cell invasion. *Cancer Lett.* **303**, 47–55 (2011).

140. Ma, X. The omentum, a niche for premetastatic ovarian cancer. *J. Exp. Med.* **217**, e20192312 (2020).

141. Petrova, V., Annicchiarico-Petruzzelli, M., Melino, G. & Amelio, I. The hypoxic tumour microenvironment. *Oncogenesis* **7**, 1–13 (2018).

142. Paredes, F., Williams, H. C. & San Martin, A. Metabolic adaptation in hypoxia and cancer. *Cancer Lett.* **502**, 133–142 (2021).

143. He, M. *et al.* Hypoxia-inducible factor-2α directly promotes BCRP expression and mediates the resistance of ovarian cancer stem cells to adriamycin. *Mol. Oncol.* **13**, 403–421 (2019).

144. Fiaschi, T. *et al.* Reciprocal metabolic reprogramming through lactate shuttle coordinately influences tumor-stroma interplay. *Cancer Res.* **72**, 5130–5140 (2012).

145. Gilkes, D. M., Bajpai, S., Chaturvedi, P., Wirtz, D. & Semenza, G. L. Hypoxia-inducible Factor 1 (HIF-1) Promotes Extracellular Matrix Remodeling under Hypoxic Conditions by Inducing P4HA1, P4HA2, and PLOD2 Expression in Fibroblasts*,. *J. Biol. Chem.* **288**, 10819–10829 (2013).

146. Henze, A.-T. & Mazzone, M. The impact of hypoxia on tumor-associated macrophages. *J. Clin. Invest.* **126**, 3672–3679.

147. Kirkland, S. C. Type I collagen inhibits differentiation and promotes a stem cell-like phenotype in human colorectal carcinoma cells. *Br. J. Cancer* **101**, 320–326 (2009).

148. Motegi, H., Kamoshima, Y., Terasaka, S., Kobayashi, H. & Houkin, K. Type 1 collagen as a potential niche component for CD133-positive glioblastoma cells. *Neuropathology* **34**, 378–385 (2014).

149. Lambert, A. W. *et al.* Tumor Cell-Derived Periostin Regulates Cytokines That Maintain Breast Cancer Stem Cells. (2016) doi:10.1158/1541-7786.MCR-15-0079.

150. Curry, J. M. *et al.* The use of a novel MUC1 antibody to identify cancer stem cells and circulating MUC1 in mice and patients with pancreatic cancer. *J. Surg. Oncol.* **107**, 713–722 (2013).

151. Du, W. W. *et al.* The role of versican in modulating breast cancer cell self-renewal. *Mol. Cancer Res.* **11**, 443–455 (2013).

152. Begum, A. *et al.* The extracellular matrix and focal adhesion kinase signaling regulate cancer stem cell function in pancreatic ductal adenocarcinoma. (2017) doi:10.1371/journal.pone.0180181.

153. Nie, S. *et al.* Tenascin-C: A Novel Candidate Marker for Cancer Stem Cells in Glioblastoma Identified by Tissue Microarrays. (2014) doi:10.1021/pr5008653.

154. Fukunaga-Kalabis, M. *et al.* Tenascin-C promotes melanoma progression by maintaining the ABCB5-positive side population. *Oncogene* **29**, 6115–6124 (2010).

155. Zhou, W. *et al.* Periostin secreted by glioblastoma stem cells recruits M2 tumour-associated macrophages and promotes malignant growth. *Nat. Cell Biol.* **17**, 170–182 (2015).

156. Mikheev, A. M. *et al.* Periostin is a novel therapeutic target that predicts and regulates glioma malignancy. *Neuro-Oncol.* **17**, 372–382 (2015).

157. Wang, X. *et al.* Periostin Contributes to the Acquisition of Multipotent Stem Cell-Like Properties in Human Mammary Epithelial Cells and Breast Cancer Cells. *PLoS ONE* **8**, e72962–e72962 (2013).

158. Stroopinsky, D. *et al.* MUC1 IS A POTENTIAL TARGET FOR THE TREATMENT OF ACUTE MYELOID LEUKEMIA STEM CELLS. doi:10.1158/0008-5472.CAN-13-0677.

159. Engelmann, K., Shen, H. & Finn, O. J. MCF7 side population cells with characteristics of cancer stem/progenitor cells express the tumor antigen MUC1. *Cancer Res.* **68**, 2419–2426 (2008).

160. Malanchi, I. *et al.* Interactions between cancer stem cells and their niche govern metastatic colonization. *Nature* **481**, 85–91 (2012).

161. Januchowski, R. *et al.* Increased Expression of Several Collagen Genes is Associated with Drug Resistance in Ovarian Cancer Cell Lines. *J. Cancer* **7**, 1295–1310 (2016).

162. Okuda, H. *et al.* Hyaluronan synthase HAS2 promotes tumor progression in bone by stimulating the interaction of breast cancer stem-like cells with macrophages and stromal cells. *Cancer Res.* **72**, 537–547 (2012).

163. Fang, D. D. *et al.* Expansion of CD133+ colon cancer cultures retaining stem cell properties to enable cancer stem cell target discovery. *Br. J. Cancer* **102**, 1265–1275 (2010).

164. Oktem, G. *et al.* Cancer stem cell differentiation: TGFβ1 and versican may trigger molecules for the organization of tumor spheroids. *Oncol. Rep.* **32**, 641–649 (2014).

165. Oskarsson, T. *et al.* Breast cancer cells produce tenascin C as a metastatic niche component to colonize the lungs. *Nat. Med.* (2011) doi:10.1038/nm.2379.

166. Liu, B., Xu, T., Xu, X., Cui, Y. & Xing, X. Biglycan promotes the chemotherapy resistance of colon cancer by activating NF-κB signal transduction. *Mol. Cell. Biochem.* **449**, 285–294 (2018).

167. Spaeth, E. L. *et al.* Mesenchymal Stem Cell Transition to Tumor-Associated Fibroblasts Contributes to Fibrovascular Network Expansion and Tumor Progression. *PLoS ONE* **4**, e4992–e4992 (2009).

168. Lim, E.-J., Suh, Y., Kim, S., Kang, S.-G. & Lee, S.-J. Force-mediated proinvasive matrix remodeling driven by tumor-associated mesenchymal stem-like cells in glioblastoma. *BMB Rep.* **51**, 182–187 (2018).

169. Cavarretta, I. T. *et al.* Adipose Tissue–derived Mesenchymal Stem Cells Expressing Prodrug-converting Enzyme Inhibit Human Prostate Tumor Growth. (2010) doi:10.1038/mt.2009.237.

170. Yeung, T.-L. *et al.* TGF-β modulates ovarian cancer invasion by upregulating CAF-derived versican in the tumor microenvironment. *Cancer Res.* **73**, 5016–5028 (2013).

171. Li, M. *et al.* Microenvironment remodeled by tumor and stromal cells elevates fibroblast-derived COL1A1 and facilitates ovarian cancer metastasis. *Exp. Cell Res.* **394**, 112153 (2020).

172. Gaggioli, C. *et al.* Fibroblast-led collective invasion of carcinoma cells with differing roles for RhoGTPases in leading and following cells. *Nat. Cell Biol.* **9**, 1392–1400 (2007).

173. Hooper, S., Gaggioli, C. & Sahai, E. A chemical biology screen reveals a role for Rab21-mediated control of actomyosin contractility in fibroblast-driven cancer invasion. *Br. J. Cancer* **102**, 392–402 (2010).

174. Albig, A. R., Roy, T. G., Becenti, D. J. & Schiemann, W. P. Transcriptome analysis of endothelial cell gene expression induced by growth on matrigel matrices: identification and characterization of MAGP-2 and lumican as novel regulators of angiogenesis. *Angiogenesis* **10**, 197–216 (2007).

175. Barry-Hamilton, V. *et al.* Allosteric inhibition of lysyl oxidase-like-2 impedes the development of a pathologic microenvironment. *Nat. Med.* **16**, 1009–1017 (2010).

176. Hildenbrand, R., Dilger, I., Hörlin, A. & Stutte, H. J. Urokinase and macrophages in tumour angiogenesis. *Br. J. Cancer* **72**, 818–823 (1995).

177. Solinas, G. *et al.* Tumor-Conditioned Macrophages Secrete Migration-Stimulating Factor: A New Marker for M2-Polarization, Influencing Tumor Cell Motility. *J. Immunol.* **185**, 642–652 (2010).

178. Steitz, A. M. *et al.* Tumor-associated macrophages promote ovarian cancer cell migration by secreting transforming growth factor beta induced (TGFBI) and tenascin C. *Cell Death Dis.* **11**, 1–15 (2020).

179. Murphy, G. The ADAMs: Signalling scissors in the tumour microenvironment. *Nat. Rev. Cancer* **8**, 929–941 (2008).

180. Wai, P. Y. & Kuo, P. C. Osteopontin: regulation in tumor metastasis. (2007) doi:10.1007/s10555-007-9104-9.

181. Arnold, S. A. *et al.* Lack of host SPARC enhances vascular function and tumor spread in an orthotopic murine model of pancreatic carcinoma. *DMM Dis. Models Mech.* **3**, 57–72 (2010).

182. Agrawal, S. *et al.* Dystroglycan is selectively cleaved at the parenchymal basement membrane at sites of leukocyte extravasation in experimental autoimmune encephalomyelitis. *J. Exp. Med.* **203**, 1007–1016 (2006).

183. Campo-Verde-Arbocco, F. *et al. Human renal adipose tissue induces the invasion and progression of renal cell carcinoma*. www.impactjournals.com/oncotarget (2017).

184. Ribeiro, R. *et al. Human periprostatic adipose tissue promotes prostate cancer aggressiveness in vitro*. vol. 31 32–32 http://www.jeccr.com/content/31/1/32 (2012).

185. Park, J. & Scherer, P. E. Adipocyte-derived endotrophin promotes malignant tumor progression. *J. Clin. Invest.* **122**, 4243–4256 (2012).

186. Iyengar, P. *et al.* Adipocyte-derived collagen VI affects early mammary tumor progression in vivo, demonstrating a critical interaction in the tumor/stroma microenvironment. *J. Clin. Invest.* **115**, 1163–1176 (2005).

187. Kenny, H. A. *et al.* Mesothelial cells promote early ovarian cancer metastasis through fibronectin secretion. *J. Clin. Invest.* **124**, 4614–4628 (2014).

188. Natarajan, S. *et al.* Collagen Remodeling in the Hypoxic Tumor-Mesothelial Niche Promotes Ovarian Cancer Metastasis. *Cancer Res* **79**, 2271–2284 (2019).

189. Pickup, M. W. *et al.* Stromally derived lysyl oxidase promotes metastasis of transforming growth factor-β-deficient mouse mammary carcinomas. *Cancer Res.* **73**, 5336–5346 (2013).

190. Condamine, T., Ramachandran, I., Youn, J.-I. & Gabrilovich, D. I. Regulation of Tumor Metastasis by Myeloid-Derived Suppressor Cells. *Annu. Rev. Med.* **66**, 97–110 (2015).

191. Yang, L. *et al.* Abrogation of TGFβ Signaling in Mammary Carcinomas Recruits Gr-1+CD11b+ Myeloid Cells that Promote Metastasis. *Cancer Cell* **13**, 23–35 (2008).

192. Pahler, J. C. *et al.* Plasticity in tumor-promoting inflammation: Impairment of macrophage recruitment evokes a compensatory neutrophil response. *Neoplasia* **10**, 329–339 (2008).

193. Nozawa, H., Chiu, C. & Hanahan, D. Infiltrating neutrophils mediate the initial angiogenic switch in a mouse model of multistage carcinogenesis. *Proc. Natl. Acad. Sci. U. S. A.* **103**, 12493–12498 (2006).

194. Mellor, A. L. & Munn, D. H. IDO expression by dendritic cells: Tolerance and tryptophan catabolism. *Nat. Rev. Immunol.* **4**, 762–774 (2004).

195. De Visser, K. E., Korets, L. V. & Coussens, L. M. De novo carcinogenesis promoted by chronic inflammation is B lymphocyte dependent. *Cancer Cell* **7**, 411–423 (2005).

196. Senthebane, D. A. *et al.* The Role of Tumor Microenvironment in Chemoresistance: To Survive, Keep Your Enemies Closer. *Int. J. Mol. Sci.* **18**, (2017).

197. Dzobo, K. Taking a Full Snapshot of Cancer Biology: Deciphering the Tumor Microenvironment for Effective Cancer Therapy in the Oncology Clinic. *Omics J. Integr. Biol.* **24**, 175–179 (2020).

198. Novak, C., Horst, E. & Mehta, G. Review: Mechanotransduction in ovarian cancer: Shearing into the unknown. *APL Bioeng.* **2**, 031701 (2018).

199. Hinshaw, D. C. & Shevde, L. A. The Tumor Microenvironment Innately Modulates Cancer Progression. *Cancer Res.* **79**, 4557–4566 (2019).

200. Eble, J. A. & Niland, S. The extracellular matrix in tumor progression and metastasis. *Clin. Exp. Metastasis* **36**, 171–198 (2019).

201. Dzobo, K. *et al.* Not Everyone Fits the Mold: Intratumor and Intertumor Heterogeneity and Innovative Cancer Drug Design and Development. *OMICS J. Integr. Biol.* **22**, 17–34 (2018).

202. Paszek, M. J. & Weaver, V. M. The tension mounts: mechanics meets morphogenesis and malignancy. *J. Mammary Gland Biol. Neoplasia* **9**, 325–342 (2004).

203. Zhao, Y. *et al.* Losartan treatment enhances chemotherapy efficacy and reduces ascites in ovarian cancer models by normalizing the tumor stroma. *Proc. Natl. Acad. Sci. U. S. A.* **116**, 2210–2219 (2019).

204. Kopper, O. *et al.* An organoid platform for ovarian cancer captures intra- and interpatient heterogeneity. *Nat. Med.* **25**, 838–849 (2019).

205. Patch, A.-M. *et al.* Whole–genome characterization of chemoresistant ovarian cancer. *Nature* **521**, 489–494 (2015).

206. Scott, C. L., Becker, M. A., Haluska, P. & Samimi, G. Patient-derived xenograft models to improve targeted therapy in epithelial ovarian cancer treatment. *Front. Oncol.* **3**, 295 (2013).

207. Ricci, F., Broggini, M. & Damia, G. Revisiting ovarian cancer preclinical models: implications for a better management of the disease. *Cancer Treat. Rev.* **39**, 561–568 (2013).

208. Lengyel, E. *et al.* Epithelial ovarian cancer experimental models. *Oncogene* **33**, 3619–3633 (2014).

209. Yang, H., Sun, L., Liu, M. & Mao, Y. Patient-derived organoids: a promising model for personalized cancer treatment. *Gastroenterol. Rep.* **6**, 243–245 (2018).

210. Ben-David, U. *et al.* Patient-derived xenografts undergo mouse-specific tumor evolution. *Nat. Genet.* **49**, 1567–1575 (2017).

211. Vandamme, T. F. Use of rodents as models of human diseases. *J. Pharm. Bioallied Sci.* **6**, 2–9 (2014).

212. Magnotti, E. & Marasco, W. A. The latest animal models of ovarian cancer for novel drug discovery. *Expert Opin. Drug Discov.* **13**, 249–257 (2018).

213. Raghavan, S. *et al.* Carcinoma-Associated Mesenchymal Stem Cells Promote Chemoresistance in Ovarian Cancer Stem Cells via PDGF Signaling. *Cancers Basel* **12**, (2020).

214. Lengyel, E. Ovarian Cancer Development and Metastasis. *Am. J. Pathol.* **177**, 1053–1064 (2010).

215. Fogg, K. C. *et al.* Ovarian Cells Have Increased Proliferation in Response to Heparin-Binding Epidermal Growth Factor as Collagen Density Increases. *Tissue Eng. Part A* **26**, 747–758 (2020).

216. Shoval, H. *et al.* Tumor cells and their crosstalk with endothelial cells in 3D spheroids. *Sci. Rep.* **7**, 10428 (2017).

217. Shishido, A. *et al.* Mesothelial cells facilitate cancer stem-like properties in spheroids of ovarian cancer cells. *Oncol. Rep.* **40**, 2105- (2018).

218. Hill, S. J. *et al.* Prediction of DNA Repair Inhibitor Response in Short Term Patient-Derived Ovarian Cancer Organoids. *Cancer Discov.* CD-18-0474 (2018) doi:10.1158/2159-8290.CD-18-0474.

219. Phan, N. *et al.* A simple high-throughput approach identifies actionable drug sensitivities in patient-derived tumor organoids. *Commun. Biol.* **2**, 78 (2019).

220. Maru, Y. & Hippo, Y. Current Status of Patient-Derived Ovarian Cancer Models. *Cells* **8**, 505 (2019).

221. Stock, K. *et al.* Capturing tumor complexity in vitro : Comparative analysis of 2D and 3D tumor models for drug discovery. *Sci. Rep.* **6**, 28951 (2016).

222. Petersen, O. W., Rønnov-Jessen, L., Weaver, V. M. & Bissell, M. J. Differentiation and cancer in the mammary gland: shedding light on an old dichotomy. *Adv. Cancer Res.* **75**, 135–161 (1998).

223. Acerbi, I. *et al.* Human breast cancer invasion and aggression correlates with ECM stiffening and immune cell infiltration. *Integr. Biol.* **7**, 1120–1134 (2015).

224. Cho, A., Howell, V. M. & Colvin, E. K. The Extracellular Matrix in Epithelial Ovarian Cancer – A Piece of a Puzzle. *Front. Oncol.* **5**, (2015).

225. Govindarajan, M., Wohlmuth, C., Waas, M., Bernardini, M. Q. & Kislinger, T. High-throughput approaches for precision medicine in high-grade serous ovarian cancer. *J. Hematol. Oncol.J Hematol Oncol* **13**, 134 (2020).

226. Zhang, Y. *et al.* Loss of BMP signaling through BMPR1A in osteoblasts leads to greater collagen cross-link maturation and material-level mechanical properties in mouse femoral trabecular compartments. *Bone* **88**, 74–84 (2016).

227. Verhaak, R. G. W. *et al.* Prognostically relevant gene signatures of high-grade serous ovarian carcinoma. *J. Clin. Invest.* **123**, 517–525 (2013).

228. Konecny, G. E., Winterhoff, B. & Wang, C. Gene-expression signatures in ovarian cancer: Promise and challenges for patient stratification. *Gynecol. Oncol.* **141**, 379–385 (2016).

229. Tothill, R. W. *et al.* Novel molecular subtypes of serous and endometrioid ovarian cancer linked to clinical outcome. *Clin. Cancer Res. Off. J. Am. Assoc. Cancer Res.* **14**, 5198–5208 (2008).

230. Kommoss, S. *et al.* Bevacizumab May Differentially Improve Ovarian Cancer Outcome in Patients with Proliferative and Mesenchymal Molecular Subtypes. *Clin. Cancer Res. Off. J. Am. Assoc. Cancer Res.* **23**, 3794–3801 (2017).

231. Konecny, G. E. *et al.* Prognostic and Therapeutic Relevance of Molecular Subtypes in High-Grade Serous Ovarian Cancer. *JNCI J. Natl. Cancer Inst.* **106**, (2014).

232. Tan, T. Z. *et al.* Functional genomics identifies five distinct molecular subtypes with clinical relevance and pathways for growth control in epithelial ovarian cancer. *EMBO Mol. Med.* **5**, 1051–1066 (2013).

233. Leong, H. S. *et al.* Efficient molecular subtype classification of high-grade serous ovarian cancer. *J. Pathol.* **236**, 272–277 (2015).

234. Palmirotta, R., Silvestris, E., D'Oronzo, S., Cardascia, A. & Silvestris, F. Ovarian cancer: Novel molecular aspects for clinical assessment. *Crit. Rev. Oncol. Hematol.* **117**, 12–29 (2017).

235. Schwede, M. *et al.* The Impact of Stroma Admixture on Molecular Subtypes and Prognostic Gene Signatures in Serous Ovarian Cancer. *Cancer Epidemiol. Prev. Biomark.* **29**, 509–519 (2020).

236. Zhang, Q., Wang, C. & Cliby, W. A. Cancer-associated stroma significantly contributes to the mesenchymal subtype signature of serous ovarian cancer. *Gynecol. Oncol.* **152**, 368–374 (2019).

237. Liu, R., Hu, R., Zeng, Y., Zhang, W. & Zhou, H.-H. Tumour immune cell infiltration and survival after platinum-based chemotherapy in high-grade serous ovarian cancer subtypes: A gene expression-based computational study. *EBioMedicine* **51**, 102602 (2020).

238. Adam, G. *et al.* Machine learning approaches to drug response prediction: challenges and recent progress. *Npj Precis. Oncol.* **4**, 1–10 (2020).

239. Piccart, M. J. *et al.* Randomized intergroup trial of cisplatin-paclitaxel versus cisplatin-cyclophosphamide in women with advanced epithelial ovarian cancer: three-year results. *J. Natl. Cancer Inst.* **92**, 699–708 (2000).

240. Kemp, Z. & Ledermann, J. Update on first-line treatment of advanced ovarian carcinoma. *Int. J. Womens Health* **5**, 45–51 (2013).

241. Bois, A. du, Neijt, J. P. & Thigpen, J. T. First line chemotherapy with carboplatin plus paclitaxel in advanced ovarian cancer - a new standard of care? *Ann. Oncol.* **10**, S35–S41 (1999).

242. Agarwal, R. & Kaye, S. B. Ovarian cancer: strategies for overcoming resistance to chemotherapy. *Nat. Rev. Cancer* **3**, 502–516 (2003).

243. Wang, L., Xu, T. & Cui, M. Are ovarian cancer stem cells the target for innovative immunotherapy? *OncoTargets Ther.* **11**, 2615–2626 (2018).

244. Konstantinopoulos, P. A., Spentzos, D. & Cannistra, S. A. Gene-expression profiling in epithelial ovarian cancer. *Nat. Clin. Pract. Oncol.* **5**, 577–587 (2008).

245. Hickman, J. A. *et al.* Three-dimensional models of cancer for pharmacology and cancer cell biology: capturing tumor complexity in vitro/ex vivo. *Biotechnol. J.* **9**, 1115–1128 (2014).

246. Cunnea, P. Modeling Platinum Sensitive and Resistant High-Grade Serous Ovarian Cancer: Development and Applications of Experimental Systems. *Front. Oncol.* **4**, 1–8 (2014).

247. Harrison, H. *et al.* Regulation of breast cancer stem cell activity by signaling through the Notch4 receptor. *Cancer Res.* **70**, 709–718 (2010).

248. Nagata, S., Hirano, K., Kanemori, M., Sun, L.-T. & Tada, T. Self-renewal and pluripotency acquired through somatic reprogramming to human cancer stem cells. *PloS One* **7**, e48699 (2012).

249. Wu, C. & Alman, B. A. Side population cells in human cancers. *Cancer Lett.* **268**, 1–9 (2008).

250. Louie, E. *et al.* Identification of a stem-like cell population by exposing metastatic breast cancer cell lines to repetitive cycles of hypoxia and reoxygenation. *Breast Cancer Res. BCR* **12**, R94 (2010).

251. Alvero, A. B. *et al.* Molecular phenotyping of human ovarian cancer stem cells unravel the mechanisms for repair and chemo-resistance. *Cell Cycle Georget. Tex* **8**, 158–166 (2009).

252. Houghton, J. A. & Taylor, D. M. Growth characteristics of human colorectal tumours during serial passage in immune-deprived mice. *Br. J. Cancer* **37**, 213–223 (1978).

253. Raghavan, S. *et al.* Comparative analysis of tumor spheroid generation techniques for differential in vitro drug toxicity. *Oncotarget* **7**, 16948–16961 (2016).

254. Raghavan, S. *et al.* Formation of stable small cell number three-dimensional ovarian cancer spheroids using hanging drop arrays for preclinical drug sensitivity assays. *Gynecol. Oncol.* **138**, 181–189 (2015).

255. Mehta, G., Hsiao, A. Y., Ingram, M., Luker, G. D. & Takayama, S. Opportunities and challenges for use of tumor spheroids as models to test drug delivery and efficacy. *J. Controlled Release* **164**, 192–204 (2012).

256. Loessner, D., Flegg, J. A., Byrne, H. M., Clements, J. A. & Hutmacher, D. W. Growth of confined cancer spheroids: a combined experimental and mathematical modelling approach. *Integr. Biol. Quant. Biosci. Nano Macro* **5**, 597–605 (2013).

257. Fornari, C. *et al.* A Mathematical-Biological Joint Effort to Investigate the Tumor-Initiating Ability of Cancer Stem Cells. *PLOS ONE* **9**, e106193 (2014).

258. Molina-Peña, R. & Álvarez, M. M. A Simple Mathematical Model Based on the Cancer Stem Cell Hypothesis Suggests Kinetic Commonalities in Solid Tumor Growth. *PLOS ONE* **7**, e26233 (2012).

259. Weekes, S. L. *et al.* A multicompartment mathematical model of cancer stem cell-driven tumor growth dynamics. *Bull. Math. Biol.* **76**, 1762–1782 (2014).

260. Pearson, A. *et al.* Sampling from single-cell observations to predict tumor cell growth in-vitro and in-vivo. *Oncotarget* (2017) doi:10.18632/oncotarget.22693.

261. Chefetz, I. *et al.* A Pan-ALDH1A Inhibitor Induces Necroptosis in Ovarian Cancer Stem-like Cells. *Cell Rep.* **26**, 3061-3075.e6 (2019).

262. Hu, Y. & Smyth, G. K. ELDA: extreme limiting dilution analysis for comparing depleted and enriched populations in stem cell and other assays. *J. Immunol. Methods* **347**, 70–78 (2009).

263. Gu, Z., Eils, R. & Schlesner, M. Complex heatmaps reveal patterns and correlations in multidimensional genomic data. *Bioinforma. Oxf. Engl.* **32**, 2847–2849 (2016).

264. Stewart, J. *et al.* Analysis of wntless (WLS) expression in gastric, ovarian, and breast cancers reveals a strong association with HER2 overexpression. *Mod. Pathol.* **28**, 428–436 (2015).

265. Valkenburg, K. C., Graveel, C. R., Zylstra-Diegel, C. R., Zhong, Z. & Williams, B. O. Wnt/β-catenin Signaling in Normal and Cancer Stem Cells. *Cancers* **3**, 2050–2079 (2011).

266. Meng, E. *et al.* ALDH1A1 Maintains Ovarian Cancer Stem Cell-Like Properties by Altered Regulation of Cell Cycle Checkpoint and DNA Repair Network Signaling. *PLoS ONE* **9**, (2014).

267. Huang, P. *et al.* BMP-2 induces EMT and breast cancer stemness through Rb and CD44. *Cell Death Discov.* **3**, 17039 (2017).

268. De Sousa e Melo, F. & Vermeulen, L. Wnt Signaling in Cancer Stem Cell Biology. *Cancers* **8**, 60 (2016).

269. Vangipuram, S. D., Buck, S. A. & Lyman, W. D. Wnt pathway activity confers chemoresistance to cancer stem-like cells in a neuroblastoma cell line. *Tumour Biol. J. Int. Soc. Oncodevelopmental Biol. Med.* **33**, 2173–2183 (2012).

270. Peche, L. Y. *et al.* Human MageB2 Protein Expression Enhances E2F Transcriptional Activity, Cell Proliferation, and Resistance to Ribotoxic Stress. *J. Biol. Chem.* **290**, 29652–29662 (2015).

271. Weon, J. L. & Potts, P. R. The MAGE protein family and cancer. *Curr. Opin. Cell Biol.* **37**, 1–8 (2015).

272. Zhang, Y., Zhang, R., Ding, X. & Ai, K. EFNB2 acts as the target of miR-557 to facilitate cell proliferation, migration and invasion in pancreatic ductal adenocarcinoma by bioinformatics analysis and verification. *Am. J. Transl. Res.* **10**, 3514–3528 (2018).

273. Bergeron, S. *et al.* The serine protease inhibitor serpinE2 is a novel target of ERK signaling involved in human colorectal tumorigenesis. *Mol. Cancer* **9**, 271 (2010).

274. Buchholz, M. *et al.* SERPINE2 (Protease Nexin I) Promotes Extracellular Matrix Production and Local Invasion of Pancreatic Tumors in Vivo. *Cancer Res.* **63**, 4945–4951 (2003).

275. Stępień, T. *et al.* Elevated Concentrations of SERPINE2/Protease Nexin-1 and Secretory Leukocyte Protease Inhibitor in the Serum of Patients with Papillary Thyroid Cancer.

Disease Markers https://www.hindawi.com/journals/dm/2017/4962137/ (2017) doi:10.1155/2017/4962137.

276. Vaillant, C. *et al.* Serpine2/PN-1 Is Required for Proliferative Expansion of Pre-Neoplastic Lesions and Malignant Progression to Medulloblastoma. *PLoS ONE* **10**, (2015).
277. Yang, Y., Xin, X., Fu, X. & Xu, D. Expression pattern of human SERPINE2 in a variety of human tumors. *Oncol. Lett.* **15**, 4523–4530 (2018).
278. Holtz, A. M. *et al.* Secreted HHIP1 interacts with heparan sulfate and regulates Hedgehog ligand localization and function. *J. Cell Biol.* **209**, 739–758 (2015).
279. Chen, Q., Gao, G. & Luo, S. Hedgehog signaling pathway and ovarian cancer. *Chin. J. Cancer Res.* **25**, 346–353 (2013).
280. Szkandera, J., Kiesslich, T., Haybaeck, J., Gerger, A. & Pichler, M. Hedgehog Signaling Pathway in Ovarian Cancer. *Int. J. Mol. Sci.* **14**, 1179–1196 (2013).
281. Pang, L. Y., Hurst, E. A. & Argyle, D. J. Cyclooxygenase-2: A Role in Cancer Stem Cell Survival and Repopulation of Cancer Cells during Therapy. *Stem Cells International* https://www.hindawi.com/journals/sci/2016/2048731/ (2016) doi:10.1155/2016/2048731.
282. Sun, H. *et al.* COX-2 expression in ovarian cancer: an updated meta-analysis. *Oncotarget* **8**, 88152–88162 (2017).
283. Uddin, S. *et al.* Cyclooxygenase-2 inhibition inhibits PI3K/AKT kinase activity in epithelial ovarian cancer. *Int. J. Cancer* **126**, 382–394 (2010).
284. Wang, D., Xia, D. & DuBois, R. N. The Crosstalk of PTGS2 and EGF Signaling Pathways in Colorectal Cancer. *Cancers* **3**, 3894–3908 (2011).
285. Mohammed, M. K. *et al.* Wnt/β-catenin signaling plays an ever-expanding role in stem cell self-renewal, tumorigenesis and cancer chemoresistance. *Genes Dis.* **3**, 11–40 (2016).

286. Clark, D. W. & Palle, K. Aldehyde dehydrogenases in cancer stem cells: potential as therapeutic targets. *Ann. Transl. Med.* **4**, (2016).

287. Croker, A. K. *et al.* Differential Functional Roles of ALDH1A1 and ALDH1A3 in Mediating Metastatic Behavior and Therapy Resistance of Human Breast Cancer Cells. *Int. J. Mol. Sci.* **18**, (2017).

288. Xu, H. *et al.* CXCR2 promotes breast cancer metastasis and chemoresistance via suppression of AKT1 and activation of COX2. *Cancer Lett.* **412**, 69–80 (2018).

289. Zhang, T. *et al.* Core signaling pathways in ovarian cancer stem cell revealed by integrative analysis of multi-marker genomics data. *PLOS ONE* **13**, e0196351 (2018).

290. Bao, B., Azmi, A. S., Ali, S., Zaiem, F. & Sarkar, F. H. Metformin may function as anti-cancer agent via targeting cancer stem cells: the potential biological significance of tumor-associated miRNAs in breast and pancreatic cancers. *Ann. Transl. Med.* **2**, 59 (2014).

291. Hirsch, H. A., Iliopoulos, D., Tsichlis, P. N. & Struhl, K. Metformin selectively targets cancer stem cells, and acts together with chemotherapy to block tumor growth and prolong remission. *Cancer Res.* **69**, 7507–7511 (2009).

292. Shank, J. J. *et al.* Metformin targets ovarian cancer stem cells in vitro and in vivo. *Gynecol. Oncol.* **127**, 390–397 (2012).

293. Bapat, S. A., Mali, A. M., Koppikar, C. B. & Kurrey, N. K. Stem and progenitor-like cells contribute to the aggressive behavior of human epithelial ovarian cancer. *Cancer Res.* **65**, 3025–3029 (2005).

294. Steffensen, K. D. *et al.* Prevalence of epithelial ovarian cancer stem cells correlates with recurrence in early-stage ovarian cancer. *J. Oncol.* (2011) doi:10.1155/2011/620523.

295. Okamoto, A. *et al.* Indoleamine 2,3-Dioxygenase Serves as a Marker of Poor Prognosis in Gene Expression Profiles of Serous Ovarian Cancer Cells. *Clin. Cancer Res.* **11**, 6030–6039 (2005).

296. Stewart, J. M. *et al.* Phenotypic heterogeneity and instability of human ovarian tumor-initiating cells. *Proc. Natl. Acad. Sci. U. S. A.* **108**, 6468–6473 (2011).

297. Helland, Ø. *et al.* First in-mouse development and application of a surgically relevant xenograft model of ovarian carcinoma. *PLoS ONE* **9**, (2014).

298. Dobbin, Z. C. *et al.* Using heterogeneity of the patient-derived xenograft model to identify the chemoresistant population in ovarian cancer. *Oncotarget* **5**, 8750–8764 (2014).

299. Hirschhaeuser, F. *et al.* Multicellular tumor spheroids: An underestimated tool is catching up again. *J. Biotechnol.* **148**, 3–15 (2010).

300. Friedrich, J., Seidel, C., Ebner, R. & Kunz-Schughart, L. A. Spheroid-based drug screen: Considerations and practical approach. *Nat. Protoc.* **4**, 309–324 (2009).

301. Dontu, G. *et al.* In vitro propagation and transcriptional profiling of human mammary stem/progenitor cells. *Genes Dev.* **17**, 1253–1270 (2003).

302. Chen, S.-F. *et al.* Nonadhesive culture system as a model of rapid sphere formation with cancer stem cell properties. *PLoS ONE* **7**, (2012).

303. Cojoc, M. *et al.* Aldehyde Dehydrogenase Is Regulated by β-Catenin/TCF and Promotes Radioresistance in Prostate Cancer Progenitor Cells. *Cancer Res.* **75**, 1482–1494 (2015).

304. Tanei, T. *et al.* Association of breast cancer stem cells identified by aldehyde dehydrogenase 1 expression with resistance to sequential paclitaxel and epirubicin-based chemotherapy for breast cancers. *Clin. Cancer Res.* **15**, 4234–4241 (2009).

305. Luvero, D., Milani, A. & Ledermann, J. A. Treatment options in recurrent ovarian cancer: latest evidence and clinical potential. *Ther. Adv. Med. Oncol.* **6**, 229–239 (2014).

306. Lee, J. O. *et al.* Metformin overcomes resistance to cisplatin in triple-negative breast cancer (TNBC) cells by targeting RAD51. *Breast Cancer Res.* **21**, 115 (2019).

307. Hu, L., McArthur, C. & Jaffe, R. B. Ovarian cancer stem-like side-population cells are tumourigenic and chemoresistant. *Br. J. Cancer* **102**, 1276–1283 (2010).

308. Lin, L. *et al.* STAT3 is necessary for proliferation and survival in colon cancer-initiating cells. *Cancer Res.* **71**, 7226–7237 (2011).

309. Wang, L. *et al.* BMP-2 inhibits the tumorigenicity of cancer stem cells in human osteosarcoma OS99-1 cell line. *Cancer Biol. Ther.* **11**, 457–463 (2011).

310. Dhawan, A. *et al.* Mathematical modelling of phenotypic plasticity and conversion to a stem-cell state under hypoxia. *Sci. Rep.* **6**, (2016).

311. Wallace, D. & Guo, X. Properties of Tumor Spheroid Growth Exhibited by Simple Mathematical Models. *Front. Oncol.* **3**, (2013).

312. Däster, S. *et al.* Induction of hypoxia and necrosis in multicellular tumor spheroids is associated with resistance to chemotherapy treatment. *Oncotarget* **8**, 1725–1736 (2016).

313. Enderling, H. Cancer stem cells: Small subpopulation or evolving fraction? *Integr. Biol. U. K.* **7**, 14–23 (2015).

314. Bai, S. *et al.* EGFL6 regulates the asymmetric division, maintenance and metastasis of ALDH+ ovarian cancer cells. *Cancer Res.* **76**, 6396–6409 (2016).

315. Jia, L.-Y. *et al.* Anti-Proliferation Effect of Theasaponin E1 on the ALDH-Positive Ovarian Cancer Stem-Like Cells. *Mol. J. Synth. Chem. Nat. Prod. Chem.* **23**, (2018).

316. Foo, J. & Michor, F. Evolution of resistance to anti-cancer therapy during general dosing schedules. *J. Theor. Biol.* **263**, 179–188 (2010).

317. Werner, B. *et al.* The cancer stem cell fraction in hierarchically organized tumors can be estimated using mathematical modeling and patient-specific treatment trajectories. *Cancer Res.* **76**, 1705–1713 (2016).

318. Nazari, F., Pearson, A. T., Nör, J. E. & Jackson, T. L. A mathematical model for IL-6-mediated, stem cell driven tumor growth and targeted treatment. *PLOS Comput. Biol.* **14**, e1005920 (2018).

319. Enderling, H., Chaplain, M. A. J., Anderson, A. R. A. & Vaidya, J. S. A mathematical model of breast cancer development, local treatment and recurrence. *J. Theor. Biol.* **246**, 245–259 (2007).

320. Parra-Guillen, Z. P., Berraondo, P., Grenier, E., Ribba, B. & Troconiz, I. F. Mathematical model approach to describe tumour response in mice after vaccine administration and its applicability to immune-stimulatory cytokine-based strategies. *AAPS J.* **15**, 797–807 (2013).

321. Xie, X. *et al.* A Comprehensive Model for Predicting Recurrence and Survival in Cases of Chinese Postoperative Invasive Breast Cancer. *Asian Pac. J. Cancer Prev. APJCP* **18**, 727–733 (2017).

322. Mehta, P., Novak, C., Raghavan, S., Ward, M. & Mehta, G. Self-Renewal and CSCs In Vitro Enrichment: Growth as Floating Spheres. *Methods Mol. Biol. Clifton NJ* **1692**, 61–75 (2018).

323. Love, M. I., Huber, W. & Anders, S. Moderated estimation of fold change and dispersion for RNA-seq data with DESeq2. *Genome Biol.* **15**, 550 (2014).

324. Durinck, S., Spellman, P. T., Birney, E. & Huber, W. Mapping Identifiers for the Integration of Genomic Datasets with the R/Bioconductor package biomaRt. *Nat. Protoc.* **4**, 1184–1191 (2009).

325. Tomasetti, C. & Levy, D. Role of symmetric and asymmetric division of stem cells in developing drug resistance. *Proc. Natl. Acad. Sci.* **107**, 16766–16771 (2010).

326. Pulaski, H. L. *et al.* Identifying alemtuzumab as an anti-myeloid cell antiangiogenic therapy for the treatment of ovarian cancer. *J. Transl. Med.* **7**, 49 (2009).

327. Banerjee, S. & Kaye, S. B. New strategies in the treatment of ovarian cancer: current clinical perspectives and future potential. *Clin. Cancer Res. Off. J. Am. Assoc. Cancer Res.* **19**, 961–968 (2013).

328. Hu, Z. *et al.* The Repertoire of Serous Ovarian Cancer Non-genetic Heterogeneity Revealed by Single-Cell Sequencing of Normal Fallopian Tube Epithelial Cells. *Cancer Cell* **37**, 226-242.e7 (2020).

329. Lisio, M.-A., Fu, L., Goyeneche, A., Gao, Z. & Telleria, C. High-Grade Serous Ovarian Cancer: Basic Sciences, Clinical and Therapeutic Standpoints. *Int. J. Mol. Sci.* **20**, 952 (2019).

330. Baci, D. *et al.* The Ovarian Cancer Tumor Immune Microenvironment (TIME) as Target for Therapy: A Focus on Innate Immunity Cells as Therapeutic Effectors. *Int. J. Mol. Sci.* **21**, 3125 (2020).

331. Torre, L. A. *et al.* Ovarian cancer statistics, 2018. *CA. Cancer J. Clin.* **68**, 284–296 (2018).

332. Street, W. Cancer Facts & Figures 2020. 76 (1930).

333. Bell, D. *et al.* Integrated genomic analyses of ovarian carcinoma. *Nature* **474**, 609–615 (2011).

334. Al-Alem, L. F. *et al.* Ovarian cancer stem cells: What progress have we made? *Int. J. Biochem. Cell Biol.* **107**, 92–103 (2019).

335. Fessler, E., Borovski, T. & Medema, J. P. Endothelial cells induce cancer stem cell features in differentiated glioblastoma cells via bFGF. *Mol. Cancer* **14**, 157 (2015).

336. Lu, J. *et al.* Endothelial Cells Promote the Colorectal Cancer Stem Cell Phenotype Through a Soluble Form of Jagged-1. *Cancer Cell* **23**, 171–185 (2014).

337. McCoy, M. G. *et al.* Endothelial cells promote 3D invasion of GBM by IL-8-dependent induction of cancer stem cell properties. *Sci. Rep.* **9**, 9069 (2019).

338. McLean, K. *et al.* Human ovarian carcinoma–associated mesenchymal stem cells regulate cancer stem cells and tumorigenesis via altered BMP production. *J. Clin. Invest.* **121**, 3206–3219 (2011).

339. Ning, Y. *et al.* Co-culture of ovarian cancer stem-like cells with macrophages induced SKOV3 cells stemness via IL-8/STAT3 signaling. *Biomed. Pharmacother. Biomedecine Pharmacother.* **103**, 262–271 (2018).

340. McLean, K. *et al.* Leukemia Inhibitory Factor Functions in Parallel with Interleukin-6 to Promote Ovarian Cancer Growth. *Oncogene* **38**, 1576–1584 (2019).

341. Motohara, T., Yoshida, G. J. & Katabuchi, H. The hallmarks of ovarian cancer stem cells and niches: Exploring their harmonious interplay in therapy resistance. *Semin. Cancer Biol.* (2021) doi:10.1016/j.semcancer.2021.03.038.

342. Yin, M. *et al.* Tumor-Associated Macrophages (TAMs): A Critical Activator In Ovarian Cancer Metastasis. *OncoTargets Ther.* **12**, 8687–8699 (2019).

343. Gupta, V., Yull, F. & Khabele, D. Bipolar Tumor-Associated Macrophages in Ovarian Cancer as Targets for Therapy. *Cancers* **10**, 366 (2018).

344. Breslin, S. & O'Driscoll, L. Three-dimensional cell culture: the missing link in drug discovery. *Drug Discov. Today* **18**, 240–249 (2013).

345. Chen, J. *et al.* Observation of ovarian cancer stem cell behavior and investigation of potential mechanisms of drug resistance in three-dimensional cell culture. *J. Biosci. Bioeng.* **118**, 214–222 (2014).

346. S. Franco, S. *et al.* In vitro models of cancer stem cells and clinical applications. *BMC Cancer* **16**, 738 (2016).

347. Yang, Z. *et al.* Plasma cells shape the mesenchymal identity of ovarian cancers through transfer of exosome-derived microRNAs. *Sci. Adv.* **7**, eabb0737 (2021).

348. Yang, Z. *et al.* Reprogramming of stromal fibroblasts by SNAI2 contributes to tumor desmoplasia and ovarian cancer progression. *Mol. Cancer* **16**, 163 (2017).

349. Regier, M. C. *et al.* Transitions from mono- to co- to tri-culture uniquely affect gene expression in breast cancer, stromal, and immune compartments. *Biomed. Microdevices* **18**, 70 (2016).

350. Witte, C. J. de *et al.* Patient-Derived Ovarian Cancer Organoids Mimic Clinical Response and Exhibit Heterogeneous Inter- and Intrapatient Drug Responses. *Cell Rep.* **31**, (2020).

351. Jenkins, R. W. *et al.* Ex Vivo Profiling of PD-1 Blockade Using Organotypic Tumor Spheroids. *Cancer Discov.* **8**, 196–215 (2018).

352. Eckhardt, B. L. *et al.* Clinically relevant inflammatory breast cancer patient-derived xenograft–derived ex vivo model for evaluation of tumor-specific therapies. *PLOS ONE* **13**, e0195932 (2018).

353. Heo, E. J. *et al.* Patient-Derived Xenograft Models of Epithelial Ovarian Cancer for Preclinical Studies. *Cancer Res. Treat. Off. J. Korean Cancer Assoc.* **49**, 915–926 (2017).

354. Shao, X. *et al.* Inhibition of M2-like macrophages by all- trans retinoic acid prevents cancer initiation and stemness in osteosarcoma cells. *Acta Pharmacol. Sin.* **40**, 1343–1350 (2019).

355. Wen, J. *et al.* IL-8 promotes cell migration through regulating EMT by activating the Wnt/β-catenin pathway in ovarian cancer. *J. Cell. Mol. Med.* **24**, 1588–1598 (2020).

356. Molli, P. R., Li, D. Q., Murray, B. W., Rayala, S. K. & Kumar, R. PAK signaling in oncogenesis. *Oncogene* **28**, 2545–2555 (2009).

357. Jia, R., Zhao, H. & Wang, S. Neuregulin Signaling in the Tumor Microenvironment. in *Tumor Microenvironment: Signaling Pathways – Part B* (ed. Birbrair, A.) 1–29 (Springer International Publishing, 2021). doi:10.1007/978-3-030-47189-7_1.

358. Fang, D. *et al.* Epithelial-Mesenchymal Transition of Ovarian Cancer Cells Is Sustained by Rac1 through Simultaneous Activation of MEK1/2 and Src Signaling Pathways. *Oncogene* **36**, 1546–1558 (2017).

359. Al Ameri, W. *et al.* Cell Type-Specific TGF-β Mediated EMT in 3D and 2D Models and Its Reversal by TGF-β Receptor Kinase Inhibitor in Ovarian Cancer Cell Lines. *Int. J. Mol. Sci.* **20**, (2019).

360. Guo, Y., Cui, W., Pei, Y. & Xu, D. Platelets promote invasion and induce epithelial to mesenchymal transition in ovarian cancer cells by TGF-β signaling pathway. *Gynecol. Oncol.* **153**, 639–650 (2019).

361. Kong, F.-F. *et al.* FOXM1 regulated by ERK pathway mediates TGF-β1-induced EMT in NSCLC. *Oncol. Res.* **22**, 29–37 (2014).

362. Rafehi, S. *et al.* TGFβ signaling regulates epithelial-mesenchymal plasticity in ovarian cancer ascites-derived spheroids. *Endocr. Relat. Cancer* **23**, 147–159 (2016).

363. Yu, C.-P. *et al.* FoxM1 promotes epithelial-mesenchymal transition of hepatocellular carcinoma by targeting Snai1. *Mol. Med. Rep.* **16**, 5181–5188 (2017).

364. Xiong, Y. *et al.* iASPP induces EMT and cisplatin resistance in human cervical cancer through miR-20a-FBXL5/BTG3 signaling. *J. Exp. Clin. Cancer Res.* **36**, 48 (2017).

365. Zhu, J. *et al.* Galectin-1 induces metastasis and epithelial-mesenchymal transition (EMT) in human ovarian cancer cells via activation of the MAPK JNK/p38 signalling pathway. *Am. J. Transl. Res.* **11**, 3862–3878 (2019).

366. Aldinucci, D., Borghese, C. & Casagrande, N. The CCL5/CCR5 Axis in Cancer Progression. *Cancers* **12**, 1765 (2020).

367. Long, H. *et al.* Autocrine CCL5 signaling promotes invasion and migration of CD133+ ovarian cancer stem-like cells via NF-κB-mediated MMP-9 upregulation. *Stem Cells Dayt. Ohio* **30**, 2309–2319 (2012).

368. Sánchez-Tilló, E. *et al.* β-catenin/TCF4 complex induces the epithelial-to-mesenchymal transition (EMT)-activator ZEB1 to regulate tumor invasiveness. *Proc. Natl. Acad. Sci. U. S. A.* **108**, 19204–19209 (2011).

369. Mullany, L. K. *et al.* Specific TP53 Mutants Overrepresented in Ovarian Cancer Impact CNV, TP53 Activity, Responses to Nutlin-3a, and Cell Survival. *Neoplasia N. Y. N* **17**, 789–803 (2015).

370. Stuart, T. *et al.* Comprehensive Integration of Single-Cell Data. *Cell* **177**, 1888-1902.e21 (2019).

371. Xu, S., Grande, F., Garofalo, A. & Neamati, N. Discovery of a novel orally active small-molecule gp130 inhibitor for the treatment of ovarian cancer. *Mol. Cancer Ther.* **12**, 937–949 (2013).

372. Liang, R. *et al.* STAT3 signaling in ovarian cancer: a potential therapeutic target. *J. Cancer* **11**, 837–848 (2020).

373. Xu, S. *et al.* Discovery of an orally active small-molecule irreversible inhibitor of protein disulfide isomerase for ovarian cancer treatment. *Proc. Natl. Acad. Sci.* **109**, 16348–16353 (2012).

374. Xu, S. *et al.* Inhibition of protein disulfide isomerase in glioblastoma causes marked downregulation of DNA repair and DNA damage response genes. *Theranostics* **9**, 2282–2298 (2019).

375. Nallanthighal, S., Heiserman, J. P. & Cheon, D.-J. The Role of the Extracellular Matrix in Cancer Stemness. *Front. Cell Dev. Biol.* **7**, (2019).

376. Chan, T.-S., Shaked, Y. & Tsai, K. K. Targeting the Interplay Between Cancer Fibroblasts, Mesenchymal Stem Cells, and Cancer Stem Cells in Desmoplastic Cancers. *Front. Oncol.* **9**, (2019).

377. Shea, M. P., O'Leary, K. A., Wegner, K. A., Vezina, C. M. & Schuler, L. A. High collagen density augments mTOR-dependent cancer stem cells in ERα+ mammary carcinomas, and increases mTOR-independent lung metastases. *Cancer Lett.* **433**, 1–9 (2018).

378. Amann, A. *et al.* Development of an Innovative 3D Cell Culture System to Study Tumour - Stroma Interactions in Non-Small Cell Lung Cancer Cells. *PLOS ONE* **9**, e92511 (2014).

379. Duval, K. *et al.* Modeling Physiological Events in 2D vs. 3D Cell Culture. *Physiology* **32**, 266–277 (2017).

380. Tsai, S. *et al.* Development of primary human pancreatic cancer organoids, matched stromal and immune cells and 3D tumor microenvironment models. *BMC Cancer* **18**, 335 (2018).

381. Burdall, S. E., Hanby, A. M., Lansdown, M. R. & Speirs, V. Breast cancer cell lines: friend or foe? *Breast Cancer Res.* **5**, 89–95 (2003).

382. Lamichhane, S. P. *et al.* Recapitulating epithelial tumor microenvironment in vitro using three dimensional tri-culture of human epithelial, endothelial, and mesenchymal cells. *BMC Cancer* **16**, 581 (2016).

383. Bogdanowicz, D. R. & Lu, H. H. Multifunction Co-culture Model for Evaluating Cell–Cell Interactions. *Methods Mol. Biol. Clifton NJ* **1202**, 29–36 (2014).

384. Schneeberger, V. E., Allaj, V., Gardner, E. E., Poirier, J. T. & Rudin, C. M. Quantitation of Murine Stroma and Selective Purification of the Human Tumor Component of Patient-Derived Xenografts for Genomic Analysis. *PLoS ONE* **11**, e0160587 (2016).

385. Yang, L. *et al.* Targeting cancer stem cell pathways for cancer therapy. *Signal Transduct. Target. Ther.* **5**, 1–35 (2020).

386. Zou, B., Sun, S., Qi, X. & Ji, P. Aldehyde dehydrogenase activity is a cancer stem cell marker of tongue squamous cell carcinoma. *Mol. Med. Rep.* **5**, 1116–1120 (2012).

387. Takigawa, H. *et al.* Mesenchymal Stem Cells Induce Epithelial to Mesenchymal Transition in Colon Cancer Cells through Direct Cell-to-Cell Contact. *Neoplasia* **19**, 429–438 (2017).

388. Kletukhina, S., Neustroeva, O., James, V., Rizvanov, A. & Gomzikova, M. Role of Mesenchymal Stem Cell-Derived Extracellular Vesicles in Epithelial–Mesenchymal Transition. *Int. J. Mol. Sci.* **20**, 4813 (2019).

389. Romeo, E., Caserta, C. A., Rumio, C. & Marcucci, F. The Vicious Cross-Talk between Tumor Cells with an EMT Phenotype and Cells of the Immune System. *Cells* **8**, 460 (2019).

390. Sigurdsson, V. *et al.* Endothelial induced EMT in breast epithelial cells with stem cell properties. *PloS One* **6**, e23833 (2011).

391. Ghuwalewala, S. *et al.* CD44highCD24low molecular signature determines the Cancer Stem Cell and EMT phenotype in Oral Squamous Cell Carcinoma. *Stem Cell Res.* **16**, 405–417 (2016).

392. Mladinich, M., Ruan, D. & Chan, C.-H. Tackling Cancer Stem Cells via Inhibition of EMT Transcription Factors. *Stem Cells International* https://www.hindawi.com/journals/sci/2016/5285892/ (2016) doi:10.1155/2016/5285892.

393. Tanabe, S., Quader, S., Cabral, H. & Ono, R. Interplay of EMT and CSC in Cancer and the Potential Therapeutic Strategies. *Front. Pharmacol.* **11**, (2020).

394. Zhang, G. *et al.* How BMP-2 induces EMT and breast cancer stemness through Rb and CD44? *Cell Death Dis.* **9**, 1–3 (2018).

395. Zhou, L. *et al.* Identification of cancer-type specific expression patterns for active aldehyde dehydrogenase (ALDH) isoforms in ALDEFLUOR assay. *Cell Biol. Toxicol.* **35**, 161–177 (2019).

396. Li, G. *et al.* ALDH1A3 induces mesenchymal differentiation and serves as a predictor for survival in glioblastoma. *Cell Death Dis.* **9**, (2018).

397. Yamashita, D. *et al.* Identification of ALDH1A3 as a Viable Therapeutic Target in Breast Cancer Metastasis–Initiating Cells. *Mol. Cancer Ther.* **19**, 1134–1147 (2020).

398. Durinikova, E. *et al.* ALDH1A3 upregulation and spontaneous metastasis formation is associated with acquired chemoresistance in colorectal cancer cells. *BMC Cancer* **18**, 848 (2018).

399. Chen, W.-C. *et al.* Cancer stem cell marker CD90 inhibits ovarian cancer formation via β3 integrin. *Int. J. Oncol.* **49**, 1881–1889 (2016).

400. Connor, E. V. *et al.* Thy-1 predicts poor prognosis and is associated with self-renewal in ovarian cancer. *J. Ovarian Res.* **12**, 112 (2019).

401. Gao, M.-Q., Choi, Y.-P., Kang, S., Youn, J. H. & Cho, N.-H. CD24 + cells from hierarchically organized ovarian cancer are enriched in cancer stem cells. *Oncogene* **29**, 2672–2680 (2010).

402. Nakamura, K. *et al.* CD24 expression is a marker for predicting clinical outcome and regulates the epithelial-mesenchymal transition in ovarian cancer via both the Akt and ERK pathways. *Oncol. Rep.* **37**, 3189–3200 (2017).

403. Meng, E. *et al.* CD44+/CD24- ovarian cancer cells demonstrate cancer stem cell properties and correlate to survival. *Clin. Exp. Metastasis* **29**, 939–948 (2012).

404. Pan, X. & Ma, X. A Novel Six-Gene Signature for Prognosis Prediction in Ovarian Cancer. *Front. Genet.* **11**, (2020).

405. Jaggupilli, A. & Elkord, E. Significance of CD44 and CD24 as Cancer Stem Cell Markers: An Enduring Ambiguity. *Clin. Dev. Immunol.* **2012**, e708036 (2012).

406. Shen, Y.-A. *et al.* CD44 and CD24 coordinate the reprogramming of nasopharyngeal carcinoma cells towards a cancer stem cell phenotype through STAT3 activation. *Oncotarget* **7**, 58351–58366 (2016).

407. Kumar, A., Bhanja, A., Bhattacharyya, J. & Jaganathan, B. G. Multiple roles of CD90 in cancer. *Tumor Biol.* **37**, 11611–11622 (2016).

408. Du, B. & Shim, J. S. Targeting Epithelial–Mesenchymal Transition (EMT) to Overcome Drug Resistance in Cancer. *Molecules* **21**, 965 (2016).

409. Sun, X. & Yu, Q. Intra-tumor heterogeneity of cancer cells and its implications for cancer treatment. *Acta Pharmacol. Sin.* **36**, 1219–1227 (2015).

410. Wang, Q.-E. DNA damage responses in cancer stem cells: Implications for cancer therapeutic strategies. *World J. Biol. Chem.* **6**, 57–64 (2015).

411. Chung, S. S. & Vadgama, J. V. Curcumin and Epigallocatechin Gallate Inhibit the Cancer Stem Cell Phenotype via Down-regulation of STAT3–NFκB Signaling. *Anticancer Res.* **35**, 39–46 (2015).

412. Kim, B. R. *et al.* BMP-2 induces motility and invasiveness by promoting colon cancer stemness through STAT3 activation. *Tumour Biol. J. Int. Soc. Oncodevelopmental Biol. Med.* **36**, 9475–9486 (2015).

413. Liang, F. *et al.* The crosstalk between STAT3 and p53/RAS signaling controls cancer cell metastasis and cisplatin resistance via the Slug/MAPK/PI3K/AKT-mediated regulation of EMT and autophagy. *Oncogenesis* **8**, 1–15 (2019).

414. Lim, E.-J., Suh, Y., Kim, S., Kang, S.-G. & Lee, S.-J. Force-mediated proinvasive matrix remodeling driven by tumor-associated mesenchymal stem-like cells in glioblastoma. *BMB Rep.* **51**, 182–187 (2018).

415. Ghosh, D. *et al.* Senescent mesenchymal stem cells remodel extracellular matrix driving breast cancer cells to a more-invasive phenotype. *J. Cell Sci.* **133**, (2020).

416. Sonego, M. *et al.* TIMP-1 Is Overexpressed and Secreted by Platinum Resistant Epithelial Ovarian Cancer Cells. *Cells* **9**, 6 (2019).

417. Yang, F. *et al.* Detailed Molecular Mechanism and Potential Drugs for COL1A1 in Carboplatin-Resistant Ovarian Cancer. *Front. Oncol.* **10**, 576565 (2021).

418. Baron-Hay, S., Boyle, F., Ferrier, A. & Scott, C. Elevated serum insulin-like growth factor binding protein-2 as a prognostic marker in patients with ovarian cancer. *Clin. Cancer Res. Off. J. Am. Assoc. Cancer Res.* **10**, 1796–1806 (2004).

419. Hermawan, A. & Putri, H. Bioinformatics Analysis of TIMP1, HK2 and IGFBP7 as Potential Biomarkers and Therapeutic Targets of Paclitaxel Resistance in Breast Cancer. *Middle East J. Cancer* **12**, 198–207 (2021).

420. Sterzyńska, K. *et al.* Mutual Expression of ALDH1A1, LOX, and Collagens in Ovarian Cancer Cell Lines as Combined CSCs- and ECM-Related Models of Drug Resistance Development. *Int. J. Mol. Sci.* **20**, 54 (2019).

421. Chiang, Y.-C. *et al.* Overexpression of CHI3L1 is associated with chemoresistance and poor outcome of epithelial ovarian carcinoma. *Oncotarget* **6**, 39740–39755 (2015).

422. Januchowski, R., Zawierucha, P., Ruciński, M. & Zabel, M. Microarray-based detection and expression analysis of extracellular matrix proteins in drug-resistant ovarian cancer cell lines. *Oncol. Rep.* **32**, 1981–1990 (2014).

423. Pannuru, P. *et al.* miR-let-7f-1 regulates SPARC mediated cisplatin resistance in medulloblastoma cells. *Cell. Signal.* **26**, 2193–2201 (2014).

424. Sterzyńska, K. *et al.* The Role of Matrix Gla Protein (MGP) Expression in Paclitaxel and Topotecan Resistant Ovarian Cancer Cell Lines. *Int. J. Mol. Sci.* **19**, (2018).

425. Atiya, H., Frisbie, L., Pressimone, C. & Coffman, L. Mesenchymal Stem Cells in the Tumor Microenvironment. in *Tumor Microenvironment: Non-Hematopoietic Cells* (ed. Birbrair, A.) 31–42 (Springer International Publishing, 2020). doi:10.1007/978-3-030-37184-5_3.

426. Santi, A., Kugeratski, F. G. & Zanivan, S. Cancer Associated Fibroblasts: The Architects of Stroma Remodeling. *Proteomics* **18**, (2018).

427. Bregenzer, M. E. *et al.* Physiologic Patient Derived 3D Spheroids for Anti-neoplastic Drug Screening to Target Cancer Stem Cells. *J. Vis. Exp. JoVE* (2019) doi:10.3791/59696.

428. Qian, J. *et al.* A pan-cancer blueprint of the heterogeneous tumor microenvironment revealed by single-cell profiling. *Cell Res.* **30**, 745–762 (2020).

429. Matulonis, U. A. *et al.* Ovarian cancer. *Nat. Rev. Dis. Primer* **2**, 1–22 (2016).

430. Millstein, J. *et al.* Prognostic gene expression signature for high-grade serous ovarian cancer. *Ann. Oncol.* **31**, 1240–1250 (2020).

431. Lo Gullo, R., Eskreis-Winkler, S., Morris, E. A. & Pinker, K. Machine learning with multiparametric magnetic resonance imaging of the breast for early prediction of response to neoadjuvant chemotherapy. *Breast Edinb. Scotl.* **49**, 115–122 (2020).

432. Yin, J.-Y. *et al.* Prediction models for platinum-based chemotherapy response and toxicity in advanced NSCLC patients. *Cancer Lett.* **377**, 65–73 (2016).

433. Yu, K.-H. *et al.* Predicting Ovarian Cancer Patients' Clinical Response to Platinum-Based Chemotherapy by Their Tumor Proteomic Signatures. *J. Proteome Res.* **15**, 2455–2465 (2016).

434. Kourou, K., Exarchos, T. P., Exarchos, K. P., Karamouzis, M. V. & Fotiadis, D. I. Machine learning applications in cancer prognosis and prediction. *Comput. Struct. Biotechnol. J.* **13**, 8–17 (2015).

435. Huang, S. *et al.* Applications of Support Vector Machine (SVM) Learning in Cancer Genomics. *Cancer Genomics Proteomics* **15**, 41–51 (2018).

436. Yuan, B. *et al.* CellBox: Interpretable Machine Learning for Perturbation Biology with Application to the Design of Cancer Combination Therapy. *Cell Syst.* **12**, 128-140.e4 (2021).

437. Dijkgraaf, E. M. *et al.* Chemotherapy alters monocyte differentiation to favor generation of cancer-supporting M2 macrophages in the tumor microenvironment. *Cancer Res.* **73**, 2480–2492 (2013).

438. Nakajima, S. *et al.* Neoadjuvant Chemotherapy Induces IL34 Signaling and Promotes Chemoresistance via Tumor-Associated Macrophage Polarization in Esophageal Squamous Cell Carcinoma. *Mol. Cancer Res.* **19**, 1085–1095 (2021).

439. Kuwada, K. *et al.* The epithelial-to-mesenchymal transition induced by tumor-associated macrophages confers chemoresistance in peritoneally disseminated pancreatic cancer. *J. Exp. Clin. Cancer Res.* **37**, 307 (2018).

440. Larionova, I. *et al.* Interaction of tumor-associated macrophages and cancer chemotherapy. *OncoImmunology* **8**, e1596004 (2019).

441. Couderc, B. *et al. Mesenchymal stromal cells release CXCL1/2/8 and induce chemoresistance and macrophage polarization*. http://biorxiv.org/lookup/doi/10.1101/482513 (2018) doi:10.1101/482513.

442. Moens, S. *et al.* The mitotic checkpoint is a targetable vulnerability of carboplatin-resistant triple negative breast cancers. *Sci. Rep.* **11**, 3176 (2021).

443. Mikuła-Pietrasik, J. *et al.* Comprehensive review on how platinum- and taxane-based chemotherapy of ovarian cancer affects biology of normal cells. *Cell. Mol. Life Sci.* **76**, 681–697 (2019).

444. Bocci, G., Di Paolo, A. & Danesi, R. The pharmacological bases of the antiangiogenic activity of paclitaxel. *Angiogenesis* **16**, 481–492 (2013).

445. Michailidou, M. *et al.* Microvascular Endothelial Cell Responses in vitro and in vivo: Modulation by Zoledronic Acid and Paclitaxel? *J. Vasc. Res.* **47**, 481–493 (2010).

446. Zamora, A. *et al.* Paclitaxel induces lymphatic endothelial cells autophagy to promote metastasis. *Cell Death Dis.* **10**, 1–12 (2019).

447. Winkler, J., Abisoye-Ogunniyan, A., Metcalf, K. J. & Werb, Z. Concepts of extracellular matrix remodelling in tumour progression and metastasis. *Nat. Commun.* **11**, 5120 (2020).

448. Lee, M. X. & Tan, D. S. Weekly versus 3-weekly paclitaxel in combination with carboplatin in advanced ovarian cancer: which is the optimal adjuvant chemotherapy regimen? *J. Gynecol. Oncol.* **29**, (2018).

449. Sakellaropoulos, T. *et al.* A Deep Learning Framework for Predicting Response to Therapy in Cancer. *Cell Rep.* **29**, 3367-3373.e4 (2019).

450. Cheng, C.-C. *et al.* STAT3 exacerbates survival of cancer stem-like tumorspheres in EGFR-positive colorectal cancers: RNAseq analysis and therapeutic screening. *J. Biomed. Sci.* **25**, (2018).

451. Huang, C. *et al.* Machine learning predicts individual cancer patient responses to therapeutic drugs with high accuracy. *Sci. Rep.* **8**, 16444 (2018).

452. Yuzhalin, A. E., Urbonas, T., Silva, M. A., Muschel, R. J. & Gordon-Weeks, A. N. A core matrisome gene signature predicts cancer outcome. *Br. J. Cancer* **118**, 435–440 (2018).

453. Le Naour, A. *et al.* Tumor cells educate mesenchymal stromal cells to release chemoprotective and immunomodulatory factors. *J. Mol. Cell Biol.* **12**, 202–215 (2020).

454. Krishnamurthy, S. *et al.* Endothelial Cell-Initiated Signaling Promotes the Survival and Self-Renewal of Cancer Stem Cells. *Cancer Res.* **70**, 9969–9978 (2010).

455. Wei, L. *et al.* Genome-wide CRISPR/Cas9 library screening identified PHGDH as a critical driver for Sorafenib resistance in HCC. *Nat. Commun.* **10**, 4681 (2019).

456. Colvin, E. K. Tumor-Associated Macrophages Contribute to Tumor Progression in Ovarian Cancer. *Front. Oncol.* **4**, (2014).

457. Bachmann, M. F. & Oxenius, A. Interleukin 2: from immunostimulation to immunoregulation and back again. *EMBO Rep.* **8**, 1142–1148 (2007).

458. Zachary, A. A. & Leffell, M. S. HLA Mismatching Strategies for Solid Organ Transplantation – A Balancing Act. *Front. Immunol.* **7**, 575 (2016).

459. Chen, M.-H. *et al.* ALDH1A3, the Major Aldehyde Dehydrogenase Isoform in Human Cholangiocarcinoma Cells, Affects Prognosis and Gemcitabine Resistance in Cholangiocarcinoma Patients. *Clin. Cancer Res.* **22**, 4225–4235 (2016).

460. Armand, E. J., Li, J., Xie, F., Luo, C. & Mukamel, E. A. Single-Cell Sequencing of Brain Cell Transcriptomes and Epigenomes. *Neuron* **109**, 11–26 (2021).

461. Bai, D., Peng, J. & Yi, C. Advances in single-cell multi-omics profiling. *RSC Chem. Biol.* **2**, 441–449 (2021).

462. Vistain, L. F. & Tay, S. Single-Cell Proteomics. *Trends Biochem. Sci.* **46**, 661–672 (2021).

463. Chen, B., Khodadoust, M. S., Liu, C. L., Newman, A. M. & Alizadeh, A. A. Profiling tumor infiltrating immune cells with CIBERSORT. *Methods Mol. Biol. Clifton NJ* **1711**, 243–259 (2018).

464. Gregorutti, B., Michel, B. & Saint-Pierre, P. Correlation and variable importance in random forests. *Stat. Comput.* **27**, 659–678 (2017).

465. Rogers, J. & Gunn, S. Identifying Feature Relevance Using a Random Forest. in *Subspace, Latent Structure and Feature Selection* (eds. Saunders, C., Grobelnik, M., Gunn, S. & Shawe-Taylor, J.) 173–184 (Springer, 2006). doi:10.1007/11752790_12.